Late Pleistocene climate and circulation history of the western equatorial Pacific

Dissertation

In fulfilment of the requirements for the degree "Dr. rer. nat."
Of the Faculty of Mathematics and Natural Sciences
At Kiel University

Submitted by
Nicholas Michael Fraser

Kiel, 2016

Referent: Prof. Dr. Wolfgang Kuhnt

Koreferent: Prof. Dr. Ralph Schneider

Tag der Disputation: Freitag, den 13. Februar 2015

Zum Druck genehmigt:

Der Dekan: Prof. Dr. Wolfgang J. Duschl

Eidesstattliche Erklärung

Hiermit erkläre ich an Eides statt, dass die vorliegende Dissertation mit dem Titel 'Late Pleistocene climate and circulation history of the western equatorial Pacific', abgesehen von der Beratung durch meine akademischen Lehrer, in Inhalt und Form meine eigene Arbeit darstellt.

Ich habe diese Arbeit, ganz oder zum Teil, an keiner anderen Stelle im Rahmen eines Prüfungsverfahrens vorgelegt, veröffentlich oder zur Veröffentlichung eingereicht.

Kiel, den

Nicholas Michael Fraser

Acknowledgements

This PhD thesis would not have been possible without the help and support of many people. First and foremost, I thank my PhD supervisors Professor Wolfgang Kuhnt and Ann Holbourn for giving me the chance to undertake this position, and for all their efforts in guiding and advising me over the past four years. I am especially grateful for their extensive help in reading and improving my manuscripts, and for giving me the experience of participating in a research cruise on the R/V Sonne in 2011. I also owe thanks to Ken Johnson and Willem Renema who initiated and organised the Throughflow project, the source of my PhD funding, and for the many training and networking opportunities this project has offered.

I am grateful to the many other scientists who have contributed and helped me in my research, in particular Marcus Regenberg, Timothé Bolliet, Nils Andersen, Thomas Blanz, Silvia Koch, Dörte Mikschl, Dieter Garbe-Schönberg and Karen Bremer, and furthermore I thank Professor Ralph Scheider for acting as the second referee on this thesis.

I would also like to acknowledge all of the PhD students, Postdocs and Hiwis in MiPa and the Insistut für Geowissenschaften that I have worked and made friends with over the past years: Elena, Sven, Mohammed, Janne, Yiming, Thomas, Emma, Laura, Jeroen, Karlos, Jan, Kevin, Hendri, Janika, Larissa, Sebastian, and anyone else who I might have missed! I also thank all of my fellow PhD students in the Throughflow project, for the fun fieldtrips, conferences and other meetings: Nathan, Vibor, Anja, Sonja, Viola, Vedrana, Emanuela, Nadia, Amanda, Bill and Simone. It was great working with you, and I wish you all good luck in the future.

I am especially indebted to my parents, who have given me unwavering support at every step of my education. Without their help I would not be in the position I am today. And last, but not least, I thank Nicole for just about everything else, especially for her constant words of encouragement during the last few months.

Abstract

Reconstructions of past climate variability derived from sedimentary archives have highlighted the response of the global climate system to orbital and millennial scale forcings. Investigating these forcings and responses allows us to further understand the present day climate of the Earth, and predict its future evolution under conditions of increased anthropogenic greenhouse gas concentrations. However, in some regions of the world the exact mechanisms of past climate change remain relatively unknown, due to a lack of high-resolution proxy records, and uncertainties in the relationships between climate indices and the proxies themselves. In this work, we attempt to shed light on past variability of the ocean-atmosphere system in the western equatorial Pacific, a region that encompasses the warmest pool of water in the world and thus has a direct effect on global climate through the redistribution of heat and moisture from the tropics to the mid- and high-latitudes. This region also contains the Indonesian Throughflow (ITF), an important oceanic gateway that connects the Pacific and Indian Oceans, and plays an important role in past changes in the global thermohaline circulation.

In **Study 1**, we apply a multi-proxy geochemical analysis to sediment core MD06-3075 (06°28.6 N, 125°49.9 E, 1878 m water depth) situated in the Davao Gulf, southern Mindanao. This core provides a 120-kyr long record of past hydrologic variability at the boundary between the Indonesian archipelago and the open Pacific Ocean. Sediment runoff records from Mindanao are derived from X-ray Fluorescence (XRF) core scanning, and show that past changes in runoff were in antiphase with local precessional insolation forcing during periods of strong precessional cyclicity (e.g. in Marine Isotope Stage 5), whilst runoff was muted during periods of weak insolation forcing and lower sea level. These results are corroborated by coccolithophore-based paleoproductivity estimates, which co-vary with XRF log-ratios due to variable freshwater stratification of the water column. These changes are attributed to variability in both the position of the Inter-tropical Convergence Zone, and the strength of the Walker circulation modulated by sea level and exposure of the Sunda Shelf. Differing trends observed in seawater $\delta^{18}O$ ($\delta^{18}O_{sw}$) records from this site suggest that $\delta^{18}O_{sw}$ is a better recorder of wider regional-

scale changes in the hydrologic cycle, compared to XRF log-ratios and paleoproductivity estimates which react primarily to changes in local precipitation and runoff.

In **Study 2** we attempt to elucidate changes in deep and intermediate-depth circulation in the West Pacific and ITF over the most recent glacial-interglacial cycle, with a particular focus on the past two glacial terminations. This is carried out via a compilation of new and previously published benthic foraminiferal $\delta^{13}C$ records, which acts as a non-conservative tracer of past ocean circulation. Our most striking finding is that an increase in the proportion of $\delta^{13}C$-depleted North Pacific Intermediate Water (NPIW) at ~1600 m depth in Core MD06-3067 in the western equatorial Pacific was coeval with increasing ventilation of Antarctic Intermediate Water (AAIW) in Core MD97-2120 in the southwest Pacific during glacial terminations. These results imply that major reorganizations of intermediate water masses in the Pacific occurred during past deglacials. Records compiled for the ITF and Timor Sea regions suggest that at the onset of the last deglacial period, the ITF was separated by an AAIW-dominated 'southeastern' passage, and a NPIW-dominated 'northwestern' passage, with the latter becoming progressively more influenced by AAIW during the deglacial transition and Holocene.

In **Study 3**, we evaluate the use of two common geochemical proxies for sea surface temperature (SST) reconstructions in the western equatorial Pacific: the Mg/Ca ratio of the planktonic foraminifera *Globigerinoides ruber*, and the $U^{K'}_{37}$ alkenone unsaturation index. We compile existing core-top data from the eastern Indian Ocean and South China Sea with new core-top measurements from the Makassar Strait, Java Sea and Timor Sea. Our results indicate that the $U^{K'}_{37}$ thermometer is less sensitive to SST at temperatures >25 °C than existing global calibrations would suggest, with temperatures biased towards quiescent, low-productivity months in regions of strong seasonal temperature variability (e.g. in the Java upwelling region). In contrast, Mg/Ca ratios show a less consistent seasonally-weighted SST signal. However, significant uncertainties remain with regards to analytical procedures and post-depositional effects (e.g. dissolution, bioturbation) which warrant further investigation in the future.

Zusammenfassung

Von sedimentären Archiven abgeleitete Rekonstruktionen vergangener Klimavariabilität haben die Reaktionen des globalen Klimasystems auf Antriebe sowohl auf der Ebene der Orbital- als auch auf der der Jahrtausend-Zeitskalen aufgezeigt. Untersucht man diese Antriebe und Reaktionen, kann das moderne globale Klima besser verstanden und dessen zukünftige Entwicklung auf der Grundlage von steigender anthropogen verursachter Treibhausgaskonzentration vorhergesagt werden. In einigen Regionen der Welt sind die genauen Mechanismen vergangener Klimaveränderungen jedoch nicht nur auf Grund fehlender hochauflösender Proxy-Aufzeichnungen, sondern auch auf Grund von Ungewissheiten in der Beziehung zwischen den Klima-Indizes und den Proxys selbst relativ unbekannt. In der vorliegenden Arbeit versuchen wir über die vergangene Variabilität des Ozean-Atmosphäre-Systems im westlichen Äquatorial-Pazifik Aufschluss zu geben. Diese Region umfasst das wärmste Wassergebiet der Welt und hat durch die Umverteilung von Wärme und Feuchtigkeit von den Tropen in die mittleren und hohen Breitengrade einen direkten Einfluss auf das globale Klima. Sie enthält außerdem den Indonesischen Durchstrom (Indonesian Throughflow, ITF), eine wichtige Meerespassage, die den Pazifischen und den Indischen Ozean miteinander verbindet und eine wichtige Rolle hinsichtlich der Veränderungen der thermohalinen Zirkulation in der Vergangenheit spielt

In **Studie 1** führen wir an dem Sedimentkern MD06-3075 (06°28.6 N, 125°49.9 E, 1878 m Wassertiefe) aus dem Davao-Golf in Südmindanao eine geochemische Multiproxy-Analyse durch. Dieser Kern bietet ein 120-kyr-langes Archiv vergangener hydrologischer Variabilität an der Grenze zwischen dem indonesischen Archipel und dem offenen Pazifischen Ozean. Aufzeichnungen über fluviatilen Sedimenteintrag von Mindanao erhalten wir durch eine Röntgenfluoreszenzanalyse (X-ray Fluorescence, XRF) des Kerns. Sie zeigt, dass vergangene Änderungen im Regenwasserabfluss während Phasen starker präzessionaler Zyklizität (z. B. im Marinen Isotopenstadium 5) in einer Gegenphase zum Einfluss der lokalen präzessionalen Sonneneinstrahlung stattfanden und dass im Gegenzug dazu der Regenwasserabfluss in Phasen schwachen Einflusses der Sonneneinstrahlung und tiefen Meerespiegels gedämpft wurde. Diese Ergebnisse werden

von Schätzungen über die Paläoproduktivität auf der Grundlage von Coccolithophoriden bestätigt. welche auf Grund variabler Süßwasserschichtung der marinen Wassersäule mit dem XRF-Logarithmus-Verhältnis kovariieren. Diese Änderungen sind auf die Variabilität sowohl der Lage der Innertropischen Konvergenzzone als auch der Ausprägung der Walker-Zirkulation zurückzuführen, die ihrerseits vom Meeresspiegel und damit vom bedeckten bzw. freiliegenden Zustand des Sundaschelfs reguliert wird. Abweichende Tendenzen in Aufzeichnungen von Meereswasser $\delta^{18}O$ ($\delta^{18}O_{sw}$) dieses Ortes legen nahe, dass $\delta^{18}O_{sw}$ die Veränderungen des hydrologischen Zyklus in der weiteren Region besser aufzeichnet als die XRF-Logarithmus-Verhältnisse und als die Schätzungen der Paläoproduktivität, welche beide hauptsächlich auf Änderungen in lokalem Niederschlag und Regenwasserabfluss reagieren.

In **Studie 2** geben wir einen Einblick in die Veränderungen in der Tiefen- und der intermediären Zirkulation im West-Pazifik und im ITF im letzten glazialen-interglazialen Zyklus, wobei der besondere Fokus auf den letzten zwei glazialen Terminationen liegt. Dies geschieht anhand einer Zusammenstellung neuer und bereits veröffentlichter Aufzeichnungen von $\delta^{13}C$-Werten benthischer Foraminiferen, die als nicht-konservativer Indikator vergangener Ozeanzirkulation fungieren. Unser bedeutendstes Ergebnis ist, dass während der glazialen Terminationen der Anteil von $\delta^{13}C$-abgereichertem nordpazifischem intermediären Wasser (NPIW) in ca. 1600 m Tiefe im Kern MD06-3067 im westlichen Äquatorial-Pazifik gleichzeitig mit der Ventilation des antarktischen intermediären Wassers (AAIW) im Kern MD97-2120 im Südwest-Pazifik steigt. Diese Ergebnisse implizieren, dass in vergangenen Deglaziationen intermediäre Wassermassen im Pazifik im Wesentlichen umgeordnet wurden. Für den ITF und die Timorsee zusammengestellte Aufzeichnungen legen nahe, dass der ITF zu Beginn der letzten Deglaziation in die AAIW-dominierte „südöstliche“ Passage einerseits und in die NPIW-dominierte „nordwestliche“ Passage andererseits unterteilt wurde. Letztere wurde während der Deglaziation und dem Holozän immer stärker vom AAIW beeinflusst.

In **Studie 3** werten wir die Anwendung zweier gebräuchlicher geochemischer Proxys für die Rekonstruktion der Oberflächenwassertemperatur (sea surface temperature, SST) im westlichen Äquatorial-Pazifik aus: Erstens das Mg/Ca-Verhältnis der planktonischen

Foraminiferen *Globigerinoides ruber* und zweitens den $U^{K'}_{37}$-Alkenon-Untersättigungsindex. Wir stellen bestehende Daten der Core-Tops aus dem östlichen Indischen Ozeans und dem Südchinesischen Meer mit ebensolchen neuen Messungen aus der Straße von Makassar, der Javasee und der Timorsee zusammen. Unsere Ergebnisse zeigen, dass das $U^{K'}_{37}$-Thermometer bei der Messung der SST bei über 25 °C nicht in dem Maße reagiert, wie es bestehende globale Kalibrierungen andeuten. In Regionen starker saisonaler Temperaturschwankungen (z. B. in dem Auftriebsgebiet bei Java) kommt es zu einer Verzerrung der Temperaturangaben in Monaten mit geringem Auftrieb und niedriger Produktivität. Im Gegensatz dazu zeigt das Mg/Ca-Verhältnis ein weniger beständiges saisonales SST-Signal. Hinsichtlich der analytischen Verfahren und der Post-Ablagerungseffekte (z. B. Lösungsprozesse, Bioturbation) bleiben jedoch wesentliche Ungewissheiten bestehen. Dies erfordert weitergehende Untersuchungen in der Zukunft.

Table of Contents

Acknowledgements iv
Abstract vi
Zusammenfassung ix
Table of Contents xiii
List of Figures xviii
List of Tables xxi
List of Abbreviations xxii

1 Introduction 1
1.1 Motivations and objectives 2
1.2 Structure of the thesis 3
1.3 Western equatorial Pacific hydroclimate 4
1.3.1 Modern climatology 4
1.3.2 Late Pleistocene climate evolution 7
1.3.2.1. Glacial-interglacial cycles 7
1.3.2.2. Millennial-scale climate variability 10
1.4 Surface to deep circulation in the western equatorial Pacific 13
1.5 References 15

2 Proxies for paleoclimate reconstruction 23
2.1 Foraminifera 24
2.2 Stable isotopes of foraminifera 25
2.2.1 Oxygen isotopes 25
2.2.2 Carbon isotopes 26
2.2.3 Analytical procedure for stable isotope measurements 27
2.3 Paleotemperature reconstructions 28
2.3.1 Mg/Ca ratios of foraminifera 28
2.3.2 $U^{K'}_{37}$ alkenone unsaturation ratios 29
2.4 Radiocarbon dating 30
2.5 X-ray fluorescence core scanning 31

2.6 Paleoproductivity estimates from coccolithophore assemblages 32
2.7 References 33

3 Precipitation variability in the West Pacific Warm Pool over the past 120 ka: evidence from the Davao Gulf, Southern Philippines 41
3.1 Abstract 42
3.2 Introduction 42
3.3 Materials and Study Area 46
3.4 Methods 48
3.4.1 Accelerator Mass Spectrometry ^{14}C dating 48
3.4.2 Stable isotope analysis 48
3.4.3 XRF core scanning 49
3.4.4 Coccolith counts 49
3.4.5 Carbonate content 50
3.4.6 $U^{K'}_{37}$ SST estimates 50
3.4.7 Calculation of seawater $\delta^{18}O$ ($\delta^{18}O_{sw}$) 50
3.5 Results 52
3.5.1 Accelerator Mass Spectrometry ^{14}C dating 52
3.5.2 Stable isotopes 52
3.5.3 SST record 53
3.5.4 $\delta^{18}O_{sw}$ reconstructions 54
3.5.5 XRF core scanning 54
3.5.6 Primary Productivity 56
3.5.7 Carbonate Content 56
3.6 Discussion 57
3.6.1 Proxies of paleoprecipitation in the WPWP 57
3.6.1.1. $\delta^{18}O_{sw}$ as a proxy of past convective activity 57
3.6.1.2. Proxies of sedimentary discharge 58
3.6.2 WPWP precipitation over the past 120ka 59
3.6.2.1. Orbitally paced precipiation changes at Mindanao 59
3.6.2.2. Sub-orbital forcing of WPWP hydroclimate 63
3.7 Conclusion 65

3.8 Acknowledgements 66
3.9 References 66
3.10 Supplementaty Information 74
3.10.1 Calibration of $U^{K'}_{37}$ alkenone unsaturation ratios to SST 74
3.10.2 SSTs of the tropical West Pacific 74
3.10.3 Supplementary Tables 77
3.10.4 Supplementary Figures 78
3.10.5 Supplementary Information References 82

4 Deglacial changes in West Pacific circulation: insights from benthic foraminiferal $\delta^{13}C$ 86
4.1 Abstract 87
4.2 Introduction 88
4.3 Modern Oceanography of the West Pacific 90
4.3.1 Intermediate depth waters of the Pacific Ocean 90
4.3.2 Deepwater circulation in the Pacific Ocean 93
4.3.3 Intermediate and deep water transport in the ITF 93
4.4 Materials and Methods 95
4.4.1 Stable Isotope Records 95
4.4.1.1. Data selection criteria 95
4.4.1.2. Analytical procedure 98
4.4.2 Chronology of compiled datasets 99
4.5 Results 100
4.5.1 Chronology 100
4.5.2 $\delta^{18}O$ of benthic foraminifera during Terminations I and II 102
4.5.3 $\delta^{13}C$ of benthic foraminifera during Terminations I and II 102
4.5.4 Long-term Pacific intermediate $\delta^{18}O$ and $\delta^{13}C$ variability 105
4.6 Discussion 107
4.6.1 Robustness of the benthic foraminiferal $\delta^{13}C$ proxy as a water mass tracer 107
4.6.2 Reorganisations of Pacific water masses during the last glacial cycle 108

4.6.3 Evolution of intermediate and deep water masses in the Indonesian Throughflow 110
4.6.3.1. Last Glacial Maximum 110
4.6.3.2. Deglacial Evolution 112
4.6.3.3. Holocene 113
4.7 Conclusions 113
4.8 Acknowledgements 114
4.9 References 115
4.10 Supplementary Information 125

5 Geochemical proxies of sea surface temperature in the tropical West Pacific: Insights from modern core-tops 128
5.1 Abstract 129
5.2 Introduction 130
5.3 Study area and modern climatology 133
5.4 Data and Methods 135
5.4.1 Material and sampling strategy 135
5.4.2 Age control 135
5.4.3 Mg/Ca 136
5.4.4 $U^{K'}_{37}$ 138
5.4.5 Climatological datasets 139
5.5 Results and Discussion 140
5.5.1 Mg/Ca and $U^{K'}_{37}$ in surface sediments of the West Pacific 140
5.5.2 Seasonal relationships of SST proxies 143
5.5.3 Residual patterns of $U^{K'}_{37}$ and Mg/Ca SST 145
5.5.4 Analytical concerns for the $U^{K'}_{37}$ 'warm-end' 147
5.5.5 Secondary influences on foraminiferal Mg/Ca 150
5.6 Conclusions and Recommendations 152
5.7 References 154
5.8 Supplementary Information 161

6 Conclusions and Outlook 168

List of Figures

Chapter 1

Figure 1.1 - Global average annual distribution of sea surface temperature, salinity and productivity 5
Figure 1.2 – Modern climatologies of precipitation patterns and wind directions in the western equatorial Pacific during January and July 6
Figure 1.3 – Precipitation anomalies in the western equatorial Pacific associated with the strong El Niño and La Niña events of 1997-98, and 1998-99, respectively 7
Figure 1.4 – Orbital scale trends in sea surface temperature records from the western equatorial Pacific 8
Figure 1.5 – Speleothem records of past hydrologic variability from the western equatorial Pacific 9
Figure 1.6 – Differences in topography and bathymetry in the western equatorial Pacific between the present day and LGM conditions, when sea level was ~120 m lower 11
Figure 1.7 – Simplified schematic of surface and intermediate circulation patterns in the western equatorial Pacific and Indonesian Throughflow 14

Chapter 3

Figure 3.1 – Location map of sediment core MD06-3075 and other discussed records, together with major surface ocean currents of the western equatorial Pacific 45
Figure 3.2 – Modern climatology of the WPWP region, and at the location of core MD06-3075 47
Figure 3.3 – Age model development for core MD06-3075 51
Figure 3.4 – Stable isotope and SST records for the past 120 ka for core MD06-3075 ... 53
Figure 3.5 – Proxy records for past hydrologic variability for core MD06-3075 over the past 120 ka 55
Figure 3.6 – Comparison of hydrologic records from core MD06-3075 over the past 120 ka with speleothem records from East Asia and the West Pacific, and past sea level 60
Figure 3.7 – Expanded hydroclimate records of core MD06-3075 and speleothem

records from East Asia and the West Pacific, covering the past 20 ka 64
Supplementary Information Figure 3.1 – Comparison of $U^{K'}_{37}$ SST record with different calibrations in core MD06-3075 78
Supplementary Information Figure 3.2 – Comparison of SST and oxygen isotope records over the past 20 ka between cores MD06-3075 and MD98-2181 79
Supplementary Information Figure 3.3 – XRF raw counts of elements Ca, Fe, Ti, Al, Si, and K in core MD06-3075 80
Supplementary Information Figure 3.4 – Normalized power spectra of XRF-derived log(Fe/Ca) and local summer insolation in core MD06-3075 81

Chapter 4

Figure 4.1 – Modern oceanography of intermediate and deep waters of the Pacific Ocean 91
Figure 4.2 – Latitudinal-depth distributions of various geochemical tracers in the West Pacific 92
Figure 4.3 – Bathymetric map of the West Pacific and Indonesian Throughflow regions, and locations of sediment cores used in this study 95
Figure 4.4 – Benthic foraminiferal $\delta^{18}O$ records for all cores compiled in this study covering Termination I and II 101
Figure 4.5 – Benthic foraminiferal $\delta^{13}C$ records for all cores compiled in this study covering Termination I and II 103
Figure 4.6 – Benthic foraminiferal $\delta^{18}O$ records for Cores MD97-2120 and MD06-3067 (red) extending for the past 160 kyr 106
Figure 4.7 – Compilation of intermediate-depth West Pacific and ITF benthic foraminiferal $\delta^{13}C$ records covering Termination I 111
Supplementary Information Figure 1 – Age-depth relationship for new records presented in this study, including cores MD06-3067, SO217-18522, SO217-18526 and SO217-18540 111

Chapter 5

Figure 5.1 – Maps of modern satellite-derived SST and productivity in the WEP during January and July 134

Figure 5.2 – Distribution of Mg/Ca and $U^{K'}_{37}$ measurements compiled in this study, together with monthly climatologies of SST and productivity for samples regions 137

Figure 5.3 – Comparison of small-scale SST structure between satellite-derived and World Ocean Atlas derived SST products.....139

Figure 5.4 – Compiled raw and cleaning-corrected Mg/Ca core-top measurements versus mean annual SST, together with spatial distribution in the WEP 141

Figure 5.5 – Compiled $U^{K'}_{37}$ core-top measurements versus mean annual SST, together with spatial distribution in the WEP 142

Figure 5.6 – Spatial correlation of $U^{K'}_{37}$ and Mg/Ca versus monthly SST, mean annual SST, annual maximum SST, annual minimum SST and productivity-weighted SST.....144

Figure 5.7 – Maps of normalized residual SST patterns calculated from existing core-top calibrations for compiled $U^{K'}_{37}$ and Mg/Ca measurements 146

Figure 5.8 – Alkenone concentrations versus $U^{K'}_{37}$ residual SST for new measurements, together with spatial distribution in the Makassar Strait, Java Sea and Timor Sea.....149

Figure 5.9 – Carbonate ion saturation states for our study region, versus water depth, Mg/Ca and Mg/Ca residual SST of compiled measurements.....151

List of Tables

Chapter 3

Supplementary Information Table 3.1 – AMS ^{14}C dates and tie points used to contrain the age model of core MD06-3075 77

Chapter 4

Table 4.1 – Summary of sediment cores compiled in this study 96
Supplementary Information Table 4.1 – Summary of AMS ^{14}C dates used to construct new (Cores SO217-18522, SO217-18526, SO217-18540) and update existing (MD06-3067) age models for this study 125

Chapter 5

Supplementary Information Table 5.1 - Summary of compiled new and previously published $U^{K'}_{37}$ and Mg/Ca measurements 161

List of Abbreviations

AAIW ..... Antarctic Intermediate Water
AMOC ..... Atlantic Meridional Overturning Circulation
AMS ..... Accelerator Mass Spectrometry
AVHRR ..... Andvanced Very High Resolution Radiometer
BA ..... Bølling-Allerød Period
D-O ..... Dangaard-Oeschger
EAM ..... East Asian Monsoon
EDML ..... EPICA ice core from Dronning Maud Land
EEP ..... Eastern Equatorial Pacific
ENSO ..... El Niño Southern Oscillation
EPICA ..... European Project for Ice Coring in Antarctica
GISP ..... Greenland Ice Sheet Project
HS ..... Heinrich Stadial
IAM ..... Indo-Australian Monsoon
ICP-OES ..... Inductively Coupled Plasma Optical Emission Spectrometer
IIW ..... Indonesian Intermediate Water
IOCW ..... Indian Ocean Intermediate Water
ITCZ ..... Inter-tropical Convergence Zone
ITF ..... Indonesian Throughflow
KC ..... Kuroshio Current
LGM ..... Last Glacial Maximum
maSST ..... Mean Annual Sea Surface Temperature
MC ..... Mindanao Current
MIS ..... Marine Isotope Stage
NEC ..... North Equatorial Current
NECC ..... North Equatorial Counter Current
NPIW ..... North Pacific Intermediate Water
NPP ..... Net Primary Productivity
PDB ..... Pee Dee Belemnite
PDW ..... Pacific Deep Water

PMOC ..... Pacific Meridional Overturning Circulation
SCS ..... South China Sea
SEC ..... South Equatorial Current
SMOW ..... Standard Mean Ocean Water
SSS ..... Sea Surface Salinity
SST ..... Sea Surface Temperature
THC ..... Thermohaline circulation
WEP ..... Western Equatorial Pacific
WOCE ..... World Ocean Circulation Experiment
WPWP ..... West Pacific Warm Pool
XRF ..... X-ray Fluorescence
YD ..... Younger Dryas

Chapter 1

Introduction

1.1 Motivation and Objectives

In the modern day, the addition of greenhouse gases to the atmosphere from human activities has the potential to cause significant changes in the Earth's climate (Intergovernmental Panel on Climate Change, 2013). These climate changes may have wide ranging socio-economic impacts, and thus increasing our understanding of the reaction of the Earth system to external (e.g. solar, orbital) and internal (e.g. greenhouse gases, ocean circulation, ice-albedo) forcings remains a critically important challenge. Exploration of past records of climate change found in natural archives (e.g. marine sediments, ice cores, speleothems, tree rings, corals) allows us to understand how the Earth has responded in the past to these climate forcings over a range of timescales, and can therefore aid us in making predictions of future climate.

During the Quaternary period (~2.6 Ma to present), the Earth experienced a continuous series of glacial (cold) and interglacial (warm) cycles in response to changes in orbital parameters (Imbrie et al., 1984), which are captured and documented in paleoclimate archives from around the globe. Ice cores from Antarctica (e.g. EPICA community members, 2004; Jouzel et al., 2007) and deep marine sediments (Lisiecki and Raymo, 2004) suggest that glacial and interglacial cycles varied on ~100 kyr timescales, consistent with the eccentricity component of orbital forcing. In glacial times, the volume and extent of polar ice sheets was significantly greater than the present day, resulting in sea levels up to 120 m lower (Lambeck and Chappell, 2001). Additionally, atmospheric CO_2 was about 80 - 100 ppm lower during glacial times (Petit et al., 1999) due to an increase in carbon storage in the deep oceans, which was subsequently released to the atmosphere during periods of warming (Sigman and Boyle, 2000; Toggweiler et al., 2006).

In addition to these orbital-scale climate fluctuations, rapid shifts in climate, for example Heinrich Events documented in North Atlantic marine sediments (Heinrich, 1988) and Dansgaard-Oeschger Events documented in Greenland ice cores (Dansgaard et al., 1993), can affect global climate on relatively short (sub-centennial) timescales. These rapid events have been shown to be driven by high-latitude northern hemisphere climate instabilities, for example through the discharge of icebergs and/or flooding of glacial

lakes into the North Atlantic, resulting in a shutdown of the Atlantic Meriodional Overturning Circulation (AMOC), a critical component of the global Thermohaline Circulation (THC). As such, much paleoclimate research in the past decades has focused on polar regions. However, the exact mechanisms and responses of past climate change in some regions of the world, for example in the western equatorial Pacific (WEP), the focus of this thesis, remain enigmatic.

The western equatorial Pacific (WEP) region, consisting of the western Pacific Ocean, the Maritime Continent of Indonesia, Papua New Guinea and the Philippines, and North Australia, encompasses the warmest pool of water in the world today, which supplies heat and moisture to the extra-tropical regions. This region also encompasses the Indonesian Throughflow, the sole pathway of mid-latitude waters masses between the Pacific and Indian Oceans, which has a direct influence on the distribution of heat, salt and nutrients between oceanic basins. Atmospheric and oceanic teleconnections between the WEP and the mid- and high-latitudes may therefore play an important role in past climate changes. However, given its geographic size, much of our knowledge of past climate and circulation in this region over the late Quaternary period is gained from relatively few records from marine sediment cores and speleothems. The focus of this work is therefore to add new (and re-assess existing) records of tropical climate and circulation in the WEP region. We primarily consider the most recent glacial-interglacial cycles of the late Quaternary, with new records of tropical hydroclimate extending over the past 120 ka (Chapter 3), and new records of deep and intermediate circulation over the past 160 ka (Chapter 4). Additionally, we aim to critically assess proxy methods for paleoclimate reconstructions, to understand their application and limitations when applied to this complex region.

1.2 Structure of the thesis

This thesis is subdivided into 6 main chapters, as outlined below:

The remainder of **Chapter 1** provides a brief introduction to the current state of knowledge regarding the modern, and late Pleistocene, climate and oceanography of the West Pacific region.

Chapter 2 gives an overview of paleoclimate proxy methods that have been employed within the scope of this thesis, in terms of the physical/chemical/biological basis of each proxy, sample preparation and measurement techniques, interpretations and limitations.

Chapter 3 is a multi-proxy study focused on changes in WEP hyroclimate on orbital and suborbital timescales, entitled 'Precipitation variability in the West Pacific Warm Pool over the past 120 ka: evidence from the Davao Gulf, Southern Philippines', by N. Fraser, W. Kuhnt, A. Holbourn, T. Bolliet, N. Andersen, T. Blanz and L. Beaufort. This manuscript is published in the journal *Paleoceanography* (doi: 10.1002/2013PA002599).

Chapter 4 is a study on changes in intermediate and deep ocean circulation in the WEP over the two most recent glacial terminations, entitled 'Deglacial changes in West Pacific circulation: insights from benthic foraminiferal $\delta^{13}C$' by N. Fraser, A. Holbourn, W. Kuhnt, T. Bolliet, N. Andersen, J. Schröder, S. Beil, M. Hendrizan, K. Tachikawa and L. Vidal. This manuscript is currently in preparation for submission to the journal *Palaeogeography, Palaeoclimatology, Palaeoecology.*

Chapter 5 is entitled 'Geochemical proxies of sea surface temperature in the tropical West Pacific: Insights from modern core-tops'. This chapter is an exploratory study of the application and limitations of two commonly used geochemical proxies of sea surface temperature (SST) in the West Pacific- the Mg/Ca ratio of planktonic foraminifera, and the coccolithophore-derived $U^{K'}_{37}$ index.

Final conclusions of this thesis are given in **Chapter 6**, with recommendations and suggestions for the direction of future work.

1.3 Western Equatorial Pacific hydroclimate

1.3.1 Modern climatology

The climate of the WEP is strongly influenced by the modern West Pacific Warm Pool (WPWP), a large pool of surface water in excess of 28 °C which supplies significant amounts of moisture to the atmosphere via evaporation and convection. High rainfall rates driven by intense convection lead to the relatively fresh sea surface salinities (SSS) observed in the WPWP surface layer. This warm, low salinity surface layer induces a well-stratified upper water column, resulting in generally oligotrophic conditions (Figure 1.1).

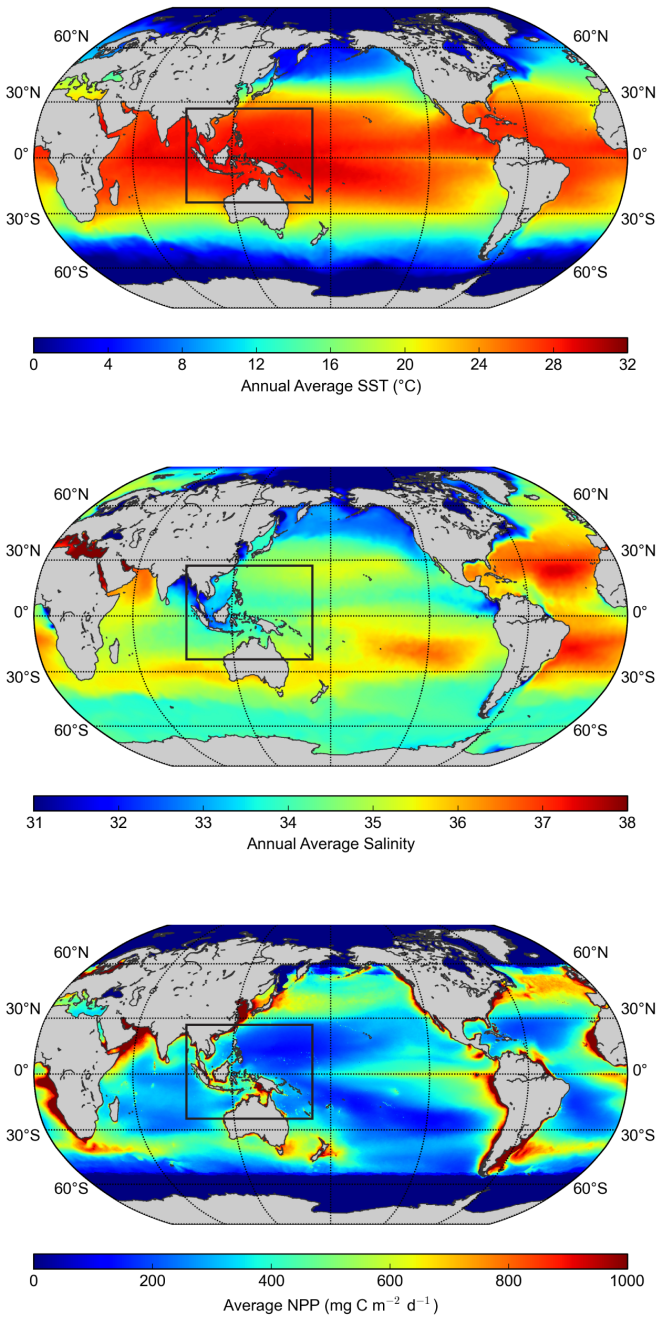

Figure 1.1 – (top) Global annual average SST, from the ¼-degree gridded World Ocean Atlas 2013 (Locarnini et al., 2013). (middle) Global annual average sea surface salinities, from the ¼-degree gridded World Ocean Atlas 2013 (Zweng et al., 2013). (bottom) Satellite-derived global annual average Net Primary Productivity (NPP) (Behrenfeld et al., 2006). Black box indicates location of WEP, the focus of this study.

Seasonal climatic patterns in the WEP are governed primarily by the annual latitudinal migration of the Intertropical Convergence Zone (ITCZ), a narrow band of convergent surface winds close to the equator, in response to varying interhemispheric temperature gradients (Waliser and Gautier, 1993; Schneider et al., 2014). During the boreal summer, higher insolation and surface temperatures to the North of the equator drives the center of convergence northwards, resulting in high precipitation anomalies in South-East China and the northern regions of the maritime continent. In contrast, North Australia and the southern maritime continent remain relatively dry. The opposite patterns occur during the austral summer (Figure 1.2). The seasonal reversal of wind directions and associated rainfall patterns are additionally associated with the Asian monsoon systems, which can be further sub-divided into the East Asian Monsoon (EAM) and Indo-Australian Monsoon (IAM).

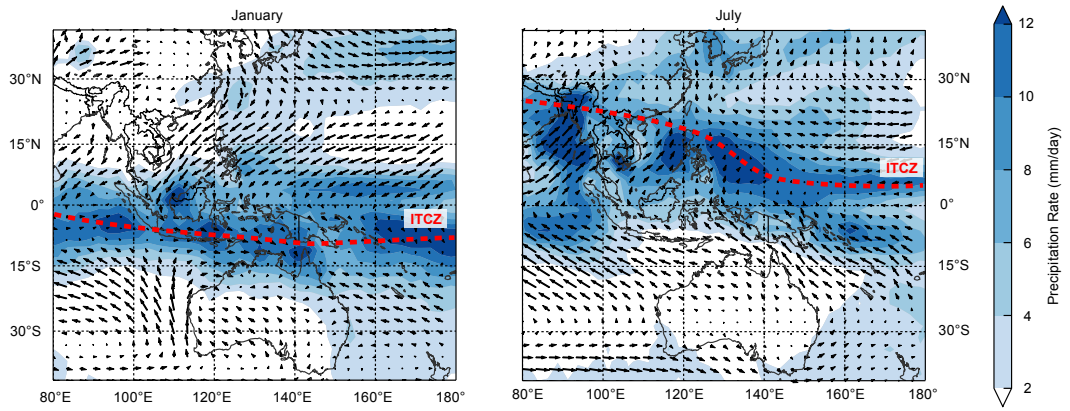

Figure 1.2 – Modern climatologies of precipitation patterns and wind directions in the WEP during January (left) and July (right). Precipitation patterns are derived from the global merged dataset of Xie and Arkin (1997). Wind directions are derived from the NCEP/NCAR reanalysis project, available at http://www.esrl.noaa.gov (Kalnay et al., 1996). Position of ITCZ is denoted by red dashed line, following Waliser and Gautier (1993).

The strength of convection in the WEP is furthermore modulated by the strength of the Walker Circulation, an atmospheric circulation cell constituting a rising branch in the West Pacific, and a subsiding branch in the East Pacific (Bjerknes, 1969; Ropelewski and Halpert, 1986). Easterly trade winds associated with the Walker Circulation drive heat and moisture to the West Pacific, resulting in a large zonal SST gradient across the

tropical Pacific Ocean. The strength of the modern Walker Circulation is modified on irregular two to ten year timescales by variability of the El Niño Southern Oscillation (ENSO) (McPhaden, 1999). During the warm phase of the ENSO cycle, named 'El Niño', a reversal of the equatorial trade winds induces an expansion and migration of warm surface waters towards the East Pacific, and a shoaling of the thermocline in the West Pacific. The reduced zonal SST gradient reinforces a weakened Walker Circulation state, resulting in weaker convection and a net drying across the WEP region (Figure 1.3). During the cold phase of the ENSO cycle, named 'La Niña', the opposite effect occurs with a strengthening of easterly trade winds across the Pacific, a stronger zonal SST gradient and average wetter conditions in the WEP.

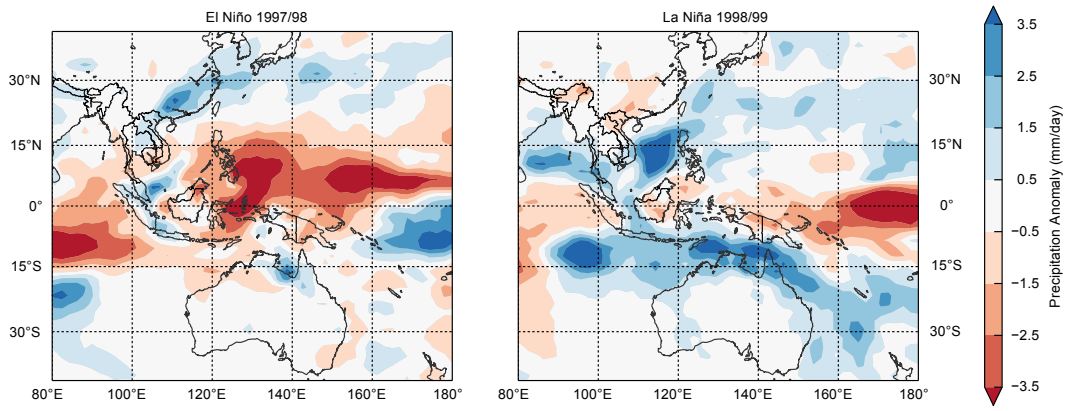

Figure 1.3 – Precipitation anomalies in the WEP associated with a strong El Niño (left) and La Niña (right) event. Data is derived from the NCEP/NCAR reanalysis project, available at http://www.esrl.noaa.gov (Kalnay et al., 1996). Composites were made for months October-March of 1997-98 and 1998-99, which represented the peak El Niño and La Niña conditions, respectively.

1.3.2 Late Pleistocene climate evolution

1.3.2.1 Glacial-interglacial cycles

On long (orbital) timescales, the evolution of climate in the WEP remains controversial, primarily due to a low number of high-resolution records extending over multiple glacial cycles. Several SST records show consistent variability with amplitudes between glacial and interglacial states on the order of 2 - 4 °C (e.g. Lea et al., 2000; de Garidel-Thoron et

al., 2005, 2007; Stott et al., 2007; Xu et al., 2010; Bolliet et al., 2011; Tachikawa et al., 2014). These records suggest a strong coupling of tropical SST with atmospheric CO_2 concentrations, varying most strongly on eccentricity (~100-kyr) timescales (Lea et al., 2000; de Garidel-Thoron et al., 2005; Tachikawa et al., 2014) (Figure 1.4).

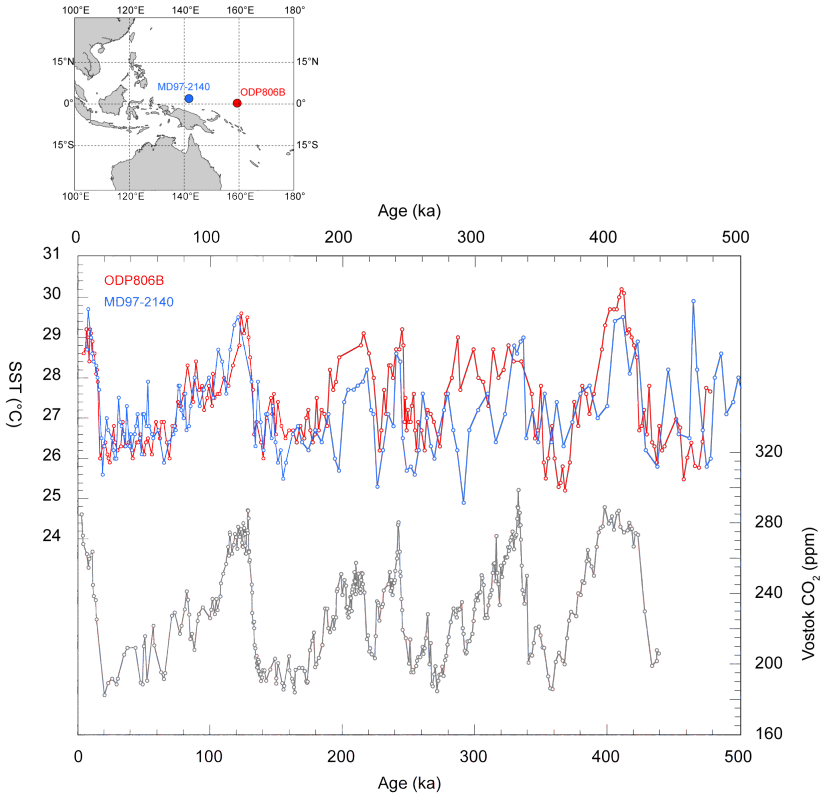

Figure 1.4 – Orbital scale trends in WPWP SST, from marine cores ODP806B (red) (Lea et al., 2000) and MD97-2140 (blue) (de Garidel-Thoron, 2005). Map shows location of core sites. Grey line represents atmospheric CO_2 concentrations derived from the Vostok ice core record from Antarctica (Petit et al., 1999).

However, these SST reconstructions are strongly dependent on the proxy used, and the potential for bias induced by growth effects (e.g. seasonality, production depth of the proxy carrier) and post-depositional processes, which can result in divergent SST trends (de Garidel Thoron et al., 2007; Timmermann et al., 2014). Critical assessment of these tropical SST records is important in constraining the sensitivity of tropical temperatures to radiative and CO_2 forcing, particularly with regards to proxy-model comparisons of

climate sensitivity (Hargreaves et al., 2012; Tachikawa et al., 2014).

Orbital-scale hydrological variability in the WEP has been resolved primarily through a handful of speleothem (Wang et al., 2001, 2008; Meckler et al., 2012; Carolin et al., 2013) and marine sediment core records (Oppo et al., 2003; Shiau et al., 2012; Tachikawa et al., 2011). Unlike SST records that primarily respond to glacial-interglacial climate variations, hydrologic variability has been associated with a significant precessional (~23 kyr) component (Figure 1.5) (Clement et al., 2004).

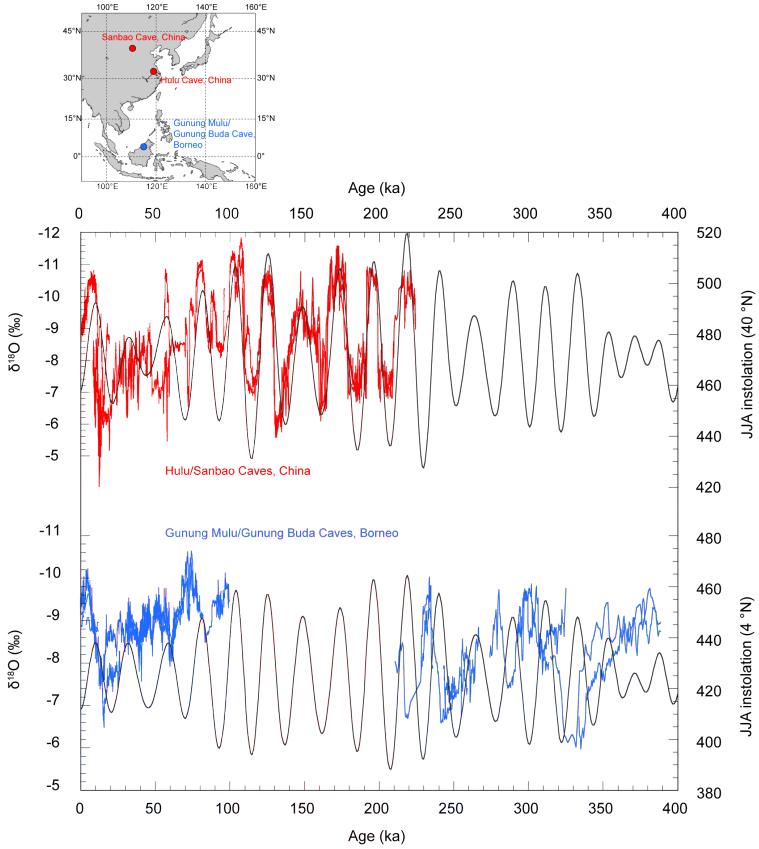

Figure 1.5 – Speleothem records of past hydrologic variability from the WPWP region. The Hulu/Sanbao Cave composite $\delta^{18}O$ record (red, top) is interpreted as a proxy of EAM strength (Wang et al., 2001, 2008), whilst the Gunung Mulu/Gunung Buda record from Borneo is interpreted as a proxy for central WPWP convection (Partin et al., 2007; Meckler et al., 2012; Carolin et al., 2013). Boreal summer (JJA) insolation at respective latitudes are plotted over speleothem $\delta^{18}O$ records.

The mechanisms driving such a strong precessional signal remain contentious. Throughout the tropics, a North-South 'seesaw-like' pattern has emerged among hydroclimate records (Wang et al., 2001, 2007, 2008; Cruz et al., 2005; Cheng et al., 2012), where those in the Northern Hemisphere show wetter conditions during Northern Hemisphere summer insolation maxima, and vice versa. This meridional pattern points towards a precessionally-paced ITCZ-like forcing of tropical hydroclimate driven by changes in interhemispheric temperature gradients. However, such a mechanism is unlikely to be the sole driver of hydrologic change in the WEP, where significant changes in atmospheric circulation may also result from changes in the strength of the Walker circulation and ENSO states on precessional timescales (Clement et al., 1999; Timmermann et al., 2007). Additionally, variable exposure of the Sunda Shelf induced by glacial-interglacial sea level changes may have played an important role in defining moisture transport and convection in the past (DiNezio et al., 2011; DiNezio and Tierney, 2013) (Figure 1.6).

1.3.2.2 Millennial-scale climate variability

In addition to glacial-interglacial and precessional variability documented in West Pacific paleoclimate records, millennial-scale hydroclimate fluctuations have been observed which have been widely associated with rapid climate events that occurred in polar regions. During Marine Isotope Stage (MIS) 3, rapid climate fluctuations in response to Heinrich stadials are documented in high-resolution oxygen isotope ($\delta^{18}O$) records from speleothems (Wang et al., 2001; Carolin et al., 2013) and marine sediments (Dannenmann et al., 2003; Saikku et al., 2009; Shiau et al., 2011), as well as in terrestrial archives (Müller et al., 2008). These records implicate a southward shift in the position of the ITCZ in response to Northern Hemisphere cooling events, consistent with deuterium and $\delta^{18}O$ records from Greenland which suggest a southward shift of Greenland moisture sources during these time periods (Masson-Delmotte et al., 2005). However, several studies have instead suggested a more prominent role for long-term ENSO variability as a major control on the tropical West Pacific hydrological cycle (Stott et al., 2002; Turney et al., 2004).

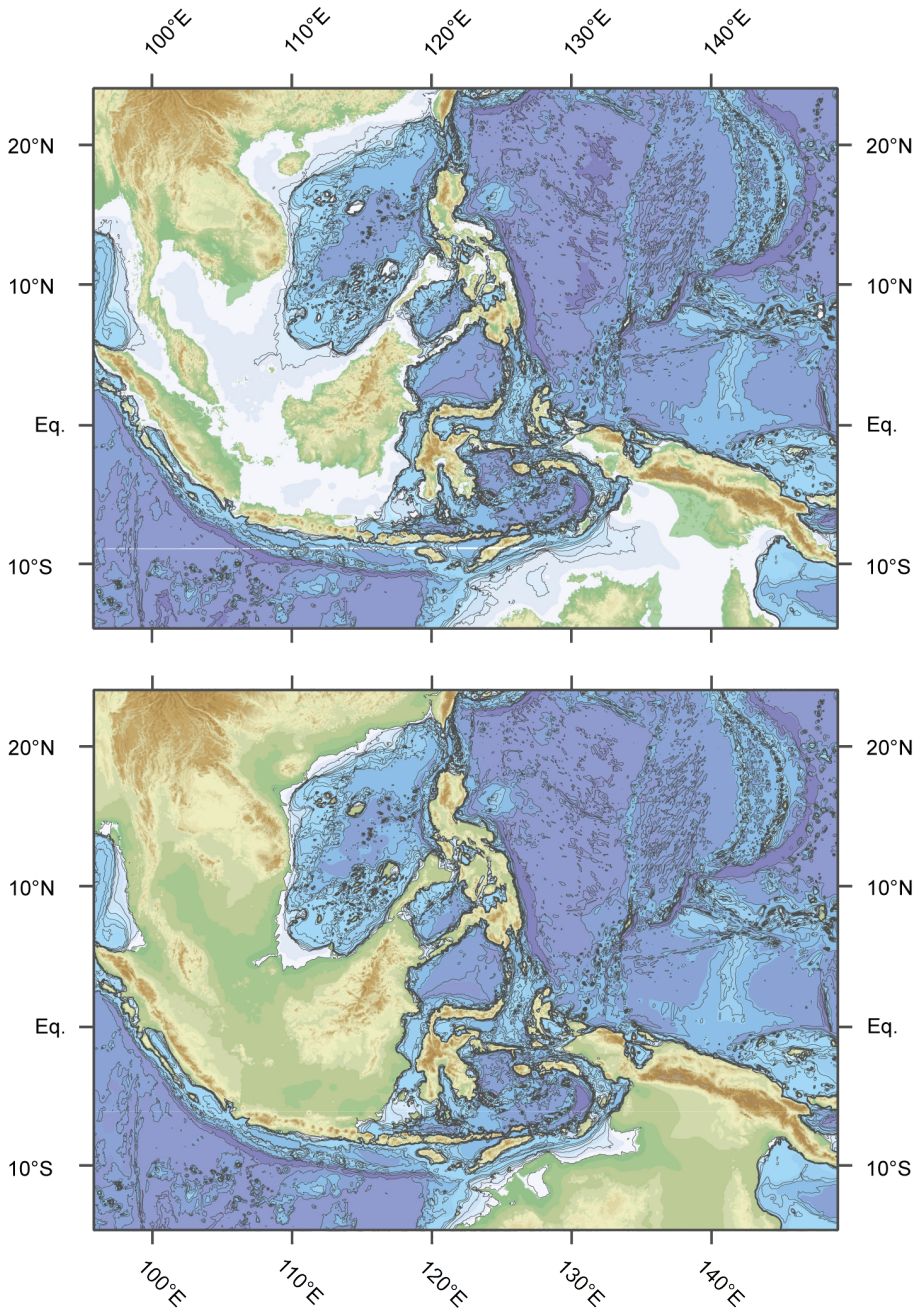

Figure 1.6 – Differences in topography and bathymetry in the Indo-Pacific between the present day (top) and LGM conditions (bottom), when sea level was ~120 m lower.

The last deglaciation is a time period of particular attention in past research into millennial-scale variability of WEP climate, in part due to the ability to produce high-resolution age models of sediment cores or speleothems via ^{14}C or U-series dating, respectively, which allow accurate detection of the timing of stadial and interstadial events. A recent study by Gibbons et al. (2014) compiled new and existing sediment core records of past changes in seawater $\delta^{18}O$ ($\delta^{18}O_{sw}$) across the Indo-Pacific region, and found that $\delta^{18}O_{sw}$ changes during Heinrich Stadial 1 (HS1) and the Younger Dryas stadial are consistent with a southward-displaced ITCZ in response to differential warming of the southern hemisphere relative to the northern hemisphere (Shakun et al., 2012). Such a finding is furthermore consistent with a number of speleothem records covering the Asian and Indo-Pacific region (Wang et al., 2001; Partin et al., 2007; Denniston et al., 2013; Ayliffe et al., 2013), which show reduced $\delta^{18}O$ (interpreted as wetter conditions) in southern regions, and increased $\delta^{18}O$ in records from the north.

However, whilst a consensus is emerging of past millennial-scale variability in WEP hydroclimate driven by displacement of the ITCZ in response to northern hemisphere cooling and warming, the exact spatial pattern of past changes in salinity and/or precipitation in the WEP remain uncertain. Recent modeling results of Mohtadi et al. (2014) highlight this fact, suggesting that the eastern side of the Indonesian archipelago may have been influenced by an incursion of increased precipitation during HS1, where a simple ITCZ-based analogy would instead predict drier conditions. Such findings highlight the non-homogenous nature of past variability of the ITCZ position, where large meridional displacements may have occurred over smaller zonal extents than the global average (McGee et al., 2014). The competing influence of the Walker circulation on WEP climate on is also largely unaccounted for on millennial timescales, yet recent studies have highlighted the importance in past changes of sea level and variable subsidence of air masses over the Sunda Shelf in driving past hydroclimate variability in the WEP (DiNezio et al., 2011; DiNezio and Tierney, 2013).

Resolving the both the orbital and sub-orbital dynamics of WEP hydroclimate variability therefore requires a larger number of continuous, late Pleistocene records, and critical interpretation of these records in terms of the exact proxy responses to past climate

changes. In this work, we present new multi-proxy records from the Davao Gulf, Southern Philippines, to reconstruct hydroclimate variability in the WEP over the past 120 ka (Chapter 3). This position is ideally placed to capture large-scale hydrologic changes recorded in surface waters of the West Pacific, as well as local precipitation variability from riverine sediment discharge into the Davao Gulf. We interpret these records within the framework of existing hydroclimate records from the WEP to further our knowledge on the past response of hydroclimate in this region to both precessional and millennial scale climate forcings.

1.4 Surface to deep ocean circulation in the western equatorial Pacific

The WEP, often referred to as a 'water mass crossroads' (Fine et al., 1994), represents a complex region of surface, intermediate and deep circulation where a number water masses converge and mix. Coupled with the Indonesian Throughflow (ITF), the conduit through which ~12 Sv of relatively cool, low-salinity waters are transported from the Pacific to the Indian Ocean (Gordon et al., 2005), the western equatorial Pacific plays an important role in the modern and past transport of heat, salt and carbon between oceanic reservoirs. Despite this, the circulation patterns of the WEP and ITF have received relatively little attention in both modern oceanographic surveys, and paleoceanographic studies. Chapter 4 of this thesis attempts to provide new insights into changes in deep and intermediate circulation patterns in the WEP and ITF over the last glacial cycle, via a compilation of benthic foraminiferal carbon isotope records from marine sediment cores. Thus, a detailed description of the modern deep and intermediate circulation patterns in this region, and an outline of the current state of knowledge regarding past changes in these patterns, can be found in the introductory section of Chapter 4 and are not outlined here.

The modern upper circulation of the WEP (Figure 1.7) is characterised by the two major Pacific Ocean gyres, which drive the westward flowing North Equatorial Current (NEC) and South Equatorial Current (SEC), separated slightly north of the equator by the reverse-flowing North Equatorial Counter-Current (NECC). As these currents reach the western Pacific landmasses, the NEC splits into two currents, one flowing northward to form the Kuroshio Current (KC), and another flowing southwards to form the

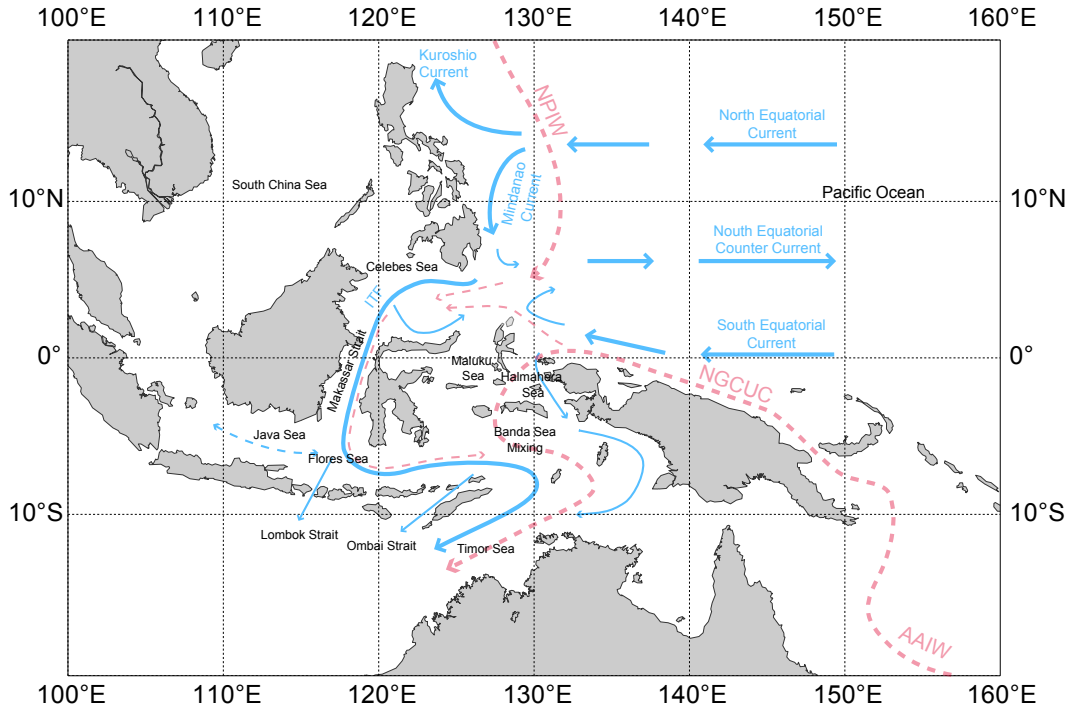

Figure 1.7 – Simplified schematic of circulation patterns in the WEP and ITF region. Blue arrows show surface and thermocline circulation (modified from Gordon et al., 2005), whilst red arrows indicate pathways of intermediate-depth waters from the Pacific through the ITF. Note that the main surface and thermocline flow of the ITF flows through the northwestern Makassar Strait route, whilst the strongest intermediate water flow is through the southwestern Banda Sea route, with only a minor contribution in the northwestern passage.

Mindanao Current (MC) (Toole et al., 1990; Qu et al., 2003), which eventually forms the dominant part of the ITF surface and thermocline flow (Gordon and Fine, 1996). In the south, the SEC flows northwards along the coast of Papua New Guinea, with a portion returning to the NECC, and a portion also joining the ITF. Within the ITF, the strongest flow (70-80 %) occurs within the surface and thermocline layers in the 'northwestern' route, comprising the Celebes Sea and Makassar Strait (within which the strength of the surface component is further modulated by the seasonal reversal of low-salinity Java Sea waters), with a smaller fraction flowing through the Halmahera and Banda Seas in the 'southeastern' route (Gordon, 2005; Sprintall et al., 2014). Throughout these transport

pathways, ITF water masses are vigorously mixed via monsoon-induced upwelling and strong tidal forces (Ffield and Gordon, 1996; Koch-Larrouy et al., 2008). Water masses eventually exit the ITF region predominantly via the Timor Strait and Ombai Strait, with a smaller contribution through the Lombok Strait (Gordon, 2005; Sprintall et al., 2014).

Recent studies into past changes of the upper circulation structure of the WEP and ITF have primarily focused on the ITF outflow passages (e.g. Xu et al., 2006; Xu et al., 2008; Zuraida et al., 2009; Holbourn et al., 2011). An overall decrease in the strength of the cool ITF thermocline outflow during cold glacial and stadial periods is observed, together with a strong control of sea level in inhibiting the warmer ITF surface flow in the Java Sea-Makassar Strait connection during deglacial transitions. These studies implicate past changes in the strength of the global THC, and variability in the IAM and position of the ITCZ in driving past changes in the ITF structure. However, a recent study of Holocene centennial-scale changes in ITF structure from the Celebes Sea and Makassar Strait has suggested a more prominent role for ENSO-like variability in driving changes in the ITF surface transport, with El-Niño episodes associated with a shoaling of the ITF surface layer, and vice versa (Fan et al., 2013). Such a finding would be consistent with modern observations of reduced ITF surface transport during El-Niño episodes (Susanto et al., 2012). Whilst we do not explicitly investigate past changes of the surface and thermocline flow in the WEP and ITF in this thesis, such changes may be related to similar processes which drive hydroclimate variability investigated in Chapter 3, and thus establishing the climatic and oceanographic context of marine sediment cores studied here may be important in understanding the coupled ocean-atmosphere system.

1.5 References

Ayliffe, L. K., Gagan, M. K., Zhao, J. X., Drysdale, R. N., Hellstrom, J. C., Hantoro, W. S., Griffiths, M. L., Scott-Gagan, H., St Pierre, E., Cowley, J. A., and Suwargadi, B. W. (2013). Rapid interhemispheric climate links via the Australasian monsoon during the last deglaciation. Nature communications, 4.

Behrenfeld, M. J., O'Malley, R. T., Siegel, D. A., McClain, C. R., Sarmiento, J. L., Feldman, G. C., Milligan, A. J., Falkowski, P. G., Letelier, R. M., and Boss, E. S. (2006). Climate-driven trends in contemporary ocean productivity. Nature, 444(7120), 752-755.

Bjerknes, J. (1969). Atmospheric teleconnections from the equatorial pacific 1. Monthly Weather Review, 97(3), 163-172.

Bolliet, T., Holbourn, A., Kuhnt, W., Laj, C., Kissel, C., Beaufort, L., Kienast, M., Andersen, N., and Garbe-Schönberg, D. (2011). Mindanao Dome variability over the last 160 kyr: Episodic glacial cooling of the West Pacific Warm Pool. Paleoceanography, 26(1).

Carolin, S. A., Cobb, K. M., Adkins, J. F., Clark, B., Conroy, J. L., Lejau, S., Malang, J., and Tuen, A. A. (2013). Varied response of western Pacific hydrology to climate forcings over the last glacial period. Science, 340(6140), 1564-1566.

Cheng, H., Sinha, A., Wang, X., Cruz, F. W., and Edwards, R. L. (2012). The Global Paleomonsoon as seen through speleothem records from Asia and the Americas. Climate dynamics, 39(5), 1045-1062.

Clement, A. C., Seager, R., and Cane, M. A. (1999). Orbital controls on the El Nino/Southern Oscillation and the tropical climate. Paleoceanography, 14(4), 441-456.

Clement, A. C., Hall, A., and Broccoli, A. J. (2004). The importance of precessional signals in the tropical climate. Climate Dynamics, 22(4), 327-341.

Cruz, F. W., Burns, S. J., Karmann, I., Sharp, W. D., Vuille, M., Cardoso, A. O., Ferrari, J. A., Silva Dias, P. L., and Viana, O. (2005). Insolation-driven changes in atmospheric circulation over the past 116,000 years in subtropical Brazil. Nature, 434(7029), 63-66.

Dannenmann, S., Linsley, B. K., Oppo, D. W., Rosenthal, Y., and Beaufort, L. (2003). East Asian monsoon forcing of suborbital variability in the Sulu Sea during Marine Isotope Stage 3: Link to Northern Hemisphere climate. Geochemistry, Geophysics, Geosystems, 4(1), 1-13.

Dansgaard, W., Johnsen, S. J., Clausen, H. B., Dahl-Jensen, D., Gundestrup, N. S., Hammer, C. U., Hvidberg, C. S., Steffensen, J. P., and Bond, G. (1993). Evidence for general instability of past climate from a 250-kyr ice-core record. Nature, 364(6434), 218-220.

de Garidel-Thoron, T., Rosenthal, Y., Bassinot, F., and Beaufort, L. (2005). Stable sea surface temperatures in the western Pacific warm pool over the past 1.75 million years. Nature, 433(7023), 294-298.

de Garidel-Thoron, T., Rosenthal, Y., Beaufort, L., Bard, E., Sonzogni, C., and Mix, A. C. (2007). A multiproxy assessment of the western equatorial Pacific hydrography during the last 30 kyr. Paleoceanography, 22(3).

Denniston, R. F., Wyrwoll, K. H., Asmerom, Y., Polyak, V. J., Humphreys, W. F., Cugley, J., Woods, D., LaPointe, Z., Peota, J., and Greaves, E. (2013). North Atlantic

forcing of millennial-scale Indo-Australian monsoon dynamics during the Last Glacial period. Quaternary Science Reviews, 72, 159-168.

DiNezio, P. N., Clement, A., Vecchi, G. A., Soden, B., Broccoli, A. J., Otto-Bliesner, B. L., and Braconnot, P. (2011). The response of the Walker circulation to Last Glacial Maximum forcing: Implications for detection in proxies. Paleoceanography, 26(3).

DiNezio, P. N., and Tierney, J. E. (2013). The effect of sea level on glacial Indo-Pacific climate. Nature Geoscience, 6(6), 485-491.

EPICA Community Members (2004). Eight glacial cycles from an Antarctic ice core. Nature, 429(6992), 623-628.

Fan, W., Jian, Z., Bassinot, F., and Chu, Z. (2013). Holocene centennial-scale changes of the Indoneisan and South China Sea throughflows: Evidences from the Makassar Strait. Global Planetary Change, 111, 111-117.

Ffield, A., and Gordon, A. L. (1996). Tidal mixing signatures in the Indonesian Seas. Journal of Physical Oceanography, 26(9), 1924-1937.

Fine, R. A., Lukas, R., Bingham, F. M., Warner, M. J., and Gammon, R. H. (1994). The western equatorial Pacific: A water mass crossroads. Journal of Geophysical Research: Oceans (1978–2012), 99(C12), 25063-25080.

Gibbons, F. T., Oppo, D. W., Mohtadi, M., Rosenthal, Y., Cheng, J., Liu, Z., and Linsley, B. K. (2014). Deglacial $\delta^{18}O$ and hydrologic variability in the tropical Pacific and Indian Oceans. Earth and Planetary Science Letters, 387, 240-251.

Gordon, A. L., and Fine, R. A. (1996). Pathways of water between the Pacific and Indian oceans in the Indonesian seas. Nature, 379, 146-149.

Gordon, A. L. (2005). Oceanography of the Indonesian Seas and their Throughflow. Oceanography, 18, 14-27.

Hargreaves, J. C., Annan, J. D., Yoshimori, M., and Abe-Ouchi, A. (2012). Can the Last Glacial Maximum constrain climate sensitivity?. Geophysical Research Letters, 39(24).

Heinrich, H. (1988). Origin and consequences of cyclic ice rafting in the northeast Atlantic Ocean during the past 130,000 years. Quaternary research, 29(2), 142-152.

Holbourn, A., Kuhnt, W., and Xu, J. (2011). Indonesian Throughflow variability during the last 140 ka: the Timor Sea outflow. Geological Society Special Publications, 355, 283-303.

Imbrie, J., Hays, J. D., Martinson, D. G., McIntyre, A., Mix, A. C., Morley, J. J., Pisias, N. G., Prell, W. L., and Shackleton, N. J. (1984). The orbital theory of Pleistocene climate: Support from a revised chronology of the marine delta18 O record.

Milankovitch and climate: Understanding the response to astronomical forcing, 1, 269.

Intergovernmental Panel on Climate Change (2013). Climate Change 2013: The Physical Science Basis. Contribution of Working Group I to the Fifth Assessment Report of the Intergovernmental Panel on Climate Change.

Jouzel, J., Masson-Delmotte, V., Cattani, O., Dreyfus, G., Falourd, S., Hoffmann, G., Minster, B., Nouet, J., Barnola, J. M., Chapellaz, J., Fischer, H., Gallet, J. C., Johnsen, S., Leuenberger, M., Loulergue, L., Luethi, D., Oerter, H., Parrenin, F., Raisbeck, G., Raynaud, D., Schilt, A., Schwander, J., Selmo, E., Souchez, R., Spahni, R., Stauffer, B., Steffense, J. P., Stenni, B., Stocker, T.F., Tison, J.L., Werner, M., and Wolff, E. W. (2007). Orbital and millennial Antarctic climate variability over the past 800,000 years. science, 317(5839), 793-796.

Kalnay, E., Kanamitsu, M., Kistler, R., Collins, W., Deaven, D., Gandin, L., Iredell, M., Saha, S., White, G., Woollen, J., Zhu, Y., Leetmaa, A., Reynolds, R., Chelliah, M., Ebisuzaki, W., Higgins, W., Janowiak, J., Mo, K. C., Ropelewski, C., Wang, J., Jenne, R., and Joseph, D. (1996), The NCEP/NCAR 40-Year Reanalysis Project. Bull. Amer. Meteor. Soc., 77, 437–471.

Koch-Larrouy, A., Madec, G., Iudicone, D., Atmadipoera, A., and Molcard, R. (2008). Physical processes contributing to the water mass transformation of the Indonesian Throughflow. Ocean Dynamics, 58(3-4), 275-288.

Lambeck, K., and Chappell, J. (2001). Sea level change through the last glacial cycle. Science, 292(5517), 679-686.

Lea, D. W., Pak, D. K., and Spero, H. J. (2000). Climate impact of late Quaternary equatorial Pacific sea surface temperature variations. Science, 289(5485), 1719-1724.

Lisiecki, L. E., and Raymo, M. E. (2005). A Pliocene-Pleistocene stack of 57 globally distributed benthic δ18O records. Paleoceanography, 20(1).

Locarnini, R. A., Mishonov, A. V., Antonov, J. I., Boyer, T. P., Garcia, H. E., Baranova, O. K., Zweng, M. M., Paver, C. R., Reagan, J. R., Johnson, D. R., Hamilton, M., and Seidov, D. (2013), World Ocean Atlas 2013, Volume 1: Temperature. S. Levitus, Ed., A. Mishonov Technical Ed., NOAA Atlas NESDIS 73, 40 pp.

Masson-Delmotte, V., Jouzel, J., Landais, A., Stievenard, M., Johnsen, S. J., White, J. W. C., Werner, M., Sveinbjornsdottir, A., and Fuhrer, K. (2005). GRIP deuterium excess reveals rapid and orbital-scale changes in Greenland moisture origin. Science, 309(5731), 118-121.

McGee, D., Donohoe, A., Marshall, J., and Ferreira, D. (2014). Changes in ITCZ location and cross-equatorial heat transport at the Last Glacial Maximum, Heinrich Stadial 1, and the mid-Holocene. Earth and Planetary Science Letters, 390, 69-79.

McPhaden, M. J. (1999). Genesis and evolution of the 1997-98 El Niño. Science, 283(5404), 950-954.

Meckler, A. N., Clarkson, M. O., Cobb, K. M., Sodemann, H., and Adkins, J. F. (2012). Interglacial hydroclimate in the tropical West Pacific through the Late Pleistocene. Science, 336(6086), 1301-1304.

Mohtadi, M., Prange, M., Oppo, D. W., De Pol-Holz, R., Merkel, U., Zhang, X., Steinke, S., and Lückge, A. (2014). North Atlantic forcing of tropical Indian Ocean climate. Nature, 509(7498), 76-80.

Muller, J., Kylander, M., Wüst, R. A., Weiss, D., Martinez-Cortizas, A., LeGrande, A. N., Jennerjahn, T., Behling, H., Anderson, W. T., and Jacobson, G. (2008). Possible evidence for wet Heinrich phases in tropical NE Australia: the Lynch's Crater deposit. Quaternary Science Reviews, 27(5), 468-475.

Oppo, D. W., Linsley, B. K., Rosenthal, Y., Dannenmann, S., and Beaufort, L. (2003). Orbital and suborbital climate variability in the Sulu Sea, western tropical Pacific. Geochemistry, Geophysics, Geosystems, 4(1), 1-20.

Partin, J. W., Cobb, K. M., Adkins, J. F., Clark, B., and Fernandez, D. P. (2007). Millennial-scale trends in west Pacific warm pool hydrology since the Last Glacial Maximum. Nature, 449(7161), 452-455.

Petit, J. R., Jouzel, J., Raynaud, D., Barkov, N. I., Barnola, J. M., Basile, I., Bender, M., Chappelaz, J., Davis, M., Delaygue, G., Delmotte, M., Kotlyakov, V. M., Legrand, M., Lipenkov, V. Y., Lorius, C., Pépin, L., Ritz, C., Saltzman, E., and Stievenard, M. (1999). Climate and atmospheric history of the past 420,000 years from the Vostok ice core, Antarctica. Nature, 399(6735), 429-436.

Qu, T., and Lukas, R. (2003). The Bifurcation of the North Equatorial Current in the Pacific*. Journal of Physical Oceanography, 33(1), 5-18.

Ropelewski, C. F., and Halpert, M. S. (1987). Global and regional scale precipitation patterns associated with the El Niño/Southern Oscillation. Monthly weather review, 115(8), 1606-1626.

Saikku, R., Stott, L., and Thunell, R. (2009). A bi-polar signal recorded in the western tropical Pacific: Northern and Southern Hemisphere climate records from the Pacific warm pool during the last Ice Age. Quaternary Science Reviews, 28(23), 2374-2385.

Schneider, T., Bischoff, T., and Haug, G. H., (2014), Migrations and dynamics of the intertropical convergence zone. Nature, 513, 45-53.

Shakun, J. D., Clark, P. U., He, F., Marcott, S. A., Mix, A. C., Liu, Z., Otto-Bliesner, B., Schmittner, A., and Bard, E. (2012). Global warming preceded by increasing carbon dioxide concentrations during the last deglaciation. Nature, 484(7392), 49-54.

Shiau, L. J., Chen, M. T., Clemens, S. C., Huh, C. A., Yamamoto, M., and Yokoyama, Y.

(2011). Warm pool hydrological and terrestrial variability near southern Papua New Guinea over the past 50k. Geophysical Research Letters, 38(8).

Shiau, L. J., Chen, M. T., Huh, C. A., Yamamoto, M., and Yokoyama, Y. (2012). Insolation and cross-hemispheric controls on Australian monsoon variability over the past 180 ka: new evidence from offshore southeastern Papua New Guinea. Journal of Quaternary Science, 27(9), 911-920.

Sigman, D. M., and Boyle, E. A. (2000). Glacial/interglacial variations in atmospheric carbon dioxide. Nature, 407(6806), 859-869.

Sprintall, J., Gordon, A. L., Koch-Larrouy, A., Lee, T., Potemra, J. T., Pujiana, K., and Wijffels, S. E. (2014). The Indonesian seas and their role in the coupled ocean-climate system. Nature Geoscience.

Stott, L., Poulsen, C., Lund, S., and Thunell, R. (2002). Super ENSO and global climate oscillations at millennial time scales. Science, 297(5579), 222-226.

Stott, L., Timmermann, A., and Thunell, R. (2007). Southern hemisphere and deep-sea warming led deglacial atmospheric CO2 rise and tropical warming. science, 318(5849), 435-438.

Susanto, R. D., Ffield, A., Gordon, A. L., and Adi, T. R. (2012). Variability of Indonesian throughflow within Makassar Strait, 2004-2009. Journal of Geophysical Research: Oceans (1978–2012), 117(C9).

Tachikawa, K., Cartapanis, O., Vidal, L., Beaufort, L., Barlyaeva, T., and Bard, E. (2011). The precession phase of hydrological variability in the Western Pacific Warm Pool during the past 400 ka. Quaternary Science Reviews, 30(25), 3716-3727.

Tachikawa, K., Timmermann, A., Vidal, L., Sonzogni, C., and Timm, O. E. (2014). CO_2 radiative forcing and Intertropical Convergence Zone influences on western Pacific warm pool climate over the past 400ka. Quaternary Science Reviews, 86, 24-34.

Timmermann, A., Lorenz, S. J., An, S. I., Clement, A., and Xie, S. P. (2007). The effect of orbital forcing on the mean climate and variability of the tropical Pacific. Journal of Climate, 20(16), 4147-4159.

Timmermann, A., Sachs, J., and Elison Timm, O. (2014). Assessing divergent SST behavior during the last 21 ka derived from alkenones and G. ruber Mg/Ca in the Equatorial Pacific. Paleoceanography.

Toggweiler, J. R., Russell, J. L., and Carson, S. R. (2006). Midlatitude westerlies, atmospheric CO2, and climate change during the ice ages. Paleoceanography, 21(2).

Toole, J. M., Millard, R. C., Wang, Z., and Pu, S. (1990). Observations of the Pacific North Equatorial Current bifurcation at the Philippine coast. Journal of Physical Oceanography, 20(2), 307-318.

Turney, C. S., Kershaw, A. P., Clemens, S. C., Branch, N., Moss, P. T., and Fifield, L. K. (2004). Millennial and orbital variations of El Nino/Southern Oscillation and high-latitude climate in the last glacial period. Nature, 428(6980), 306-310.

Waliser, D. E., and Gautier, C. (1993). A satellite-derived climatology of the ITCZ. Journal of Climate, 6(11), 2162-2174.

Wang, Y. J., Cheng, H., Edwards, R. L., An, Z. S., Wu, J. Y., Shen, C. C., and Dorale, J. A. (2001). A high-resolution absolute-dated late Pleistocene monsoon record from Hulu Cave, China. Science, 294(5550), 2345-2348.

Wang, Y., Cheng, H., Edwards, R. L., Kong, X., Shao, X., Chen, S., Wu, J., Jiang, X., Wang, X., and An, Z. (2008). Millennial-and orbital-scale changes in the East Asian monsoon over the past 224,000 years. Nature, 451(7182), 1090-1093.

Xie, P., and P.A. Arkin (1997). Global precipitation: A 17-year monthly analysis based on gauge observations, satellite estimates, and numerical model outputs. Bull. Amer. Meteor. Soc., 78, 2539 - 2558.

Xu, J., Kuhnt, W., Holbourn, A., Andersen, N., and Bartoli, G. (2006). Changes in the vertical profile of the Indonesian Throughflow during Termination II: Evidence from the Timor Sea. Paleoceanography, 21(4).

Xu, J., Holbourn, A., Kuhnt, W., Jian, Z., and Kawamura, H. (2008). Changes in the thermocline structure of the Indonesian outflow during Terminations I and II. Earth and Planetary Science Letters, 273(1), 152-162.

Xu, J., Kuhnt, W., Holbourn, A., Regenberg, M., and Andersen, N. (2010). Indo-Pacific Warm Pool variability during the Holocene and Last Glacial Maximum. Paleoceanography, 25(4).

Zweng, M. M., Reagan, J. R., Antonov, J. I., Locarnini, R. A., Mishonov, A. V., Boyer, T. P., Garcia, H. E., Baranova, O. K., Johnson, D. R., Seidov, D., and Biddle, M. M. (2013), World Ocean Atlas 2013, Volume 2: Salinity. S. Levitus, Ed., A. Mishonov Technical Ed., NOAA Atlas NESDIS 74, 39 pp.

Zuraida, R., Holbourn, A., Nürnberg, D., Kuhnt, W., Dürkop, A., and Erichsen, A. (2009). Evidence for Indonesian Throughflow slowdown during Heinrich events 3-5. Paleoceanography, 24(2).

Chapter 2

Proxies for paleoclimate reconstructions

2.1 Foraminifera

Foraminifera have proven to be a valuable archive for paleoclimate and paleoceanographic studies, allowing detailed reconstructions of past ecology (e.g. through assemblage analysis) and water-column chemistry due to the inclusion of trace metals and isotopes within their calcium carbonate ($CaCO_3$) tests. In this thesis, we have performed a range of geochemical analyses on both planktonic and benthic foraminifera. For reconstructions of past sea-surface conditions, we primarily used the planktonic foraminifera *Globigerinoides ruber* (white). This species is most commonly found in tropical and subtropical surface waters (Bé and Tolderlund, 1971), where mean annual SSTs are in excess of 15 °C (Kucera, 2007). It is typically limited to the upper 50 m of the water column (Dekens et al., 2002; Farmer et al., 2007) and is thus well suited for recording variations in surface conditions. However, the exact seasonal and depth distribution of *G. ruber* in the western equatorial Pacific is still debated, with modern ecological data derived only from a handful of sediment trap and plankton tow studies, and thus proxy signatures must be carefully interpreted with regard to these factors.

Benthic foraminifera, by contrast, provide an archive of deep-ocean conditions as they live either at the sediment-water interface (epifaunal species) or within the upper few centimeters of deposited sediments (infaunal species), with a distribution associated with the downward flux of organic material (Jorissen et al., 1995). In studies presented here, we used a few selected species of benthic foraminifera for geochemical analysis, namely *Cibicidoides (Planulina) wuellerstorfi, Cibicidoides pachyderma, Cibicidoides mundulus* and *Uvigerina* spp. *Cibicidoides* species are infaunal and thus geochemical signatures recorded in their tests are primarily a function of ambient bottom-water conditions. In contrast, *Uvigerina* species are infaunal and their geochemical records may be further influenced by processes occurring within pore-waters of deposited sediments. In addition, so-called 'vital effects', broadly defined as species-specific chemical fractionation effects in foraminifera shells as a result of external (e.g. nutrient supply) and internal (e.g. biological growth) influences (Erez, 1978; McCorkle et al., 1990), can cause significant geochemical discrepancies between different foraminifera species.

2.2 Stable isotopes of foraminifera

2.2.1 Oxygen isotopes

Stable oxygen isotopes ($\delta^{18}O$) in foraminifera are recorded as a function of the temperature and the $\delta^{18}O$ of seawater ($\delta^{18}O_{sw}$) in which the foraminifera precipitates its test (Shackleton, 1974; Bemis et al., 1998). $\delta^{18}O_{sw}$ is itself a function of the global average $\delta^{18}O_{sw}$ composition, which varies by ~1 ‰ between glacial and interglacial periods as a result of the growth and decay of continental ice sheets (known commonly as the 'ice-volume effect') (Fairbanks, 1989; Schrag et al., 2002), and the effect of the local precipitation-evaporation balance which is strongly correlated to salinity (Schmidt, 1999).

In the deep sea, the $\delta^{18}O$ of benthic foraminifera is primarily a response to ice-volume variability as temperature and salinity changes are more uniform than in surface waters (Lisiecki and Raymo, 2005). In Chapters 3 and 4 we have used the $\delta^{18}O$ signature of benthic foraminifera in sediment cores primarily for the purpose of chronological constraints. The timing of major benthic $\delta^{18}O$ excursions can be correlated to $\delta^{18}O$ excursions occurring in ice cores (e.g. the EDML ice core in Antarctica, EPICA Community Members, 2004) to provide age control of sediment cores. Where possible, we used the epifaunal species *C. wuellerstorfi* to record benthic $\delta^{18}O$ variability, but in instances of low abundances, it is replaced by *C. mundulus, C. pachyderma or Uvigerina spp.* Different species of benthic foraminifera have been shown to record different $\delta^{18}O$ signals in their calcite tests, as a result of vital effects. For example, whilst *C. wuellerstorfi* records $\delta^{18}O$ in equilibrium with seawater $\delta^{18}O$ (Marchitto et al., 2014), *Uvigerina spp.* shows a consistent offset from equilibrium $\delta^{18}O$ with the most recent estimates suggesting an offset of -0.47 ‰ (Marchitto et al., 2014), slightly higher than previous estimates of -0.64 ‰ (Shackleton, 1974). Where necessary, we have applied corrections for these species-specific offsets, which are discussed in more detail in individual chapters.

For developing chronostratigraphies from correlations of benthic foraminifera and ice core $\delta^{18}O$ records, an additional correction has to be applied to age tie-points to account

for the travel time of deep-water masses carrying the $\delta^{18}O$ signal from the polar regions (where the signal is acquired) to the tropics (where the signal is measured). New records from two intermediate-depth sediment cores presented here (Cores MD06-3075 and MD06-3067) require a correction of ~1000 years based upon modern day radiocarbon ages of intermediate-depth waters in this region. Such an approach has been justified through the use of paired planktonic-benthic radiocarbon ages (e.g. Stott et al., 2007; Khider et al., 2014) and the consistent timing of the Laschamp excursion in Core MD06-3067 (~40.8 ka, Bolliet et al., 2011) with the respective measured radiometric age (~40.7 ka, Singer et al., 2009).

$\delta^{18}O$ measurements on the planktonic foraminifera *G. ruber* have been used in this thesis primarily to estimate changes in surface $\delta^{18}O_{sw}$, which has been applied as a proxy for past changes in hydrology in the West Pacific (Gibbons et al., 2014, and references therein). This method relies on the combination of foraminiferal $\delta^{18}O$ with independent temperature estimations (e.g. from $U^{K'}_{37}$ or Mg/Ca analysis - see section 2.3) to estimate $\delta^{18}O_{sw}$, which can be further corrected for ice volume using established sea-level curves (e.g. Waelbroeck et al., 2002), leaving only the relative $\delta^{18}O_{sw}$ change associated with the evaporation-precipitation balance. Here, we use the equation of Bemis et al. (1998) to calculate $\delta^{18}O_{sw}$ from $\delta^{18}O$ and SST measurements:

$$\delta^{18}O_{sw\ (vs.\ SMOW)} = 0.27 + (SST\ (°C) - 16.5 + (4.8 \times \delta^{18}O_{(vs.\ PDB)}))/4.8$$

2.2.2 Carbon isotopes

Stable carbon isotopes ($\delta^{13}C$) in seawater primarily reflect the recycling of ^{13}C-depleted organic matter, and the fractionation of $\delta^{13}C$ during air-sea exchange. As such, water masses acquire distinct $\delta^{13}C$ signatures in their source regions, which can become more depleted in ^{13}C as the water mass ages through further recycling of organic matter. $\delta^{13}C$ measurements made on benthic foraminifera therefore have the potential to be used as non-conservative tracers of past variations in deep-water circulation and ventilation (Duplessy et al., 1984; Duplessy et al., 1988).

However, the use of this proxy relies heavily on the assumptions that the $\delta^{13}C$ signature captured in benthic foraminiferal tests is fully representative of changes in the $\delta^{13}C$ of bottom-water dissolved inorganic carbon ($\delta^{13}C_{DIC}$). Infaunal benthic foraminifera species (e.g. *Uvigerina spp.*) are therefore unsuitable recorders of past $\delta^{13}C$ variability, due to their growth in pore waters that do not reflect the ambient seawater $\delta^{13}C$ composition (McCorkle et al., 1990). Instead, epifaunal species that live above the sediment-surface layer are the typical target for $\delta^{13}C$ measurements, as they are assumed to record $\delta^{13}C$ directly as a function of bottom-water $\delta^{13}C_{DIC}$. Even so, it has been shown that $\delta^{13}C$ values of some epibenthic foraminifera (including *Cibicidoides* species) can be influenced by extreme seasonal productivity and export of organic matter to the seafloor, which is subsequently oxidised via respiration. Growth of epibenthic foraminifera in this low-$\delta^{13}C$ organic 'fluff' layer can have the effect of unpredictably lowering benthic foraminiferal $\delta^{13}C$, typically by 0.2 to 0.6 ‰ (the 'phytodetritus effect'; Mackensen et al., 1993; Mackensen et al., 2001).

2.2.3 Analytical procedure for stable isotope measurements

Measurements of $\delta^{18}O$ and $\delta^{13}C$ are made together on the same samples. For benthic foraminifera, between 1 and 5 tests were picked from each sample, whilst approximately 10 planktonic foraminifera tests were picked due to their lower mass. Foraminifera were crushed into fragments under a microscope to ensure all chambers were open, agitated in an ultrasonic bath for several seconds, and dried at 40 °C. Stable isotopes were measured with the Finnigan MAT 253 mass spectrometer at the Leibniz Laboratory for Radiometric Dating and Stable Isotope Research in Kiel, Germany. The system is coupled to a Carbo-Kiel Device (Type IV) for automated CO2 preparation from carbonate samples for isotopic analysis. Samples were reacted by individual acid addition (99% H3PO4 at 75 °C). Standard external error is better than ±0.10 ‰ for $\delta^{18}O$ and better than ±0.05 ‰ for $\delta^{13}C$.

2.3 Paleotemperature reconstructions

2.3.1 Mg/Ca ratios of foraminifera

Mg/Ca ratios measured in foraminifera allow estimation of water column temperatures, both in the mixed and thermocline layers through the use of planktonic species, and bottom water conditions through the use of benthic species. Mg/Ca thermometry relies on the thermodynamically-preferential substitution of Ca^{2+} by Mg^{2+} in calcium carbonate with increasing temperatures. However, Mg uptake in foraminiferal tests displays a larger sensitivity to temperature than inorganic precipitates, and additionally varies between species to species (Lea et al., 1999), implicating further biological controls on foraminiferal Mg/Ca. The planktonic foraminifera *G. ruber* has been the focus of particular attention in paleoclimate studies, as it is considered to live in the surface layer of the ocean and may therefore be the most suitable recorder for past SST. A wide range of species-specific calibrations of *G. ruber* Mg/Ca to SST exist, based upon culturing experiments, core-top sediments and sediment traps (e.g. Nürnberg et al., 1996; Lea et al, 1999; Lea et al., 2000; Dekens et al., 2002; Anand et al., 2003; Regenberg et al., 2009), and are parameterized by an exponential equation of the form:

$$\mathrm{Mg/Ca} = b \cdot \mathrm{e}^{aT}$$

These calibrations show general agreement on the sensitivity (i.e. *a*, the exponential constant) of *G. ruber* Mg/Ca to temperature, in the range of 9 - 11 % / °C, but show some differences in absolute temperature due to variability in *b*, the pre-exponential constant. In the high temperature range of the West Pacific, where SSTs are typically above 25 °C, this can lead to differences in absolute temperatures in excess of 3 °C.

A number of additional controls on foraminiferal Mg/Ca have been investigated, including salinity (Hönisch et al., 2013), pH (Kisakürek et al., 2008) and postdepositional dissolution driven by ($[CO_3^{2-}]$) concentrations (Regenberg et al., 2006, 2014). In addition to these factors, the addition of Mg-rich gametogenic calcite has also been suggested as an important control on foraminiferal Mg/Ca. However, little or no gametogenic calcite crust is observed in *G. ruber* (Caron et al., 1990), so this likely has little effect on whole-

shell Mg/Ca of *G. ruber*. However, analytical methods and inter-laboratory offets can have significant influences on the Mg/Ca signal recorded (Rosenthal et al., 2004), and thus significant uncertaintieis in Mg/Ca paleothermometry remain. Chapter 5 of this thesis seeks to investigate some of these influences based upon core-top measurements of *G. ruber* Mg/Ca in the West Pacific.

For Mg/Ca analyses of *G. ruber*, approximately 30 tests were picked, crushed into fragments under a microscope and checked for potential contaminants. Samples were subsequently cleaned following the established protocol of Martin and Lea (2002), including the reductive cleaning step. Samples were analyzed with the ICP-OES (Inductively Coupled Plasma-Optical Emission Spectrometer) (Spectro Ciros SOP) with cooled cyclonic spraychamber and microconcentric nebulization (200 µl min^{-1}) at the Institute of Geosciences, University of Kiel. Intensity ratio calibration followed the method of de Villiers et al. (2002). Internal analytical precision was 0.1 - 0.2 %.

2.3.2 $U^{K'}_{37}$ alkenone unsaturation ratios

Alkenone unsaturation ratios are an organic biomarker proxy for SST, based upon the relative proportions of C_{37} methyl alkenones produced in the surface ocean by a few species of coccolithophores, principally *Emiliania huxleyi* and *Gephyrocapsa oceanica*. The U^{K}_{37} index, first developed by Brassell et al (1986), was given with the equation:

$$U^{K}_{37} = (C_{37:2} - C_{37:4}) / (C_{37:2} + C_{37:3} + C_{37:4})$$

Later work (e.g. Prahl and Wakeham, 1987; Sikes et al., 2000) found that inclusion of the $C_{37:4}$ alkenones in this equation did not offer an improvement over the simplified, and now commonly accepted, $U^{K'}_{37}$ index:

$$U^{K'}_{37} = C_{37:2} / (C_{37:2} + C_{37:3})$$

This index varies with values between zero and one (with zero being the coldest, and one being the warmest). Attempts to calibrate $U^{K'}_{37}$ to temperature typically rely on culturing

experiments, where the growth temperature can be exactly controlled (e.g. Prahl and Wakeham, 1987), or through statistical comparison of core-tops or sediment trap measurements with modern climatological data (either derived from in-situ measurements, global climatological atlases or more recently from satellite measurements) (e.g. Sonzogni et al., 1997a, b; Pelejero and Grimalt, 1997; Müller et al., 1998; Conte et al., 2006). The potential advantage of the $U^{K'}_{37}$ index over foraminiferal Mg/Ca ratios is that it appears resistant to dissolution and degradation effects. However, the $U^{K'}_{37}$ index is still subject to considerable uncertainty in ecological (both in terms of depth and seasonality of alkenone production) and post-depositional (e.g. bioturbation) effects. A more thorough discussion of these potential effects is given in Chapter 5.

In this thesis, $U^{K'}_{37}$ SST measurements have been made on a 120-kyr long sediment core record from the equatorial West Pacific (Chapter 3), and on a range of core-top samples from the Makassar Strait, Java Sea and Timor Sea (Chapter 5). The analytical method for measuring alkenones at the University of Kiel, Germany, is fully described by Rincón-Martínez et al. (2010), and can be summarised as follows: Approximately 1 g of freeze-dried sediments are solvent extracted with 25 mL dichloromethane at 75°C at a pressure of 80 bars on an accelerated solvent extractor. An internal standard was added to quantify organic compounds. Aliquots (1 - 5 %) of the total lipid fractions were separated using a double-column multidimensional gas chromatography with two Agilent 6890 gas chromatographs for $C_{37:2}$ and $C_{37:3}$ alkenone identification and quantification.

2.4 Radiocarbon (^{14}C) dating

Measurement of the radiocarbon (^{14}C) content of both planktonic and benthic foraminifera has been widely employed in paleoceanography research, predominantly for its use in developing the age model of marine sediment cores, but also as a proxy for deep ocean circulation and ventilation. In this thesis, ^{14}C dating been applied for generating age model of several marine cores. Approximately 600-800 tests of the surface-dwelling planktonic foraminifera *G. ruber* were picked from the >250 μm fraction. Where abundances of *G. ruber* were not sufficient, we included additional planktonic species such as *G. sacculifer* and *P. obliquiloculata*. Samples were measured via Accelerator Mass Spectrometry (AMS) ^{14}C dating at the Leibniz Laboratory, Kiel

University, following the protocol described by Nadeau et al. (1997) and Schleicher et al. (1998). To account for past reservoir ages of surface waters in this region, we apply a reservoir correction of 480 years to samples younger than 13 ka, and 630 years to samples older than 13 ka in sediment core MD06-3075, following the suggestion of Broecker et al. (2004) for sediment core MD98-2181, located nearby within the Davao Gulf. For other sediment cores used in this thesis (e.g. in Chapter 4), we use a constant reservoir age correction of 400 years, following Butzin et al. (2005), who found that changes in reservoir ages between glacial and modern times in the West Pacific were likely small. Conventional ages were converted to calendar ages following the radiocarbon calculator of Fairbanks et al. (2005) (Chapter 3), or the Calib 7.0 program using the Marine13 calibration curve (Reimer et al., 2013) (Chapter 4).

2.5 X-ray fluorescence core scanning

X-ray fluorescence (XRF) scanning provides a non-destructive method of measuring the elemental composition of rocks and sediments (Ramsey et al., 1995), leading to the development of scanners for fast and reliable measurement of sediment core characteristics (Jansen et al., 1998; Weltje and Tjallingii, 2008). The XRF intensities of elements that are common in siliciclastic rocks, for example Fe, Al and Ti, are shown to correlate well with the clay composition of marine sediments (Jansen et al., 1998; Arz et al., 1998). This has given rise to the interpretation of variations in these elements (which are typically normalised to calcium and presented as log-ratios to reduce matrix effects (Weltje and Tjallingii, 2008) as semi-quantitative indicators of paleoclimate conditions, with increased log-ratios interpreted as periods of increased weathering and transport of clays from the terrestrial to the marine environment. This approach has been successfully employed in a number of records from the WEP in recent years to infer changes in sediment runoff driven by changes in past precipitation (Kissel et al., 2010; Mohtadi et al., 2011; Tachikawa et al., 2011). However, it has been noted that other factors such as pore-water content, organic matter content and porosity can have a significant effect on measured XRF intensities of some elements (Tjallingii et al., 2007; Weltje and Tjallingii, 2008).

In this thesis, we use XRF-derived log(Fe/Ca) ratios in Marine Core MD06-3075 as a proxy for past changes in rainfall at Mindanao (Chapter 3). XRF analysis was performed on the archive half of the core in 1 cm resolution. Measurements were made using the Avaatech core-scanner at the Marum Center, University of Bremen.

2.6 Paleoproductivity estimates from coccolithophore assemblages

Coccolithophores represent one of the major groups of phytoplankton throughout the worlds oceans, and their assemblages respond primarily to changes nutrient profiles of the upper water column (>200 m water depth), and can thus be used as a proxy for pat changes in productivity (Molfino and McIntyre, 1990). In particular, the abundance of the lower photic zone (<60 m water depth) dwelling species *Florisphaera profunda* has been shown to correlate well with the depth of the nutricline. When upper photic zone is nutrient depleted (i.e. low productivity), the nutricline is deepened which leads to enhanced growth of *F. profunda* relative to other species. When the upper photic zone is nutrient rich, the opposite effect occurs (Andruleit et al., 2002).

Such ecological patterns have been employed to record variations in past productivity in the tropical regions on orbital (Molfino and McIntyre, 1990; McIntyre and Molfino, 1996; Beaufort et al., 1997) and sub-orbital timescales (de Garidel-Thoron et al., 2001). Successful calibration of *F. profunda* abundances to productivity has been made through a core-top compilation in the Indian Ocean, resulting in the following equation (Beaufort et al., 1997):

$$\text{Productivity}\,(\text{gC}/\text{m}^2/\text{yr}) = 617 - \left[279\log(\%Fp + 3)\right]$$

In Chapter 3, we use assemblages of coccolithophores to reconstruct past changes in productivity in Core MD06-3075. Coccolithophores were counted using an automated recognition system (SYRACO) following the protocol of Dollfus and Beaufort (1999) and Beaufort and Dollfus (2004). Sample resolution was 10 cm, with six main species dominating the assemblages: *F. profunda, Emiliania huxleyi, Gephrocapsa oceanica, Gephyrocapsa muellerae, Gephyrocapsa ericsonii and Helicosphaera spp.*

2.7 References

Anand, P., Elderfield, H., & Conte, M. H. (2003). Calibration of Mg/Ca thermometry in planktonic foraminifera from a sediment trap time series. Paleoceanography, 18(2).

Andruleit, H., & Rogalla, U. (2002). Coccolithophores in surface sediments of the Arabian Sea in relation to environmental gradients in surface waters. Marine Geology, 186(3), 505-526.

Arz, H. W., Pätzold, J., & Wefer, G. (1998). Correlated millennial-scale changes in surface hydrography and terrigenous sediment yield inferred from last-glacial marine deposits off northeastern Brazil. Quaternary Research, 50(2), 157-166.

Bé, A. W. H., & Tolderlund, D. S. (1971). Distribution and ecology of living planktonic foraminifera in surface waters of the Atlantic and Indian Oceans. The micropaleontology of oceans, 105-149.

Beaufort, L., Lancelot, Y., Camberlin, P., Cayre, O., Vincent, E., Bassinot, F., & Labeyrie, L. (1997). Insolation cycles as a major control of equatorial Indian Ocean primary production. Science, 278(5342), 1451-1454.

Beaufort, L., & Dollfus, D. (2004). Automatic recognition of coccoliths by dynamical neural networks. Marine Micropaleontology, 51(1), 57-73.

Bemis, B. E., Spero, H. J., Bijma, J., & Lea, D. W. (1998). Reevaluation of the oxygen isotopic composition of planktonic foraminifera: Experimental results and revised paleotemperature equations. Paleoceanography, 13(2), 150-160.

Bolliet, T., Holbourn, A., Kuhnt, W., Laj, C., Kissel, C., Beaufort, L., Kienast, M., Andersen, N., and Garbe-Schönberg, D. (2011). Mindanao Dome variability over the last 160 kyr: Episodic glacial cooling of the West Pacific Warm Pool. Paleoceanography, 26(1).

Brassell, S. C., Eglinton, G., Marlowe, I. T., Pflaumann, U., & Sarnthein, M. (1986). Molecular stratigraphy: a new tool for climatic assessment. Nature, 320(6058), 129-133.

Broecker, W. S. (1982). Ocean chemistry during glacial time. Geochimica et Cosmochimica Acta, 46(10), 1689-1705.

Broecker, W., Barker, S., Clark, E., Hajdas, I., Bonani, G., & Stott, L. (2004). Ventilation of the glacial deep Pacific Ocean. Science, 306(5699), 1169-1172.

Butzin, M., Prange, M., & Lohmann, G. (2005). Radiocarbon simulations for the glacial ocean: the effects of wind stress, Southern Ocean sea ice and Heinrich events. Earth and Planetary Science Letters, 235(1), 45-61.

Caron, D. A., Roger Anderson, O., Lindsey, J. L., Faber Jr, W. W., & Lin Lim, E. E. (1990). Effects of gametogenesis on test structure and dissolution of some spinose planktonic foraminifera and implications for test preservation. Marine Micropaleontology, 16(1), 93-116.

Conte, M. H., Sicre, M. A., Rühlemann, C., Weber, J. C., Schulte, S., Schulz-Bull, D., & Blanz, T. (2006). Global temperature calibration of the alkenone unsaturation index ($U^{K'}_{37}$) in surface waters and comparison with surface sediments. Geochemistry, Geophysics, Geosystems, 7(2).

de Garidel-Thoron, T., Beaufort, L., Linsley, B. K., & Dannenmann, S. (2001). Millennial-scale dynamics of the east Asian winter monsoon during the last 200,000 years. Paleoceanography, 16(5), 491-502.

de Villiers, S., Greaves, M., & Elderfield, H. (2002). An intensity ratio calibration method for the accurate determination of Mg/Ca and Sr/Ca of marine carbonates by ICP-AES. Geochemistry, Geophysics, Geosystems, 3(1).

Dekens, P. S., Lea, D. W., Pak, D. K., & Spero, H. J. (2002). Core top calibration of Mg/Ca in tropical foraminifera: Refining paleotemperature estimation. Geochemistry, Geophysics, Geosystems, 3(4), 1-29.

Dollfus, D., & Beaufort, L. (1999). Fat neural network for recognition of position-normalised objects. Neural Networks, 12(3), 553-560.

Duplessy, J. C., Shackleton, N. J., Matthews, R. K., Prell, W., Ruddiman, W. F., Caralp, M., & Hendy, C. H. (1984). ^{13}C Record of benthic foraminifera in the last interglacial ocean: Implications for the carbon cycle and the global deep water circulation. Quaternary Research, 21(2), 225-243.

Duplessy, J. C., Shackleton, N. J., Fairbanks, R. G., Labeyrie, L., Oppo, D., & Kallel, N. (1988). Deepwater source variations during the last climatic cycle and their impact on the global deepwater circulation. Paleoceanography, 3(3), 343-360.

EPICA Community Members (2004). Eight glacial cycles from an Antarctic ice core. Nature, 429(6992), 623-628.

Erez, J. (1978). Vital effect on stable-isotope composition seen in foraminifera and coral skeletons, Nature, 273, 199-202.

Fairbanks, R. G. (1989). A 17, 000-year glacio-eustatic sea level record: influence of glacial melting rates on the Younger Dryas event and deep-ocean circulation. Nature, 342(6250), 637-642.

Fairbanks, R. G., Mortlock, R. A., Chiu, T. C., Cao, L., Kaplan, A., Guilderson, T. P., Fairbanks, T. W., Bloom, A. L, Grootes, P. M., and Nadeau, M. J. (2005). Radiocarbon calibration curve spanning 0 to 50,000 years BP based on paired

$^{230}Th/^{234}U/^{238}U$ and ^{14}C dates on pristine corals. Quaternary Science Reviews, 24(16), 1781-1796.

Farmer, E. C., Kaplan, A., de Menocal, P. B., and Lynch-Stieglitz, J. (2007). Corroborating ecological depth preferences of planktonic foraminifera in the tropical Atlantic with the stable oxygen isotope ratios of core top specimens. Paleoceanography, 22(3).

Gibbons, F. T., Oppo, D. W., Mohtadi, M., Rosenthal, Y., Cheng, J., Liu, Z., and Linsley, B. K. (2014). Deglacial $\delta^{18}O$ and hydrologic variability in the tropical Pacific and Indian Oceans. Earth and Planetary Science Letters, 387, 240-251.

Hönisch, B., Allen, K. A., Lea, D. W., Spero, H. J., Eggins, S. M., Arbuszewski, J., deMenocal, P., Rosentahl, Y., Russell, A. D., and Elderfield, H. (2013). The influence of salinity on Mg/Ca in planktic foraminifers–Evidence from cultures, core-top sediments and complementary $\delta^{18}O$. Geochimica et Cosmochimica Acta, 121, 196-213.

Jansen, J. H. F., Van der Gaast, S. J., Koster, B., and Vaars, A. J. (1998). CORTEX, a shipboard XRF-scanner for element analyses in split sediment cores. Marine Geology, 151(1), 143-153.

Jorissen, F. J., de Stigter, H. C., and Widmark, J. G. (1995). A conceptual model explaining benthic foraminiferal microhabitats. Marine Micropaleontology, 26(1), 3-15.

Khider, D., Jackson, C. S., and Stott, L. D. (2014). Assessing millennial-scale variability during the Holocene: A perspective from the western tropical Pacific. Paleoceanography, 29(3), 143-159.

Kisakürek, B., Eisenhauer, A., Böhm, F., Garbe-Schönberg, D., and Erez, J. (2008). Controls on shell Mg/Ca and Sr/Ca in cultured planktonic foraminiferan *Globigerinoides ruber* (white). Earth and Planetary Science Letters, 273(3), 260-269.

Kissel, C., Laj, C., Kienast, M., Bolliet, T., Holbourn, A., Hill, P., Kuhnt, W., and Braconnot, P. (2010). Monsoon variability and deep oceanic circulation in the western equatorial Pacific over the last climatic cycle: Insights from sedimentary magnetic properties and sortable silt. Paleoceanography, 25(3).

Kucera, M. (2007). Planktonic foraminifera as tracers of past oceanic environments. Developments in marine geology, 1(6), 213-262.

Lea, D. W., Mashiotta, T. A., and Spero, H. J. (1999). Controls on magnesium and strontium uptake in planktonic foraminifera determined by live culturing. Geochimica et Cosmochimica Acta, 63(16), 2369-2379.

Lea, D. W., Pak, D. K., and Spero, H. J. (2000). Climate impact of late Quaternary

equatorial Pacific sea surface temperature variations. Science, 289(5485), 1719-1724.

Lisiecki, L. E., and Raymo, M. E. (2005). A Pliocene-Pleistocene stack of 57 globally distributed benthic δ18O records. Paleoceanography, 20(1).

Mackensen, A., Hubberten, H. W., Bickert, T., Fischer, G., and Fütterer, D. K. (1993). The $\delta^{13}C$ in benthic foraminiferal tests of Fontbotia wuellerstorfi (Schwager) relative to the $\delta^{13}C$ of dissolved inorganic carbon in southern ocean deep water: implications for glacial ocean circulation models. Paleoceanography, 8(5), 587-610.

Mackensen, A., Rudolph, M., and Kuhn, G. (2001). Late Pleistocene deep-water circulation in the subantarctic eastern Atlantic. Global and Planetary Change, 30(3), 197-229.

Marchitto, T. M., Curry, W. B., Lynch-Stieglitz, J., Bryan, S. P., Cobb, K. M., and Lund, D. C. (2014). Improved oxygen isotope temperature calibrations for cosmopolitan benthic foraminifera. Geochimica et Cosmochimica Acta, 130, 1-11.

Martin, P. A., and Lea, D. W. (2002). A simple evaluation of cleaning procedures on fossil benthic foraminiferal Mg/Ca. Geochemistry, Geophysics, Geosystems, 3(10), 1-8.

McCorkle, D. C., Keigwin, L. D., Corliss, B. H., and Emerson, S. R. (1990). The influence of microhabitats on the carbon isotopic composition of deep-sea benthic foraminifera. Paleoceanography, 5(2), 161-185.

McIntyre, A., and Molfino, B. (1996). Forcing of Atlantic equatorial and subpolar millennial cycles by precession. Science, 274(5294), 1867-1870.

Mohtadi, M., Lückge, A., Steinke, S., Groeneveld, J., Hebbeln, D., and Westphal, N. (2010). Late Pleistocene surface and thermocline conditions of the eastern tropical Indian Ocean. Quaternary Science Reviews, 29(7), 887-896.

Molfino, B., and McIntyre, A. (1990). Precessional forcing of nutricline dynamics in the equatorial Atlantic. Science, 249(4970), 766-769.

Müller, P. J., Kirst, G., Ruhland, G., von Storch, I., and Rosell-Melé, A. (1998). Calibration of the alkenone paleotemperature $U^{K'}_{37}$ index based on core-tops from the eastern South Atlantic and the global ocean (60° N - 60° S). Geochimica et Cosmochimica Acta, 62(10), 1757-1772.

Nadeau, M. J., Schleicher, M., Grootes, P. M., Erlenkeuser, H., Gottdang, A., Mous, D. J. W., Sarnthein, M., and Willkomm, H. (1997). The Leibniz-Labor AMS facility at the Christian-Albrechts University, Kiel, Germany. Nuclear Instruments and Methods in Physics Research Section B: Beam Interactions with Materials and Atoms, 123(1), 22-30.

Nürnberg, D., Bijma, J., and Hemleben, C. (1996). Assessing the reliability of magnesium

in foraminiferal calcite as a proxy for water mass temperatures. Geochimica et Cosmochimica Acta, 60(5), 803-814.

Pelejero, C., and Grimalt, J. O. (1997). The correlation between the $U^{K'}_{37}$ index and sea surface temperatures in the warm boundary: The South China Sea. Geochimica et Cosmochimica Acta, 61(22), 4789-4797.

Prahl, F. G., and Wakeham, S. G. (1987). Calibration of unsaturation patterns in long-chain ketone compositions for palaeotemperature assessment. Nature, 330, 367-369.

Ramsey, M. H., Potts, P. J., Webb, P. C., Watkins, P., Watson, J. S., and Coles, B. J. (1995). An objective assessment of analytical method precision: comparison of ICP-AES and XRF for the analysis of silicate rocks. Chemical Geology, 124(1), 1-19.

Reimer, P. J., et al. (2013). IntCal13 and Marine13 radiocarbon age calibration curves 0–50,000 years cal BP. Radiocarbon, 55(4), 1869-1887.

Regenberg, M., Nürnberg, D., Steph, S., Groeneveld, J., Garbe-Schönberg, D., Tiedemann, R., and Dullo, W. C. (2006). Assessing the effect of dissolution on planktonic foraminiferal Mg/Ca ratios: Evidence from Caribbean core tops. Geochemistry, Geophysics, Geosystems, 7(7).

Regenberg, M., Steph, S., Nürnberg, D., Tiedemann, R., and Garbe-Schönberg, D. (2009). Calibrating Mg/Ca ratios of multiple planktonic foraminiferal species with δ^{18}O-calcification temperatures: Paleothermometry for the upper water column. Earth and Planetary Science Letters, 278(3), 324-336.

Regenberg, M., Regenberg, A., Garbe-Schönberg, D., and Lea, D. W. (2014). Global dissolution effects on planktonic foraminiferal Mg/Ca ratios controlled by the calcite-saturation state of bottom waters. Paleoceanography, 29(3), 127-142.

Rincón-Martínez, D., Lamy, F., Contreras, S., Leduc, G., Bard, E., Saukel, C., Blanz, T., Mackensen, A., and Tiedemann, R. (2010). More humid interglacials in Ecuador during the past 500 kyr linked to latitudinal shifts of the equatorial front and the Intertropical Convergence Zone in the eastern tropical Pacific. Paleoceanography, 25(2).

Rosenthal, Y., and Lohmann, G. P. (2002). Accurate estimation of sea surface temperatures using dissolution-corrected calibrations for Mg/Ca paleothermometry. Paleoceanography, 17(3), 16-1.

Rosenthal, Y., et al. (2004). Interlaboratory comparison study of Mg/Ca and Sr/Ca measurements in planktonic foraminifera for paleoceanographic research. Geochemistry, Geophysics, Geosystems, 5(4).

Schleicher, M., Grootes, P. M., Nadeau, M. J., and Schoon, A. (1998). The carbonate 14C background and its components at the Leibniz AMS facility. Radiocarbon, 40(1), 85-93.

Schmidt, G. A. (1999). Forward modeling of carbonate proxy data from planktonic foraminifera using oxygen isotope tracers in a global ocean model. Paleoceanography, 14(4), 482-497.

Schrag, D. P., Adkins, J. F., McIntyre, K., Alexander, J. L., Hodell, D. A., Charles, C. D., and McManus, J. F. (2002). The oxygen isotopic composition of seawater during the Last Glacial Maximum. Quaternary Science Reviews, 21(1), 331-342.

Singer, B. S., Guillou, H., Jicha, B. R., Laj, C., Kissel, C., Beard, B. L., and Johnson, C. M. (2009). $^{40}Ar/^{39}Ar$, K–Ar and $^{230}Th–^{238}U$ dating of the Laschamp excursion: a radioisotopic tie-point for ice core and climate chronologies. Earth and Planetary Science Letters, 286(1-2), 80-88.

Shackleton, N. J. (1974). Attainment of isotopic equilibrium between ocean water and the benthonic foraminifera genus Uvigerina: isotopic changes in the ocean during the last glacial.

Sikes, E. L., Volkman, J. K., Robertson, L. G., and Pichon, J. J. (1997). Alkenones and alkenes in surface waters and sediments of the Southern Ocean: Implications for paleotemperature estimation in polar regions. Geochimica et Cosmochimica Acta, 61(7), 1495-1505.

Shackleton, N. J., Hall, M. A., Line, J., and Shuxi, C. (1983). Carbon isotope data in core V19-30 confirm reduced carbon dioxide concentration in the ice age atmosphere. Nature, 306, 319-322.

Sonzogni, C., Bard, E., Rostek, F., Lafont, R., Rosell-Mele, A., and Eglinton, G. (1997). Core-top calibration of the alkenone index vs sea surface temperature in the Indian Ocean. Deep Sea Research Part II: Topical Studies in Oceanography, 44(6), 1445-1460.

Sonzogni, C., Bard, E., Rostek, F., Dollfus, D., Rosell-Melé, A., and Eglinton, G. (1997b). Temperature and salinity effects on alkenone ratios measured in surface sediments from the Indian Ocean. Quaternary Research, 47(3), 344-355.

Stott, L., Timmermann, A., and Thunell, R. (2007). Southern hemisphere and deep-sea warming led deglacial atmospheric CO2 rise and tropical warming. science, 318(5849), 435-438.

Tachikawa, K., Cartapanis, O., Vidal, L., Beaufort, L., Barlyaeva, T., and Bard, E. (2011). The precession phase of hydrological variability in the Western Pacific Warm Pool during the past 400 ka. Quaternary Science Reviews, 30(25), 3716-3727.

Tjallingii, R., Röhl, U., Kölling, M., and Bickert, T. (2007). Influence of the water content on X-ray fluorescence core-scanning measurements in soft marine sediments. Geochemistry, Geophysics, Geosystems, 8(2).

Waelbroeck, C., Labeyrie, L., Michel, E., Duplessy, J. C., McManus, J. F., Lambeck, K.,

Balbon, E., and Labracherie, M. (2002). Sea-level and deep water temperature changes derived from benthic foraminifera isotopic records. Quaternary Science Reviews, 21(1), 295-305.

Weltje, G. J., and Tjallingii, R. (2008). Calibration of XRF core scanners for quantitative geochemical logging of sediment cores: theory and application. Earth and Planetary Science Letters, 274(3), 423-438.

Chapter 3

Precipitation variability within the West Pacific Warm Pool over the past 120 ka: evidence from the Davao Gulf, southern Philippines.

Nicholas Fraser, Wolfgang Kuhnt, Ann Holbourn, Timothé Bolliet, Nils Andersen, Thomas Blanz, Luc Beaufort

Published in *Paleoceanography* (doi: 10.1002/2013PA002599)

3.1 Abstract

Proxy records of hydrologic variability in the West Pacific Warm Pool (WPWP) have revealed wide-scale changes in past convective activity in response to orbital and sub-orbital climate forcings. However, attributing proxy responses to regional changes in WPWP hydrology versus local variations in precipitation requires independent records linking the terrestrial and marine realms. We present high-resolution stable isotope, $U^{K'}_{37}$ sea-surface temperature, X-ray fluorescence (XRF) core scanning and coccolithophore-derived paleoproductivity records covering the past 120 ka from International Marine Global Change (IMAGES) Program Core MD06-3075 (6°29' N, 125°50' E, water depth 1878 m), situated in the Davao Gulf on the southern side of Mindanao. XRF-derived log(Fe/Ca) records provide a robust proxy for runoff-driven sedimentary discharge from Mindanao, whilst past changes in local productivity are associated with variable freshwater runoff and stratification of the surface layer. Significant precessional-scale variability in sedimentary discharge occurred during Marine Isotope Stage (MIS) 5, with peaks in discharge contemporaneous with Northern Hemisphere summer insolation minima. We attribute these changes to the latitudinal migration of the Intertropical Convergence Zone (ITCZ) over the WPWP together with variability in the strength of the Walker circulation acting on precessional timescales. Between 60 and 15 ka sedimentary discharge at Mindanao was muted, displaying little orbital- or millennial-scale variability, likely in response to weakened precessional insolation forcing and lower sea level driving increased subsidence of air masses over the exposed Sunda Shelf. These results highlight the high degree of local variability in the precipitation response to past climate changes in the WPWP.

3.2. Introduction

The West Pacific Warm Pool (WPWP) forms one of the world's largest and most important centres of tropical convection, supplying heat and moisture to the mid and high latitudes, and playing an active role in global climate dynamics (Cane et al., 1998; Hoerling et al., 2001). Pressure gradients between the eastern subtropical Pacific and the Australian and Indonesian maritime landmasses drive easterly trade winds which push warm surface waters westward and result in a large zonal sea surface temperature (SST)

gradient between the eastern and western tropical Pacific. This feedback mechanism reinforces convergence of wind and surface waters in the West Pacific, resulting in permanent year-round warm pool where SSTs exceed 28 °C. By way of comparison, SSTs in the Eastern Equatorial Pacific average 25 to 27 °C due to upwelling induced by equatorial trade winds (Bjerknes, 1969).

The Intertropical Convergence Zone (ITCZ), a narrow band of convective winds and intense precipitation situated close to the equator, migrates seasonally over the WPWP in response to interhemispheric temperature gradients (Schneider et al., 2014). During boreal summer, the ITCZ migrates northwards, resulting in high precipitation over China and the northern regions of the Indonesian archipelago, whilst southern Indonesia and Australia experience relatively dry conditions. The opposite effect occurs during boreal winter. These patterns of precipitation are closely linked with the East-Asian Monsoon (EAM) and Indo-Australian Monsoon systems. Variability in the El Niño Southern Oscillation (ENSO) acting on irregular two to ten year timescales also has a direct influence on WPWP convection; during strong El Niño years a breakdown in the Walker circulation causes weakened easterly trade winds and a shift in the centre of tropical convection towards the Central Pacific, resulting in a net reduction in precipitation over the Indonesian landmass (Ropelewski and Halpert, 1987). During La Niña years, the opposite effect is observed, with a warmer WPWP extending further towards East Asia, driving enhanced rainfall over this region.

During the late Pleistocene, paleoclimate records of past convective activity in the tropics show a strong sensitivity to precessional cyclicity. Records from the Northern (Southern) Hemisphere typically indicate a reduction in precipitation during Northern (Southern) Hemisphere summer insolation maxima, when perihelion occurs close to summer solstice (e.g. Wang et al., 2001; 2007; 2008; Cruz et al., 2005; Tachikawa et al., 2011; Meckler et al., 2012; Cheng et al., 2012). Such patterns implicate changes in the seasonal distribution of insolation between the Northern and Southern Hemispheres as a control on past precipitation variability, which can be attributed to meridional 'shifts' of the local summer ITCZ position associated with changes in cross-equatorial heat transport (Donahoe et al., 2013; McGee et al., 2014) and to thermodynamic changes in humidity and moisture advection between hemispheres (Merlis et al., 2013). Abrupt Northern

Hemisphere climate signals such as Dansgaard–Oeschger interstadials and Heinrich stadials, which are documented in Greenland ice cores (e.g. GISP2), are furthermore imprinted upon these orbital-scale trends from the WPWP (e.g. Wang et al., 2001; Stott et al., 2002; Dannenmann et al., 2003; Saikku et al., 2009; Carolin et al., 2013; Ayliffe et al., 2013; Denniston et al., 2013), and are consistent with a northward (southward) meridional displacement of the ITCZ in response to Northern Hemisphere warming (cooling). Persistent changes in zonal circulation patterns associated with the Walker Circulation and mean ENSO conditions have also been posited as important controls on proxy records of convection from both the East and West Pacific (Tudhope et al., 2001; Beaufort et al., 2001; Stott et al., 2002; Koutavas et al., 2002; Martinez et al., 2003; Turney et al., 2004), a finding that has been replicated in recent modeling approaches (DiNezio et al., 2011; DiNezio and Tierney, 2013).

Thus far, most reconstructions of past convective variability in the WPWP have focused upon oxygen isotope ($\delta^{18}O$) records from speleothems (Partin et al., 2007; Griffiths et al., 2009; Meckler et al., 2012; Carolin et al., 2013, Ayliffe et al., 2013; Denniston et al., 2013) and δ18O records of surface seawater ($\delta^{18}O_{sw}$) derived from planktonic foraminifera (Stott et al., 2002; Medina-Elizalde and Lea, 2005; de Garidel-Thoron, 2007; Saikku et al., 2009; Gibbons et al., 2014). These isotopic records primarily reflect large-scale hydrologic variability rather than local precipitation changes (Gibbons et al., 2014), and require an understanding of the roles of evaporation feedbacks and source water $\delta^{18}O$ on the $\delta^{18}O$ signal recorded in surface seawater and cave dripwater. Resolving local precipitation patterns in the WPWP therefore requires detailed, independent proxy records which are not influenced by widespread regional changes. Here we present a multi-proxy record combining foraminiferal $\delta^{18}O$, X-ray fluorescence (XRF) derived sedimentary runoff, and coccolithophore-based $U^{K'}_{37}$ sea surface temperature (SST) and paleoproductivity estimates from Core MD06-3075 located in the Davao Gulf (06°28.6' N, 125°49.9' E, 1878m water depth), 50km off the coast of Mindanao (Figure 3.1). This sheltered bay sits within the WPWP on the eastern side of the Indonesian archipelago, and provides a favourable location for linking marine and terrestrial records of precipitation and runoff, and monitoring past climatic changes related to the evolution of the WPWP over the late Pleistocene.

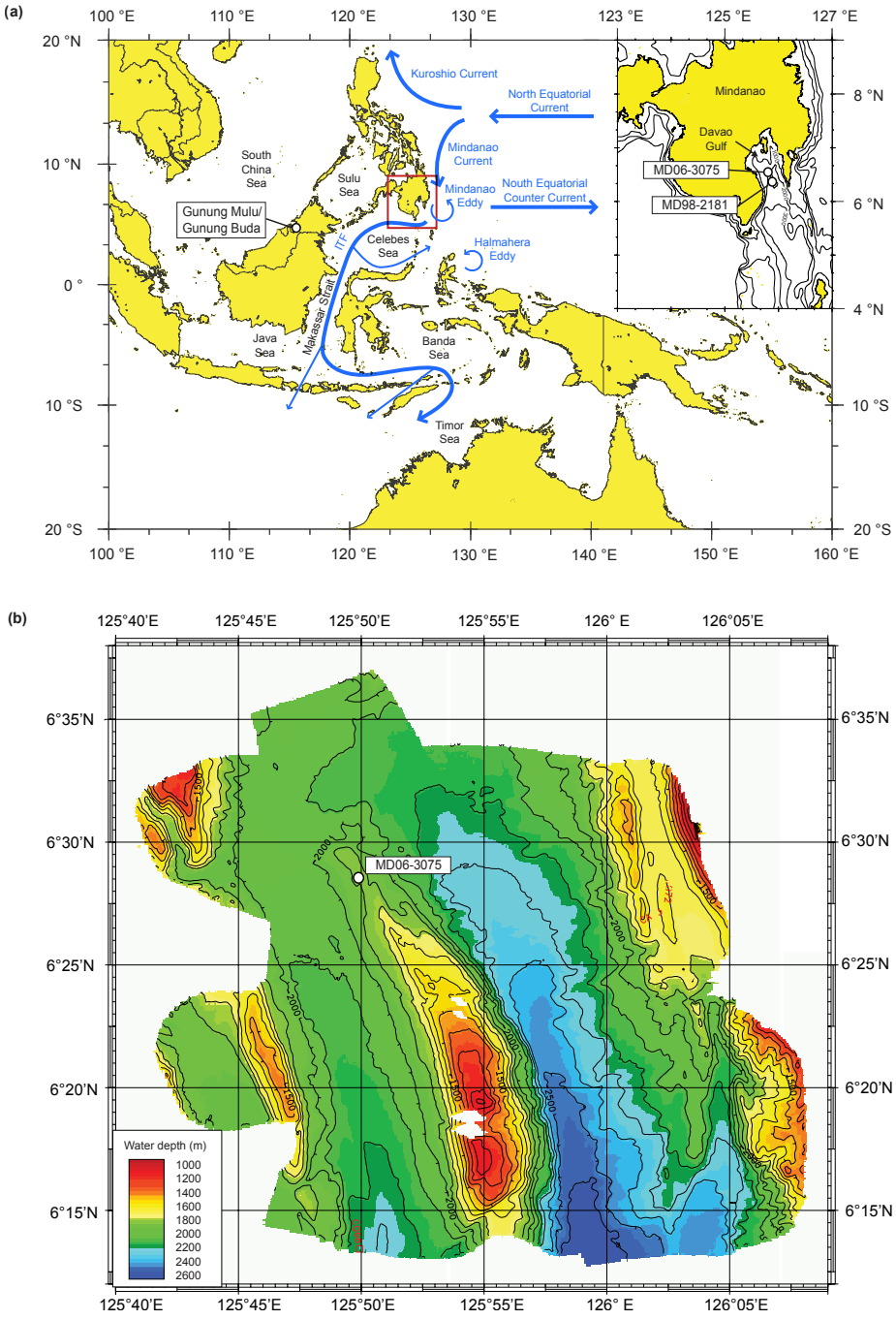

Figure 3.1 - (a) Location map of Cores MD06-3075 (this study) and MD98-2181 (Stott et al., 2002, 2007; Saikku et al.. 2009), and speleothem records from Gunung Buda/Gunung Mulu Caves, Borneo (Partin et al., 2007; Meckler et al., 2012; Carolin et al., 2013). The main oceanic currents acting in the WPWP region are shown by blue arrows. (b) Bathymetric map of the Davao Gulf including the coring position of Core MD06-3075 (Laj et al., 2006).

3.3 Materials and Study Area

Core MD06-3075 was retrieved with a Calypso piston corer during the Marco Polo II cruise aboard the Marion Dufresne in June 2006, as part of the IMAGES coring program (Laj et al., 2006). It is comprised of 30.75 m of homogenous dark olive gray silty clay, interrupted by irregular dispersed ash layers (1 to 5 cm thick). Additionally, a gap in the core is noted between 192 and 208 cm, due to the presence of a large piece of broken core liner. The coring location was chosen due to its position on a topographic high, reducing the likelihood of turbidite deposition (Figure 3.1). The Davao Gulf acts as a catchment basin for several large rivers from Mindanao, most notably the Davao River, making this site ideally placed to capture precipitation-induced runoff signals from Mindanao. The majority of thermocline waters at this site originate from the North Equatorial Current (NEC) (Toole et al., 1990), whilst the intermediate circulation is dominated by Antarctic Intermediate Water (AAIW), which passes over a shallow sill (~800m depth) extending southwards from Mindanao (Qu et al., 1999; Kashino et al., 1996) (Figure 3.1).

The core site sits within the center of the modern-day WPWP, with an annual average SST of 28.7 °C. SSTs are highest in boreal summer, above 29 °C, and cool by approximately 1 to 1.5 °C in boreal winter (Figure 3.2b). Seasonal precipitation and wind patterns are linked with the migration of the ITCZ. Precipitation is highest (>4.5 mm/day) when a northern-positioned ITCZ induces convergence over Mindanao between June and October, and lowest (< 4 mm/day) when the ITCZ is positioned to the south between February and April (Figure 3.2b). However, this seasonal cycle of precipitation is relatively weak compared to the extreme monsoonal precipitation cycles found in northern Australia or southern China, since the core site is positioned relatively centrally within the latitudinal range of the maximum northward and southward ITCZ position. Oxygen isotopes of precipitation falling in Mindanao show generally lower values between June and September, and higher values between January to May, likely caused by changing wind directions and associated changes in the sources and transport pathways of atmospheric vapour (Figure 3.2b). Precipitation records from the past decades in the Davao Gulf also indicate the important effect ENSO has at this location;

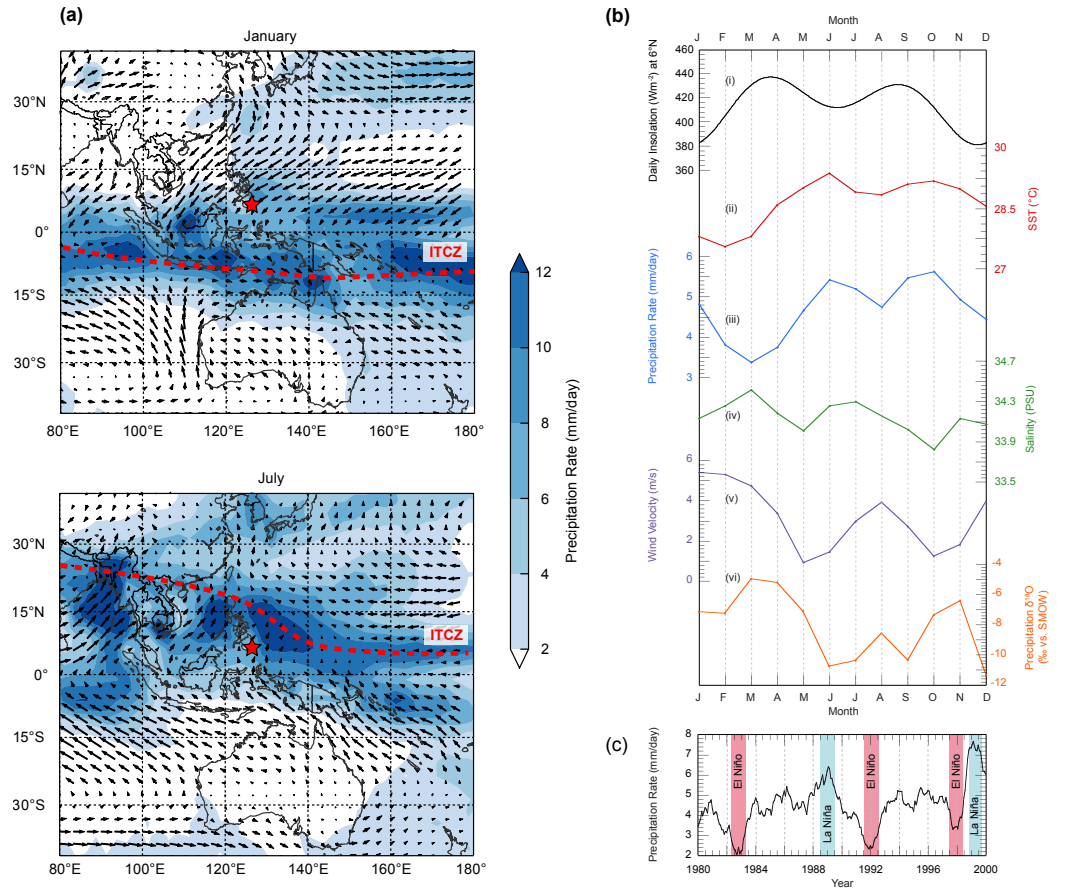

Figure 3.2 - (a) Wind and precipitation rates in the WPWP during January (top) and July (bottom). Wind data are derived from the NCEP reanalysis project, available at http://www.esrl.noaa.gov/psd/. Precipitation data were extracted from the Xie and Arkin (1997) CMAP precipitation estimates available at http://iridl.ldeo.columbia.edu. Red dashed line represents the mean monthly position of the ITCZ, following Waliser and Gautier (1993). Location of Core MD06-3075 is shown by a red star. (b) Monthly climatology in the Davao Gulf showing: (i) insolation at 6 ºN, (ii) average SST (World Ocean Atlas 2009 (Locarnini et al., 2010)), (iii) average precipitation rates (extracted from the Xie and Arkin (1997) CMAP precipitation estimate available at http://iridl.ldeo.columbia.edu/), (iv) average salinity (World Ocean Atlas 2009 (Antonov et al., 2010)), (v) average wind velocities (NCEP reanalysis data at http://www.esrl.noaa.gov/psd/). (vi) $\delta^{18}O$ measured in precipitation (Global Network of Isotopes in Precipitation (IAEA/WMO, 2013)) across a composite of 5 stations situated in southern Mindanao. (b) Average precipitation rates over the 1980-2000 period with strongest El Niño (red bars) and La Niña (blue bars) years based on NINO3.4 index anomalies.

during strong El Niño years, precipitation is suppressed and Mindanao experiences generally dry conditions, whilst during La Niña years, the reverse situation occurs (Figure 3.2c).

3.4 Methods

3.4.1. Accelerator Mass Spectrometry ^{14}C dating

For accelerator mass spectrometry (AMS) ^{14}C dating, approximately 600 to 800 well preserved tests of the near-surface dwelling planktonic foraminifera *Globigerinoides ruber* were picked from the >250 μm size fraction, where abundance allowed. In instances of low abundance, mixed planktonic samples consisting of *G. ruber*, *Globigerinoides sacculifer* and *Pulleniatina obliquiloculata* were analysed. AMS ^{14}C dating was performed at the Leibniz Laboratory, Kiel University, following the protocol described by Nadeau et al., (1997) and Schleicher et al., (1998). Conventional ages were converted to calendar ages following Fairbanks et al. (2005), after applying a reservoir age correction of 480 years for samples younger than 13 ka, and 630 years for older samples, consistent with other recent studies in this region (e.g. Saikku et al., 2009; Bolliet et al., 2011).

3.4.2 Stable isotope analysis

For $\delta^{18}O$ analysis, approximately 10 tests of *G. ruber*, and between 1 and 5 tests of the benthic species *Planulina wuellerstorfi* were picked at 10 cm intervals. Over the upper 900 cm of the core, the spacing of the *G. ruber* sampling intervals was decreased to 2 cm. In rare cases where *P. wuellerstorfi* was absent, *Cibicidoides pachyderma* or *Uvigerina* spp. were used. *Cibicidoides* and *Planulina* calcify with $\delta^{18}O$ values at or close to isotopic equilibrium with ambient seawater (Bemis et al., 1998; Marchitto et al., 2014), whilst *Uvigerina* spp. require an additional correction of -0.47 ‰ (following Marchitto et al. (2014)), to bring values in line with isotopic equilibrium values of ambient seawater. Samples were crushed into fragments under the microscope to ensure all chambers were open, then agitated in ethanol in an ultrasonic bath for several seconds, and dried at 40 °C. Stable oxygen isotopes were measured with the Finnigan MAT 253 mass spectrometer at the Leibniz

Laboratory, Kiel University. The system is coupled to a Carbo-Kiel Device (Type IV) for automated CO_2 preparation from carbonate samples for isotopic analysis. Samples were reacted by individual acid addition (99% H_3PO_4 at 75 °C). Standard external error is better than ±0.09 ‰. Replicate measurements on 25 pairs of *G. ruber* indicate a reproducibility (1σ) of ±0.11 ‰ for $\delta^{18}O$, whilst replicate measurements on 17 paired benthic foraminifera samples indicate a reproducibility (1σ) of ±0.10 ‰.

3.4.3 XRF core scanning

The archive half of the core was scanned for major element intensities in 1 cm resolution at the Marum Center, University of Bremen using the Avaatech core-scanner. Intensities of elements common in continental siliciclastic rocks, especially clays (e.g. Ti, Fe, Al) are used as qualititative proxies for land derived sedimentary discharge (Arz et al., 1998), and thus XRF records serve as a proxy for precipitation-induced runoff. Measured intensities are normalized by calcium and presented as log-ratios to reduce matrix effects (Aitchison, 1982; Weltje and Tjallingii, 2008).

3.4.4 Coccolith counts

Coccoliths were counted at 10 cm resolution following the procedure outlined in Bolliet et al. (2011). Six taxa dominate the assemblage: *Emiliania huxleyi, Florisphaera profunda, Gephyrocapsa oceanica, Gephyrocapsa ericsonii, Gephyrocapsa muellerae* and *Helicosphaera* spp. Coccolithophore assemblages have been shown to be reliable indicators of oceanic productivity (Beaufort et al., 1997). In particular, the relative abundance of the lower photic zone (150 to 200 m water depth) dwelling species *F. profunda* has been related to the depth of the nutricline (Molfino and McIntyre, 1990; Beaufort et al., 1997; Andruleit and Rogalla, 2002); when the nutricline is shallow, the upper photic zone dwelling species dominate coccolith assemblages (Molfino and McIntyre, 1990) whilst the opposite situation occurs when the nutricline deepens. The relative abundance of *F. profunda* (*%Fp*) has been successfully calibrated to primary productivity (PP, gC m^{-2} yr^{-1}) by Beaufort et al. (1997) in the Indian Ocean, resulting in the equation applied in this study:

$$PP = 617 - [279 \times \log(\%Fp + 3)]$$

3.4.5 Carbonate content

Carbonate content was measured on dried and crushed bulk sediment by full reaction with 6 N HCl using a 'carbonate bomb' device (Müller and Gastner, 1971) at the University of Kiel. Samples were measured at 30 cm resolution throughout the core. Standard error of the 'carbonate bomb' device is ±1 %.

3.4.6 $U^{K'}_{37}$ SST estimates

SSTs were estimated at 10 cm resolution using the alkenone-based $U^{K'}_{37}$ proxy. Alkenones were extracted from 1 g of homogenized bulk sediments and analyzed with double column gas chromatography at the University of Kiel, following the procedure fully outlined in Rincón-Martínez et al. (2010). We calibrated measured $U^{K'}_{37}$ to temperature following Sonzogni et al. (1997) (see Supplementary Information for further discussion), which has been developed for high temperature (24–29 °C) core-tops from the Indian Ocean with the equation:

$$U^{K'}_{37} = (0.023 \times SST\ (°C)) + 0.316$$

3.4.7 Calculation of seawater $\delta^{18}O$ ($\delta^{18}O_{sw}$)

Surface $\delta^{18}O_{sw}$ was calculated from $\delta^{18}O$ measurements on *G. ruber* and $U^{K'}_{37}$ temperatures from the same sample depth. Differences in seasonal growth patterns and ecologies of $\delta^{18}O$-recording foraminifera and $U^{K'}_{37}$-recording coccolithophores (c.f. Timmermann et al., 2014) could introduce uncertainty into calculated $\delta^{18}O_{sw}$, where SSTs would preferentially be measured on Mg/Ca from paired foraminifera samples. However, a temperature bias of ~5 °C would be required to produce a shift in $\delta^{18}O_{sw}$ of ~1 ‰, which is significantly larger than maximum temperature bias that have been observed between Mg/Ca and $U^{K'}_{37}$ SST reconstructions in this region, and thus the effect on the long-term variability of $\delta^{18}O_{sw}$ is assumed to be small. The equation of

Bemis et al. (1998) was used for the calculation:

$$\delta^{18}O_{sw}\ (\text{vs. SMOW}) = 0.27 + [\text{SST } (°C) - 16.5 + (4.8 \times \delta^{18}O(\text{vs. PDB}))]/4.8$$

After calculation of $\delta^{18}O_{sw}$, a correction was applied to the samples to remove the $\delta^{18}O$ signal associated with the global ice volume effect (Waelbroeck et al., 2002).

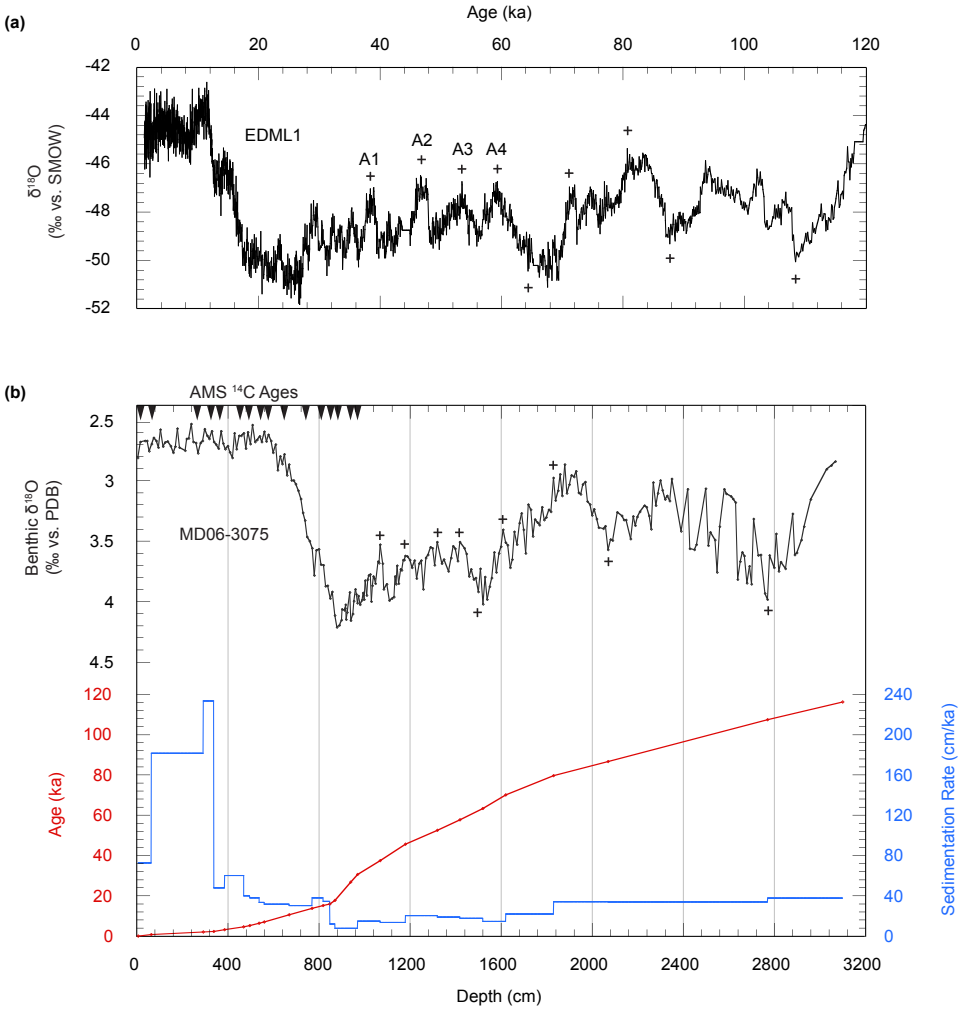

Figure 3.3 - Age model development for Core MD06-3075 (data available in Supplementary Information Table 1). (a) EDML1 chronology for the past 120 kyr based upon the $\delta^{18}O$ record for the EPICA ice core from Dronning Maud Land (EDML1) by Ruth et al. (2007). (b) Benthic $\delta^{18}O$ (black line) and sedimentation rates (green line) versus depth for Core MD06-3075. Red line displays the final age model. Arrows indicate sample depths for AMS ^{14}C analysis. Crosses indicate tie points with the EDML1

3.5 Results

3.5.1 Chronology

The age model for Core MD06-3075 (Supplementary Information Table 3.1) is based upon 16 reservoir-corrected AMS ^{14}C age dates in the upper core to a depth of 970 cm, approximately 31 ka (Figure 3.3). Below 970 cm, the age model was generated by correlation of benthic oxygen isotope data to the EDML1 chronology developed for the EPICA ice core from Dronning Maud Land (EDML) by Ruth et al. (2007). Nine tie points were used between Core MD06-3075 and EDML1 to constrain ages between 31 and 116 ka. The final age model was generated by linear interpolation between AMS ^{14}C ages and tie points. High sedimentation rates in the upper ~5 m of the core are likely artificially introduced by sediment oversampling caused by the piston coring system (Széréméta et al., 2004). Below 5 m, sedimentation rates vary between 8 and 38 cm/kyr.

3.5.2 Stable isotopes

Benthic $\delta^{18}O$ records show well-defined glacial-interglacial isotopic stages with fluctuations in $\delta^{18}O$ between 2.5 and 4.2 ‰, and a maximum amplitude of 1.7 ‰ over Termination I (Figure 3.4). A transition from values of ~2.8 ‰ to ~3.8 ‰ in the oldest part of the core likely represents the transition between Marine Isotope Stage (MIS) 5e and 5d. The four other main substages of MIS 5 are additionally identified (a – d). The $\delta^{18}O$ records from *G. ruber* also show the main glacial-interglacial cycles as seen in the benthic record (Figure 3.4), with values fluctuating between -3.2 and -0.8 ‰, and a maximum amplitude of ~2.2 ‰ over Termination I. During MIS 5, *G. ruber* $\delta^{18}O$ varies between -2.7 and -1.6 ‰, prior to a significant increase during the cold MIS 4 period where values reach a maximum of -1.1 ‰. During MIS 3, values fluctuate between -1.9 and -1.0 ‰, though the resolution in this portion of the record is too low to attribute these variations to individual Dansgaard–Oeschger interstadials and Heinrich stadials. $\delta^{18}O$ values decrease rapidly between ~18 and 13 ka (from -0.8 to -2.0 ‰), before a brief excursion to more positive values representing the Younger Dryas (YD, ~12.8-11.5 ka) cooling event (Supplementary Information Figure 3.2). $\delta^{18}O$ continues to decrease at a

reduced rate throughout the Holocene, reaching a minimum in the late Holocene with values of ~-3.0 ‰, including a core-top value of -3.1 ‰.

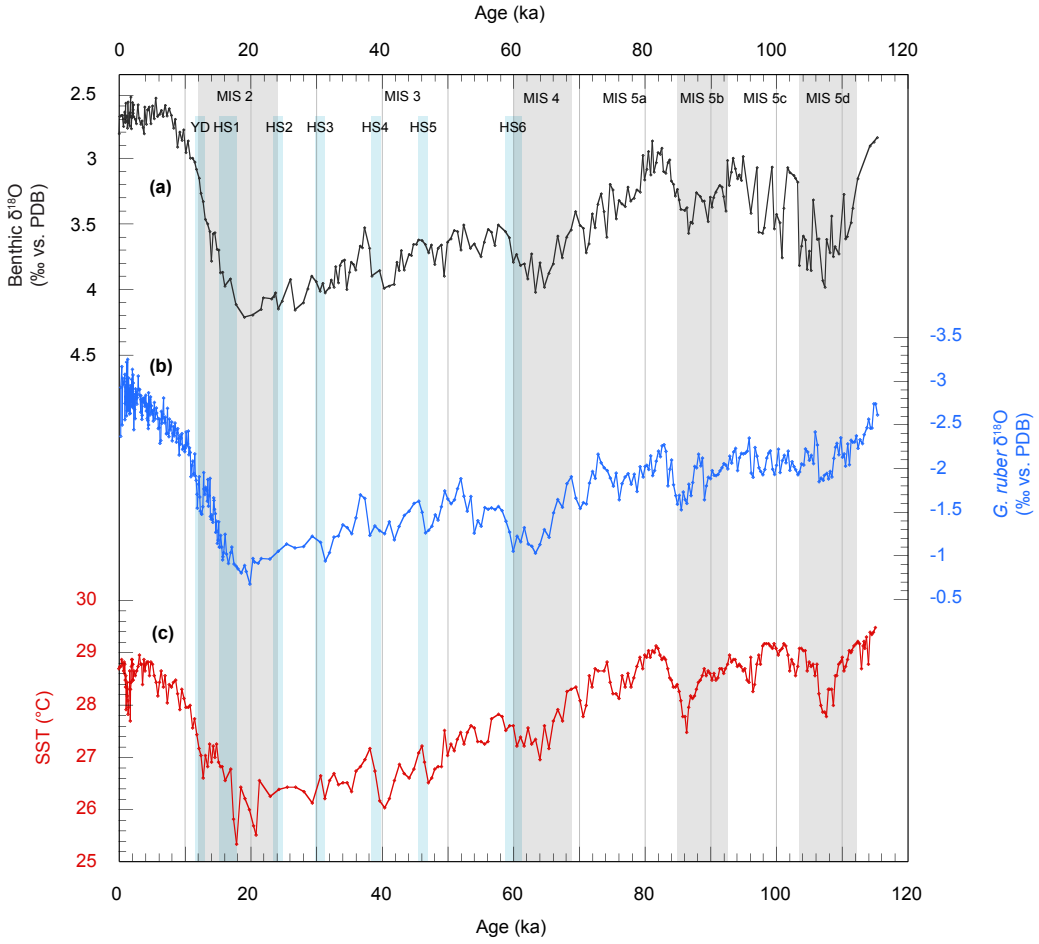

Figure 3.4 - (a) Benthic $\delta^{18}O$ record of Core MD06-3075. (b) Planktonic $\delta^{18}O$ record of Core MD06-3075 based upon the surface dwelling foraminifera *G. ruber*. (c) $U^{K'}_{37}$-derived SST record of Core MD06-3075. Grey vertical bars indicate major marine isotope stages, blue vertical bars indicate HS1-6 and the YD.

3.5.3 SST record

$U^{K'}_{37}$ derived temperatures suggest an SST range of 25.3 °C to 29.2 °C with a deglacial warming amplitude of 3.4 °C (Figure 3.4). An average of the upper three Holocene measurements gives a core-top SST estimate of 28.7 °C, consistent with modern day

annual SSTs at our locality (28.7 °C) (Locarnini et al., 2010). Temperature maxima during MIS 5a, 5c and latest 5e are found to be in excess of those in the Holocene by ~0.5 °C, and the variability between MIS 5 substages is on the order of 1.5 °C. The coolest temperatures are found at ~18 ka, at the beginning of Heinrich Stadial 1 (HS1, ~18-14.6 ka). A temperature plateau at 27.2 °C is consistent with the timing of the Bølling-Allerød (BA, ~14.6 - 12.8 ka) period, whilst the YD is punctuated by a brief cooling episode (Supplementary Information Figure 3.2). An additional cooling episode is observed in the late Holocene between 2 and 1 ka, with temperatures ~0.9 °C cooler than those between 5 and 2 ka and between 1 and 0 ka.

3.5.4 $\delta^{18}O_{sw}$ reconstructions

$\delta^{18}O_{sw}$ was calculated from $\delta^{18}O_{calcite}$ of the near-surface dwelling foraminifera *G. ruber*, corrected for temperature and ice volume effects. Resulting near surface $\delta^{18}O_{sw}$ shows maximum variability between ~-0.3 ‰ and ~1 ‰ (Figure 3.5), with a core top $\delta^{18}O_{sw}$ value of -0.28 ‰. $\delta^{18}O_{sw}$ shows a component of precessional-scale variability during MIS 5 and 4, with lower values during Northern Hemisphere insolation minima, although these trends are imprinted by significant millennial-scale variability. A distinct maximum with values close to 1 ‰ is reached during late MIS 4, preceding a long-term decreasing trend that continues until the present day, where values reach their minimum at ~-0.3 ‰. A prominent negative excursion in $\delta^{18}O_{sw}$ during the BA period interrupts the long-term increasing trend from the LGM to present.

3.5.5 XRF Core Scanning

In this study we use log(Fe/Ca) as a proxy for terrigenous-derived versus marine-derived sediment composition. Raw counts of elements Ca, Fe, Ti, Al, Si and K indicate that Fe represents a major element (Supplementary Information Figure 3.3). Counts of Al, Si and K show differing long-term trends to Fe and Ti, which may indicate a different source or continental weathering mechanism for these elements. Tjallingii et al. (2007) have demonstrated that pore-water contents can have a large impact on XRF intensities of some lighter elements, such as Al and Si, which may make their usage as indicators for

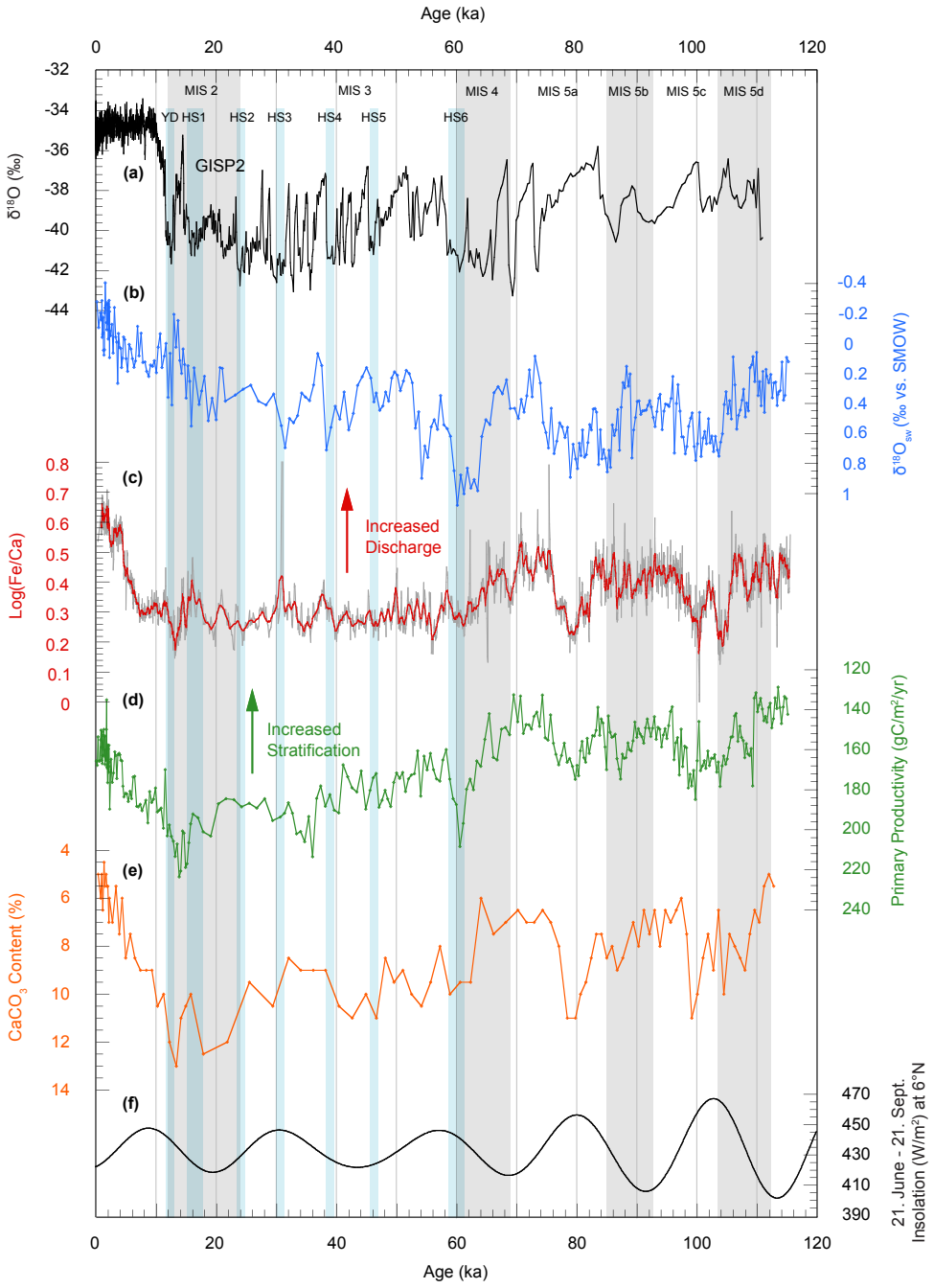

Figure 3.5 - (a) Greenland (GISP2) ice core $\delta^{18}O$ (Stuiver and Grootes, 2000). (b) Estimated ice-volume corrected $\delta^{18}O_{sw}$ from $\delta^{18}O$ measurements on *G. ruber* and $U^{K'}_{37}$-derived SSTs in Core MD06-3075. (c) XRF records of log(Fe/Ca) from Core MD06-3075. (d) Paleoproductivity records from Core MD06-3075 calculated from abundances of *F. profunda* using the equation of Beaufort et al. (1997). Note inverted scale. (e) Calcium carbonate content (%) in Core MD06-3075. Note inverted scale. (f) Mean summer (June 21st to September 21st) insolation at 6°N. Grey vertical bars indicate major marine isotope stages, blue vertical bars indicate HS1-6 and the YD.

runoff unsuitable. Orbital-scale fluctuations in log(Fe/Ca) are noted during MIS 4 and 5, with lower values exhibited between 105 – 98 ka, 82 – 76 ka and 64 – 60 ka (Figure 3.5). During the globally cool period between 60 ka and 20 ka, log(Fe/Ca) remains relatively low and stable and does not display significant millennial scale variability. A slight increase in log(Fe/Ca) is noted consistent with the timing of HS1, followed by a decrease during the BA period, and a return to higher values in the YD. Log-ratios plateau from 11 to 7 ka, prior to a substantial increase between 7 and 5 ka and an additional plateau in the late Holocene.

3.5.6 Primary Productivity

Primary productivity, inferred from counts of the coccolithophore *F. profunda*, shows variability between 130 - 220 $gC/m^2/yr$ (F. profunda relative abundances of 22 - 53 %), when using the calibration of Beaufort et al. (1997) (Figure 3.5). Lowest productivities are observed during MIS 5, with peaks and troughs demonstrating an anti-phase relationship with log(Fe/Ca). MIS 4 is characterised by increased productivity, with a prominent peak occurring at 60 ka with a maximum value of 208 $gC/m^2/yr$. A general increasing trend is noted throughout MIS 3 and MIS 2, reaching maximum values during the BA period and subsequently decreasing steadily throughout the Younger Dryas and Holocene.

3.5.7 Carbonate Content

Carbonate content varies between 4.5 and 13 % over the past 120 ka (Figure 3.5). Peaks and troughs in carbonate content generally follow a similar pattern to primary productivity. In MIS 5 two distinct peaks in carbonate content occur at ~80 and ~100 ka, contemporaneous with peaks in productivity. Values during MIS 3 fluctuate between 11 and 8 %, and increase to the highest values during the LGM (12 %) and BA period (13 %). Carbonate content decreases steadily from the BA period to its minimum value of 4.5 % in the late Holocene.

3.6 Discussion

3.6.1 Proxies of paleoprecipitation in the WPWP

3.6.1.1 $\delta^{18}O_{sw}$ as a proxy of past convective activity

The deglacial evolution of *G. ruber* $\delta^{18}O$ from Core MD06-3075 is in agreement with previous Davao Gulf records (Stott et al., 2002), indicating a decrease in $\delta^{18}O$ during Termination I on the order of ~2.2 ‰ (Figure 3.4; Supplementary Information Figure 3.2). Only 1.0 - 1.2 ‰ of this variability can be attributed to the global ice volume effect (Fairbanks, 1989; Schrag et al., 2002), and the remaining 1.0 - 1.2 ‰ is thus accounted for by warming and hydrologic changes in the surface layer from the LGM to present. Observed linear correlations between $\delta^{18}O_{sw}$ and salinity (Schmidt, 1999) suggest that ice-volume and temperature corrected foraminiferal $\delta^{18}O_{sw}$ estimates have the potential to be employed as a proxy for paleosalinity of surface waters, linked to past changes in the balance of evaporation and precipitation. However, the relationship between $\delta^{18}O_{sw}$ and salinity is regionally dependent, exhibiting a global ~0.5 ‰ change in $\delta^{18}O_{sw}$ per unit change in PSU (Schmidt, 1999), which is reduced to ~0.3 ‰/PSU in the tropics due to intense evaporation and transport processes (LeGrande and Schmidt, 2006). Past changes in these relationships may also induce large uncertainties into paleosalinity estimations, making simple $\delta^{18}O_{sw}$-salinity conversions unsuitable (LeGrande and Schmidt, 2011; Leduc et al., 2013). Instead, $\delta^{18}O_{sw}$ may be better interpreted as a tracer of variability in the hydrologic cycle, influenced by large-scale changes in the transport of vapour, and balance of precipitation and evaporation in the Pacific Ocean (Oppo et al., 2007; Gibbons et al., 2014), in addition to small-scale processes linked to local precipitation effects.

Interpretation of $\delta^{18}O_{sw}$ in the WPWP is further complicated by the numerous marginal seas which influence local atmospheric and surface water circulation. For example, the $\delta^{18}O$ records of *G. ruber* from two cores situated in the Sulu Sea, ODP Site 769 (Linsley, 1996) and MD97-2141 (Oppo et al., 2003), exhibit a decrease of ~1.3 ‰ over Termination I, in line with the variability associated with the ice volume effect

(Fairbanks, 1989; Schrag et al., 2002), but 0.9 ‰ lower than the variability measured in the Davao Gulf. These large differences in deglacial $\delta^{18}O$ amplitudes over relatively short distances in the WPWP cannot be reasonably explained by temperature differences, and instead are likely influenced by variable exchange of fresh South China Sea (SCS) surface waters over the deglacial period (Oppo et al., 2003). This example highlights that the use of $\delta^{18}O$, and by extension $\delta^{18}O_{sw}$, as proxies for local hydrologic changes is highly subjective to regional sea level and surface water exchange mechanisms. This has widespread implications not just on marine records of $\delta^{18}O$, but also on the growing number of speleothem archives from the tropical Pacific and East Asian region (Wang et al., 2001, 2008; Partin et al., 2007; Meckler et al., 2012; Carolin et al., 2013; Ayliffe et al., 2013; Denniston et al., 2013), since source water $\delta^{18}O$ is an important control on $\delta^{18}O$ recorded in speleothems (Breitenbach et al., 2010; Moerman et al., 2013).

3.6.1.2 Proxies of sedimentary discharge

Associating XRF log-ratios of terrigenous (i.e. Fe, Ti) versus marine (Ca) elements with continental sedimentary discharge relies on the assumption that dilution of Ca in the sediment matrix is driven primarily by variability in accumulation rates of the terrigenous fraction, and that additional processes for modulating Ca intensity (e.g. changes in the rate of biogenic carbonate production and deposition) are second-order. Measurements of CaCO3 content and paleoproductivity inferred from coccolithophore assemblages over the past 120 ka in Core MD06-3075 demonstrate an anti-phase relationship with log(Fe/Ca) (Figure 3.5), suggesting that biogenic carbonate production may play a role in determining XRF log-ratios at this locality. However, carbonate content is generally low, varying between 4.5 and 13 %, and thus the terrigenous component represents the overwhelming majority of the sediment fraction in our core. In addition, the depth of the modern lysocline in the West Pacific sits at 3400 m (Berger et al., 1982), well below the depth of our core at 1878 m, and likely experienced only modest changes since the LGM (Anderson and Archer, 2002), suggesting that changes in carbonate dissolution and preservation had an insignificant effect on Ca variability. Individual test weights of G. ruber, which can be used as an indicator of dissolution, also show no significant trends over the deglacial portion of our record.

We therefore suggest that the proportions of Fe and Ca in our core were driven mainly by variability in the accumulation rates of terrigenous sediment driven by fluvial discharge of continental-sourced sediment into the Davao Gulf, with carbonate production acting as a second-order control. Variability in productivity in Core MD06-3075 was likely effected by transport of freshwater and detrital material into the surface waters of the Davao Gulf. During periods of high discharge, increased freshwater stratification and sediment loading of the upper surface waters could act to constrain productivity and deepen the nutricline, resulting in higher abundances of *F. profunda*. Additionally, increased silica input during periods of high discharge may result in blooms of predominantly siliceous phytoplankton (Weldeab et al., 2007), reducing productivity of calcareous species. This interpretation of log(Fe/Ca) records as an indicator of fluvial discharge is further supported by published pollen records from the same core (Bian et al., 2011) which suggest dry conditions during the LGM compared to the Holocene, as observed in our log(Fe/Ca) records, as well as reduced accumulation rates during the glacial portion of our record, which would be consistent with reduced sedimentary discharge. Taken together, our XRF log-ratios and paleoproductivity reconstructions from the Davao Gulf present a robust picture of local rainfall variability over Mindanao during the past 120 ka.

3.6.2 WPWP precipitation over the past 120 ka

3.6.2.1 Orbitally paced precipitation changes at Mindanao

Orbital scale trends of sedimentary discharge based upon log(Fe/Ca) ratios and paleoproductivity estimates suggest an anti-phase relationship with local boreal summer insolation forcing – discharge is higher and productivity lower during boreal summer insolation minima, and vice versa (Figure 3.6). This is corroborated by cross-spectral analysis, which shows a strong coherency (>95% confidence interval) of log(Fe/Ca) and boreal summer insolation (June 21st - September 21st) at 6 °N in the precession band, with a phase spectrum indicating a lead of insolation over log(Fe/Ca) by ~176° (i.e. close to perfect antiphase) (Supplementary Information Figure 3.4). The last interglacial period in particular is characterised by precessional-scale variability, which may be a result of the

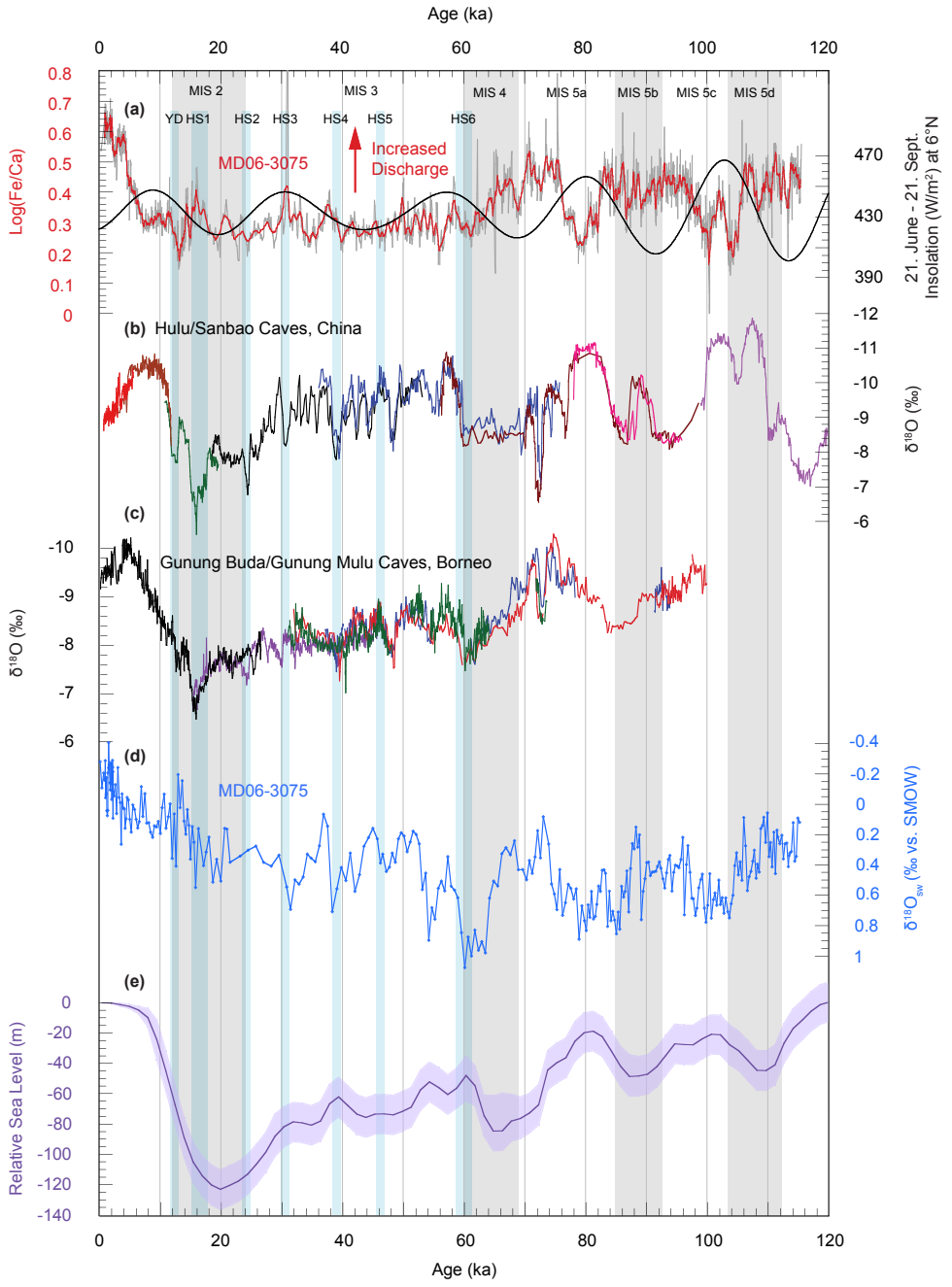

Figure 3.6 - (a) XRF records of log(Fe/Ca) from Core MD06-3075 superimposed with mean boreal summer (June 21st to September 21st) insolation at 6°N. (b) Composite speleothem $\delta^{18}O$ records from Hulu and Sanbao caves in China (Wang et al., 2001, 2008). (c) Composite speleothem $\delta^{18}O$ records from Gunung Mulu and Gunung Buda Caves in Borneo (Partin et al., 2007; Carolin et al., 2013). (d) Estimated ice-volume corrected $\delta^{18}O_{sw}$ from $\delta^{18}O$ measurements on *G. ruber* and $U^{K'}_{37}$-derived SSTs in Core MD06-3075. (e) Relative sea level change based upon Waelbroeck et al. (2002). Grey vertical bars indicate major marine isotope stages, blue vertical bars indicate HS1-6 and the YD.

stronger precessional insolation forcing during this time interval. Trends of $\delta^{18}O_{sw}$ show general agreement with log(Fe/Ca) and paleoproductivity during the last interglacial period (Figure 3.5), with higher values during low sedimentary discharge periods between 65 to 60 ka, 82 to 75 ka, and 105 to 96 ka. However, the timing of some major shifts in $\delta^{18}O_{sw}$, for example the prominent positive excursion centred at 85 ka, do not show entire agreement with log(Fe/Ca) and productivity records, and thus these proxies may be partly influenced by different factors.

Between the middle and end of MIS 4, a marked increase in productivity is observed, likely in response to reduced freshwater input (and thus reduced sedimentary discharge) combined with lower SSTs, which may have been a result of enhanced vertical mixing of the water column. In contrast to MIS 4 and 5, MIS 3 is defined by a rather muted response to orbital forcing, with low values of log(Fe/Ca) accompanied by increasing productivity indicating a long-term regional drying (Figure 3.5). This muted hydroclimate response at times of weakened precessional forcing in the WPWP has also been documented in speleothem records covering several late-Pleistocence glacial-interglacial cycles in Borneo (Meckler et al., 2012), whilst log(Ti/Ca) records from the north of Papua New Guinea also show less pronounced precessional-scale variability during the last glacial period (Tachikawa et al., 2011). However, it is interesting to note that despite the 'dry' conditions inferred from log(Fe/Ca) and productivity records in Core MD06-3075, $\delta^{18}O_{sw}$ shows a long term decreasing trend from the end of MIS 4 to the LGM. These differing trends likely reflect decoupling of local precipitation, which is more faithfully recorded in terrestrial proxies, versus changes in regional hydrology which are recorded in $\delta^{18}O_{sw}$.

Comparison of hydroclimate records from Core MD06-3075 with speleothem $\delta^{18}O$ records from Borneo (Partin et al., 2007; Carolin et al., 2013) and China (Wang et al., 2001, 2008) indicates that convection patterns are linked across the WPWP (Figure 3.6). A general anti-phase relationship is observed between log(Fe/Ca) at Mindanao and speleothem $\delta^{18}O$ in China during MIS 5. During Northern Hemisphere summer insolation maxima, reduced $\delta^{18}O$ values in Chinese speleothems (interpreted as a strengthened EAM state (Wang et al., 2001, 2008)) are correlated with low log(Fe/Ca)

values at Mindanao (interpreted as reduced runoff). In the modern day, both regions receive greater rainfall during the boreal summer when the ITCZ is located to the North, and thus this dipole-like pattern is not explained by modern analogies to a northward shift of the ITCZ. Instead, the precipitation pattern during MIS 5 suggests that increased northerly penetration of monsoon rainfall in response to Northern Hemisphere summer insolation maxima is balanced by reduced precipitation at Mindanao. However, such an anti-phase pattern is not evident during the last glacial period and the Holocene, implying a different response during periods of weakened precessional forcing.

In contrast, speleothem $\delta^{18}O$ records from Borneo are shown to be in phase with boreal fall insolation (Carolin et al., 2013), despite their latitudinal position being only ~2° south of Core MD06-3075, implying different controls on hydrology in the marine versus land realm of the Indo-Pacific region. This finding is consistent with modeling studies that show regional sensitivity to the seasonal distribution of insolation in the tropical West Pacific (Tierney et al., 2012). In addition, the pattern of ITCZ displacement as a response to past climate change may not have been globally or even regionally consistent, and larger meridional displacements could have occurred over small zonal extents (McGee et al., 2014). Phase shifts between records of convection from Mindanao and those in Borneo, and a lack of response to precessional insolation forcing during the last glacial period, is therefore further evidence that a simplistic view of homogenous ITCZ latitudinal migration driven by precession cannot fully explain changes in convective activity in the WPWP over the entire length of our record.

In the modern day, ENSO variability also has a significant impact on precipitation at Mindanao (Figure 3.2), thus we may expect that long-term changes in the mean ENSO state could have impacted past precipitation. A simplified modeling approach by Clement et al. (1999) highlighted the influence of the precessional cycle on ENSO variability, however the proposed ENSO response in this model combined with the modern influence of ENSO at our core site (Figure 3.2) would suggest precipitation anomalies opposite in sign to our observed log(Fe/Ca) records. Attempts to reconstruct ENSO conditions in the late Pleistocene, for example through reconstructions of cross-equatorial temperature gradients (e.g. Lea et al., 2000; Koutavas et al., 2002) have also

lacked agreement on the magnitude or mechanisms of past ENSO variability, whilst little support for an ENSO signature has been found based upon $\delta^{18}O_{sw}$ reconstructions in the East and West Pacific occurring over the last deglacial period (Leduc et al., 2009; Gibbons et al., 2014).

The role of sea-level changes has been recently highlighted as an important driver of the strength and position of the Walker circulation, where increased Sunda Shelf exposure during glacial sea-level lowstands can act to reduce convective motion over the maritime continent (DiNezio et al., 2011; DiNezio and Tierney, 2013). These findings may help to explain the muted response of precipitation to precessional forcing during the last glacial period, as sea level was lower and Sunda Shelf exposure was higher (Figure 3.6), which could have promoted widespread subsidence over the Indonesian landmass. This mechanism would be furthermore consistent with log(Ti/Ca) records from North of Papua New Guinea, which showed reduced values during the last glacial period when the shelf between Australia and Papua New Guinea was exposed (Tachikawa et al., 2011). However, with only few records of WPWP hydroclimate extending over multiple glacial-interglacial cycles, it remains a question as to whether the spatial pattern of convection is more consistent with changes associated with the Walker Circulation versus changes occurring as a result of meridional ITCZ dynamics.

3.6.2.2 Sub-orbital forcing of WPWP hydroclimate

Records of log(Fe/Ca) and productivity in Core MD06-3075 do not show consistent responses to Heinrich stadials over MIS 3 (Figure 3.5). This may in part be due to reduced sedimentation rates and lower resolution in the glacial portion of our records, which does not allow identification of individual Heinrich stadials. The upper portion of our record (from the LGM to present day) has a tighter-constrained chronology via AMS ^{14}C dating, combined with a much higher temporal resolution (Figure 3.3), and thus we can therefore make inferences of millennial-scale variability over this period. HS1 is marked with an increase in log(Fe/Ca) and reduced productivity, consistent with a period of increased sedimentary discharge, and therefore increased precipitation, at Mindanao (Figure 3.7). This trend reverses during the BA period. The regional pattern of

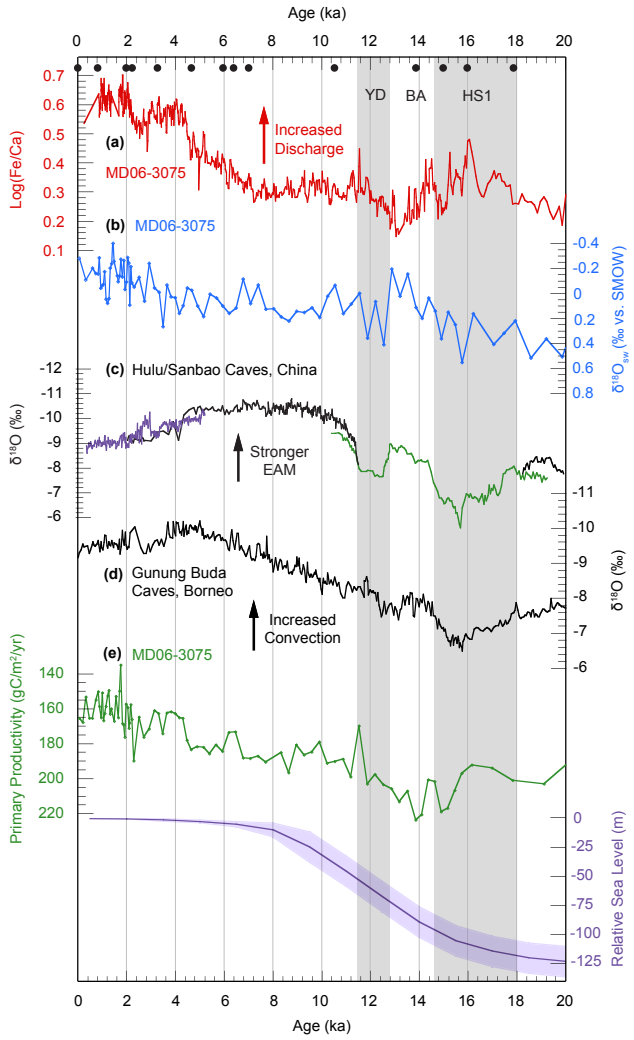

Figure 3.7 - Expanded records covering the past 20 ka. Black dots indicate ^{14}C AMS dates used for age control. (a) XRF records of log(Fe/Ca) from Core MD06-3075. (b) Estimated $\delta^{18}O_{sw}$ from $\delta^{18}O$ measurements on *G. ruber* and $U^{K'}_{37}$-derived SSTs in Core MD06-3075. (c) Composite speleothem $\delta^{18}O$ records from Hulu and Sanbao caves in China (Wang et al., 2001, 2008). (d) Spliced speleothem $\delta^{18}O$ record from Gunung Buda Caves in Borneo (Partin et al., 2007). (e) Paleoproductivity records from Core MD06-3075 calculated from abundances of *F. profunda* using the equation of Beaufort et al. (1997). Note inverted axis. (f) Relative sea level change based upon Waelbroeck et al. (2002).

convection changes during HS1, with increased precipitation at Mindanao and dry conditions in Borneo and China (Wang et al., 2001; Partin et al., 2007) is consistent with new modeling results presented by Mohtadi et al. (2014), which show that the climatic response to HS1 in the West Pacific is more complex than a simple southward shift of

the rain belts associated with a southerly positioned ITCZ; whilst western and central Indonesia experienced drier conditions, the southern Philippines may have become wetter.

In contrast to log(Fe/Ca) and productivity records, $\delta^{18}O_{sw}$ shows generally higher values during HS1 and the YD than during the BA period, though we note divergence with the closely located $\delta^{18}O_{sw}$ record of Stott et al. (2002, 2007) which may be caused by different methods of SST reconstructions used to calculate $\delta^{18}O_{sw}$ (Supplementary Information Figure 3.2). Higher $\delta^{18}O_{sw}$ during HS1 and the YD than the BA period is a consistent signal observed across the WPWP in marine sediments (Gibbons et al., 2014), as well as in speleothem $\delta^{18}O$ records from both China (Wang et al., 2001) and Borneo (Partin et al., 2007) (Figure 3.7), which is further evidence that changes in $\delta^{18}O_{sw}$ are controlled primarily by large-scale re-organizations of the hydrologic cycle, linked on millennial timescales to Northern Hemisphere climate events.

3.7 Conclusions

Records of sedimentary discharge and productivity in Core MD06-3075 from the Davao Gulf, at the boundary between the Indonesian archipelago and the open West Pacific, are linked to local precipitation variability over the past 120 ka. During MIS 5, precipitation at Mindanao responds to precessional insolation forcing with highest precipitation noted during Northern Hemisphere insolation minima and vice versa. We suggest that two mechanisms were responsible for controlling orbital-scale variability in West Pacific precipitation: (1) latitudinal migrations of the mean ITCZ position driven by precessional cyclicity. During Northern Hemisphere insolation maxima, the summer position of the ITCZ migrates northwards, inducing greater precipitation in China, which is balanced by reduced precipitation in the central WPWP region, (2) strengthening/weakening of the Walker Circulation caused by changes in the hydrologic cycle and sea level. It is likely that these two mechanisms are tightly coupled, and resolving the relative importance of each component would require a greater number of precipitation records covering several late-Quaternary precessional cycles in the WPWP. In the last glacial period, precipitation was suppressed and showed little orbital scale variability, which we attribute

to the reduced amplitude of precessional cyclicity, combined with increased subsidence of air masses over the exposed Sunda Shelf. Differing long-term trends observed in $\delta^{18}O_{sw}$ reconstructions in Core MD06-3075 likely reflect a composite of regional climatic processes, including changes in salinity, moisture sources and transport pathways, not limited to local precipitation variability.

3.8 Acknowledgements

We thank the chief scientist, Carlo Laj, the captain and crew of R/V Marion Dufresne, Catherine Kissel, Yvon Balut and the French Polar Institute for their effort and support during the Marco Polo 2 Cruise (IMAGES). We are grateful to Marie-Josée Nadeau and the Leibniz Laboratory team for AMS ^{14}C measurements, to Silvia Koch for technical assistance with $U^{K'}_{37}$ analysis, and to Ursula Röhl and the Marum Center for Marine Environmental Sciences (Bremen University) for XRF scanning. We also thank the editor, Christopher Charles, and one anonymous reviewer for valuable and constructive comments that improved the quality of this manuscript. This research was carried out as part of the Throughflow Project, funded by the Marie Curie Actions Plan, Seventh Framework Programme (Grant no. 237922). Additional funding was provided by DFG grant KU 649/26-1. Data presented in this paper are archived at www.pangaea.de.

3.9 References

Aitchison, J. (1982), The statistical analysis of compositional data, Journal of the Royal Statistical Society, Series B (Methodological), 44(2), 139-177.

Anderson, D. M., and D. Archer (2002), Glacial–interglacial stability of ocean pH inferred from foraminifer dissolution rates, Nature, 416(6876), 70-73. doi:10.1038/416070a.

Andruleit, H., and U. Rogalla (2002), Coccolithophores in surface sediments of the Arabian Sea in relation to environmental gradients in surface waters, Marine Geology, 186(3), 505-526, doi: 10.1016/S0025-3227(02)00312-2.

Antonov, J. I., D. Seidov, T. P. Boyer, R. A. Locarnini, A. V. Mishonov, H. E. Garcia, O. K. Baranova, M. M. Zweng, and D. R. Johnson (2010), World Ocean Atlas 2009, Volume 2: Salinity, S. Levitus, Ed. NOAA Atlas NESDIS 69, U.S. Government Printing Office, Washington, D.C., 1-184.

Arz, H. W., J. Pätzold, and G. Wefer (1998), Correlated millennial-scale changes in surface hydrography and terrigenous sediment yield inferred from last-glacial marine deposits off northeastern Brazil, Quaternary Research, 50(2), 157-166, doi: 10.1006/qres.1998.1992.

Ayliffe, L. K., M. K. Gagan, J. X. Zhao, R. N. Drysdale, J. C. Hellstrom, W. S. Hantoro, M. L. Griffiths, H. Scott-Gagan, E. St Pierre, J. A. Cowley, and B. W. Suwargadi (2013), Rapid interhemispheric climate links via the Australasian monsoon during the last deglaciation, Nature communications, 4, doi: 10.1038/ncomms3908.

Beaufort, L., Y. Lancelot, P. Camberlin, O. Cayre, E. Vincent, F. Bassinot, and L. Labeyrie (1997), Insolation cycles as a major control of equatorial Indian Ocean primary production, Science, 278(5342), 1451-1454, doi: 10.1126/science.278.5342.1451.

Beaufort, L., T. de Garidel-Thoron, A. C. Mix, and N. G. Pisias (2001), ENSO-like forcing on oceanic primary production during the late Pleistocene, Science, 293(5539), 2440-2444, doi: 10.1126/science.293.5539.2440.

Bemis, B. E., H. J. Spero, J. Bijma, and D. W. Lea (1998), Reevaluation of the oxygen isotopic composition of planktonic foraminifera: Experimental results and revised paleotemperature equations, Paleoceanography, 13(2), 150-160, doi: 10.1029/98PA00070.

Berger, W. H., M. C. Bonneau, and F. L. Parker (1982), Foraminifera on the deep-sea floor-lysocline and dissolution rate, Oceanologica Acta, 5(2), 249-258.

Bian, Y., Z. Jian, C. Weng, W. Kuhnt, T. Bolliet, and A. Holbourn (2011), A palynological and palaeoclimatological record from the southern Philippines since the Last Glacial Maximum, Chinese Science Bulletin, 56(22), 2359-2365, doi: 10.1007/s11434-011-4573-1.

Bjerknes, J. (1969), Atmospheric teleconnections from the equatorial pacific 1, Monthly Weather Review, 97(3), 163-172.

Bolliet, T., A. Holbourn, W. Kuhnt, C. Laj, C. Kissel, L. Beaufort, M. Kienast, N. Andersen, and D. Garbe-Schönberg (2011), Mindanao Dome variability over the last 160 kyr: Episodic glacial cooling of the West Pacific Warm Pool, Paleoceanography, 26, PA1208, doi:10.1029/2010PA001966.

Breitenbach, S. F., J. F. Adkins, H. Meyer, N. Marwan, K. K. Kumar, and G. H. Haug (2010), Strong influence of water vapor source dynamics on stable isotopes in precipitation observed in Southern Meghalaya, NE India, Earth and Planetary Science Letters, 292(1), 212-220, doi: 10.1016/j.epsl.2010.01.038.

Cane, M. A. (1998), A Role for the Tropical Pacific, Science, 282(5386), 59-61, doi: 10.1126/science.282.5386.59.

Carolin, S. A., K. M. Cobb, J. F. Adkins, B. Clark, J. L. Conroy, S. Lejau, J. Malang, and A. A. Tuen (2013), Varied Response of Western Pacific Hydrology to Climate

Forcings over the Last Glacial Period, Science, 340(6140), 1564-1566, doi: 10.1126/science.1233797.

Cheng, H., A. Sinha, X. Wang, F. W. Cruz, and R. L. Edwards (2012), The Global Paleomonsoon as seen through speleothem records from Asia and the Americas, Climate dynamics, 39(5), 1045-1062, doi: 10.1007/s00382-012-1363-7.

Clement, A. C., R. Seager, and M. A. Cane (1999), Orbital controls on the El Niño/Southern Oscillation and the tropical climate, Paleoceanography, 14(4), 441–456, doi:10.1029/1999PA900013.

Cruz, F. W., S. J. Burns, I. Karmann, W. D. Sharp, M. Vuille, A. O. Cardoso, J. A. Ferrari, P. L. Silva Dias, and O. Viana (2005), Insolation-driven changes in atmospheric circulation over the past 116,000 years in subtropical Brazil, Nature, 434(7029), 63-66, doi: 10.1038/nature03365.

Dannenmann, S., B. K. Linsley, D. W. Oppo, Y. Rosenthal, and L. Beaufort (2003), East Asian monsoon forcing of suborbital variability in the Sulu Sea during Marine Isotope Stage 3: Link to Northern Hemisphere climate, Geochemistry, Geophysics, Geosystems, 4(1), 1-13, doi: 10.1029/2002GC000390.

Denniston, R. F., K. H. Wyrwoll, Y. Asmerom, V. J. Polyak, W. F. Humphrey, H. Cugley, D. Woods, Z. LaPointe, J. Peota, and E. Greaves (2013), North Atlantic forcing of millennial-scale Indo-Australian monsoon dynamics during the Last Glacial period, Quaternary Science Reviews, 72, 159-168, doi: 10.1016/j.quascirev.2013.04.012.

de Garidel-Thoron, T., Y. Rosenthal, L. Beaufort, E. Bard, C. Sonzogni, and A. C. Mix (2007), A multiproxy assessment of the western equatorial Pacific hydrography during the last 30 kyr, Paleoceanography, 22, PA3204, doi: 10.1029/2006PA001269.

DiNezio, P. N., A. Clement, G. A. Vecchi, B. Soden, A. J. Broccoli, B. L. Otto-Bliesner, and P. Braconnot (2011), The response of the Walker circulation to Last Glacial Maximum forcing: Implications for detection in proxies, Paleoceanography, 26(3), PA3217, doi: 10.1029/2010PA002083.

DiNezio, P. N., and J. E. Tierney (2013), The effect of sea level on glacial Indo-Pacific climate. Nature Geoscience, 6, 485-491, doi: 10.1038/ngeo1823.

Donohoe, A., J. Marshall, D. Ferreira, and D. McGee (2013), The relationship between ITCZ location and cross-equatorial atmospheric heat transport: from the seasonal cycle to the last glacial maximum, Journal of Climate, 26(11), 3597-3618, doi: 10.1175/JCLI-D-12-00467.1.

Fairbanks, R. G. (1989), A 17,000-year glacio-eustatic sea level record: influence of glacial melting rates on the Younger Dryas event and deep-ocean circulation, Nature, 342(6250), 637-642, doi: 10.1038/342637a0.

Fairbanks, R. G., R. A. Mortlock, T. Chiu, L. Cao, A. Kaplan, T. P. Guilderson, T. W. Fairbanks, A. L. Bloom, P. M. Grootes, and M. -J. Nadeau (2005), Radiocarbon

calibration curve spanning 0 to 50,000 years BP based on paired $^{230}Th/^{234}U/^{238}U$ and ^{14}C dates on pristine corals, Quaternary Science Reviews, 24(16), 1781-1796, doi: 10.1016/j.quascirev.2005.04.007.

Gibbons, F. T., D. W. Oppo, M. Mohtadi, Y. Rosenthal, J. Cheng, Z. Liu, and B. K. Linsley (2014), Deglacial $\delta^{18}O$ and hydrologic variability in the tropical Pacific and Indian Oceans. Earth and Planetary Science Letters, 387, 240-251, doi: 10.1016/j.epsl.2013.11.032.

Griffiths, M., R. Drysdale, M. Gagan, J. Zhao, L. Ayliffe, J. Hellstrom, W. Hantoro, S. Frisia, Y. Feng, and I. Cartwright (2009), Increasing Australian-Indonesian monsoon rainfall linked to early Holocene sea-level rise, Nature Geoscience, 2(9), 636-639, doi: 10.1038/ngeo605.

Hoerling, M. P., J. W. Hurrell, and T. Xu (2001), Tropical origins for recent North Atlantic climate change, Science, 292(5514), 90-92, doi: 10.1126/science.1058582.

IAEA/WMO (2013), Global Network of Isotopes in Precipitation, The GNIP Database. Accessible at: http://www.iaea.org/water.

Kashino, Y., M. Aoyama, T. Kawano, N. Hendiarti, Y. Anantasena, K. Muneyama, and H. Watanabe (1996), The water masses between Mindanao and New Guinea, Journal of Geophysical Research: Oceans (1978–2012), 101(C5), 12391-12400, doi: 10.1029/95JC03797.

Koutavas, A., J. Lynch-Stieglitz, T. M. Marchitto, and J. P. Sachs (2002), El Niño-like pattern in ice age tropical Pacific sea surface temperature, Science, 297(5579), 226-230, doi: 10.1126/science.1072376.

Laj, C., and Shipboard Scientific Party (2006), Les rapports de campagnes a la mer: MD155-Marco Polo 2, IMAGES XIV cruise report, 11 juin au 6 juillet 2006, Publications de l'institut Polaire Francais, OCE/2006/06.

Lea, D. W., D. K. Pak, and H. J. Spero (2000), Climate impact of late Quaternary equatorial Pacific sea surface temperature variations, Science, 289(5485), 1719-1724, doi: 10.1126/science.289.5485.1719.

Leduc, G., L. Vidal, K. Tachikawa, F. Rostek, C. Sonzogni, L. Beaufort, and E. Bard (2007), Moisture transport across Central America as a positive feedback on abrupt climatic changes, Nature, 445(7130), 908-911, doi: 10.1038/nature05578.

Leduc, G., J. P. Sachs, O. E. Kawka, and R. R. Schneider (2013), Holocene changes in eastern equatorial Atlantic salinity as estimated by water isotopologues, Earth and Planetary Science Letters, 362, 151-162, doi: 10.1016/j.epsl.2012.12.003.

LeGrande, A. N., and G. A. Schmidt (2006), Global gridded data set of the oxygen isotopic composition in seawater, Geophysical Research Letters, 33(12), doi: 10.1029/2006GL026011.

Linsley, B. K. (1996), Oxygen-isotope record of sea level and climate variations in the

Sulu Sea over the past 150,000 years, Nature, 380, 234-237, doi: 10.1038/380234a0.

Locarnini, R. A., A. V. Mishonov, J. I. Antonov, T. P. Boyer, H. E. Garcia, O. K. Baranova, M. M. Zweng, and D. R. Johnson (2010), World Ocean Atlas 2009, Volume 1: Temperature, S. Levitus, Ed. NOAA Atlas NESDIS 68, U.S. Government Printing Office, Washington, D.C., 1-184.

Marchitto, T. M., W. B. Curry, J. Lynch-Stieglitz, S. P. Bryan, K. M. Cobb, and D. C. Lund (2014), Improved oxygen isotope temperature calibrations for cosmopolitan benthic foraminifera, Geochimica et Cosmochimica Acta, 130, 1-11, doi: 10.1016/j.gca.2013.12.034.

Martinez, I., L. Keigwin, T. T. Barrows, Y. Yokoyama, and J. Southon (2003), La Niña like conditions in the eastern equatorial Pacific and a stronger Choco jet in the northern Andes during the last glaciation, Paleoceanography, 18(2), 1033, doi: 10.1029/2002PA000877.

McGee, D., A. Donohoe, J. Marshall, and D. Ferreira (2014), Changes in ITCZ location and cross-equatorial heat transport at the Last Glacial Maximum, Heinrich Stadial 1, and the mid-Holocene, Earth and Planetary Science Letters, 390, 69-79, doi: 10.1016/j.epsl.2013.12.043.

Meckler, A., M. Clarkson, K. Cobb, H. Sodemann, and J. Adkins (2012), Interglacial hydroclimate in the tropical West Pacific through the Late Pleistocene, Science, 336(6086), 1301-1304, doi: 10.1126/science.1218340.

Medina-Elizalde, M. N., and D. W. Lea (2005), The mid-Pleistocene transition in the Tropical Pacific, Science, 310(5750), 1009-1012, doi: 10.1126/science.1115933.

Merlis, T. M., T. Schneider, S. Bordoni, and I. Eisenman (2013), Hadley circulation response to orbital precession. Part I: Aquaplanets, Journal of Climate, 26(3), 740-753, doi: 10.1175/JCLI-D-11-00716.1.

Moerman, J. W., K. M. Cobb, J. F. Adkins, H. Sodemann, B. Clark, and A. A. Tuen (2013), Diurnal to interannual rainfall $\delta^{18}O$ variations in northern Borneo driven by regional hydrology, Earth and Planetary Science Letters, 369, 108-119, doi: 10.1016/j.epsl.2013.03.014.

Mohtadi, M., M. Prange, D. W. Oppo, R. De Pol-Holz, U. Merkel, X. Zhang, S. Steinke, and A. Lückge (2014), North Atlantic forcing of tropical Indian Ocean climate, Nature, 509(7498), 76-80, doi: 10.1038/nature13196.

Molfino, B., and A. McIntyre (1990), Nutricline variation in the equatorial Atlantic coincident with the Younger Dryas, Paleoceanography, 5(6), 997–1008, doi:10.1029/PA005i006p00997.

Müller, G. and M. Gastner, (1971), The 'Karbonat-Bombe', a simple device for the determination of carbonate content in sediment, soils, and other materials, Neues Jahrbuch für Mineralogie - Monatshefte, 10, 466-469.

Nadeau, M. -J., M. Schleicher, P. Grootes, H. Erlenkeuser, A. Gottdang, D. Mous, M. Sarnthein, and H. Willkomm (1997), The Leibniz-Labor AMS facility at the Christian-Albrechts University, Kiel, Germany, Nuclear Instruments and Methods in Physics Research Section B: Beam Interactions with Materials and Atoms, 123(1), 22-30, doi: 10.1016/S0168-583X(96)00730-6.

Oppo, D., B. Linsley, Y. Rosenthal, S. Dannenmann, and L. Beaufort (2003), Orbital and suborbital climate variability in the Sulu Sea, western tropical Pacific, Geochemistry, Geophysics, Geosystems, 4(1), 1-20, doi: 10.1029/2001GC000260.

Oppo, D. W., G. A. Schmidt, and A. N. LeGrande (2007), Seawater isotope constraints on tropical hydrology during the Holocene, Geophysical Research Letters, 34(13), L13701, doi: 10.1029/2007GL030017.

Partin, J. W., K. M. Cobb, J. F. Adkins, B. Clark, and D. P. Fernandez (2007), Millennial-scale trends in west Pacific warm pool hydrology since the Last Glacial Maximum, Nature, 449(7161), 452-455, doi: 10.1038/nature06164.

Qu, T., H. Mitsudera, and T. Yamagata (1999), A Climatology of the Circulation and Water Mass Distribution near the Philippine Coast*, Journal of physical oceanography, 29(7), 1488-1505.

Rincón-Martínez, D., F. Lamy, S. Contreras, G. Leduc, E. Bard, C. Saukel, T. Blanz, A. Mackensen, and R. Tiedemann (2010), More humid interglacials in Ecuador during the past 500 kyr linked to latitudinal shifts of the equatorial front and the Intertropical Convergence Zone in the eastern tropical Pacific, Paleoceanography, 25(2), PA2210, doi: 10.1029/2009PA001868.

Ropelewski, C. F., and M. S. Halpert (1987), Global and Regional Scale Precipitation Patterns Associated with the El Niño/Southern Oscillation, Monthly Weather Review, 115, 1606–1626.

Ruth, U., J. -M. Barnola, J. Beer, M. Bigler, T. Blunier, E. Castellano, H. Fischer, F. Fundel, P. Huybrechts, and P. Kaufmann (2007), "EDML1": a chronology for the EPICA deep ice core from Dronning Maud Land, Antarctica, over the last 150 000 years, Climate of the Past Discussions, 3(2), 549-574, doi: 10.5194/cp-3-475-2007.

Saikku, R., L. Stott, and R. Thunell (2009), A bi-polar signal recorded in the western tropical Pacific: Northern and Southern Hemisphere climate records from the Pacific warm pool during the last Ice Age, Quaternary Science Reviews, 28(23), 2374-2385, doi: 10.1016/j.quascirev.2009.05.007.

Schleicher, M., P. Grootes, M. -J. Nadeau, and A. Schoon (1998), The carbonate ^{14}C background and its components at the Leibniz AMS facility, Radiocarbon, 40(1), 85-93.

Schneider, T., T. Bischoff, T., and G. H. Haug (2014), Migrations and dynamics of the intertropical convergence zone, Nature, 513(7516), 45-53, doi: 10.1038/nature13636.

Schmidt, G. A. (1999), Forward modeling of carbonate proxy data from planktonic

foraminifera using oxygen isotope tracers in a global ocean model, Paleoceanography, 14(4), 482-497, doi: 1 0.1029/1999PA900025.

Schrag, D. P., J. F. Adkins, K. McIntyre, J. L. Alexander, D. A. Hodell, C. D. Charles, and J. F. McManus (2002), The oxygen isotopic composition of seawater during the Last Glacial Maximum, Quaternary Science Reviews, 21(1), 331-342, doi: 10.1016/s0277-3791(01)00110-x.

Sonzogni, C., E. Bard, F. Rostek, D. Dollfus, A. Rosell-Melé, and G. Eglinton (1997), Temperature and salinity effects on alkenone ratios measured in surface sediments from the Indian Ocean, Quaternary Research, 47(3), 344-355, doi: 10.1006/qres.1997.1885.

Timmermann, A., J. Sachs, and O. Elison Timm (2014), Assessing divergent SST behavior during the last 21 ka derived from alkenones and G.ruber-Mg/Ca in the equatorial Pacific, Paleoceanography, 29, 680–696, doi:10.1002/2013PA002598.

Stott, L., C. Poulsen, S. Lund, and R. Thunell (2002), Super ENSO and global climate oscillations at millennial time scales, Science, 297(5579), 222-226, doi: 10.1126/science.1071627.

Stott, L., A. Timmermann, and R. Thunell (2007), Southern hemisphere and deep-sea warming led deglacial atmospheric CO2 rise and tropical warming, Science, 318(5849), 435-438, doi: 10.1126/science.1143791.

Stuiver, M. and P. M. Grootes (2000), GISP2 oxygen isotope ratios, Quaternary Research, 53(3), 277-284, doi: 10.1006/qres.2000.2127.

Széréméta, N., F. Bassinot, Y. Balut, L. Labeyrie, and M. Pagel (2004), Oversampling of sedimentary series collected by giant piston corer: Evidence and corrections based on 3.5-kHz chirp profiles, Paleoceanography, 19(1), PA1005, doi: 10.1029/2002PA000795.

Tachikawa, K., O. Cartapanis, L. Vidal, L. Beaufort, T. Barlyaeva, and E. Bard, (2011). The precession phase of hydrological variability in the Western Pacific Warm Pool during the past 400 ka. Quaternary Science Reviews, 30(25), 3716-3727. doi: 10.1016/j.quascirev.2011.09.016.

Tierney, J. E., D. W. Oppo, A. N. LeGrande, Y. Huang, Y. Rosenthal, and B. K. Linsley (2012), The influence of Indian Ocean atmospheric circulation on Warm Pool hydroclimate during the Holocene epoch, Journal of Geophysical Research: Atmospheres, 117(D19), doi: 10.1029/2012JD018060.

Tjallingii, R., U. Röhl, M. Kölling, and T. Bickert (2007), Influence of the water content on X-ray fluorescence core-scanning measurements in soft marine sediments, Geochemistry, Geophysics, Geosystems, 8(2), doi: 10.1029/2006GC001393.

Toole, J. M., R. C. Millard, Z. Wang and S. Pu, (1990), Observations of the Pacific North Equatorial Current Bifurcation at the Philippine Coast. J. Phys. Oceanography, 20, 307–318.

Tudhope, A. W., C. P. Chilcott, M. T. McCulloch, E. R. Cook, J. Chapell, R. M. Ellam, D. W. Lea, J. M. Lough and G. B. Shimmield (2001), Variability in the El Niño-Southern Oscillation through a glacial-interglacial cycle, Science, 291 (5508), 1511-1517, doi: 10.1126/science.1057969.

Turney, C. S., A. P. Kershaw, S. C. Clemens, N. Branch, P. T. Moss, and L. K. Fifield (2004), Millennial and orbital variations of El Niño/Southern Oscillation and high-latitude climate in the last glacial period, Nature, 428(6980), 306-310, doi: 10.1038/nature02386.

Waelbroeck, C., L. Labeyrie, E. Michel, J. C. Duplessy, J. F. McManus, K. Lambeck, E, Balbon, and M. Labracherie(2002), Sea-level and deep water temperature changes derived from benthic foraminifera isotopic records, Quaternary Science Review, 21, 295-305, doi: 10.1016/S0277-3791(01)00101-9.

Waliser, D. E., and Gautier, C. (1993). A satellite-derived climatology of the ITCZ. Journal of Climate, 6(11), 2162-2174.

Wang, Y., H. Cheng, R. L. Edwards, Z. An, J. Wu, C. -C. Shen, and J. A. Dorale (2001), A high-resolution absolute-dated late Pleistocene monsoon record from Hulu Cave, China, Science, 294(5550), 2345-2348, doi: 10.1126/science.1064618.

Wang, X., A. S. Auler, R. L. Edwards, H. Cheng, E. Ito, Y. Wang, X. Kong, and M. Solheid (2007), Millennial-scale precipitation changes in southern Brazil over the past 90,000 years, Geophys. Res. Lett., 34, L23701, doi:10.1029/2007GL031149.

Wang, Y., H. Cheng, R. L. Edwards, X. Kong, X. Shao, S. Chen, J. Wu, X. Jiang, X. Wang, and Z. An (2008), Millennial-and orbital-scale changes in the East Asian monsoon over the past 224,000 years, Nature, 451(7182), 1090-1093, doi: 10.1038/nature06692.

Weldeab, S., D. W. Lea, R. R. Schneider, and N. Andersen (2007), 155,000 years of West African monsoon and ocean thermal evolution, Science, 316(5829), 1303-1307, doi: 10.1126/science.1140461.

Weltje, G. J., and R. Tjallingii (2008), Calibration of XRF core scanners for quantitative geochemical logging of sediment cores: Theory and application, Earth and Planetary Science Letters, 274(3), 423-438, doi: 10.1016/j.epsl.2008.07.054.

Xie P., and P. A. Arkin, (1997), Global precipitation: a 17-year monthly analysis based on gauge observations, satellite estimates, and numerical model outputs, Bulletin of the American Meteorological Society, 78, 2539-2558.

3.10 Supplementary Information

3.10.1 Calibration of $U^{K'}_{37}$ alkenone unsaturation ratios to SST

A comparison between two different calibrations of $U^{K'}_{37}$ to SST in Core MD06-3075 is provided in Supplementary Information Figure 3.1. The calibration of Müller et al. (1998) (temperatures denoted in this section by $°C_M$) suggests an overall SST range between 25.9 $°C_M$ and 28.6 $°C_M$, with a magnitude of deglacial warming of 2.3 $°C_M$. The Sonzogni et al. (1997) calibration (temperatures denoted in this section by $°C_S$) suggests an SST range of 25.3 $°C_S$ to 29.2 $°C_S$ with a deglacial warming of 3.4 $°C_S$. An average of the upper three Holocene measurements gives a core-top SST estimate of 28.3 $°C_M$ or 28.7 $°C_S$. We suggest that the Sonzogni et al. (1997) calibration performs better over our temperature spectrum based upon: (1) the consistency between core top SSTs (28.7 $°C_S$) compared to modern day annual SSTs at our locality (28.7 °C) (Locarnini et al., 2010), in comparison to values derived from calibration of Müller et al. (1998) (28.3 $°C_M$), (2) the similar magnitude of deglacial warming over Termination I (3.4 $°C_S$) to the 3.5 °C warming amplitude derived from Mg/Ca reconstructions in the nearby Core MD98-2181 (Stott et al., 2007), compared to the 2.3 $°C_M$ magnitude in the Müller et al. (1998) calibration. Additionally, it has been suggested that towards the limits of alkenone saturation the relationship between temperature and the $U^{K'}_{37}$ index probably diverges from a linear path and displays a sigmoidal relationship (Sonzogni et al., 1997; Conte et al., 2006). This explains the lower variability in the Müller et al. (1998) calibration, which invokes a linear $U^{K'}_{37}$/T gradient over the full temperature range, whereas the Sonzogni et al. (1997) calibration is calibrated specifically to high temperatures (> 25 °C). For our main discussion, we therefore presented temperatures calculated from the equations of Sonzogni et al. (1997).

3.10.2 SSTs of the tropical West Pacific

New records of $U^{K'}_{37}$ calibrated to SST from Core MD06-3075 show a deglacial warming amplitude of 3.4 °C over Termination I (Main Text Figure 3.4), consistent with the 2 - 4 °C warming documented in other WPWP records from both coccolithophore-based $U^{K'}_{37}$ analysis (e.g. Pelejero and Grimalt, 1997; Shiau et al., 2012) and Mg/Ca analysis of

G. ruber (e.g. Stott et al., 2002, 2007; Visser et al., 2003; Rosenthal et al., 2003, Medina-Elizalde and Lea, 2005). Paired Mg/Ca and $U^{K'}_{37}$ analyses in tropical regions have demonstrated that major differences in the timing of the onset of temperature variability using the two methodologies exist over the last deglaciation (Saher et al., 2009, Western Arabian Sea; Mix, 2006, EEP; de Garidel-Thoron et al., 2007, WPWP; Steinke et al., 2008, South China Sea; Wang et al., 2013, Indian Ocean). A comparison of our $U^{K'}_{37}$ based temperature record over Termination I with the Mg/Ca derived temperature record of Core MD98-2181 (Stott et al., 2002, 2007) allows us to assess this phenomenon (Supplementary Information Figure 3.2). Both records agree on a contemporaneous temperature increase beginning between 17.5 and 18 ka, with no significant cooling trend observed in the MD06-3075 $U^{K'}_{37}$ SST record between 18 and 15 ka, as has been documented in other tropical $U^{K'}_{37}$ records (e.g. Steinke et al., 2008). During the Bølling-Allerød (BA, ~14.6 - 12.8 ka) period, $U^{K'}_{37}$ SSTs plateau at 27.2 °C whilst Mg/Ca temperatures continue a relatively unabated warming trend. Maximum divergence between the two records occurs at the end of the BA period, with temperature differences exceeding 2.5 °C.

We suggest that these differences occur as a result of the seasonal-weighting of recorded temperatures in planktonic foraminifera versus coccolithophores, mirroring proxy mismatches that have been reported in previous comparative studies of Mg/Ca and alkenone based paleothermometry (Wang et al., 2013; Timmermann et al., 2014). We expect Mg/Ca derived temperatures from *G. ruber* to be weighted towards summer surface conditions due to the seasonal dominance of *G. ruber* during June to October in the WPWP (Kawahata et al., 2002). In contrast, maximum fluxes of coccolithophores generally occur in winter months (Tanaka and Kawahata, 2001) coincident with peak wind stress (Main Text Figure 3.2), with maximum fluxes of alkenone producing coccolithophores *E. huxleyi* and *G. oceanica* occurring between December and February. Coccolithophore-based temperatures are therefore weighted significantly towards winter months. Since seasonality (in terms of the insolation difference between summer and winter) increased at our study location between 20 and 10 ka, the resulting temperature offset between the two methodologies may be representative of the more extreme summer versus winter SSTs in the WPWP.

During the last glacial period, high-resolution Mg/Ca SST records from the Davao Gulf (Saikku et al., 2009) indicate a link between high latitude climate dynamics and SST, with cooler temperatures being observed during Heinrich stadials and warmer temperatures during Dansgaard-Oeschger interstadials. In contrast, records from the Sulu Sea (Dannenmann et al., 2003) indicate that SSTs were not in phase with northern hemisphere ice core $\delta^{18}O$ records over MIS 3. $U^{K'}_{37}$ SST records from Core MD06-3075 also show little coherent response to Dansgaard-Oeschger interstadials or Heinrich stadials. However, this lack of response may be partially attributed to low sedimentation rates during the glacial period giving an average sample resolution of only ~700 yrs, which may not be high enough to resolve centennial to millennial scale variability.

An unusual feature observed in the MD06-3075 SST records is the temperatures recorded during MIS 5a and 5c, which are found to be in excess of Holocene values, when most WPWP Mg/Ca records predict temperatures ~0.5 °C cooler during MIS 5a and 5c than the Holocene (e.g. Medina-Elizalde and Lea, 2005, Bolliet et al., 2011) (Main Text Figure 3.4). The difference between these different WPWP SST reconstructions in MIS 5 may be partially explained by the afore-mentioned seasonality effect on $U^{k'}_{37}$ compared to Mg/Ca reconstructions, or by the large variability in hydrological regimes and paleoproductivity (Main Text Figure 3.4) during these periods, which may have acted to alter the depth habitats of alkenone producing coccolithophores.

3.10.3 Supplementary Tables

Supplementary Table 3.1 - AMS ^{14}C dates and tie points used to constrain the age model of Core MD06-3075[a]

Type	Depth (cm)	Calibrated Age (years BP)	Species	Notes
AMS ^{14}C date	6	0 ± 25	*G. ruber*	Conventional Age 450 +/- 25
AMS ^{14}C date	64	800 ± 50	*G. ruber*	Conventional Age 1370 +/- 30
AMS ^{14}C date	292	2050 ± 50	*G. ruber*	Conventional Age 2570 +/- 35
AMS ^{14}C date	338	2250 ± 60	*G. ruber*	Conventional Age 2710 +/- 30
AMS ^{14}C date	386	3250 ± 50	*G. ruber*	Conventional Age 3515 +/- 30
AMS ^{14}C date	470	4640 ± 90	Mixed planktonics	Conventional Age 4600 +/- 30
AMS ^{14}C date	496	5290 ± 50	Mixed planktonics	Conventional Age 5055 +/- 30
AMS ^{14}C date	538	6400 ± 40	Mixed planktonics	Conventional Age 6105 +/- 40
AMS ^{14}C date	560	7060 ± 100	*G. ruber*	Conventional Age 6645 +/- 70
AMS ^{14}C date	670	10530 ± 70	Mixed planktonics	Conventional Age 9800 +/- 50
AMS ^{14}C date	770	13840 ± 160	*G. ruber*	Conventional Age 12510 +/- 163
AMS ^{14}C date	818	15110 ± 230	*G. ruber*	Conventional Age 13600 +/- 180
AMS ^{14}C date	848	15980 ± 250	*G. ruber*	Conventional Age 14350 +/- 180
AMS ^{14}C date	870	17820 ± 220	Mixed planktonics	Conventional Age 15490 +/- 80
AMS ^{14}C date	940	26790 ± 260	*G. ruber*	Conventional Age 22910 +/- 200
AMS ^{14}C date	970	30670 ± 340	Mixed planktonics	Conventional Age 26120 +/-270
$\delta^{18}O$ event	1070	37400 (38400)	-	$\delta^{18}O$ minimum in A1 event
$\delta^{18}O$ event	1180	45600 (4660)	-	$\delta^{18}O$ minimum in A2 event
$\delta^{18}O$ event	1320	52500 (53500)	-	$\delta^{18}O$ minimum in A3 event
$\delta^{18}O$ event	1420	57700 (58700)	-	$\delta^{18}O$ minimum in A4 event
$\delta^{18}O$ event	1500	63400 (64400)	-	$\delta^{18}O$ maximum at end of MIS4
$\delta^{18}O$ event	1610	70200 (71200)	-	$\delta^{18}O$ minimum at end of MIS5a
$\delta^{18}O$ event	1830	79700 (80700)	-	$\delta^{18}O$ minimum at end of first MIS5a plateau
$\delta^{18}O$ event	2070	86700 (87700)	-	$\delta^{18}O$ maximum at end of MIS5b
$\delta^{18}O$ event	2770	107400 (108400)	-	$\delta^{18}O$ maximum at end of MIS 5d

[a] Conventional ages were converted to calendar ages following Fairbanks et al. (2005). A reservoir age correction of 480 years was applied for samples younger than 13 ka, and 630 years for older samples. Tie points were created by correlation of $\delta^{18}O$ events to the EDML1 Antarctic Ice Core chronology (Ruth et al., 2007). Absolute tie point ages are given in parentheses; a subsequent 1000-year correction was applied to benthic foraminiferal ages to account for the transit time of Southern Ocean derived deep-water masses in this region (Stott et al., 2007, Khider et al., 2014).

3.10.4 Supplementary Figures

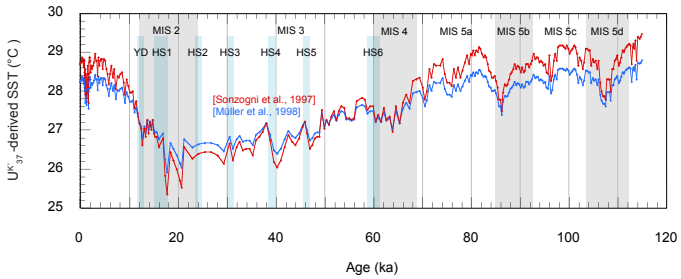

Supplementary Information Figure 3.1 - $U^{K'}_{37}$ derived SST records calibrated with the equations of Sozogni et al. (1997) (red line) and Müller et al. (1998) (blue line). Grey vertical bars indicate major marine isotope stages, blue vertical bars indicate HS1-6 and the YD.

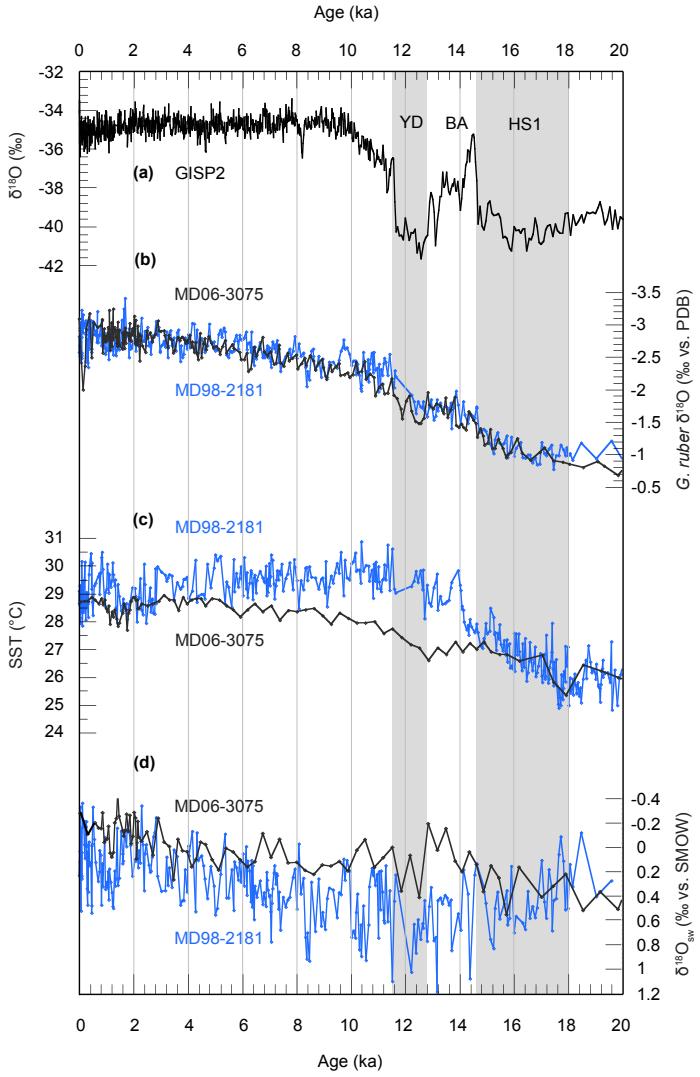

Supplementary Information Figure 3.2 - Expanded isotope and SST records covering the past 20 ka. (a) Greenland (GISP2) ice core $\delta^{18}O$ (Stuiver and Grootes, 2000). (b) Planktonic $\delta^{18}O$ record of Core MD06-3075 (black) and MD98-2181 (blue) (Stott et al., 2002; 2007) based upon the surface dwelling foraminifera *G. ruber*. (c) $U^{K'}_{37}$-derived SSTs of Core MD06-3075 (black), and Mg/Ca-derived SSTs from core MD98-2181 (blue). (d) Temperature and ice volume corrected $\delta^{18}O_{sw}$ records from MD06-3075 (black) and MD98-2181 (blue). Data from Stott et al. (2002, 2007) has been corrected for ice volume effects following Waelbroeck et al. (2002).

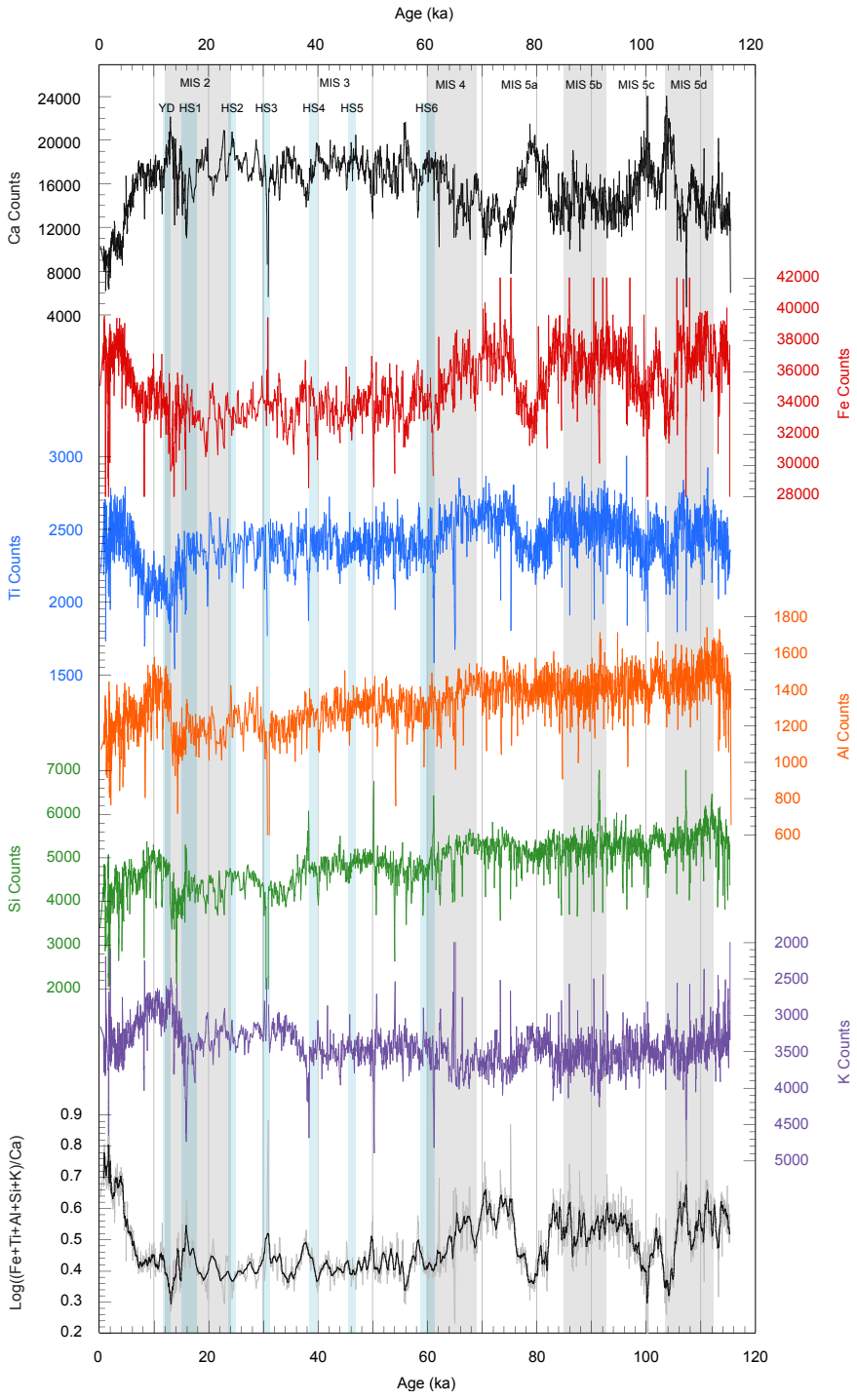

Supplementary Information Figure 3.3 - XRF raw counts of elements Ca (black), Fe (red), Ti (dark blue), Al (orange), Si (green) and K (light blue), and the log-ratio of the sum of these terrigenous elements normalised by Ca (raw data in grey; 10-point smooth in purple).

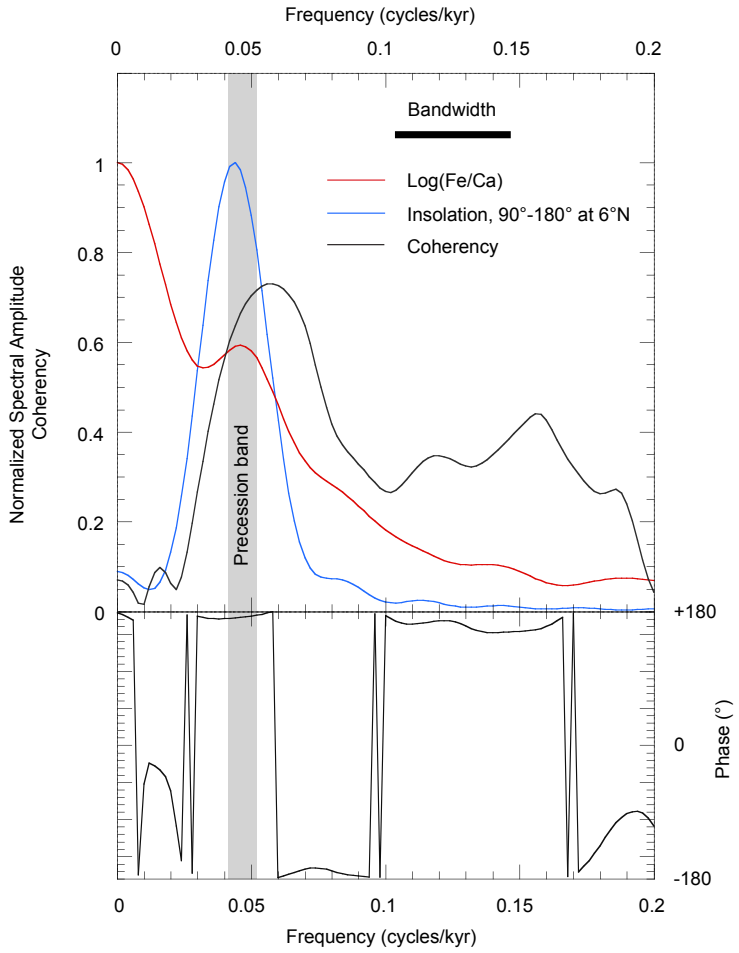

Supplementary Information Figure 3.4 - Top: Normalized power spectra of log(Fe/Ca) and boreal summer insolation (June 21st - September 21st) at 6 °N, together with cross-spectral coherency of both series. Bandwidth is shown by thick black line. 95% confidence interval of non-zero coherency is 0.551. Grey vertical band represents band of precession-scale frequencies. Bottom: Phase spectrum between log(Fe/Ca) and insolation. Positive values indicate lead of insolation over log(Fe/Ca). Cross spectral analysis was performed with Analyseries 2.0 software (Paillard et al., 2006).

3.10.5 Supplementary Information References

Bolliet, T., A. Holbourn, W. Kuhnt, C. Laj, C. Kissel, L. Beaufort, M. Kienast, N. Andersen, and D. Garbe-Schönberg (2011), Mindanao Dome variability over the last 160 kyr: Episodic glacial cooling of the West Pacific Warm Pool, Paleoceanography, 26, PA1208, doi:10.1029/2010PA001966.

Conte, M. H., M. A. Sicre, C. Rühlemann, J. C. Weber, S. Schulte, D. Schulz-Bull, and T. Blanz (2006), Global temperature calibration of the alkenone unsaturation index ($U^{k'}_{37}$) in surface waters and comparison with surface sediments, Geochem. Geophys. Geosyst., 7, Q02005, doi:10.1029/2005GC001054.

Dannenmann, S., B. K. Linsley, D. W. Oppo, Y. Rosenthal, and L. Beaufort (2003), East Asian monsoon forcing of suborbital variability in the Sulu Sea during Marine Isotope Stage 3: Link to Northern Hemisphere climate, Geochemistry, Geophysics, Geosystems, 4(1), 1-13, doi: 10.1029/2002GC000390.

de Garidel-Thoron, T., Y. Rosenthal, L. Beaufort, E. Bard, C. Sonzogni, and A. C. Mix (2007), A multiproxy assessment of the western equatorial Pacific hydrography during the last 30 kyr, Paleoceanography, 22, PA3204, doi: 10.1029/2006PA001269.

Fairbanks, R. G., R. A. Mortlock, T. Chiu, L. Cao, A. Kaplan, T. P. Guilderson, T. W. Fairbanks, A. L. Bloom, P. M. Grootes, and M. -J. Nadeau (2005) Radiocarbon calibration curve spanning 0 to 50,000 years BP based on paired $^{230}Th/^{234}U/^{238}U$ and ^{14}C dates on pristine corals, Quaternary Science Reviews, 24(16), 1781-1796, doi: 10.1016/j.quascirev.2005.04.007.

Kawahata, H., A. Nishimura, and M. K. Gagan (2002), Seasonal change in foraminiferal production in the western equatorial Pacific warm pool: evidence from sediment trap experiments, Deep Sea Research Part II: Topical Studies in Oceanography, 49(13), 2783-2800, doi: 10.1016/S0967-0645(02)00058-9.

Khider, D., C. S. Jackson, and L. D. Stott (2014), Assessing millennial-scale variability during the Holocene: a perspective from the western tropical Pacific, Paleoceanography, 29(3), 143-159, doi: 10.1002/2013PA002534.

Locarnini, R. A., A. V. Mishonov, J. I. Antonov, T. P. Boyer, H. E. Garcia, O. K. Baranova, M. M. Zweng, and D. R. Johnson (2010), World Ocean Atlas 2009, Volume 1: Temperature, S. Levitus, Ed. NOAA Atlas NESDIS 68, U.S. Government Printing Office, Washington, D.C., 1-184.

Medina-Elizalde, M. N., and D. W. Lea (2005), The mid-Pleistocene transition in the Tropical Pacific, Science, 310(5750), 1009-1012, doi: 10.1126/science.1115933.

Mix, A. C. (2006), Running hot and cold in the eastern equatorial Pacific, Quaternary Science Reviews, 25(11), 1147-1149, doi: 10.1126/science.1115933.

Müller, P. J., G. Kirst, G. Ruhland, I. von Storch, and A. Rosell-Melé (1998), Calibration of the alkenone paleotemperature index $U^{k'}_{37}$ based on core-tops from the eastern

South Atlantic and the global ocean (60°N-60°S), Geochimica et Cosmochimica Acta, 62(10), 1757-1772, doi: 10.1016/S0016-7037(98)00097-0.

Paillard, D., Labeyrie, L., Yiou, P. (1996), Macintosh program performs time-series analysis. EOS Trans. AGU, 77.

Pelejero, C., and Grimalt, J. O. (1997), The correlation between the $U^{k'}_{37}$ index and sea surface temperatures in the warm boundary: The South China Sea, Geochimica et Cosmochimica Acta, 61(22), 4789-4797, doi: 10.1016/S0016-7037(97)00280-9.

Rosenthal, Y., D. W. Oppo, and B. K. Linsley (2003), The amplitude and phasing of climate change during the last deglaciation in the Sulu Sea, western equatorial Pacific, Geophys. Res. Lett., 30, 1428, doi:10.1029/2002GL016612.

Ruth, U., J. -M. Barnola, J. Beer, M. Bigler, T. Blunier, E. Castellano, H. Fischer, F. Fundel, P. Huybrechts, and P. Kaufmann (2007), "EDML1": a chronology for the EPICA deep ice core from Dronning Maud Land, Antarctica, over the last 150 000 years, Climate of the Past Discussions, 3(2), 549-574, doi: 10.5194/cp-3-475-2007.

Saher, M., F. Rostek, S. Jung, E. Bard, R. Schneider, M. Greaves, G. Ganssen, H. Elderfield, and D. Kroon (2009), Western Arabian Sea SST during the penultimate interglacial: A comparison of $U^{k'}_{37}$ and Mg/Ca paleothermometry, Paleoceanography, 24(2), PA2212, doi: 10.1029/2007PA001557.

Saikku, R., L. Stott, and R. Thunell (2009), A bi-polar signal recorded in the western tropical Pacific: Northern and Southern Hemisphere climate records from the Pacific warm pool during the last Ice Age, Quaternary Science Reviews, 28(23), 2374-2385, doi: 10.1016/j.quascirev.2009.05.007.

Shiau, L. -J., M. -T. Chen, C. -A. Huh, M. Yamamoto, and Y. Yokoyama (2012), Insolation and cross-hemispheric controls on Australian monsoon variability over the past 180 ka: new evidence from offshore southeastern Papua New Guinea, Journal of Quaternary Science, 27(9), 911-920, doi: 10.1002/jqs.2581.

Sonzogni, C., E. Bard, F. Rostek, D. Dollfus, A. Rosell-Melé, and G. Eglinton (1997), Temperature and salinity effects on alkenone ratios measured in surface sediments from the Indian Ocean, Quaternary Research, 47(3), 344-355, doi: 10.1006/qres.1997.1885.

Steinke, S., M. Kienast, J. Groeneveld, L.-C. Lin, M.-T. Chen, and R. Rendle-Bühring (2008), Proxy dependence of the temporal pattern of deglacial warming in the tropical South China Sea: toward resolving seasonality, Quaternary Science Reviews, 27(7), 688-700, doi: 10.1016/j.quascirev.2007.12.003.

Stott, L., C. Poulsen, S. Lund, and R. Thunell (2002), Super ENSO and global climate oscillations at millennial time scales, Science, 297(5579), 222-226, doi: 10.1126/science.1071627.

Stott, L., A. Timmermann, and R. Thunell (2007), Southern hemisphere and deep-sea warming led deglacial atmospheric CO2 rise and tropical warming, Science,

318(5849), 435-438, doi: 10.1126/science.1143791.

Stuiver, M. and P. M. Grootes (2000), GISP2 oxygen isotope ratios, Quaternary Research, 53(3), 277-284. doi: 10.1006/qres.2000.2127.

Tanaka, Y., and H. Kawahata (2001), Seasonal occurrence of coccoliths in sediment traps from West Caroline Basin, equatorial West Pacific Ocean, Marine Micropaleontology, 43(3), 273-284, doi: 10.1016/S0377-8398(01)00027-5.

Timmermann, A., J. Sachs, and O. Elison Timm (2014), Assessing divergent SST behavior during the last 21 ka derived from alkenones and G.ruber-Mg/Ca in the equatorial Pacific, Paleoceanography, 29, 680–696, doi:10.1002/2013PA002598.

Visser, K., R. Thunell, and L. Stott (2003), Magnitude and timing of temperature change in the Indo-Pacific warm pool during deglaciation, Nature, 421(6919), 152-155, doi: 10.1038/nature01297.

Waelbroeck, C., L. Labeyrie, E. Michel, J. C. Duplessy, J. F. McManus, K. Lambeck, E, Balbon, and M. Labracherie(2002), Sea-level and deep water temperature changes derived from benthic foraminifera isotopic records, Quaternary Science Review, 21, 295-305, doi: 10.1016/S0277-3791(01)00101-9.

Wang, Y. V., G. Leduc, M. Regenberg, N. Andersen, T. Larsen, T. Blanz and R. R. Schneider (2013), Northern and southern hemisphere controls on seasonal sea surface temperatures in the Indian Ocean during the last deglaciation, Paleoceanography, 28, 1-14, doi: 10.1002/palo.20053.

Chapter 4

Deglacial changes in West Pacific circulation: insights from benthic foraminiferal $\delta^{13}C$

Nicholas Fraser, Ann Holbourn, Wolfgang Kuhnt, Timothé Bolliet, Nils Anderson, Jan Schröder, Sebastian Beil, Marfasran Hedrizan, Kazuyo Tachikawa, Laurence Vidal

4.1 Abstract

Significant changes in the production and ventilation rates of Pacific deep and intermediate waters have been suggested to occur during past glacial terminations. However, the mechanisms and responses of circulation in the West Pacific and Indonesian Throughflow (ITF), the sole conduit of equatorial water masses between the Pacific and Indian Oceans, remain enigmatic. In this study we compile six new and seven existing benthic foraminiferal carbon isotope records (δ13Cb), acting as a non-conservative tracer of water mass transport, from a range of sediment cores covering the West Pacific and ITF regions. Core MD06-3067, located at 6 °N off the east coast of the island of Mindanao, presents a particularly interesting new high-resolution δ13Cb record from ~1600 m water depth, characterised by two distinct troughs in δ13Cb occurring during Termination I and II. These troughs are interpreted to reflect the increased contribution of poorly-ventilated North Pacific Intermediate Water (NPIW), which in the modern day is limited to water depths <800 m, and may thus be linked to increased deglacial production of NPIW. Comparison with δ13Cb records from intermediate-depth southwest Pacific sites, which today record the δ13C signature of Antarctic Intermediate Water (AAIW), reveals that these changes were coeval with increased ventilation of AAIW during Terminations I and II, implying major deglacial reorganisations of intermediate circulation occurred throughout the Pacific. δ13Cb records from the ITF region indicate a significant improvement in ventilation occurred in the Flores Sea and Timor Sea at the onset of the last deglacial period, consistent with an increasing contribution of AAIW through the southeastern ITF route, whilst the NPIW-dominated northwestern route remained poorly ventilated. Conversely, the late Holocene is characterised by increased ventilation in the northwestern ITF route, and weak δ13Cb gradients throughout the ITF, indicative of single, southern-source of intermediate waters into ITF during modern times.

4.2 Introduction

During the late Pleistocene, orbital scale oscillations between glacial and interglacial climate states have been linked to fundamental changes in the formation and overturning rates of deep waters in high latitudes, which control the partitioning of heat and CO2 between the atmosphere and ocean (Sigman and Boyle, 2000; Sigman et al, 2010; Burke and Robinson, 2012; Sarnthein et al., 2013). Modern deep water production occurs only in the North Atlantic and Southern Oceans, and thus most studies attempting to establish mechanisms of deglacial circulation and CO2 change have tended to focus on these regions. During the last glacial termination, millennial-scale stadial periods in the Northern Hemisphere (e.g. Heinrich Stadial 1, HS-1) were balanced by warming of the Southern Hemisphere (the so-called 'bipolar seesaw' (Broecker, 1998; Barker et al., 2009; Denton et al., 2010)). Such warm periods in the Southern Hemisphere have been linked to increased upwelling of deep, carbon rich waters in the Southern Ocean, driving the release of CO2 to the atmosphere (Anderson et al., 2009; Skinner et al., 2010). However, relatively little is still known about the role of the Pacific Ocean in deglacial circulation changes, in particular regarding the transport and fate of Pacific water masses from their polar origins to equatorial regions.

In the modern day, source waters of the Pacific Ocean are derived from North Pacific Intermediate Water (NPIW), Antarctic Intermediate Water (AAIW), and Antarctic Bottom Water (AABW) (Talley, 2003; Bostock et al., 2010). Studies in the North Pacific have proposed that past increases in the production of NPIW occurred during periods of weakening of the Atlantic Meridional Overturning Circulation (AMOC) (e.g. during HS-1) (Ahagon et al., 2003; Sagawa and Ikehara, 2008; Max et al., 2014). Yet the role of the deeper North Pacific remains contentious. Today, stable salinity-induced stratification prevents the formation of deep water in the North Pacific (Warren, 1983; Emile-Geay et al., 2003). During the last deglaciation, pulses of increased surface productivity and the presence of warm, salty waters in the North Pacific (Gebhardt et al., 2008) suggest increased vertical mixing and weakening of the halocline during periods of AMOC collapse, potentially allowing the formation of deep waters (Gebhardt et al., 2008; Okazaki et al., 2010; Rae et al., 2014). However, such a mechanism remains controversial, with some records finding no significant changes in ventilation below ~2400 m during

HS-1, instead implying that the deeper half of the North Pacific water column remained relatively isolated over the deglacial transition (Galbraith et al., 2007; Lund et al., 2011; Jaccard and Galbraith, 2013).

In the South Pacific, changes in the production of AAIW during the last deglaciation have been tightly linked to rapid reorganizations of global oceanic circulation (Pahnke and Zahn, 2005; Pahnke et al., 2008; Pena et al., 2013). Periods of increased AAIW production over this time interval may be induced by a southward shift of the westerlies coincident with warming in Antarctica, resulting in enhanced upwelling and release of stored CO2 from deep waters (Toggweiler et al., 2006; Anderson et al., 2009). Such changes in the production and ventilation of AAIW are recorded by benthic foraminiferal stable carbon isotope (δ13Cb) records in the southwest Pacific Ocean, and implicate similar mechanisms acting over several recent glacial cycles (Pahnke and Zahn, 2005). Together, records from both the North and South Pacific imply that Pacific deep and intermediate water masses played an important role in the storage of heat and carbon during glacial-interglacial transitions.

The Indonesian Throughflow (ITF) provides the only exit passage for low-latitude water masses in the Pacific Ocean to pass into the Indian Ocean, and therefore also acts as a control on the distribution of deep and intermediate water masses in the Pacific and Indian Oceans. Our knowledge of the modern day ITF has increased in recent years through observational efforts (e.g. the 'INSTANT' program, Sprintall et al., (2004), Gordon et al., (2010)), with hydrographic observations in the Lifamatola passage suggesting a much stronger and cooler deep component to the ITF than previously thought (van Aken et al., 2010). However, relatively little is known about this deep ITF component over millennial and longer timescales. Holbourn et al. (2011) presented δ13Cb records from three cores located in the Timor Sea outflow, which suggested that during glacial periods δ13Cb gradients between Timor Sea deep and intermediate waters increased, whilst the inflow of well-ventilated Indian Ocean Central Waters (IOCW) to the Timor Sea also strengthened. These results imply a weakening of the deep and intermediate ITF component during glacial times, and conversely a strengthening during warm interglacial periods. However, no well-resolved δ13Cb records are currently

available within the central ITF transport passages such as the Banda and Flores Seas and Makassar Strait, which has precl¬¬uded interpretations of the changing composition of Indonesian water masses during past deglacials.

Transport of water masses with specific δ13C signatures of dissolved inorganic carbon (δ13CDIC), and subsequent capture of these signatures in the tests of benthic foraminifera, has led to the wide-scale use of δ13Cb as a non-conservative tracer for past water mass variability (Duplessy et al., 1984). Such an approach may be particularly effective in the Pacific Ocean, due to strong gradients in the modern δ13CDIC signatures between different deep and intermediate Pacific water masses. In this study we present a compilation of benthic foraminiferal stable isotope records from 13 sediment cores covering the Western Equatorial Pacific (WEP), southwest Pacific, ITF, and Timor Sea (Figure 1; Table 1), to investigate changes in intermediate and deep water mass ventilation and circulation, with a focus on the past two glacial terminations.

4.3 Modern Oceanography of the West Pacific

4.3.1 Intermediate depth waters of the Pacific Ocean

Intermediate depth waters of the Pacific Ocean are characterised by two distinct water masses: NPIW and AAIW (Talley, 1999; 2013a). NPIW is derived from mixing of waters in the Okhotsk Sea and the northwestern subtropical gyre between the Kuroshio extension and Oyashio front (Talley, 1993; You, 2003), and in the Gulf of Alaska (You et al., 2000) (Figure 1). It is recognised by a salinity minimum (< 34), low oxygen concentrations and a core density averaging ~26.8 σθ (Figure 2), spreading over the entire subtropical north Pacific at a water depth of 300 to 800 m. The δ13CDIC signature of NPIW is complicated by remineralization of organic carbon at depth, and mixing with deeper nutrient rich water masses; above the main thermocline NPIW is characterized by δ13CDIC values of 0.5 – 1 ‰, which decreases to 0 to -0.5 ‰ by water depths of ~800 m (Figure 2E). NPIW eventually exits the Pacific basin through the Celebes Sea, forming part of the ITF, via the Mindanao Current in the West Pacific (Bingham and Lukas, 1994; Fine et al., 1994).

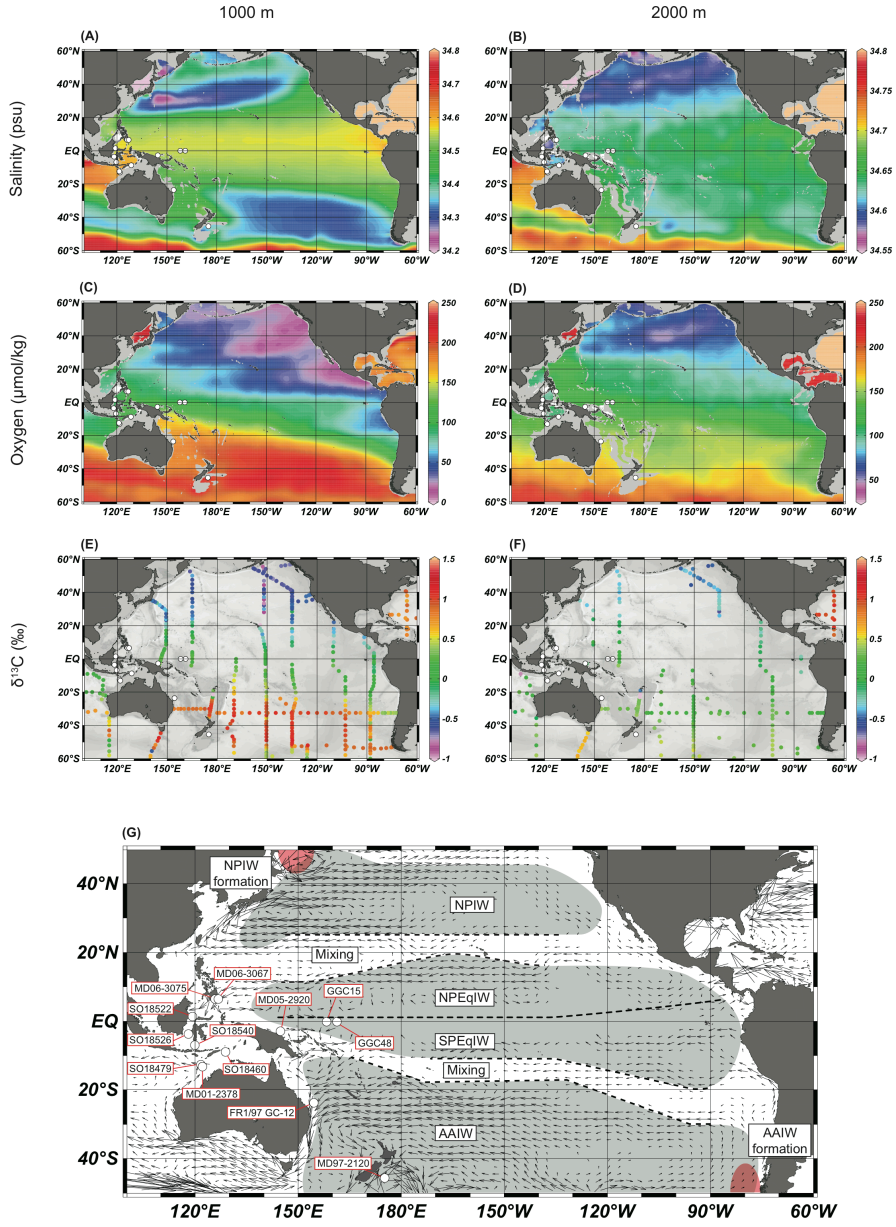

Figure 4.1 – Modern oceanography of intermediate (1000 m, left figures) and deep (2000 m, right figures) waters of the Pacific Ocean. (A) and (B) Salinity at 1000 m and 2000 m water depth (World Ocean Atlas 2009, Locarnini et al., 2010). (C) and (D) Oxygen at 1000 m and 2000 m water depth (World Ocean Atlas 2009, Locarnini et al., 2010) (E) and (F) $\delta^{13}C$ at 1000 m and 2000 m water depth derived from Pacific WOCE transects. (G) Locations of sediment cores used in this study (references in Table 4.1), together with a schematic of intermediate water masses (grey) and formation sites (red) of NPIW and AAIW in the Pacific Ocean, modified from Bostock et al., (2010). Arrows indicate the velocity field (resampled at 2 x 3 ° resolution) at 1000 m depth, as estimated from Argo floats by Katsumata and Yoshinari (2010). Figures produced with Ocean Data View (Schlitzer, 2014).

Conversely, AAIW is distinguished by high oxygen concentrations and a salinity minimum (34.3 - 34.5), with a core density averaging ~27.1 σθ (Figure 2). δ13CDIC in AAIW is elevated relative to NPIW (typical values of 0.7 to 1.3 ‰), caused by increased air-sea exchange of carbon in Antarctic surface waters compared to North Pacific surface waters (Bostock et al., 2010). AAIW is formed primarily in the southeast Pacific off southern Chile (McCartney, 1977; Hanawa and Talley, 2001) and spreads northwest across the southern subtropical Pacific, including the Coral and Tasman seas, at a depth range between 600 and 1300 m.

In the central Pacific, studies have proposed the presence of an additional independent water mass, equatorial Pacific intermediate waters (EqPIW) (Wijffels, 1993), which can be further sub-divided into both a northern (NEqPIW) and southern (SEqPIW) component, with a boundary centred at 2°N (Bingham and Lukas, 1995; Bostock et al., 2010) (Figure 1). δ13CDIC values in EqPIW typically have values between those of NPIW and AAIW (0 to 0.5 ‰), implicating mixing of the two endmembers in formation of EqPIW. However, δ13Cair-sea values (calculated from phosphate or apparent oxygen utilization (AOU) corrected δ13CDIC measurements) of EqPIW instead suggest that source waters of EqPIW are more similar to AAIW and offset from NPIW, and thus EqPIW is formed primarily from a combination of AAIW and Pacific Deep Water (PDW), with only a minor component of NPIW (Bostock et al., 2010). In the WEP, the composition of intermediate waters is complicated by the additional northward transport of AAIW in the New Guinea Coastal Undercurrent (NGCUC) (Zenk et al., 2005), which may transport AAIW significantly further north than in the central equatorial regions. It has been suggested that AAIW dominates intermediate depth waters as far north as 15°N in the WEP based upon salinity and potential density measurements (Qu and Lindstrom, 2004). Whilst Zenk et al. (2005) find no signature of AAIW north of 12 °N, particle tracking experiments indicate a seasonally variable transport of intermediate waters from the NGCUC to as far north as Mindanao and the Celebes Sea.

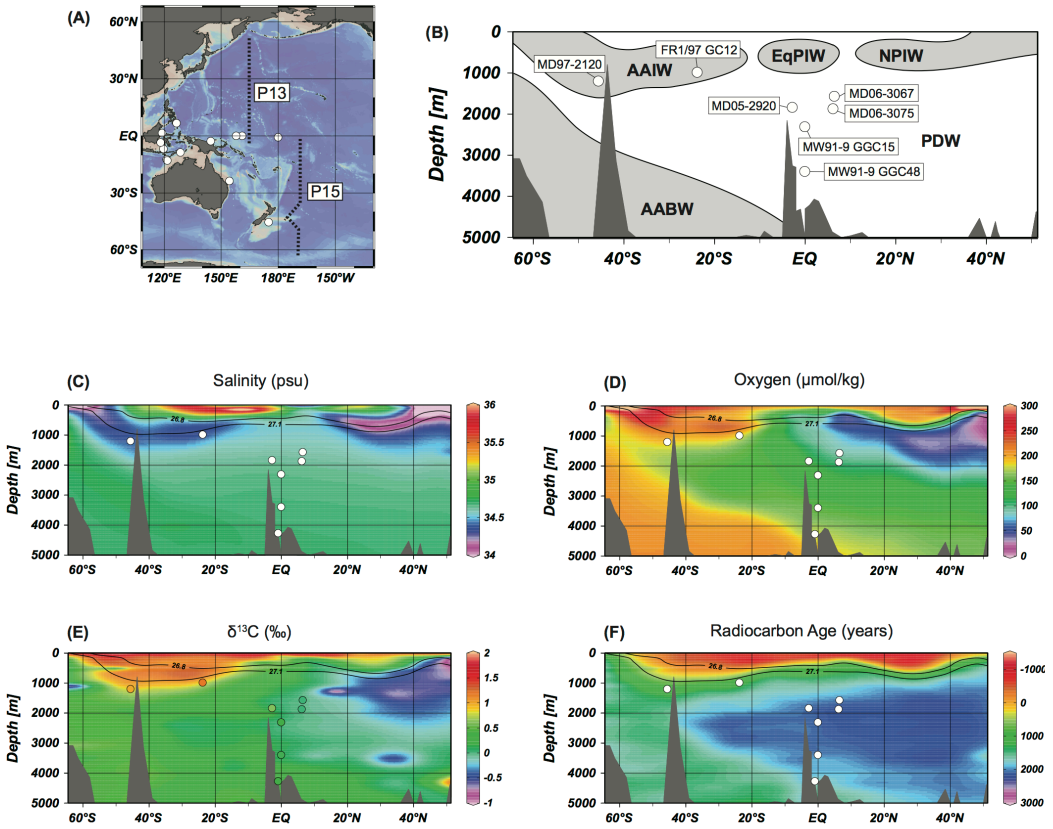

Figure 4.2 – Latitudinal-depth distributions of geochemical tracers in the West Pacific (derived from WOCE transects P13 and P15 shown in (A)). (B) shows a simplified illustration of the main Pacific water masses, together with locations of sediment cores from the West Pacific used in this study (not including sites from the Indonesian Throughflow or Timor Sea). Lower sections show variability in: (C) salinity, (D) oxygen, (E) $\delta^{13}C$ and (F) radiocarbon age (derived from ^{14}C measurements). Potential densities (σ_θ) at 26.8, corresponding to NPIW, and 27.1, corresponding to AAIW, are shown by black contours. Figures produced with Ocean Data View (Schlitzer, 2014).

4.3.2 Deepwater circulation in the Pacific Ocean

The deepest abyssal waters of the Pacific basin are derived primarily from the northward flow of Antarctic Bottom Waters (AABW), which entrain a significant amount of transformed North Atlantic Deep Water (NADW) (Schmitz, 1996). To the North this water mass decreases in density and upwells to mid-depths beneath NPIW, spreading

and forming 'nutrient-trapped', δ13CDIC-depleted Pacific Deep Water (PDW) between ~1000 to ~3000 m water depth (-0.5 to -1 ‰, Figure 2E) (Schmitz et al., 1996; Matsumoto et al., 2002). PDW can be recognized in particular by low oxygen concentrations, high silica content and old radiocarbon ages, which in some places exceed ~2 kyr (Figure 2). As PDW returns south, it mixes with relatively less δ13CDIC-depleted Upper Circumpolar Deep Water (UCDW) (Matsumoto et al., 2002), and eventually upwells to the surface, feeding both the northward flux of surface water in the Antarctic Circumpolar Current (ACC), and being recycled as dense AABW (Talley, 2013a).

4.3.3 Intermediate and deep water transport in the Indonesian Throughflow

The flow of deep and intermediate water through the Indonesian passages is complicated by numerous sills and basins, inducing density-driven overflow patterns and vertical mixing of the water column (Gordon and Fine, 1996) (Figure 3). Waters flowing through the 'northwestern' ITF route, through the Celebes Sea and Makassar Strait, are first blocked by the Sangihe Ridge (1350 m), and then by the Dewakang Sill (650 m) at the southern end of the Makassar Strait (Gordon and Fine, 1996; Gordon et al., 2003). This route is dominated by upper thermocline waters from the North Pacific subtropical gyres and NPIW entering the Celebes Sea via the Mindanao Current (Fine et al., 1994). In the 'southeastern' ITF route, which flows first into the Maluku Sea and then into the Banda Sea, sill depths are generally deeper with the main barrier, the Lifamatola Passage, blocking the transport of deep waters below 1940 m (Gordon and Fine, 1996; Gordon et al., 2003; van Aken et al., 2009). Deep and intermediate water masses entering through this passage consist of a mixture of AAIW, which may have been carried northwards via the New Guinea Coastal Undercurrent (NGCUC) (Zenk et al., 2005), together with contributions from EqPIW and PDW. In addition, water masses can be transported through the Halmahera Sea directly into the Banda Sea, though this contribution is constrained mainly to thermocline waters due to the presence of a sill at 700 m water depth.

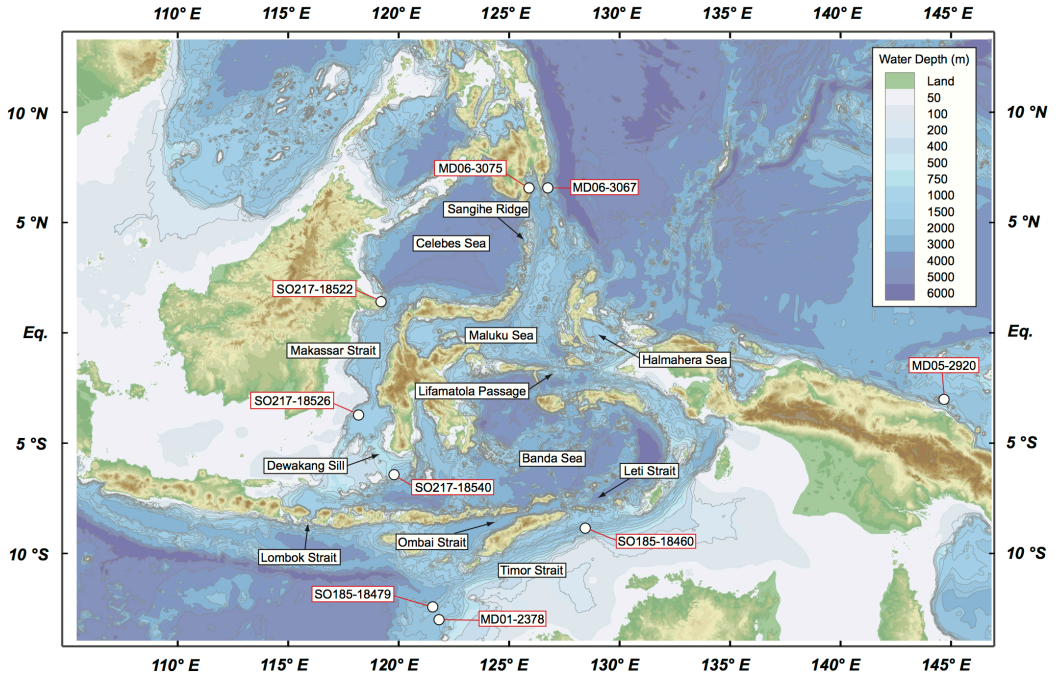

Figure 4.3 – Bathymetric map of the West Pacific and Indonesian Throughflow region, showing major ridges and passageways governing the circulation of deep and intermediate water masses. Locations of sediment cores used in this study are shown with white dots.

Upon entering the Banda Sea, vigorous vertical mixing between the shallow (warm and fresh) and deep (cold and saline) water masses occurs, forming the Indonesian Intermediate Water (IIW) with a relatively uniform deepwater salinity and temperature profile (Gordon et al., 2003; Gordon, 2005; Talley and Sprintall, 2005; Sprintall et al., 2014). From the Banda Sea, Indonesian waters can exit the ITF to the Indian Ocean through several passages: the Lombok Strait (sill depth 350 m), Ombai Strait (sill depth 3250 m), and the Timor Strait (sill depth 1250 m at the Leti Strait, 1900 m at the western passage) (Talley and Sprintall, 2005). These ITF waters form a core of low salinity/high silicate intermediate waters that are recognisable across the Indian Ocean basin (Sprintall et al., 2009). Additionally, evidence for semi-annual reversals in intermediate depth transport in the Timor Strait and Ombai Strait suggest that an inflow of Indian Ocean intermediate waters (IOCW), characterised by elevated δ13CDIC values (0.6 to 1.1 ‰; WOCE transect I10, Talley, 2013b) compared to IIW (0.3 to 0.4 ‰), into the ITF region may occur in the modern day (Sprintall et al., 2009; Sprintall et al., 2014). Records of past

changes in the influence of IIW versus IOCW in the Timor Sea may therefore provide evidence of the past strength of the deep and intermediate ITF transport.

4.4 Material and Methods

4.4.1 Stable Isotope Records

4.4.1.1 Data selection criteria

We have compiled 13 stable oxygen and carbon isotope records of benthic foraminifera (δ18Ob and δ13Cb, respectively) from sediment cores across the West Pacific and Indonesian regions, covering the last glacial termination (Termination I) and, where the length of these records is sufficient, the penultimate glacial termination (Termination II). Of these cores, eight have published δ18Ob and δ13Cb records in previous studies (see Table 1 and references therein). Three cores, MD06-3067, MD06-3075 and MD05-2920, have previously published δ18Ob records (Bolliet et al., 2011; Tachikawa et al., 2014; Fraser et al., 2014), and the corresponding δ13Cb records are presented here. We additionally complement existing stable isotope records of Core MD06-3067 with several new measurements during the last deglacial period, to increase the resolution of this portion of the record. Furthermore, we present three new δ18Ob and δ13Cb records from Cores SO217-18522, SO217-18540, SO217-18526, collected aboard the R/V Sonne during the Sonne-217 'MAJA' cruise in July and August 2011 (Kuhnt et al., 2011). These three cores are all located within the main passages of the ITF (Figure 3).

All compiled δ18Ob and δ18Ob records presented in this study are derived from measurements on the epibenthic species Cibicidoides wuellerstorfi, with the exception of records from Cores MD06-3067 and MD97-2120 where C. wuellerstorfi was occasionally replaced by other species due to low abundances. δ18Ob measurements in Core MD06-3067 were previously presented by Bolliet et al. (2011) based upon a mixture of C. wuellerstorfi, Cibicidoides pachyderma, Cibicidoides mundulus and Uvigerina

proboscidea, whilst published records of both δ18Ob and δ13Cb in Core MD97-2120 were made on a mixture of C. wuellerstorfi, Cibicidoides cicatricosus, *Cibicidoides kullenbergi (C. mundulus), Melonis barleeanum* and *Bulimina aculeata* (Pahnke and Zahn, 2005).

Cibicidoides species are epifaunal and are thus interpreted to record $\delta^{18}O_b$ and $\delta^{13}C_b$ as a function of the ambient bottom-water $\delta^{18}O$ and $\delta^{13}C_{DIC}$ composition (McCorkle et al., 1990; Graham et al.; 1981; Marchitto et al., 2014). However, offsets in isotopic ratios have been noted between different *Cibicidoides* species, attributed to differences in the incorporation of metabolic carbon and oxygen compounds into the foraminiferal tests ('vital effects') (Grossman, 1987). Based upon averaged paired measurements in Core MD97-2120, Pahnke and Zahn (2005) suggest that $\delta^{13}C_b$ values of *C. cicatricosus* are offset by -0.18 ‰, compared to *C. wuellerstorfi* and thus corrected isotopic values for these offsets. However, other studies incorporating paired measurements of *C. wuellerstorfi* and *C. kullenbergi (C. mundulus)* do not show systematic offsets between these species for either $\delta^{18}O_b$ or $\delta^{13}C_b$ (e.g. Holbourn et al., 2007; Hoogakker et al., 2010) and thus an isotopic correction is not applied in Core MD06-3067, where measurements were made both on *C. kullenbergi (C. mundulus)* and *C. wuellerstorfi*. This inconsistency between $\delta^{18}O_b$ corrections for Core MD97-210 versus Core MD06-3067 does not influence our later discussion, as we focus primarily on $\delta^{13}C_b$ variability and the $\delta^{18}O_b$ correction applied by Pahnke and Zahn (2005) to *C. kullenbergi (C. mundulus)* $\delta^{18}O_b$ values (-0.18 ‰) is not significantly larger than the typical error range for $\delta^{18}O$ measurements (~ ±0.1 ‰).

In addition to isotopic variability between species of the genus *Cibicidoides*, more significant isotopic offsets have been shown to occur between *Cibicidoides* and infaunal

benthic foraminifera genera. Stable isotope measurements on *Cibicidoides* were supplemented by the infaunal benthic foraminifera *U. proboscidea* in Core MD06-3067, and by *M. barleeanum* and *B. aculeata* in Core MD97-2120. It has been noted that $\delta^{18}O_b$ values of *Uvigerina* spp. are positively offset from *C. wuellerstorfi* by +0.64 ‰ (Shackleton and Opdyke, 1973) or +0.47 ‰ (Marchitto et al., 2014). In the past it was suggested that *Uvigerina* spp. calcifies in equilibrium with ambient seawater (Shackleton, 1974), however more recent studies have challenged this view, suggesting that *C. wuellerstorfi* calcifies in equilibrium with seawater (Bemis et al., 1998; Lynch-Stieglitz et al., 1999; Marchitto et al., 2014). To maintain consistency within our compiled datasets, we adjust all records on the assumption that *C. wuellerstorfi* calcifies in equilibrium with seawater, with *U. proboscidea* values corrected by -0.64 ‰ as originally applied in Bolliet et al. (2011). Additionally, $\delta^{13}C_b$ values of infaunal benthic foraminifera have shown significant offsets compared to epifaunal species, due to growth of infaunal species within pore waters that are sensitive to deposition and remineralization of organic carbon (McCorkle et al., 1990). Providing a singular correction for $\delta^{13}C_b$, as is applied for $\delta^{18}O_b$, is unreasonable as these processes involve several time- and environment-dependent variables (e.g. accumulation rates of organic matter; Zahn et al., 1986). We therefore remove all $\delta^{13}C_b$ measurements made on infaunal species in stable isotope records from Cores MD06-3067 and MD97-2120. The resolution of both of these cores is sufficiently high that removal of these values does not impact our later interpretation and discussion.

Table 4.1 - Summary of sediment cores compiled in this study, including core location, water depth, existing literature references, and $\delta^{13}C_b$ averages for key time slices (number of points used for averaging given in brackets).

Core	Latitude (°N)	Longitude (°E)	Water depth (m)	References	Holocene (0 - 11 ka) $\delta^{13}C$ [‰] (n)	Deglacial (11-18 ka) $\delta^{13}C$ [‰] (n)	LGM (18-23 ka) $\delta^{13}C$ [‰] (n)
				Equatorial West Pacific			
MD06-3067	6.5	126.5	1574	Bolliet et al. (2011)	0.04 (18)	-0.11 (43)	-0.07 (28)
MD06-3075	6.5	125.8	1878	Fraser et al. (2014)	0.03 (64)	-0.32 (22)	-0.38 (7)
GGC15	0.0	158.0	2311	Yu et al. (2010, 2013)	0.27 (7)	-0.08 (6)	-0.12 (3)
GGC48	0.0	161.0	3400	Yu et al. (2010, 2013)	0.20 (9)	-0.22 (8)	-0.24 (5)
MD05-2920	-2.8	144.5	1843	Tachikawa et al. (2014)	0.52 (16)	0.40 (16)	0.18 (10)
				Southwest Pacific			
FR1/97 GC-12	-23.7	154.3	990	Bostock et al. (2004)	1.07 (7)	0.83 (12)	0.53 (6)
MD97-2120	-45.5	174.9	1210	Pahnke and Zahn (2005)	0.77 (63)	0.60 (70)	0.29 (27)
				Pahnke et al. (2003)			
				Indonesian Throughflow			
SO217-18522	1.4	119.1	986	This study	0.46 (21)	0.05 (13)	-0.21 (18)
SO217-18526	-3.6	118.2	1523	This study	0.24 (58)	-0.10 (17)	-0.21 (11)
SO217-18540	-6.9	119.6	1201	This study	0.43 (21)	0.21 (11)	0.05 (7)
				Timor Sea			
SO185-18460	-8.8	128.6	1875	Holbourn et al. (2011)	0.47 (14)	0.27 (12)	-0.05 (8)
				Xu et al. (2010)			
SO185-18479	-12.5	121.4	2974	Holbourn et al. (2011)	0.48 (8)	0.09 (8)	-0.26 (6)
				Xu et al. (2010)			
MD01-2378	-13.1	121.8	1783	Holbourn et al. (2005, 2011)	0.53 (18)	0.29 (15)	0.10 (9)
				Xu et al. (2008)			

3.1.2. Analytical procedure

Analytical procedures of previously published stable isotope records are documented in their respective publications (Table 1 and references therein). For new stable isotope measurements presented in this study, between 1 and 5 tests of the benthic foraminifera species C. wuellerstorfi were picked, crushed into fragments under a microscope to ensure all chambers were open, agitated in an ultrasonic bath for several seconds, and dried at 40 °C. In new stable isotope measurements of Core MD06-3067, C. wuellerstorfi was replaced by C. mundulus or C. pachyderma in instances of low abundances. Stable isotopes were measured with the Finnigan MAT 253 mass spectrometer at the Leibniz Laboratory for Radiometric Dating and Stable Isotope Research in Kiel, Germany. The system is coupled to a Carbo-Kiel Device (Type IV) for automated CO2 preparation from carbonate samples for isotopic analysis. Samples were reacted by individual acid addition (99% H3PO4 at 75 °C). Standard external error is better than ±0.10 ‰ for δ18O and better than ±0.05 ‰ for δ13C. Replicate measurements on 13 paired benthic foraminifera samples from new measurements indicate a mean reproducibility (1σ) of ± 0.10 ‰ for δ18O and ± 0.05 ‰ for δ13C.

4.4.2 Chronology of compiled datasets

With the exception of new records presented in this study (Cores SO217-18522, SO217-18526, SO217-18540) and the record of Core MD06-3067, all records compiled here are presented on their original, published timescales (see Table 1 and references therein). Age control of Cores SO217-18522, SO217-18526, SO217-18540 is provided by accelerator mass spectrometry (AMS) 14C dating of planktonic foraminifera. The chronology of Core MD06-3067 was originally presented in Bolliet et al. (2011), however, we have added three further 14C dates in the upper part of the core to further improve the chronology of this portion of the record.

For AMS 14C dating, approximately 600 to 800 well preserved tests of the near-surface dwelling planktonic foraminifera Globigerinoides ruber were picked from the > 250 μm size fraction. In instances of low abundance, G. ruber was complemented with the

planktonic foraminifera species Globigerinoides sacculifer and Pulleniatina obliquiloculata. AMS 14C dating was performed at the Leibniz Laboratory for Radiometric Dating and Stable Isotope Research in Kiel, Germany, following the protocol established by Nadeau et al. (1997) and Schleicher et al. (1998). Conventional ages were converted to calendar ages using the radiocarbon calibration program Calib 7.0 and the MARINE13 calibration curve (Reimer et al., 2013), including a marine reservoir correction of 400 years. For consistency with our newly derived calendar ages, we also recalibrated existing conventional 14C ages in Core MD06-3067 to calendar ages following the methodology described above, as opposed to using the protocol established by Fairbanks et al. (2005) which was originally used in Bolliet et al. (2011). Age differences between new derived calendar ages (using the MARINE13 curve) and old calendar ages (using the Fairbanks et al. (2005) protocol) in Core MD06-3067 are ± 300 years (1σ), with a maximum offset in the oldest 14C age (at ~33.5 ka) of ~1000 years. The age model for the lower part of Core MD06-3067 (below ~34 ka) is presented fully in Bolliet et al. (2011), and is generated through tie points to the EPICA Dronning Maud Land (EDML) chronology of Ruth et al. (2007) with an additional 1kyr correction to account for the transport time of deepwaters to reach the WEP.

Despite differences in 14C calibration methodologies used in the remaining records we have compiled, we did not retune or recalibrate existing 14C ages, as this results in only minimal age offsets (typically less than 500 years) when compared to more recent radiocarbon calibration methods over the deglacial period, and in many cases these offsets are smaller than age-related errors induced by analytical methods. Since we focus primarily on multi-millennial trends occurring over the past two deglaciations, discussion of the precise chronology of individual records is beyond the scope of this paper.

4.5 Results

4.5.1 Chronology

A list of new AMS 14C dates and derived age-depth models of Cores MD06-3067, SO217-18522, SO217-18526, SO217-18540 are presented in Supplementary Table 1, and

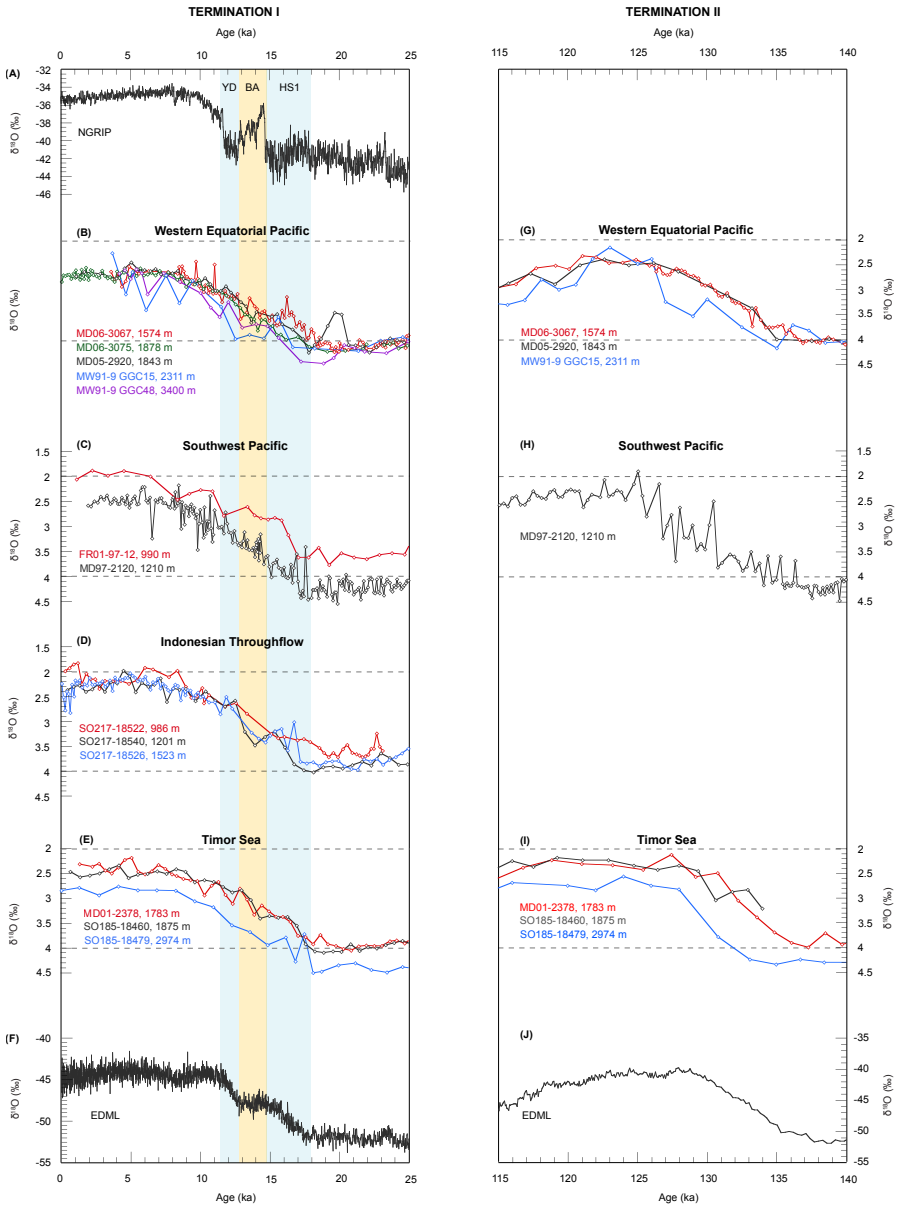

Figure 4.4 – Benthic foraminiferal $\delta^{18}O$ records for all cores compiled in this study, covering Termination I (left) and Termination II (right). (A) NGRIP $\delta^{18}O$ (Rasmussen et al., 2006). (B) and (G) Termination I and Termination II $\delta^{18}O$ records for WEP Cores MD06-3067 (red), MD06-3075 (green), MD05-2920 (black), MW91-9 GGC15 (blue) and MW91-9 GGC48 (purple). (C) and (H) Termination I and Termination II $\delta^{18}O$ records for southwest Pacific Cores FR1/97 GC12 (red) and MD97-2120 (black). (D) Termination I $\delta^{18}O$ records for for ITF Cores SO217-18522 (red), SO217-18540 (black) and SO217-18526 (blue). (E) and (I) Termination I and Termination II $\delta^{18}O$ records for Timor Sea Cores MD01-2378 (red), SO185-18460 (black) and SO185-18479 (blue). (F) and (J) Antarctic EDML $\delta^{18}O$ for Termination I and II (Ruth et al., 2007). References for all marine cores are detailed in Table 4.1.

Supplementary Figure 1, respectively. Final age models were generated by linear interpolation between AMS 14C ages. One AMS 14C age at 230 cm depth in Core MD06-3067 was not used to generate the age model, as it suggests ages ~2 kyr older than expected based upon linear trends between surrounding age control points. Bolliet et al. (2011) additionally discarded AMS 14C ages at 260 cm and 280 cm depth in Core MD06-3067, suggesting that these also provided unreliably old ages. However, reconsideration with our new AMS 14C measurements suggests that these ages do not deviate significantly from our age model, and thus we have included them in our final age model.

4.5.2 $\delta^{18}O$ of benthic foraminifera during Terminations I and II

Figure 4 provides an overview of compiled δ18Ob records, subdivided into four major regions (WEP, southwest Pacific, ITF and the Timor Sea). Since we focus primarily on deglacial circulation changes during Terminations I and II, we present records for two time slices: 0 - 25 ka and 115 - 140 ka (although only 7 of 13 records extend far enough to cover the latter period). Despite the usage of various dating methods and their associated uncertainties, all records show a general agreement over Termination I in terms of the timing of the initial decrease in δ18Ob values between 20 and 18 ka¬¬¬¬, with values decreasing relatively steadily over the deglacial period and reaching a plateau in the Holocene. Age models are less well constrained in Termination II due to tuning of records to different chronologies, and extrapolations of age models over relatively few age-control tie-points. This leads to more significant age offsets (often >2 ka) between records in terms of the timing of the onset and end of deglacial warming recorded by δ18Ob. δ18Ob values decrease over Terminations I and II with average amplitudes of 1.88 ‰ and 1.84 ‰, respectively. Larger amplitudes of δ18Ob (>2 ‰) are observed at shallower core sites, which are more susceptible to changes in water mass density. In contrast, deeper cores record lower amplitudes of δ18Ob, more in line with the global ice volume effect (associated with a deglacial whole-ocean δ18O change of 1.0 - 1.2 ‰ (Schrag et al., 2002)).

4.5.3 $\delta^{13}C$ of benthic foraminifera during Terminations I and II

A compilation of δ13Cb records spanning the last two glacial terminations is presented in Figure 5, subdivided into the same major regions used to divide δ18Ob records. Averages of Holocene (0 to 11 ka), deglacial (11 to 18ka) and LGM (18 to 23 ka) δ13Cb values are shown in Table 1. General long-term increasing trends in δ13Cb are noted in all regions during the last two glacial terminations. δ13Cb in Core MD05-2920, located at 1843 m depth off the north coast of Papua New Guinea, is elevated by 0.2 - 0.5 ‰ above other WEP sites during Terminations I and II (Figures 5A, 5E). Conversely, Core MD06-3075, situated at a similar water depth (1878 m) in the southern Philippines, shows more depleted δ13Cb values than other WEP sites, particularly during the early deglacial period of Termination I, and exhibits rapid fluctuations in excess of 0.4 ‰ (Figure 5A). Core MD06-3067, the shallowest of the WEP sites, displays similar long-term trends to deeper core sites during Termination I, although two distinct troughs are noted when δ13Cb values trend towards lower values between 17.5 and 15 ka, and between 12.5 and 10 ka (Figure 5A). An even more pronounced trough is apparent in Core MD06-3067 during Termination II, with a prolonged negative δ13Cb excursion to values between -0.6 and -0.8 ‰ occurring between 133 and 124 ka, whilst deeper WEP records show relatively steady increasing trends over the same period (Figure 5E)

In the southwest Pacific, δ13Cb values are generally higher and exhibit larger amplitudes of deglacial δ13Cb variability than other regions, varying between a minimum of 0 ‰ and maximum of 1.2 ‰ (Figure 5B). Cores FR1/97 GC12 and MD97-2120 show similar behaviour over Termination I, exhibiting minimum values at ~19.5 ka of 0.1 - 0.3 ‰, prior to an abrupt increase to values of 1 ‰ at 17 ka. A long-term increasing trend is observed between 17 ka and the Holocene, although Core MD97-2120 displays evidence of millennial-scale interruptions. Of these two cores, only Core MD97-2120 extends to Termination II, and is characterised by an abrupt increase in δ13Cb between 136 and 134 ka, prior to a 10 kyr-long plateau where values are elevated by ~1 ‰ over those observed during the penultimate glacial maximum (Figure 5F). It is interesting to note that the timing of this 10-kyr long period of high δ13Cb values occurs almost

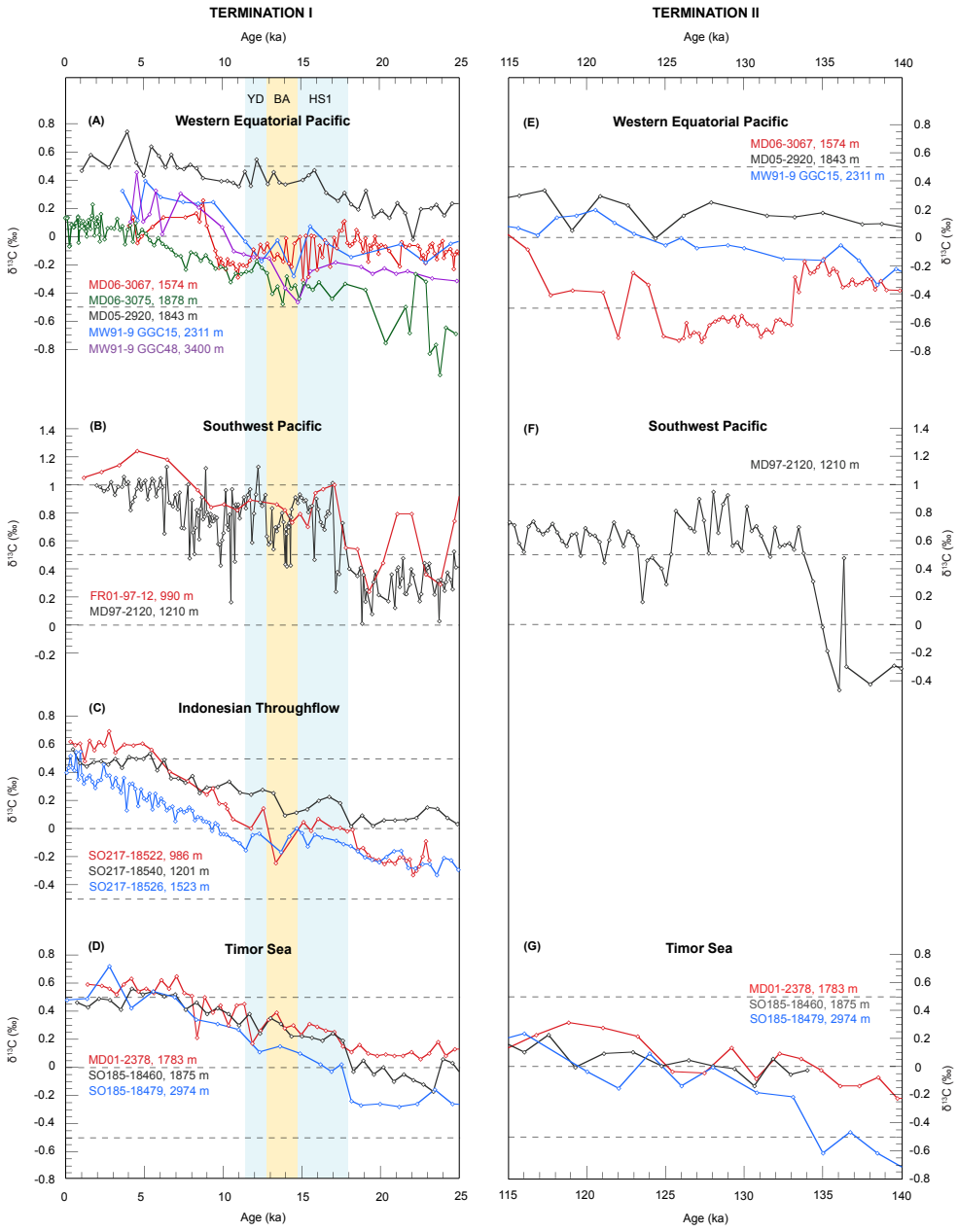

Figure 4.5 – Benthic foraminiferal $\delta^{13}C$ records for all cores compiled in this study, covering Termination I (left) and Termination II (right). (A) and (E) Termination I and Termination II $\delta^{13}C$ records for WEP Cores MD06-3067 (red), MD06-3075 (green), MD05-2920 (black), MW91-9 GGC15 (blue) and MW91-9 GGC48 (purple). (B) and (F) Termination I and Termination II $\delta^{13}C$ records for southwest Pacific Cores FR1/97 GC12 (red) and MD97-2120 (black). (C) Termination I $\delta^{13}C$ records for for ITF Cores SO217-18522 (red), SO217-18540 (black) and SO217-18526 (blue). (D) and (G) Termination I and Termination II $\delta^{13}C$ records for Timor Sea Cores MD01-2378 (red), SO185-18460 (black) and SO185-18479 (blue). References for all sediment cores are detailed in Table 4.1.

simultaneously (within a ~1 kyr error) with the prominent period of low δ13Cb values observed in Core MD06-3067.

In the Timor Sea and ITF regions, δ13Cb trends across Termination I show a steady increase from the LGM to the Holocene, with δ13Cb values of all cores converging between 0.4 - 0.6 ‰ in the late Holocene (Figures 5C and 5D). δ13Cb records from the Flores Sea (SO217-18540) exhibit higher values than those in the Celebes Sea and Makassar Strait during the LGM, and similar values (0 to 0.2 ‰) to intermediate-depth Timor Sea cores. The deepest Timor Sea core, Core SO185-18479, exhibits values 0.3 to 0.4 ‰ lower than intermediate depth cores in the same region, though δ13Cb values in all cores increase abruptly at the onset of HS-1. A similar trend is observed over Termination II in Timor Sea cores (note: ITF cores do not extend to Termination II), with Core SO185-18479 displaying lowest δ13Cb values prior to the deglaciation, before an abrupt increase on the order of 0.4 ‰ during the early deglaciation (between 135 and 133 ka) (Figure 5G).

4.5.4 Long-term Pacific intermediate $\delta^{18}O$ and $\delta^{13}C$ variability

Comparison of continuous δ18Ob records covering the past 160 kyr from Cores MD06-3067 and MD97-2120 (Figure 6), shows that major marine isotope stages are well recorded in both cores. Age discrepancies between the two cores (e.g. the timing of the onset of MIS 4) are likely caused by different methods of age-tuning; Core MD06-3067 is tuned via benthic δ18O tie points to the EDML1 ice core chronology of Ruth et al. (2007), whilst MD97-2120 is tuned via benthic δ18O tie-points to North Atlantic Core MD95-2042 (Shackleton et al., 2000) between ~40 and ~72 ka, and SSTMg/Ca tuning to the Vostok ice core δD record (Petit, 1999; Shackleton, 2000) for older sections. Such differences in age-tuning, combined with extrapolation of age models over relatively few age tie-points, may explain the large discrepancies (>5 kyr) between the two δ18Ob records, for example at the onset of MIS 4 or the relatively shorter δ18Ob plateau in Core MD97-2120 in MIS 5e. However, δ18Ob records match well during MIS 1-3 implying improved age control in the more recent portions of the records. We also note

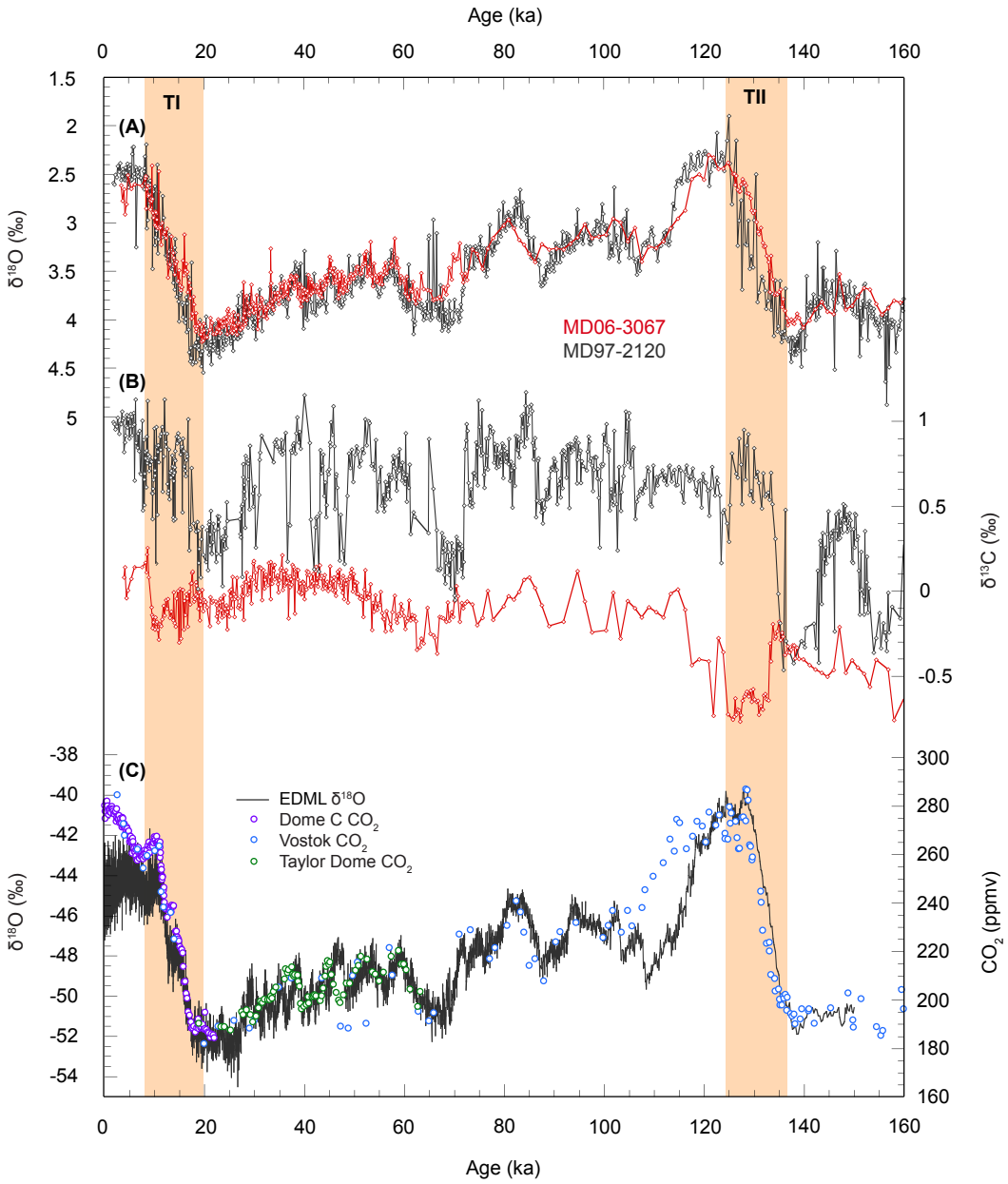

Figure 4.6 – (A) Benthic foraminiferal $\delta^{18}O$ records for Cores MD97-2120 (black) (Pahnke et al., 2003) and MD06-3067 (red) extending for the past 160 kyr. (B) Benthic foraminiferal $\delta^{13}C$ records for Cores MD97-2120 (black) (Pahnke and Zahn, 2005) and MD06-3067 (red). (C) EDML $\delta^{18}O$ (Ruth et al., 2007) and Antarctic CO_2 compilation from Dome C (Monnin et al., 2001), Vostok (Petit et al., 1999) and Taylor Dome (Indermühle et al., 2000).

slightly lighter (by 0.3 - 0.4 ‰) δ18Ob values in Core MD97-2120, relative to MD06-3067, during glacial maxima of MIS 2 and MIS 6.

The δ13Cb record from Core MD06-3067 indicates an overall increasing trend from values of -0.6 ‰ during MIS 6, to 0 ‰ during the late Holocene. Two distinct troughs in δ13Cb (discussed previously in section 4.2) during Terminations I and II present the most notable interruptions to this long-term trend, though MIS 4 is also characterised by a decrease in δ13Cb values by 0.3 ‰. Comparisons δ13Cb from Core MD06-3067 to Core MD97-2120 indicates overall elevated δ13Cb in Core MD97-2120, as is typical for AAIW compared to NPIW, with general trends of converging δ13Cb values during globally cold periods (LGM, MIS 4, late MIS 6) and diverging trends during periods of southern hemisphere warming and CO2 increase. These trends are most prominent during the last two glacial terminations when distinct increases in δ13Cb in Core MD97-2120 are remarkably well correlated to prominent δ13Cb troughs in Core MD06-3067. Significantly more millennial-scale variability is observed in Core MD97-2120 than Core MD06-3067, for example Antarctic Warm Events A1-A4 are correlated with fluctuations in benthic δ13Cb on the order of 0.8 ‰ in Core MD97-2120, whilst no such signal is observed in Core MD06-3067.

4.6 Discussion

4.6.1 Robustness of the benthic foraminiferal $\delta^{13}C$ proxy as a water mass tracer

Comparison of late Holocene core-top δ13Cb values with the modern distribution of δ13C in West Pacific water masses shows good agreement (Figure 2E), with the tongue of high δ13C AAIW recorded in Cores MD97-2120 and FR1/97 GC12, and lower δ13C values in Cores MD06-3067 and MD06-3075, which may be indicative of the influence and mixing of δ13C-depleted PDW at these sites. Core MD05-2920 sits within the pathway of the NGCUC, which entrains a significant portion of AAIW (Zenk et al., 2005), explaining elevated δ13Cb values at this site in comparison to deeper sites. This good agreement between foraminiferal and water-column δ13C measurements suggests that C. wuellerstorfi faithfully records bottom-water δ13CDIC in the modern day.

Records based on benthic foraminifera and coccolith abundances show that productivity in the WEP and Timor Sea may have been significantly higher in the last glacial period (e.g. Herguera and Berger, 1991; Müller and Opdyke, 2000; De Garidel-Thoron et al., 2001; Holbourn et al., 2005; Bolliet et al., 2011), which may have the potential to influence δ13Cb via past changes in the phytodetritus effect. However, no significant positive correlation is observed between changes in total productivity and δ13Cb over the time period of our records. For example, the most prominent negative excursion of δ13Cb values in Core MD06-3067, which occurs during Termination II (between 133 and 124 ka) (Figure 5E), is also correlated with the period of lowest primary production over the past 160 kyr, as inferred by coccolith assemblages (Bolliet et al., 2011). Instead, the phytodetritus effect is likely influenced by changes in the seasonal cycle of organic matter export rather than long-term total productivity variability (Mackensen et al., 2000). This may help to explain the low δ13Cb values observed in Core MD06-3075 when compared to surrounding West Pacific core sites (Figure 5A). These values cannot be explained by the presence of different water masses as no other surrounding cores record such a low δ13Cb signature, and instead hint at δ13Cb values altered by a seasonal phytodetritus effect, which may be expected at a site located in a marginal basin where seasonal productivity can be influenced by local riverine discharge (Fraser et al., 2014). In the context of this study, we therefore do not consider δ13Cb values in Core MD06-3075 to be reliable water mass indicators.

4.6.2 Reorganisations of Pacific water masses during the last glacial cycle

Estimates of changes in the mean whole-ocean δ13C composition suggest an overall increase by ~0.3 ‰ between the LGM and modern day (Duplessy et al., 1988; Peterson et al., 2014), a value that is also consistent with stacked records of PDW δ13C (Lisiecki, 2010). Deep WEP cores (> 2000 m water) compiled here show a δ13Cb change of comparable magnitude over the past two glacial terminations (Figure 5A) (Yu et al., 2010; 2013), indicative of an ocean-wide control on δ13C, driven by changes in the storage of carbon in deep water masses (Boyle, 1986). During the last two glacial maxima, δ13Cb records from intermediate-depth cores (Cores MD06-3067, MD97-2120) show a weak

meridional gradient (Figure 6), exhibiting values comparable to those found in deeper Pacific cores sites (Figure 5). This pattern may be explained by increased ventilation of NPIW above 2000 m during the LGM compared to the modern day (Keigwin et al., 1998; Matsumoto et al., 2002), and reduced production of AAIW in glacial times (Pahnke and Zahn, 2005), thus equatorial Pacific deep and intermediate waters masses may have been characterized by more homogenous vertical profiles than in the modern day. A similar reduction in the meridional δ13Cb gradient between Cores MD06-3067 and MD97-2120 during MIS 4 furthermore suggests that this is a common feature of globally cold periods (Figure 6).

In contrast to the last two glacial maxima, the evolution of intermediate-depth δ13Cb differed markedly across Termination I and II, implying that intermediate waters were subject to substantial reorganisation during periods of deglacial warming (Figure 5). During Terminations I and II, rapid increases in δ13Cb in southwest Pacific cores MD97-2120 and FR1/97 GC12 can be explained by an increase in the δ13C signature of AAIW source waters, driven by increased air-sea exchange as a result of a southward shift of the westerlies (Bostock et al., 2004; Pahnke and Zahn, 2005; Toggweiler et al., 2006; Bostock et al., 2010). Good agreement between the timing of the onset of deglacial CO2 rise and increasing δ13Cb in cores recording AAIW suggests that increased AAIW ventilation was related to the same upwelling mechanism driving the outgassing of stored CO2 from Southern Ocean deep water masses (Anderson et al., 2009). This mechanism may not be confined to glacial terminations, as other warming periods over the last glacial-interglacial cycle (e.g. Antarctic warm events A1-A4, MIS 5a, 5c) are characterised by δ13Cb enrichments, and cold periods (e.g. MIS 4) show δ13Cb depletions, also in phase with atmospheric CO2 concentrations (Figure 6). Elevated δ13Cb values in Core MD05-2920 during Termination I can therefore be explained by the entrainment of well-ventilated AAIW into the NGCUC, as in the modern day (Zenk et al., 2005). However, convergence of δ13Cb values of Core MD05-2920 with records of deep WEP water masses during the later part of Termination II could indicate that a lower contribution of AAIW was entrained in the NGCUC in this time period (Figure 5E).

Core MD06-3067 in the WEP shows a distinctly different δ13Cb pattern during glacial terminations, with troughs in δ13Cb correlated to elevated δ13Cb values in southwest Pacific sites during Terminations I and II (Figure 6). Reduced δ13Cb in Core MD06-3067 during HS-1 and the YD additionally shows an anti-phase relationship with millennial-scale variability imprinted on the high-resolution southwest Pacific Core MD97-2120, suggesting that both records were influenced by bi-polar see-saw climate variability (Figure 5). However, no evidence of this mechanism is observed during other stadial and interstadial periods during the last glacial cycle (Figure 6). Instead, Core MD06-3067 demonstrates a similar signal to PDW δ13Cb stacks during glacial times (Lisiecki et al., 2010), suggesting that the most prominent water mass reorgnaisations in the WEP occurred in intermediate waters during peak deglacial times.

Evidence of increased production of NPIW during deglacial periods has been previously documented (e.g. Stott et al., 2000; Sagawa and Ikehara, 2008; Okazaki et al., 2010), coeval with increased ventilation of NPIW recorded in δ13Cb reconstructions from the Okhotsk and Bering Sea (Max et al., 2014). In this context, it appears surprising that Core MD06-3067 would record a shift to more negative δ13Cb under the increased influence of NPIW. However, a recent record located to the east of Okinawa Island at 1166 m water depth (Kubota et al., 2015) found δ13Cb values only slightly more positive (0 - 0.1 ‰) than found at Core MD06-3067 during this time interval (-0.2 - 0 ‰). Troughs in δ13Cb at Core MD06-3067 may therefore be explained by a change in the mixing ratio between NPIW and AAIW endmembers; whilst NPIW became more δ13C-enriched during HS-1, it still remained relatively δ13C-depleted in comparison to AAIW. Replacement of AAIW by NPIW at this site may therefore still produce a negative excursion in δ13Cb, regardless of the change in the isotopic signature of NPIW alone.

No previous studies have reported the presence of NPIW at such depths (1574 m) and so far to the south (6° N) as in Core MD06-3067. Additionally, no such signal is recorded at comparable intermediate depths in the EEP. For example, a δ13Cb record from Core MD02-2529 at a similar depth (1619 m) and slightly more northern position (8° N) in the EEP did not detect the presence of NPIW during the last two glacial terminations (Leduc et al. 2010), suggesting a zonal asymmetry in the pathways of NPIW

between the EEP and WEP during deglacial periods. These results are in agreement with recent modelling approaches that use freshwater perturbation experiments to simulate a collapsed AMOC state, which indicate that glacial NPIW penetrated significantly further south, and deeper (to ~2500 m) in the WEP than in the modern day (Okazaki et al., 2010; Menviel et al., 2012; Chikamoto et al., 2012). These modelling studies also predict the occurrence of a strong western boundary flow at intermediate depths during a collapsed AMOC state, resulting in NPIW being transported significantly further south in the WEP than EEP, in agreement with the zonal asymmetry noted in δ13Cb records. Such agreement between model results and δ13Cb records over the last glacial termination suggests a similar, or perhaps even more intense, mechanism operated during Termination II, when δ13Cb values decreased more prominently in Core MD06-3067 than during Termination I.

4.6.3 Evolution of intermediate and deep water masses in the Indonesian Throughflow

4.6.3.1 Last Glacial Maximum

During the LGM, Cores SO217-18522 and SO217-18526 located in the Celebes Sea and Makassar Strait, respectively, record the strong inflow of low-δ13C NPIW (in comparison to high-δ13C AAIW) into the northwestern ITF route, which enters the ITF to the south of Mindanao, and is blocked by the Dewakang Sill at 650 m water depth in the southern Makassar Strait (Figure 7). Higher δ13Cb values at Core SO217-18540 in the Flores Sea compared to the two cores within the Celebes Sea and Makassar Strait suggest this site is instead influenced by well-ventilated IIW being transported via the Banda Sea to the Flores Sea. δ13Cb values in Cores SO217-18540 (Flores Sea) and SO185-18460 (eastern Timor Sea) sit between the two endmembers of northern (Core MD06-3067) and southern (Core MD05-2920) source Pacific intermediate waters during the LGM (Figure 7G), suggesting a mixed composition of these two water masses circulating in the Banda Sea and exiting the Indonesian archipelago via the Timor Sea.

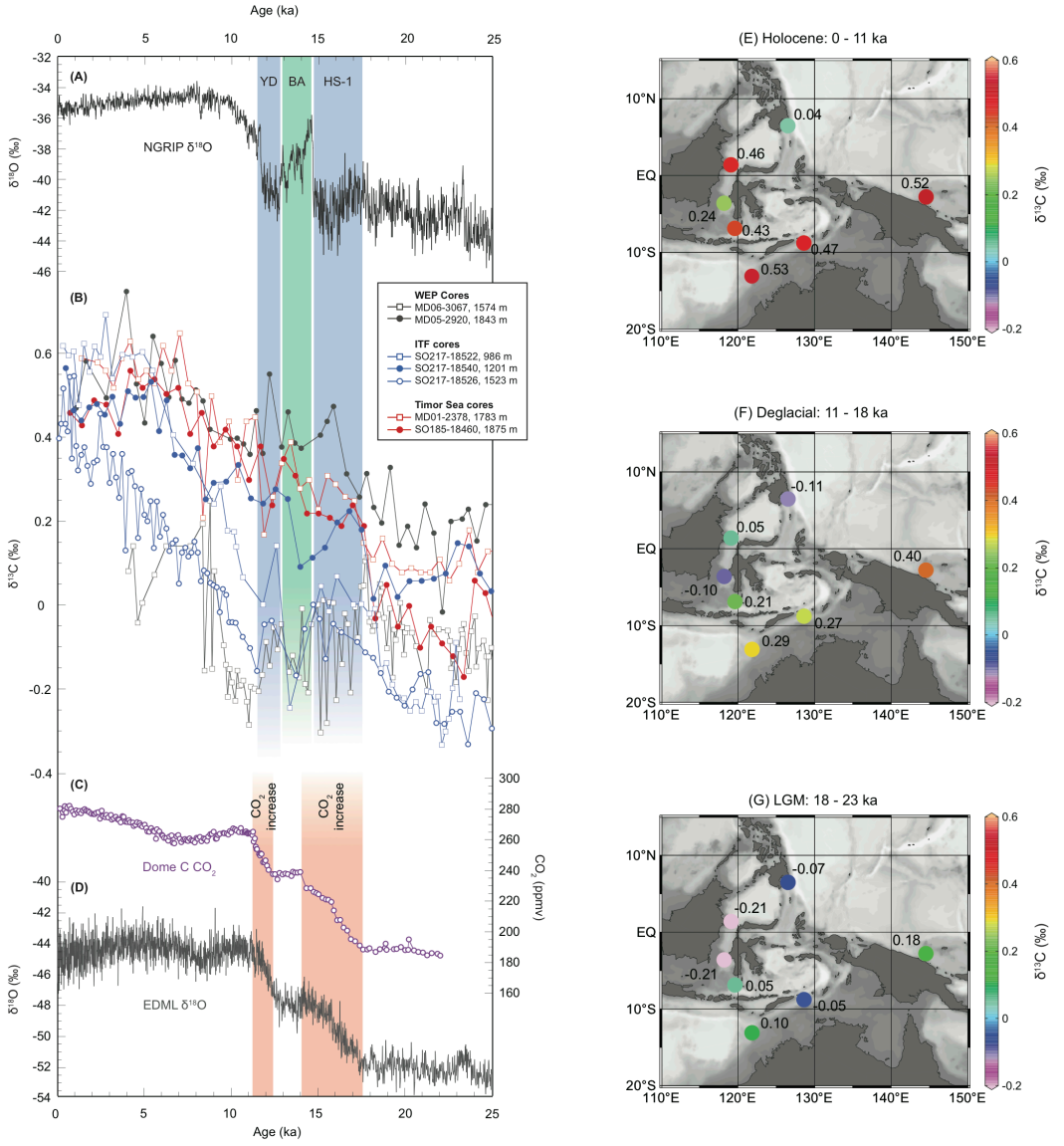

Figure 4.7 – (left) Compilation of intermediate-depth West Pacific and ITF benthic foraminiferal $\delta^{13}C$ records covering Termination I. (A) NGRIP $\delta^{18}O$ (Rasmussen et al., 2006). (B) $\delta^{13}C_b$ records from Cores MD06-3067 (black, open squares), MD05-2920 (black, filled circles), SO217-18522 (blue, open squares), S0217-18540 (blue, filled circles), SO217-18526 (blue, open circles), MD01-2378 (red, open squares), SO185-18460 (red, filled circles). (C) Dome C CO_2 concentrations (Monnin et al., 2001). (D) EDML $\delta^{18}O$ (Ruth et al., 2007). (right) Maps of benthic $\delta^{13}C$ at compiled cores sites for key time slices: (E) Holocene (0 - 11 ka, top), (F) Deglacial (11 - 18 ka, middle), (G) LGM (18 - 23 ka, bottom). Data for time slices available in Table 4.1.

In the Timor Sea, divergent δ13Cb values are noted during the LGM between Cores MD01-2378, SO185-18460 and SO185-18479 (Figures 5 and 7), with the deepest Core SO185-18479 recording δ13C-depleted values relative to the two intermediate-depth cores. Holbourn et al. (2011) suggested that this core site primarily records deepwater ventilation in the Indian Ocean as it sits considerably below the deepest sill depth of the Timor Sea Outflow (~1900 m). This larger glacial offset could therefore be caused by weaker vertical mixing between deep and intermediate waters. A δ13Cb gradient between the more westerly Core MD01-2378 and easterly Core SO185-18460, both located at similar water depths, may additionally be related to the increased influence of well-ventilated Indian Ocean Intermediate Water (IOCW) at the western site, consistent with a reduced deep ITF outflow during the LGM (Holbourn et al., 2011).

4.6.3.2 Deglacial Evolution

Between 17 and 18 ka, δ13Cb values in Flores Sea Core SO217-18540 and intermediate depth Timor Sea Cores SO185-18460 and MD01-2378 abruptly increase (Figure 7), converging with δ13Cb values in Core MD05-2920 and diverging from those in Core MD06-3067. This pattern is consistent with an increased component of well-ventilated AAIW entering the Banda Sea through the southeastern ITF entrance passages, and a reduced component of NPIW. The reduced δ13Cb gradient between intermediate-depth cores in the eastern and western Timor Sea additionally suggests an overall strengthening of the deep ITF in this time interval (Holbourn et al., 2011). A rapid increase in the ventilation of deep Timor Sea Core SO185-18479 may be related to an improvement of deepwater ventilation of IOCW at this site (Waelbroeck et al., 2006), or through greater mixing and weaker vertical stratification with ITF outflow waters. A similar evolution of δ13Cb in the same three Timor Sea cores during Termination II suggests that this pattern is a common feature of deglacial transitions (Figure 5)

Conversely, δ13Cb values in Celebes Sea and Makassar Strait Cores SO217-18522 and SO217-18526 remain lower than those in the Flores Sea and Timor Sea, and similar to those observed in MD06-3067 during HS-1 (Figure 7), and thus likely remained predominantly under the influence of NPIW. Over the remainder of the last deglacial

period, δ13Cb variability in Core SO217-18526 closely tracks changes in MD06-3067, indicating that deeper waters in the Makassar Strait continued to be sourced primarily from NPIW. However, Core SO217-18522 in the Celebes Sea shows an improvement in ventilation, beginning during the late BA period and eventually converging with δ13Cb values of Flores Sea and Timor Sea cores during the early Holocene. This suggests that shallow intermediate waters (< 1000 m) in the northwestern ITF passage were gradually replaced by a better-ventilated source over the deglacial period, whilst deeper intermediate waters (> 1500m) remained relatively poorly ventilated.

4.6.3.2 Holocene

From the mid- to late-Holocene, δ13Cb records of cores from the Timor Sea and ITF region converge on a narrow band of values between 0.4 - 0.8 ‰ (Figure 7). These values are higher than those reported at ~2000 m depth in the eastern Indian Ocean (~0.3 ‰; Waelbroeck et al., 2006), suggesting that Timor Sea sites were bathed predominantly by well-ventilated IIW rather than IOCW during the late Holocene. Core SO217-18526 in the southern Makassar Strait exhibits lower δ13Cb values (by 0.3 - 0.4 ‰) during the early and mid-Holocene compared to other ITF records, but converges on values of 0.4 ‰ during the last ~2 kyrs. This implies a gradual improvement in ventilation of the deeper waters in the southern Makassar Strait during the Holocene, and a further reduced influence of NPIW. This would be consistent with modern observations of NPIW restricted to lower thermocline waters within the ITF (Ilahude and Gordon, 1996). Such a uniform distribution of δ13Cb in the ITF during the Holocene suggests that low-density NPIW does not form a significant component of the ITF deep and intermediate water masses. Instead, NPIW is replaced by a better-ventilated, southern sourced intermediate water mass which dominates the ITF pathways in the Holocene, in stark contrast to the LGM and deglacation.

4.7 Conclusions

δ13Cb records from Core MD06-3067 show that mid-depth waters of the WEP received a greater contribution from NPIW during the last two glacial terminations, which may be related to the increased production and depth distribution of NPIW. Such an extension of NPIW into equatorial waters at ~1500 m depth has not documented in the EEP, suggesting a meridional asymmetry in the distribution of NPIW driven by the increased strength of deep western boundary currents, consistent with recent modelling experiments (Okazaki et al., 2010). Periods of lower δ13Cb values in Core MD06-3067 in the WEP are associated with elevated δ13Cb in southwest Pacific Cores MD97-2120 and FR1/97 GC12, which track changes in the ventilation and production history of AAIW (Bostock et al., 2004; Pahnke and Zahn, 2005). This close coupling of changes in the North and South Pacific provides support for widescale reorganisations of intermediate-depth Pacific waters during the past two glacial terminations.

δ13Cb records from the ITF region provide evidence for variable contributions of NPIW, PDW and AAIW to ITF intermediate and deep transport across the last glacial termination. At the onset of deglacial warming, abrupt increases in δ13Cb in the Timor Sea and Flores Sea suggest an increased contribution of AAIW to intermediate waters of the ITF. Additionally, east-west δ13Cb gradients between mid-depth Timor Sea cores imply that the ITF outflow strengthened during this time period, recording lower contributions from IOCW. Conversely, reduced δ13Cb values in Celebes Sea and Makassar Strait cores during the early deglacial are consistent with the reduced δ13C signature of NPIW source waters, though the lack of this low-δ13Cb signal in the Timor Sea outflow suggests that the northwestern ITF passages had made a minor contribution to the main ITF deep transport in this time period. From the late deglacial to the modern day, δ13Cb signatures across the Indonesian region converge on a narrow band of values consistent with a predominantly southern source of intermediate and deep waters in the modern ITF.

4.9 References

Ahagon, N., Ohkushi, K. I., Uchida, M., and Mishima, T. (2003), Mid-depth circulation in the northwest Pacific during the last deglaciation: Evidence from foraminiferal radiocarbon ages, Geophysical Research Letters, 30(21), doi: 10.1029/2003GL018287.

Anderson, R. F., Ali, S., Bradtmiller, L. I., Nielsen, S. H. H., Fleisher, M. Q., Anderson, B. E., and Burckle, L. H. (2009), Wind-driven upwelling in the Southern Ocean and the deglacial rise in atmospheric CO2, Science, 323(5920), 1443-1448, doi: 10.1126/science.1167441.

Barker, S., Diz, P., Vautravers, M. J., Pike, J., Knorr, G., Hall, I. R., and Broecker, W. S. (2009). Interhemispheric Atlantic seesaw response during the last deglaciation. Nature, 457(7233), 1097-1102, doi: 10.1038/nature07770.

Bemis, B. E., Spero, H. J., Bijma, J., and Lea, D. W. (1998). Reevaluation of the oxygen isotopic composition of planktonic foraminifera: Experimental results and revised paleotemperature equations. Paleoceanography, 13(2), 150-160, doi: 10.1029/98PA00070.

Bingham, F. M., and Lukas, R. (1994), The southward intrusion of North Pacific Intermediate Water along the Mindanao coast, Journal of physical oceanography, 24(1), 141-154, doi: 10.1175/1520-0485(1994)024<0141:TSIONP>2.0.CO;2.

Bingham, F. M., and Lukas, R. (1995), The distribution of intermediate water in the western equatorial Pacific during January–February 1986, Deep Sea Research Part I: Oceanographic Research Papers, 42(9), 1545-1573, doi: 10.1016/0967-0637(95)00064-D.

Bolliet, T., Holbourn, A., Kuhnt, W., Laj, C., Kissel, C., Beaufort, L., Kienast, M., Andersen, N., and Garbe-Schönberg, D. (2011). Mindanao Dome variability over the last 160 kyr: Episodic glacial cooling of the West Pacific Warm Pool. Paleoceanography, 26(1), doi: 10.1029/2010PA001966.

Bostock, H. C., Opdyke, B. N., Gagan, M. K., and Fifield, L. K. (2004), Carbon isotope evidence for changes in Antarctic Intermediate Water circulation and ocean ventilation in the southwest Pacific during the last deglaciation, Paleoceanography, 19(4), doi: 10.1029/2004PA001047.

Bostock, H. C., Opdyke, B. N., and Williams, M. J. (2010), Characterising the intermediate depth waters of the Pacific Ocean using $\delta^{13}C$ and other geochemical tracers, Deep Sea Research Part I: Oceanographic Research Papers, 57(7), 847-859, doi: 10.1016/j.dsr.2010.04.005.

Boyle, E. A. (1986), Deep ocean circulation, preformed nutrients, and atmospheric carbon dioxide: Theories and evidence from oceanic sediments, Mesozoic and Cenozoic Oceans, 49-59, doi: 10.1029/GD015p0049.

Broecker, W. S. (1998), Paleocean circulation during the last deglaciation: a bipolar seesaw?, Paleoceanography, 13(2), 119-121, doi: 10.1029/97PA03707.

Burke, A., and Robinson, L. F. (2012), The Southern Ocean's role in carbon exchange during the last deglaciation, Science, 335(6068), 557-561, doi: 10.1126/science.1208163.

Chikamoto, M. O., Menviel, L., Abe-Ouchi, A., Ohgaito, R., Timmermann, A., Okazaki, Y., Harada, N., Oka, A., and Mouchet, A. (2012), Variability in North Pacific intermediate and deep water ventilation during Heinrich events in two coupled climate models, Deep Sea Research Part II: Topical Studies in Oceanography, 61, 114-126, doi: 10.1016/j.dsr2.2011.12.002.

De Garidel-Thoron, T., Beaufort, L., Linsley, B. K., and Dannenmann, S. (2001), Millennial-scale dynamics of the east Asian winter monsoon during the last 200,000 years, Paleoceanography, 16(5), 491-502, doi: 10.1029/2000PA000557.

Denton, G. H., Anderson, R. F., Toggweiler, J. R., Edwards, R. L., Schaefer, J. M., and Putnam, A. E. (2010). The last glacial termination. Science, 328(5986), 1652-1656, doi: 10.1126/science.1184119.

Duplessy, J. C., Shackleton, N. J., Matthews, R. K., Prell, W., Ruddiman, W. F., Caralp, M., and Hendy, C. H. (1984), ^{13}C Record of benthic foraminifera in the last interglacial ocean: Implications for the carbon cycle and the global deep water circulation. Quaternary Research, 21(2), 225-243, doi: 10.1016/0033-5894(84)90099-1.

Duplessy, J. C., Shackleton, N. J., Fairbanks, R. G., Labeyrie, L., Oppo, D., and Kallel, N. (1988), Deepwater source variations during the last climatic cycle and their impact on the global deepwater circulation. Paleoceanography, 3(3), 343-360, doi: 10.1029/PA003i003p00343.

Emile-Geay, J., Cane, M. A., Naik, N., Seager, R., Clement, A. C., and van Geen, A. (2003). Warren revisited: Atmospheric freshwater fluxes and "Why is no deep water formed in the North Pacific". Journal of Geophysical Research: Oceans (1978–2012), 108(C6), doi: 10.1029/2001JC001058.

Fairbanks, R. G., Mortlock, R. A., Chiu, T. C., Cao, L., Kaplan, A., Guilderson, T. P., Fairbanks, T. W., Bloom, A. L., Grootes, P. M., and Nadeau, M. J. (2005), Radiocarbon calibration curve spanning 0 to 50,000 years BP based on paired $^{230}Th/^{234}U/^{238}U$ and ^{14}C dates on pristine corals, Quaternary Science Reviews, 24(16), 1781-1796, doi: 10.1016/j.quascirev.2005.04.007.

Fine, R. A., Lukas, R., Bingham, F. M., Warner, M. J., and Gammon, R. H. (1994), The western equatorial Pacific: A water mass crossroads, Journal of Geophysical Research: Oceans (1978–2012), 99(C12), 25063-25080, doi: 10.1029/94JC02277.

Fraser, N., Kuhnt, W., Holbourn, A., Bolliet, T., Andersen, N., Blanz, T., Beaufort, L. (2014), Precipitation variability within the West Pacific Warm Pool over the past 120 ka: evidence from the Davao Gulf, southern Philippines. Paleoceanography, doi: 10.1002/2013PA002599.

Galbraith, E. D., Jaccard, S. L., Pedersen, T. F., Sigman, D. M., Haug, G. H., Cook, M., Southon, J. R., and Francois, R. (2007), Carbon dioxide release from the North Pacific abyss during the last deglaciation. Nature, 449(7164), 890-893, doi; 10.1038/nature06227.

Gebhardt, H., Sarnthein, M., Grootes, P. M., Kiefer, T., Kuehn, H., Schmieder, F., and Röhl, U. (2008), Paleonutrient and productivity records from the subarctic North Pacific for Pleistocene glacial terminations I to V, Paleoceanography 23, PA4212, doi: 10.1029/2007PA001513.

Gordon, A. L., and Fine, R. A. (1996), Pathways of water between the Pacific and Indian oceans in the Indonesian seas, Nature, 379(6561), 146-149, doi: 10.1038/379146a0.

Gordon, A. L., Giulivi, C. F., and Ilahude, A. G. (2003), Deep topographic barriers within the Indonesian seas. Deep Sea Research Part II: Topical Studies in Oceanography, 50(12), 2205-2228, doi: 10.1016/S0967-0645(03)00053-5.

Gordon, A. L. (2005), Oceanography of The Indonesian Seas, Oceanography, 18(4), 14, doi: 10.5670/oceanog.2005.01.

Gordon, A. L., Sprintall, J., Van Aken, H. M., Susanto, D., Wijffels, S., Molcard, R., Ffield, A., Pranowo, W., and Wirasantosa, S. (2010), The Indonesian throughflow during 2004–2006 as observed by the INSTANT program, Dynamics of Atmospheres and Oceans, 50(2), 115-128, doi: 10.1016/j.dynatmoce.2009.12.002.

Graham, D. W., Corliss, B. H., Bender, M. L., and Keigwin Jr, L. D. (1981), Carbon and oxygen isotopic disequilibria of recent deep-sea benthic foraminifera, Marine Micropaleontology, 6(5), 483-497, doi; 10.1016/0377-8398(81)90018-9.

Grossman, E. L. (1987), Stable isotopes in modern benthic foraminifera; a study of vital effect, The Journal of Foraminiferal Research, 17(1), 48-61, doi: 10.2113/gsjfr.17.1.48.

Hanawa, K., and Talley, L. D. (2001), Mode waters, International Geophysics Series, 77, 373-386.

Herguera, J. C., and Berger, W. (1991), Paleoproductivity from benthic foraminifera abundance: Glacial to postglacial change in the west-equatorial Pacific, Geology, 19(12), 1173-1176, doi: 10.1130/0091-7613(1991)019<1173:PFBFAG>2.3.CO;2.

Holbourn, A., Kuhnt, W., Kawamura, H., Jian, Z., Grootes, P., Erlenkeuser, H., and Xu, J. (2005), Orbitally paced paleoproductivity variations in the Timor Sea and Indonesian Throughflow variability during the last 460 kyr, Paleoceanography, 20(3), doi: 10.1029/2004PA001094.

Holbourn, A., Kuhnt, W., Schulz, M., Flores, J. A., and Andersen, N. (2007), Orbitally-paced climate evolution during the middle Miocene "Monterey" carbon-isotope excursion, Earth and Planetary Science Letters, 261(3), 534-550, doi: 10.1016/j.epsl.2007.07.026.

Holbourn, A., Kuhnt, W., and Xu, J. (2011), Indonesian Throughflow variability during the last 140 ka: the Timor Sea outflow, Geological Society, London, Special Publications, 355(1), 283-303, doi: 10.1144/SP355.14.

Hoogakker, B., Elderfield, H., Oliver, K., and Crowhurst, S. (2010), Benthic foraminiferal oxygen isotope offsets over the last glacial-interglacial cycle, Paleoceanography, 25(4), doi: 10.1029/2009PA001870.

Indermühle, A., Monnin, E., Stauffer, B., Stocker, T. F., and Wahlen, M. (2000). Atmospheric CO2 concentration from 60 to 20 kyr BP from the Taylor Dome ice core, Antarctica. Geophysical Research Letters, 27(5), 735-738, doi: 10.1029/1999GL010960.

Jaccard, S. L., and Galbraith, E. D. (2013), Direct ventilation of the North Pacific did not reach the deep ocean during the last deglaciation, Geophysical Research Letters, 40(1), 199-203, doi: 10.1029/2012GL054118.

Katsumata, K., and Yoshinari, H. (2010), Uncertainties in global mapping of Argo drift data at the parking level, Journal of Oceanography, 66, 553-569, doi: 10.1007/s10872-010-0046-4.

Keigwin, L. D. (1998). Glacial-age hydrography of the far northwest Pacific Ocean. Paleoceanography, 13(4), 323-339, doi: 10.1029/98PA00874.

Kuhnt, W., and the Shipboard Scientific Party (2011), Cruise report of Sonne 217 MAJA - Variability of the Indonesian Throughflow within the Makassar-Java Passage, July 15 - August 16, 2011.

Leduc, G., Vidal, L., Tachikawa, K., and Bard, E. (2010), Changes in Eastern Pacific ocean ventilation at intermediate depth over the last 150 kyr BP, Earth and Planetary Science Letters, 298(1), 217-228, doi: 10.1016/j.epsl.2010.08.002.

Lund, D. C., Mix, A. C., and Southon, J. (2011), Increased ventilation age of the deep northeast Pacific Ocean during the last deglaciation, Nature Geoscience, 4(11), 771-774, doi: 10.1038/ngeo1272.

Lisiecki, L. E. (2010), A simple mixing explanation for late Pleistocene changes in the Pacific-South Atlantic benthic δ 13 C gradient, Climate of the Past, 6(3), 305-314, doi: 10.5194/cp-6-305-2010.

Locarnini, R. A., A. V. Mishonov, J. I. Antonov, T. P. Boyer, H. E. Garcia, O. K. Baranova, M. M. Zweng, and D. R. Johnson (2010), World Ocean Atlas 2009, Volume 1: Temperature, S. Levitus, Ed. NOAA Atlas NESDIS 68, U.S. Government Printing Office, Washington, D.C., 1-184.

Lynch-Stieglitz, J., Curry, W. B., and Slowey, N. (1999). Weaker Gulf Stream in the Florida straits during the last glacial maximum. Nature, 402(6762), 644-648, doi:

10.1038/45204.

Mackensen, A., Hubberten, H. W., Bickert, T., Fischer, G., and Fütterer, D. K. (1993), The $\delta^{13}C$ in benthic foraminiferal tests of Fontbotia wuellerstorfi (Schwager) relative to the $\delta^{13}C$ of dissolved inorganic carbon in southern ocean deep water: implications for glacial ocean circulation models, Paleoceanography, 8(5), 587-610, doi: 10.1029/93PA01291.

Mackensen, A., Schumacher, S., Radke, J., and Schmidt, D. N. (2000), Microhabitat preferences and stable carbon isotopes of endobenthic foraminifera: clue to quantitative reconstruction of oceanic new production?, Mar. Micropaleontol., 40, 233–258.

Mackensen, A., Rudolph, M., and Kuhn, G. (2001), Late Pleistocene deep-water circulation in the subantarctic eastern Atlantic, Global and Planetary Change, 30(3), 197-229, doi: 10.1016/S0921-8181(01)00102-3.

Marchitto, T. M., Lehman, S. J., Ortiz, J. D., Flückiger, J., and van Geen, A. (2007), Marine radiocarbon evidence for the mechanism of deglacial atmospheric CO2 rise, Science, 316(5830), 1456-1459, doi: 10.1126/science.1138679.

Marchitto, T. M., Curry, W. B., Lynch-Stieglitz, J., Bryan, S. P., Cobb, K. M., and Lund, D. C. (2014), Improved oxygen isotope temperature calibrations for cosmopolitan benthic foraminifera, Geochimica et Cosmochimica Acta, 130, 1-11, doi: 10.1016/j.gca.2013.12.034.

Matsumoto, K., Oba, T., Lynch-Stieglitz, J., and Yamamoto, H. (2002), Interior hydrography and circulation of the glacial Pacific Ocean, Quaternary Science Reviews, 21(14), 1693-1704, doi: 10.1016/S0277-3791(01)00142-1.

Max, L., Lembke-Jene, L., Riethdorf, J. R., Tiedemann, R., Nürnberg, D., Kühn, H., and Mackensen, A. (2014), Pulses of enhanced North Pacific Intermediate Water ventilation from the Okhotsk Sea and Bering Sea during the last deglaciation, Climate of the Past, 10(2), 591-605, doi: 10.5194/cp-10-591-2014.

McCartney, M. S. (1977), Subantarctic mode water, A voyage of discovery, 24, 103-119.

McCorkle, D. C., Keigwin, L. D., Corliss, B. H., and Emerson, S. R. (1990), The influence of microhabitats on the carbon isotopic composition of deep-sea benthic foraminifera, Paleoceanography, 5(2), 161-185, doi: 10.1029/PA005i002p00161.

Menviel, L., Timmermann, A., Elison Timm, O., Mouchet, A., Abe-Ouchi, A., Chikamoto, M. O., Harada, N., Ohgaito, R., and Okazaki, Y. (2012), Removing the North Pacific halocline: Effects on global climate, ocean circulation and the carbon cycle, Deep Sea Research Part II: Topical Studies in Oceanography, 61, 106-113, doi: 10.1016/j.dsr2.2011.03.005.

Menviel, L., England, M. H., Meissner, K. J., Mouchet, A., and Yu, J. (2014), Atlantic-Pacific seesaw and its role in outgassing CO2 during Heinrich events, Paleoceanography, 29(1), 58-70, doi: 10.1002/2013PA002542.

Monnin, E., Indermühle, A., Dällenbach, A., Flückiger, J., Stauffer, B., Stocker, T. F., Raynaud, D., and Barnola, J. M. (2001). Atmospheric CO2 concentrations over the last glacial termination. Science, 291(5501), 112-114, doi: 10.1126/science.291.5501.112.

Müller, A., and Opdyke, B. N. (2000), Glacial-interglacial changes in nutrient utilization and paleoproductivity in the Indonesian Throughflow sensitive Timor Trough, easternmost Indian Ocean, Paleoceanography, 15(1), 85-94, doi: 10.1029/1999PA900046.

Nadeau, M. J., Schleicher, M., Grootes, P. M., Erlenkeuser, H., Gottdang, A., Mous, D. J. W., Sarnthein, M., and Willkomm, H. (1997). The Leibniz-Labor AMS facility at the Christian-Albrechts University, Kiel, Germany. Nuclear Instruments and Methods in Physics Research Section B: Beam Interactions with Materials and Atoms, 123(1), 22-30, doi: 10.1016/S0168-583X(96)00730-6.

Okazaki, Y., Timmermann, A., Menviel, L., Harada, N., Abe-Ouchi, A., Chikamoto, M. O., Mouchet, A., and Asahi, H. (2010), Deepwater formation in the North Pacific during the last glacial termination, Science, 329(5988), 200-204, doi: 10.1126/science.1190612.

Pahnke, K., Zahn, R., Elderfield, H., and Schulz, M. (2003), 340,000-year centennial-scale marine record of Southern Hemisphere climatic oscillation, Science, 301(5635), 948-952, doi: 10.1126/science.1084451.

Pahnke, K., and Zahn, R. (2005), Southern Hemisphere water mass conversion linked with North Atlantic climate variability, Science, 307(5716), 1741-1746, doi: 10.1126/science.1102163.

Pahnke, K., Goldstein, S. L., and Hemming, S. R. (2008), Abrupt changes in Antarctic Intermediate Water circulation over the past 25,000 years, Nature Geoscience, 1(12), 870-874, doi: 10.1038/ngeo360.

Pena, L. D., Goldstein, S. L., Hemming, S. R., Jones, K. M., Calvo, E., Pelejero, C., and Cacho, I. (2013), Rapid changes in meridional advection of Southern Ocean intermediate waters to the tropical Pacific during the last 30kyr, Earth and Planetary Science Letters, 368, 20-32, doi: 10.1016/j.epsl.2013.02.028.

Peterson, C. D., Lisiecki, L. E., and Stern, J. V. (2014). Deglacial whole-ocean δ13C change estimated from 480 benthic foraminiferal records. Paleoceanography, doi: 10.1002/2013PA002552.

Petit, J. R., Jouzel, J., Raynaud, D., Barkov, N. I., Barnola, J. M., Basile, I., Bender, M., Chappellaz, J., Davis, M., Delaygue, G., Delmotte, M., Kotlyakov, V. M., Legrand, M., Lipenkov, V. Y., Lorius, C., Pepin, L., Ritz, C., Saltzman, E., and Stievenard, M. (1999), Climate and atmospheric history of the past 420,000 years from the Vostok ice core, Antarctica, Nature, 399(6735), 429-436, doi: 10.1038/20859.

Qu, T., and Lindstrom, E. J. (2004), Northward Intrusion of Antarctic Intermediate Water in the Western Pacific, Journal of physical oceanography, 34(9), 2104-2118, doi: 10.1175/1520-0485(2004)034<2104:NIOAIW>2.0.CO;2.

Rae, J. W., Sarnthein, M., Foster, G. L., Ridgwell, A., Grootes, P. M., and Elliott, T. (2014), Deep water formation in the North Pacific and deglacial CO2 rise, Paleoceanography, doi: 10.1002/2013PA002570.

Reimer, P. J., Bard, E., Bayliss, A., Beck, J. W. et al., (2013), IntCal13 and Marine13 radiocarbon age calibration curves 0–50,000 years cal BP, Radiocarbon, 55(4), 1869-1887, doi: 10.2458/azu_js_rc.55.16947.

Ruth, U., Barnola, J. M., Beer, J., Bigler, M., Blunier, T., Castellano, E., Fischer, H., Fundel, F., Huybrechts, P., Kaufmann, P., Kipfstuhl, S., Lambrecht, A., Morganti, A., Oerter, H., Parrenin, F., Rybak, O., Severi, M., Udisti, R., Wilhelms, F., and Wolff, E. (2007). "EDML1": a chronology for the EPICA deep ice core from Dronning Maud Land, Antarctica, over the last 150 000 years. Climate of the Past Discussions, 3(2), 549-574, doi: 10.5194/cp-3-475-2007.

Sagawa, T., and Ikehara, K. (2008), Intermediate water ventilation change in the subarctic northwest Pacific during the last deglaciation, Geophysical Research Letters, 35(24), doi: 10.1029/2008GL035133.

Sarnthein, M., Schneider, B., and Grootes, P. M. (2013), Peak glacial 14C ventilation ages suggest major draw-down of carbon into the abyssal ocean, Climate of the Past Discussions, 9(1), 925-965, doi: 10.5194/cp-9-2595-2013.

Schleicher, M., Grootes, P. M., Nadeau, M. J., and Schoon, A. (1998). The carbonate 14C background and its components at the Leibniz AMS facility. Radiocarbon, 40(1), 85-93.

Schlitzer, R., Ocean Data View, http://odv.awi.de, 2014.

Schmitz Jr, W. J. (1996), On the World Ocean Circulation: Volume 2 The Pacific and Indian Oceans/A Global Update, No. WHOI-96-08, Woods Hole Oceanographic Institution.

Schrag, D. P., Adkins, J. F., McIntyre, K., Alexander, J. L., Hodell, D. A., Charles, C. D., and McManus, J. F. (2002), The oxygen isotopic composition of seawater during the

Last Glacial Maximum, Quaternary Science Reviews, 21(1), 331-342, doi: 10.1016/S0277-3791(01)00110-X.

Shackleton, N. J., and Opdyke, N. D. (1973), Oxygen isotope and palaeomagnetic stratigraphy of Equatorial Pacific core V28-238: Oxygen isotope temperatures and ice volumes on a 10^5 year and 10^6 year scale, Quaternary research, 3(1), 39-55, doi: 10.1016/0033-5894(73)90052-5.

Shackleton, N. J. (1974). Attainment of isotopic equilibrium between ocean water and the benthonic foraminifera genus Uvigerina: isotopic changes in the ocean during the last glacial.

Sigman, D. M., and Boyle, E. A. (2000), Glacial/interglacial variations in atmospheric carbon dioxide, Nature, 407(6806), 859-869, doi: 10.1038/35038000.

Sigman, D. M., Hain, M. P., and Haug, G. H. (2010), The polar ocean and glacial cycles in atmospheric CO2 concentration, Nature, 466(7302), 47-55, doi: 10.1038/nature09149.

Skinner, L. C., Fallon, S., Waelbroeck, C., Michel, E., and Barker, S. (2010), Ventilation of the deep Southern Ocean and deglacial CO2 rise. Science, 328(5982), 1147-1151, doi: 10.1126/science.1183627.

Sprintall, J., Wijffels, S., Gordon, A. L., Ffield, A., Molcard, R., Susanto, R. D., Soesilo, I., Sopaheluwakan, J., Surachman, Y., and Aken, H. M. (2004), INSTANT: A new international array to measure the Indonesian Throughflow, Eos, Transactions American Geophysical Union, 85(39), 369-376, doi: 10.1029/2004EO390002.

Sprintall, J., Wijffels, S. E., Molcard, R., and Jaya, I. (2009). Direct estimates of the Indonesian Throughflow entering the Indian Ocean: 2004–2006. Journal of Geophysical Research: Oceans (1978–2012), 114(C7), doi: 10.1029/2008JC005257.

Sprintall, J., Gordon, A. L., Koch-Larrouy, A., Lee, T., Potemra, J. T., Pujiana, K., and Wijffels, S. E. (2014), The Indonesian seas and their role in the coupled ocean-climate system, Nature Geoscience, doi: 10.1038/ngeo2188.

Stott, L. D., Neumann, M., and Hammond, D. (2000), Intermediate water ventilation on the Northeastern Pacific Margin during the Late Pleistocene inferred from benthic foraminiferal $\delta^{13}C$, Paleoceanography, 15(2), 161-169, doi: 10.1029/1999PA000375.

Tachikawa, K., Timmermann, A., Vidal, L., Sonzogni, C., and Timm, O. E. (2014). CO_2 radiative forcing and Intertropical Convergence Zone influences on western Pacific warm pool climate over the past 400ka. Quaternary Science Reviews, 86, 24-34, doi: 10.1016/j.quascirev.2013.12.018.

Talley, L. D. (1993), Distribution and formation of North Pacific intermediate water, Journal of Physical Oceanography, 23(3), 517-537, doi: 10.1175/1520-0485(1993)023<0517:DAFONP>2.0.CO;2.

Talley, L. D. (1999), Some aspects of ocean heat transport by the shallow, intermediate and deep overturning circulations. Mechanisms of global climate change at millennial time scales, 1-22

Talley, L. D. (2003). Shallow, intermediate, and deep overturning components of the global heat budget. Journal of Physical Oceanography, 33(3), 530-560.

Talley, L. D., and Sprintall, J. (2005), Deep expression of the Indonesian Throughflow: Indonesian intermediate water in the South Equatorial Current, Journal of Geophysical Research: Oceans (1978–2012), 110(C10)., doi: 10.1029/GM112p0001.

Talley, L. D. (2013), Closure of the global overturning circulation through the Indian, Pacific, and Southern Oceans: Schematics and transports, *Oceanography* 26(1), 80–97, doi: 10.5670/oceanog.2013.07.

Talley, L. D. (2013b), Hydrographic Atlas of the World Ocean Circulation Experiment (WOCE). Volume 4: Indian Ocean. International WOCE Project Office, Southampton, UK.

Toggweiler, J. R., Russell, J. L., and Carson, S. R. (2006), Midlatitude westerlies, atmospheric CO2, and climate change during the ice ages, Paleoceanography, 21(2), doi: 10.1029/2005PA001154.

van Aken, H. M., Brodjonegoro, I. S., and Jaya, I. (2009), The deep-water motion through the Lifamatola Passage and its contribution to the Indonesian throughflow, Deep Sea Research Part I: Oceanographic Research Papers, 56(8), 1203-1216, doi: 10.1016/j.dsr.2009.02.001.

Waelbroeck, C., Levi, C., Duplessy, J. C., Labeyrie, L., Michel, E., Cortijo, E., Bassinot, F., and Guichard, F. (2006), Distant origin of circulation changes in the Indian Ocean during the last deglaciation, Earth and Planetary Science Letters, 243(1), 244-251, doi: 10.1016/j.epsl.2005.12.031.

Warren, B. A. (1983), Why is no deep water formed in the North Pacific?, Journal of Marine Research, 41(2), 327-347.

Xu, J., Kuhnt, W., Holbourn, A., Regenberg, M., and Andersen, N. (2010). Indo-Pacific Warm Pool variability during the Holocene and Last Glacial Maximum. Paleoceanography, 25(4), doi: 10.1144/SP355.14.

Wijffels, S. E. (1993). Exchanges between hemispheres and gyres: A direct approach to the mean circulation of the equatorial Pacific, Doctoral Thesis, Massachusetts Institute of Technology/Woods Hole Oceanographic Institution Joint Program.

You, Y., Suginohara, N., Fukasawa, M., Yasuda, I., Kaneko, I., Yoritaka, H., and Kawamiya, M. (2000), Roles of the Okhotsk Sea and Gulf of Alaska in forming the North Pacific Intermediate Water, Journal of Geophysical Research: Oceans (1978–2012), 105(C2), 3253-3280, doi: 10.1029/1999JC900304.

You, Y. (2003), The pathway and circulation of North Pacific Intermediate Water.,Geophysical research letters, 30(24), doi: 10.1029/2003GL018561.

Yuan, X., and Talley, L. D. (1992), Shallow salinity minima in the North Pacific, Journal of physical oceanography, 22(11), 1302-1316, doi: 10.1175/1520-0485(1992)022<1302:SSMITN>2.0.CO;2.

Yu, J., Broecker, W. S., Elderfield, H., Jin, Z., McManus, J., and Zhang, F. (2010), Loss of carbon from the deep sea since the Last Glacial Maximum, Science, 330(6007), 1084-1087, doi: 10.1126/science.1193221.

Yu, J., Anderson, R. F., Jin, Z., Rae, J. W., Opdyke, B. N., and Eggins, S. M. (2013), Responses of the deep ocean carbonate system to carbon reorganization during the Last Glacial–interglacial cycle, Quaternary Science Reviews, 76, 39-52, doi: 10.1016/j.quascirev.2013.06.020.

Zahn, R., Winn, K., and Sarnthein, M. (1986). Benthic foraminiferal δ13C and accumulation rates of organic carbon: Uvigerina peregrina group and Cibicidoides wuellerstorfi. Paleoceanography, 1(1), 27-42, doi: 10.1029/PA001i001p00027.

Zenk, W., Siedler, G., Ishida, A., Holfort, J., Kashino, Y., Kuroda, Y., Miyama, T., and Müller, T. J. (2005), Pathways and variability of the Antarctic Intermediate Water in the western equatorial Pacific Ocean, Progress in Oceanography, 67(1), 245-281, doi: 10.1016/j.pocean.2005.05.003.

4.10 Supplementary Information

Supplementary Table 4.1 - Summary of AMS ^{14}C dates used to construct new (Cores SO217-18522, SO217-18526, SO217-18540) and update existing (MD06-3067) age models for this study. All other age models are presented on their original, published timescales (see Table 4.1 of main text for references). Conventional ages were converted to calendar ages using the radiocarbon calibration program Calib 7.0 and the MARINE13 calibration curve (*Reimer et al.*, 2013), including a marine reservoir correction of 400 years.

Core	Depth in core (cm)	Conventional ^{14}C age (yrs)	Error (± yrs)	Calendar Age BP (yrs)	Error (± yrs)
SO217-18522	100	3270	30	3010	60
SO217-18522	203	8445	45	8970	70
SO217-18522	327	12360	70	13770	100
SO217-18522	416	15180	90	17910	120
SO217-18522	516	18050	110	21250	180
SO217-18522	616	19830	140	23320	200
SO217-18526	97	1680	25	1200	50
SO217-18526	596	9440	50	10230	40
SO217-18526	656	11270	60	12720	60
SO217-18526	696	12980	70	14700	240
SO217-18526	716	13370	70	15410	130
SO217-18526	1016	25470	250	29070	270
SO217-18540	200	8420	45	8940	70
SO217-18540	300	13810	80	16050	130
SO217-18540	400	19550	150	22980	320
SO217-18540	500	25650	280	29360	670
MD06-3067[a]	11	3655	30	3560	50
MD06-3067[a]	60	4655	30	4870	40
MD06-3067[a]	110	7870	40	8340	40
MD06-3067[a]	160	10100	45	11110	60
MD06-3067[b]	182	12070	65	13520	110
MD06-3067[a]	210	13725	60	16020	110
MD06-3067[b, c]	230	16600	90	19600	130
MD06-3067[b]	253	16650	90	19620	130
MD06-3067[a]	260	16970	90	19980	130
MD06-3067[a]	280	19110	100	22570	130
MD06-3067[a]	370	25410	190	29050	230
MD06-3067[a]	420	29690	300	33460	310

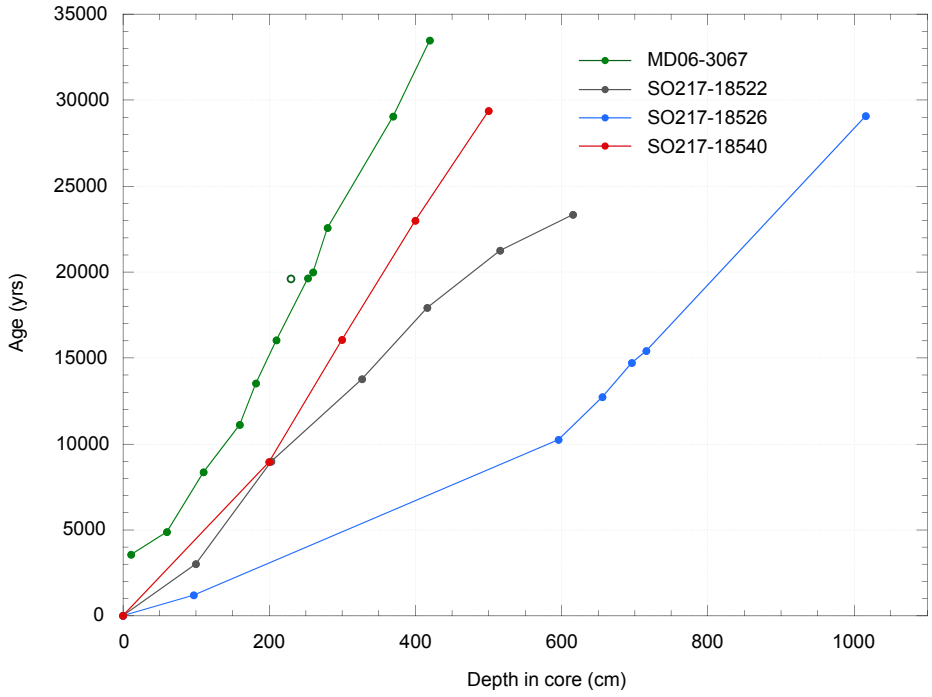

Supplementary Figure 4.1 – Age-depth relationship for new records presented in this study, including MD06-3067 (green), SO217-18522 (black), SO217-18526 (blue), SO217-18540 (red). Open circle represents ^{14}C age that was not used in the generation of the final age model for core MD06-3067.

Chapter 5

Geochemical proxies of sea surface temperature in the tropical West Pacific: Insights from modern core-tops

Nicholas Fraser, Elena Lo Giudice Cappelli, Marcus Regenberg, Wolfgang Kuhnt, Ann Holbourn, Thomas Blanz.

5.1 Abstract

Precise quantification of past changes in sea surface temperature (SST) in tropical regions is hampered by uncertainties in the relationship between SST and geochemical proxy records. In this study, we compile new and previously published core-top measurements of two commonly used proxies of SST, the Mg/Ca ratio of the planktonic foraminifera *G. ruber* (n = 146), and the $U^{K'}_{37}$ alkenone unsaturation index (n = 107), from the South China Sea, Makassar Strait, Java Sea, Timor Sea and eastern Indian Ocean. Measurements were compared with modern satellite-derived temperature and productivity data to gain insights into their modern relationships with SST, with a particular focus on seasonal bias recorded by the two proxies. $U^{K'}_{37}$ measurements show an expected positive correlation with mean annual sea surface temperatures (maSST) ($U^{K'}_{37}$ = 0.322 + 0.022maSST, r^2 = 0.55), but a lower sensitivity to temperature than has been documented in global core-cop calibrations, consistent with a 'flattening' of the $U^{K'}_{37}$-SST relationship at temperatures exceeding 24 °C. Raw Mg/Ca measurements show a higher sensitivity to maSST ($Mg/Ca = 0.111e^{0.131T}$, r^2 = 0.54) than previous calibrations would suggest, although the sensitivity is reduced when samples are corrected for variable inter-laboratory cleaning procedures ($Mg/Ca_{cor} = 0.335e^{0.091T}$, r^2 = 0.45), highlighting the uncertainties associated with analytical procedures of Mg/Ca-based SST reconstructions. Regressions of both Mg/Ca and $U^{K'}_{37}$ measurements with monthly satellite-derived SSTs document stronger correlations of both proxies with winter and spring SSTs, although correlations are not statistically stronger than with maSST. Analysis of residual SST patterns show that $U^{K'}_{37}$ SST estimates over-estimate maSST in regions of strong seasonal temperature variability, such as in the Java upwelling region and Timor Sea. Mg/Ca residual SST patterns show a less clear seasonal pattern, and are likely influenced significantly by secondary effects, including carbonate ion saturation states and salinity. Mg/Ca SST estimates from the South China Sea in particular tend to under-estimate SST, in response to calcite undersaturation in this region.

5.2 Introduction

Paleoclimate records of sea surface temperature (SST) are commonly reconstructed from the use of the coccolithophore-based alkenone unsaturation index, $U^{K'}_{37}$, or the Mg/Ca ratio of the surface-dwelling planktonic foraminifera *Globigerinoides ruber*. However, the use of these proxies relies on the understanding of a number of processes which may bias reconstructed SST records towards warmer or cooler temperatures, including (but not limited to): (1) The preferential growth of foraminifera or coccolithophores in a particular season/period of the year. (2) Variability in depth habitats of foraminifera or coccolithophores. (3) Mixing of proxy signals via lateral advection of particles or bioturbation of deposited sediment. (4) Diagenetic alteration of signals during post-depositional processes (e.g. carbonate dissolution). (5) Biological inclusion of $U^{K'}_{37}$ and Mg/Ca signals into coccolithophores and foraminifera, including species-specific (and inter-species) variability. Thus, attributing a proxy measurement to a specific temperature signal requires careful consideration of these effects, including potential spatial and temporal variability.

The $U^{K'}_{37}$ paleothermometer is an organic biomarker proxy, based upon the proportions of the di- and tri-unsaturated C_{37} methyl alkenones produced in the surface ocean by coccolithophores, principally *Emiliania huxleyi* and *Gephyrocapsa oceanica* (Brassell et al., 1986), where the $C_{37:2}$ alkenone is favourably produced at high temperatures. Modern calibrations of $U^{K'}_{37}$ to SST have been made through comparison of coretop and sediment trap measurements with modern surface-water properties derived from climatological atlases (e.g. Sonzogni et al., 1997a, b; Pelejero and Grimalt, 1997; Müller et al., 1998; Conte et al., 2006), and through laboratory culture experiments (e.g. Prahl and Wakeham, 1987; Prahl et al., 1988). In recent paleoclimate studies, the most widely applied $U^{K'}_{37}$ calibrations are the global linear coretop calibration of Müller et al. (1998), and the polynomial calibration of Conte et al. (2006) which attempts to account for the potential 'flattening' of the $U^{K'}_{37}$-T relationship at warm (>24 °C) and cool (<10 °C) temperatures. At the warm end of the calibration spectrum (24 - 30 °C), both of these core-top calibrations are indistinguishable, within error ranges, from the culture-derived regressions of Prahl et al. (1988).

These existing $U^{K'}_{37}$ core-top calibrations are typically made through direct correlation between measured $U^{K'}_{37}$ values and mean annual SST (maSST) at various water depths, and exhibit a decrease in correlation coefficients below 50 m water depth, suggesting that alkenone-producers are limited to the photic zone (Müller et al., 1998; Pelejero and Grimalt, 1997; Kienast et al., 2012). Other calibrations have attempted to weight the observed temperature signal to a seasonal preference through the preferential weighting of SST towards months of higher productivity, which is assumed to correlate to the months of dominant alkenone-producing coccolithophore blooms (e.g. Sonzogni et al., 1997b). However, more recent studies in regions of highly variable productivity regimes along the West Coast of North and South America observe that SSTs recorded in coretop-$U^{K'}_{37}$ samples are biased towards the months of weak upwelling and low nutrient availability (Prahl et al., 2010; Kienast et al., 2012). Thus, a seasonal weighting of SST towards months of high productivity may not be suitable for calibration purposes. Furthermore, a recent global compilation of alkenone fluxes in sediment traps reveals no statistical difference in the $U^{K'}_{37}$ calibration slope when using flux-weighted SSTs versus maSSTs (Rosell-Melé and Prahl, 2013).

The basis for the use of Mg/Ca ratios as a paleotemperature proxy relies upon the thermo-dynamically favourable substitution of Mg^{2+} for Ca^{2+} in the calcium carbonate shells of planktonic foraminifera at higher temperatures. As with the $U^{K'}_{37}$ index, a range of modern calibrations have been made via measurements of foraminifera from core-tops, sediment traps and culture experiments, which provide a range of sensitivities of foraminiferal Mg/Ca to temperature (Nürnberg et al., 1996; Lea et al., 1999; Lea et al., 2000; Dekens et al., 2002; Anand et al., 2003; Regenberg et al., 2009). The exact mechanisms responsible for differences in Mg/Ca calibrations is still controversial, but recent studies have proposed that alteration of foraminiferal Mg/Ca can occur through the variable effects of salinity (Hönisch et al., 2013), pH (Kisakürek et al., 2008) and postdepositional dissolution driven by ($[CO_3^{2-}]$) concentrations (Regenberg et al., 2006, 2014). A potential advantage of the Mg/Ca paleothermometer is that measurements can be paired with oxygen isotope ($\delta^{18}O$) measurements on the same foraminiferal samples, which may give further insights into the regional habitat depths and seasonality of individual species (e.g. Regenberg et al., 2006; Steph et al., 2009; Mohtadi et al., 2011).

However, differing $\delta^{18}O$-temperature and $\delta^{18}O$-salinity relationships used in deriving expected equilibrium calcite $\delta^{18}O$ values can induce considerable uncertainty into these methods, which are further compounded by low-quality salinity and seawater $\delta^{18}O$ ($\delta^{18}O_{sw}$) data in some regions. Such a problem is particularly prevalent in the tropical West Pacific. Consequently, the most reliable method of determining the seasonal patterns of foraminiferal growth in this region remains through the use of sediment traps (e.g. Wiesner et al., 1996; Kawahata et al., 2002; Mohtadi et al., 2009), though these are also only sparsely distributed.

The importance of understanding different seasonal signals recorded in proxies has been underlined by several studies comparing $U^{K'}_{37}$ and Mg/Ca-derived SST trends over the last deglacial period and Holocene (e.g. Mix et al., 2006; Steinke et al., 2008; Saher et al., 2009; Schneider et al., 2010; Wang et al., 2013; Laepple et al., 2013; Timmermann et al., 2014). In the tropical West Pacific, both $U^{K'}_{37}$ and Mg/Ca reconstructions show reasonable agreement on the magnitude of deglacial warming between 2 and 4 ° C (e.g. Pelejero et al., 1999; Kienast et al., 2001; Stott et al., 2002, 2007; Rosenthal et al., 2003; Visser et al., 2003; Steinke et al., 2008; Fraser et al., in review), with lower sensitivity (1 - 1.5 °C) recorded in one $U^{K'}_{37}$ record located close to Papua New Guinea (De Garidel-Thoron et al., 2007). However, more significant differences in the timing and evolution of deglacial SST change have been noted between the two proxies. SST records derived from Mg/Ca typically begin to rise in concert with southern hemisphere warming between 17 and 18 ka, with a relatively uninterrupted trend to a peak warmth at ~8 ka, and a cooling trend (by 0.5 to 1 °C) through the Holocene. In contrast, $U^{K'}_{37}$ SST records suggest the onset of warming occurred later, between 15 and 16 ka, and are interrupted by a SST plateau or slight cooling during the Bølling-Allerød (BA) and Younger Dryas (YD) periods. From the end of the YD, $U^{K'}_{37}$ records document a relatively steadily increasing SST trend through the Holocene, in contrast to Mg/Ca records. A recent proxy-model comparison of East and West Pacific deglacial SST trends finds support for the effect of different seasonal sensitivities, and past changes in the strength of the seasonal cycle, in driving these proxy mismatches (Timmermann et al., 2014). Increasing our understanding of the modern day production of coccolithophores and foraminifera,

and the potential temperature bias this may induce, is therefore an important step in assessing how these relationships may have changed in the past.

In this study, we attempt to provide insights into factors affecting the $U^{K'}_{37}$ index and Mg/Ca ratios of *G. ruber* in the tropical West Pacific. In the first part of our following discussion, we take a first-order approach to reconstructing seasonality of proxy recorders, by comparing measured $U^{K'}_{37}$ and Mg/Ca values to satellite-derived SST and net primary productivity (NPP) climatologies. In the second part of our discussion, we investigate additional factors that may affect proxy records of SST in this region. Lastly, we discuss the potential impacts these results have on existing paleotemperature records from the West Pacific, and make recommendations for future investigations.

5.3 Study area and modern climatology

This study focuses on coretop measurements from the South China Sea (Pelejero and Grimalt, 1997; Regenberg et al., 2014), the Eastern Indian Ocean including the west coast of Sumatra and south coast of Java (Mohtadi et al., 2011), and the Makassar, Java and Timor Seas (new measurements of this study). Seasonality of SSTs in this region is broadly characterised by the latitudinally varying insolation cycle, i.e. samples in the northern hemisphere are characterised by warmer SSTs during boreal summer, and vice versa in the southern hemisphere (Figure 5.1). More central regions that lie within a few degrees of the equator (e.g. the Makassar Strait, and western Sumatra in this study) generally show a weaker seasonal SST cycle than those at higher latitudes (< 5 °N). These seasonal SST patterns drive associated wind and precipitation changes, which also have an influence on NPP (Figure 5.1). Whilst the West Pacific is generally characterised by oligotrophic conditions, in some areas such as southern Java, the eastern Timor Sea and the northern South China Sea, seasonal wind directions induce upwelling resulting in a stronger seasonal cycle of SST and NPP.

Attempts to quantify the modern seasonal export fluxes of coccolithophores and foraminifera in the West Pacific have been made through a handful of sediment trap studies. In the northern South China Sea, coccolithophores show the highest flux rates during the boreal winter and spring, where assemblages are dominated by the alkenone-

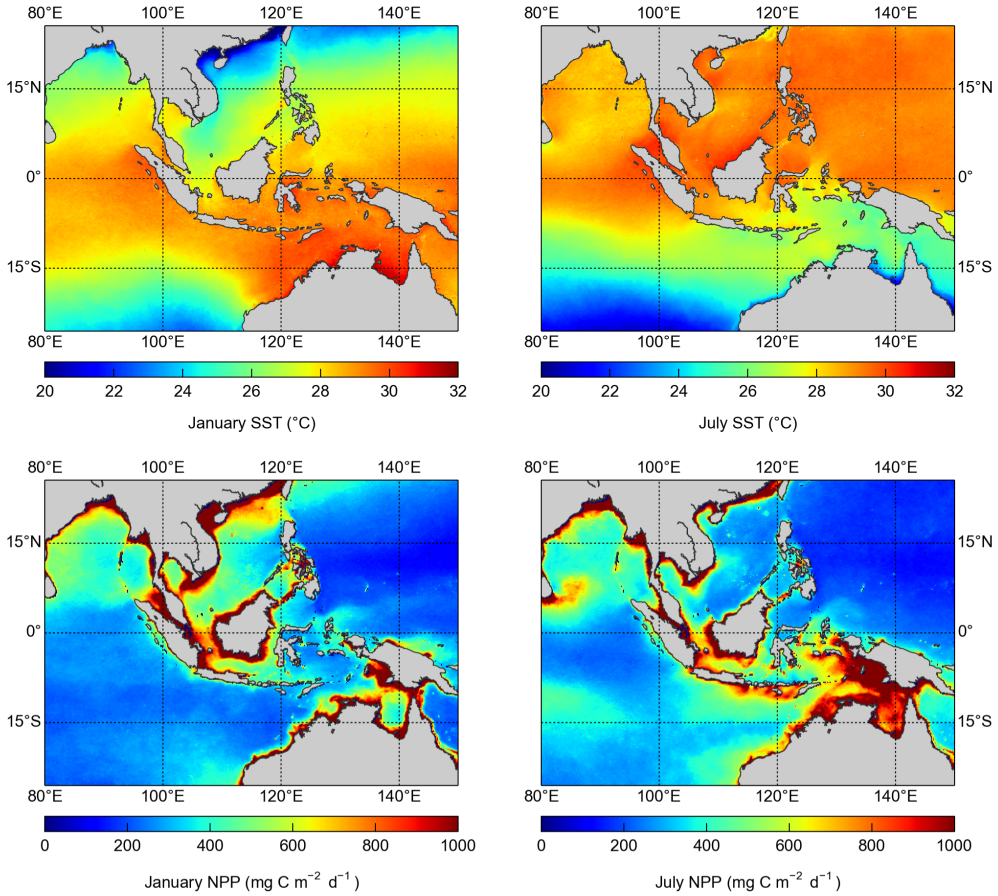

Figure 5.1 - (top) SST derived from the Advanced Very High Resolution Radiometer (AVHRR) satellite climatology (Reynolds et al., 2007) during January (left) and July (right). (bottom) NPP calculated from the Vertically Generalized Production Model (VPGM) using the Sea-viewing Wide Field-of-View Season (SeaWiFS) chlorophyll product (Behrenfeld et al., 2006) during January (left) and July (right).

producing species *E. huxleyi* and *G. oceanica* (Wiesner et al., 1996; Chen et al., 2007), whilst the central South China Sea is characterised by maximum coccolithophore fluxes in late boreal spring and summer (Wiesner et al., 1996). Maximum fluxes of *G. ruber* in the South China Sea occurred at similar times as coccolithophore maxima, with maximum fluxes in the north during boreal winter, and in the central basin during late boreal summer (Wiesner et al., 1996). Sediment traps in the West Caroline Basin, to the north of New Guinea in the open West Pacific, show maximum coccolithophore fluxes during the boreal fall and winter, though the seasonal variability is markedly weaker than in the South China Sea (Tanaka and Kawahata, 2001). However, anti-phased signals of *E.*

huxleyi, which shows maximum abundances in boreal winter, and *G. oceanica*, which shows maximum abundances in boreal summer, mean that the seasonal export pattern of alkenones is unclear. At the same location in the West Caroline Basin, the largest fluxes of *G. ruber* are observed between August and October (Kawahata et al., 2002). A similar pattern of *G. ruber* fluxes is also noted in the Java upwelling zone, with peak abundances occurring between July and November during the main upwelling season (Mohtadi et al., 2011), which may indicate a cold-bias in SST recorded by *G. ruber* in this region.

5.4 Data and Methods

5.4.1 Materials and sampling strategy

New $U^{K'}_{37}$ and Mg/Ca measurements in this study were made on multi-cores and piston cores gathered on two cruises - the Sonne-185 'VITAL' cruise in the Timor Sea which took place in September and October 2005 (Kuhnt et al., 2005), and the Sonne-217 'MAJA' cruise in the Makassar Strait and Java Sea which took place in July and August 2011 (Kuhnt et al., 2011) (Figure 5.2). Mg/Ca measurements were made on core-top (0-1 cm) samples from multi-cores retrieved at a range of depths between ~300 m and ~2500 m. Due to the procedure of storing multi-core samples in rose bengal and ethanol solution, these core-tops were unsuitable for $U^{K'}_{37}$ analyses, which were instead made on core-tops (0-1 cm) from piston cores.

5.4.2 Age control

Age control of existing core-top datasets compiled here are documented fully in their respective publications. Samples from the Eastern Indian Ocean are assumed to be predominantly of a modern age, on the basis of the presence of an intact organic fluff layer on most multicore samples (Mohtadi et al., 2011). Those samples that did not have such a layer were submitted for AMS ^{14}C dating, which recorded modern calendar ages (>1950 AD) in all but four samples, the oldest of which recorded an age of ~830 BP. These older ages are attributed to lower sedimentation rates on the outer slope, and stronger bioturbation on the shelf. Core-top samples from the South China Sea are assumed to be of a late Holocene age, on the basis of high sedimentation rates (>5

cm/kyr) and the presence of stained benthic foraminifera (Pelejero and Grimalt, 1997; Regenberg et al., 2010, 2014).

New core-top samples derived from multi-cores in the Timor Sea, Makassar Strait and Java Sea are assumed to represent modern to late Holocene ages, based upon the presence of stained benthic foraminifera and an organic fluff layer on a number of samples (Kuhnt et al., 2011). Samples derived from piston cores could potentially sample a different time period than multi-core samples, due to disturbance of the upper sediment layer caused by the piston coring system. However, several published and unpublished downcore records based upon these samples document high sedimentation rates (>10 cm/kyr) (e.g Xu et al., 2010; Holbourn et al., 2011, and references therein) and thus we expect that core-top samples from piston cores document late-Holocene sediments nonetheless.

5.4.3 Mg/Ca

A total of 146 core-top Mg/Ca measurements on the planktonic foraminifera *G. ruber* were compiled, from previous core-top studies in the South China Sea (Regenberg et al., 2014, n = 22), the eastern Indian Ocean (Mohtadi et al., 2011, n = 61) and from new measurements made in the Makassar Strait, Java Sea and Timor Sea (n = 63) (Figure 5.2). Analytical methods of previous studies are documented in their respective publications. For new measurements made here, approximately 30 tests of the planktonic foraminifera *G. ruber* were picked from core-top (0-1 cm) samples, crushed into fragments under a microscope and checked for potential contaminants. Samples were subsequently cleaned following the established protocol of Martin and Lea (2002), including the reductive cleaning step. Samples were analyzed with the ICP-OES (Inductively Coupled Plasma-Optical Emission Spectrometer) (Spectro Ciros SOP) with cooled cyclonic spraychamber and microconcentric nebulization (200 µl min^{-1}) at the Institute of Geosciences, University of Kiel. Intensity ratio calibration followed the method of de Villiers et al. (2002) and internal analytical precision was 0.1 - 0.2 %. 24 duplicate measurements give a mean reproducibility of ±0.15 mmol/mol (± ~0.3 °C).

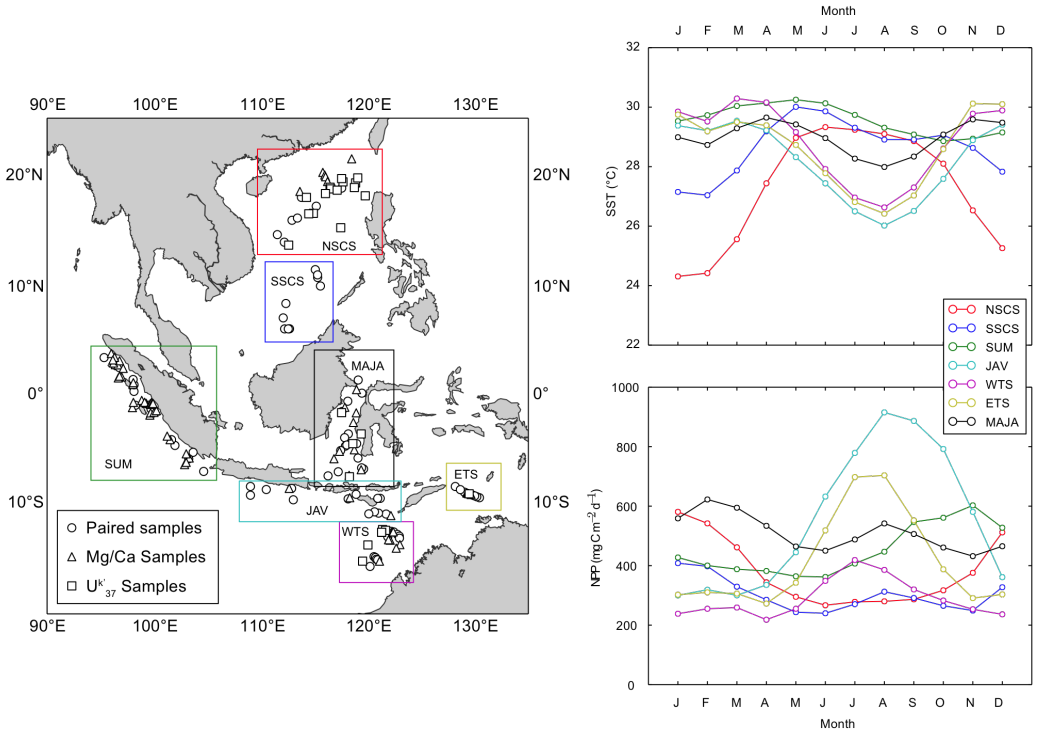

Figure 5.2 - (left) Distribution of Mg/Ca and $U^{K'}_{37}$ measurements compiled from new and existing datasets in this study. Circles represent 'paired' samples where $U^{K'}_{37}$ and Mg/Ca measurements are made at the same location, whilst triangles and squares represent locations where only Mg/Ca or $U^{K'}_{37}$ measurements are made, respectively. Colored boxes represent regions with similar hydrographic properties, abbreviated by: SUM = Coastal Sumatra, JAV = Java Upwelling Zone, WTS = Western Timor Sea, ETS = Eastern Timor Sea, MAJA = Makassar Strait and Java Sea, SSCS = Southern South China Sea, NSCS = Northern South China Sea. (right) Satellite derived monthly SST (top) and NPP (bottom) climatologies for different regions defined on map.

From the South China Sea, we only included measurements from the 300 - 350 µm size fraction (defined as 'Group III' in Regenberg et al., 2014), whilst in the eastern Indian Ocean measurements were from the 250 - 355 µm size fraction (Mohtadi et al., 2011). For new measurements made in this study, we picked and analysed *G. ruber* from the 250 - 315 µm size fraction. Mg/Ca ratios in *G. ruber* have been suggested to show systematic increases with increasing shell size, as a result of changing habitats during their lifecycle. However, Elderfield et al. (2002) show that Mg/Ca differences between the 250 - 300 µm and 300 - 350 µm size fraction are on the order of ~0.1 mmol/mol (equivalent to a change of ~0.2 °C), whilst other studies have found no significant increases in the

Mg/Ca sensitivity of *G. ruber* with increasing size (Ni et al., 2007; Xu et al., 2010). This likely results from the small amount of Mg/Ca-rich gametogenic calcite added to *G. ruber* tests, in comparison to other planktonic species that add a larger gametogenic crust and show a more pronounced increase in Mg/Ca with increasing test size (e.g. *Globigerinoides sacculifer*, Ni et al., 2007). Thus, for the purposes of this study we assume that the minor differences in size fractions have no bearing on measured Mg/Ca values.

More pronounced variability in Mg/Ca can result from different analytical methods, particularly with regard to the method of Mg/Ca cleaning used. Rosenthal et al. (2004) showed that cleaning samples using the 'reductive step' resulted in a 15% loss of Mg (equivalent to ~1.6 °C cooler temperatures) compared to those cleaned without the reductive step. In core-tops compiled in this study, Mg/Ca measurements from the South China Sea, Makassar Strait, Java Sea and Timor Sea were made on reductively cleaned samples. In contrast, samples from the eastern Indian Ocean (i.e. those from the study of Mohtadi et al., 2011) were not reductively cleaned. Thus, we shall also investigate the applicability of such a correction to non-reductively cleaned Mg/Ca samples.

5.4.4 $U^{k'}_{37}$

A total of 107 $U^{k'}_{37}$ measurements were compiled from the same regions as Mg/Ca measurements (South China Sea - Pelejero and Grimalt, 1997, n = 31; eastern Indian Ocean - Mohtadi et al., 2001, n= 26; Makassar Strait, Java and Timor Sea - This study, n = 50) (Figure 5.2). Analytical methods for previously measured $U^{k'}_{37}$ samples are documented in their respective publications (Pelejero and Grimalt, 1997; Mohtadi et al., 2011). New $U^{k'}_{37}$ measurements were made on approximately ~1 g of freeze-dried sediments at the University of Kiel, Germany. The full methodology for sample extraction and measurement is documented in Rincón-Martínez et al. (2010). Analytical precision is better than 0.02 $U^{K'}_{37}$ units (~0.6 °C). The $U^{k'}_{37}$ index was calculated using the ratio of di- and tri-unsaturated C_{37} methyl alkenones, with the formula:

$$U_{37}^{K'} = \frac{C_{37:2}}{C_{37:2} + C_{37:3}}$$

5.4.5 Climatological datasets

Climatologies of SST are obtained from the Advanced Very High Resolution Radiometer (AVHRR), which averages SST measurements over the period January 1985 to December 2002 (Reynolds et al., 2007) on a 4096 by 2048 pixel grid (~9 km resolution at the equator). NPP climatologies are derived from a monthly NPP dataset calculated from the Vertically Generalized Production Model (VPGM) using the Sea-viewing Wide Field-of-View Season (SeaWiFS) chlorophyll product (Behrenfeld et al., 2006), and is averaged over the period September 1997 to August 2006 on a 2160 by 1080 pixel grid (~18 km resolution at the equator). This approach differs from other Mg/Ca and $U^{K'}_{37}$ calibration studies, which typically use climatological data derived from the World Ocean Atlas (WOA) (Locarnini et al., 2013). However, the resolution of in-situ SST measurements used to derive WOA climatologies in the West Pacific is poor, and does not resolve shelf and shelf-edge dynamics as well as satellite climatologies (Figure 5.3).

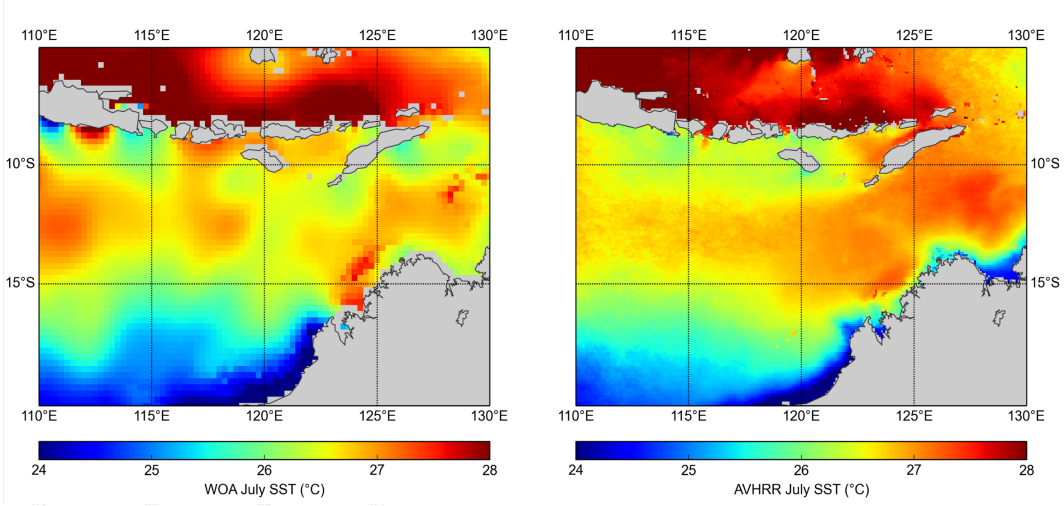

Figure 5.3 - Example of small-scale SST structure captured for a one-month (July) climatology by the World Ocean Atlas (left) (Locarnini et al., 2013) compared AVHRR satellite measurements (right) (Reynolds et al., 2007).

5.5 Results and Discussion

5.5.1 Mg/Ca and $U^{K'}_{37}$ in surface sediments of the West Pacific

New Mg/Ca measurements of *G. ruber* show values ranging from 4.26 to 5.50 mmol/mol (see Supplementary Information). When combined with existing datasets from the South China Sea and eastern Indian Ocean, raw Mg/Ca values show a positive correlation with maSST ($Mg/Ca = 0.111e^{0.131T}$, $r^2 = 0.54$, $p < 0.01$). This temperature sensitivity of ~13% is somewhat higher than has been reported in other Mg/Ca calibration studies, which have sensitivities in the range of 9 to 11 % (Figure 5.4) (Lea et al., 2000; Dekens et al., 2002; Regenberg et al., 2009). However, correcting Mg/Ca values from the eastern Indian Ocean to account for differences in cleaning methodology (following the 15 % reduction in Mg/Ca of Rosenthal et al., 2004) results in a lower temperature sensitivity of ~9 % ($Mg/Ca_{cor} = 0.335e^{0.091T}$, $r^2 = 0.45$, $p < 0.01$) (Figure 5.4).

This sensitivity is almost identical to that reported by Dekens et al. (2002) and Lea et al. (2000), although the two calibrations differ by more than 3 °C in their absolute temperature estimations, whilst our relationship falls between the two. For the remainder of this study, we therefore discuss Mg/Ca in terms of its cleaning-corrected values (Mg/Ca_{cor}), except where it becomes appropriate to discuss the difference between the two datasets. The lowest Mg/Ca_{cor} values are recorded in the South China Sea, with another group of low Mg/Ca_{cor} values observed in the Java upwelling region. In the Makassar Strait, Java Sea, Timor Sea and coastal Sumatra, Mg/Ca values are generally higher but demonstrate significant scatter (upwards of 1 mmol/mol), in excess of the range expected from analytical uncertainty (~0.3 mmol/mol) or intra-region climate variability (typically <1 °C).

New measurements of $U^{K'}_{37}$ range between 0.933 and 0.989 $U^{K'}_{37}$ units (See Supplementary Information). Compiled new and existing $U^{K'}_{37}$ measurements also show a positive correlation with maSST ($U^{K'}_{37} = 0.322 + 0.022$maSST, $r^2 = 0.55$, $p < 0.01$) (Figure 5.5). This relationship has a similar sensitivity to temperature (0.022 units/ °C) as documented in a productivity-weighted calibration from the Indian Ocean (0.023 units/°C - Sonzogni et al., 1997b), and lower sensitivity than documented in

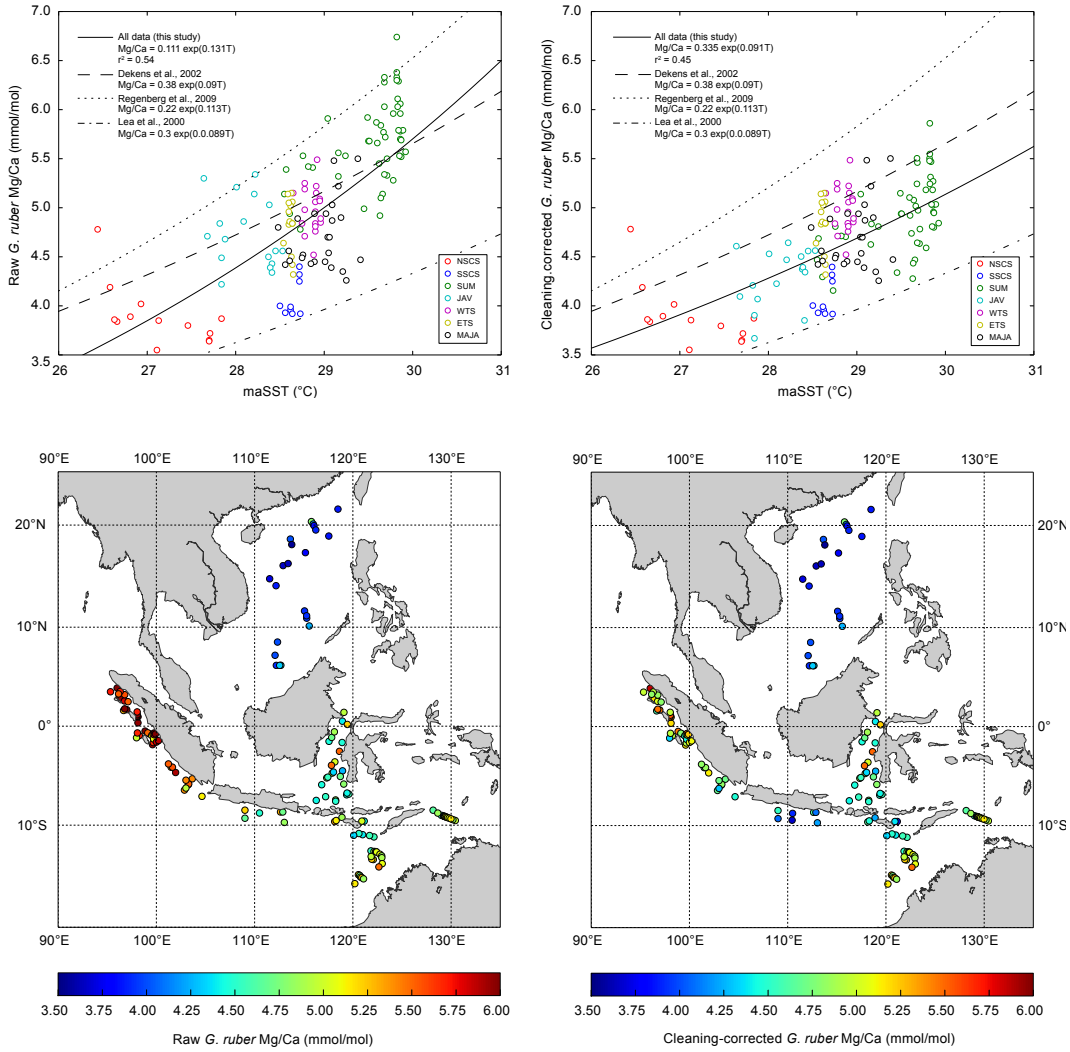

Figure 5.4 - (top) Mg/Ca measurements from compiled datasets versus AVHRR maSST estimates. Raw measurements are shown on the left, and cleaning-corrected measurements on the right. Samples are color-coded based upon regions, following the scheme shown in Figure 5.2. Additional Mg/Ca calibrations are additionally plotted. (bottom) Spatial distribution of raw (left) and cleaning-corrected (right) Mg/Ca measurements.

the two most commonly used global calibrations (Müller et al., 1998; Conte et al., 2006), which both have sensitivities greater than 0.03 units/°C in the warm end of the temperature spectrum. With the exception of several samples from the Java upwelling

region, all samples record lower $U^{K'}_{37}$ values than would be predicted using these global calibrations and maSSTs.

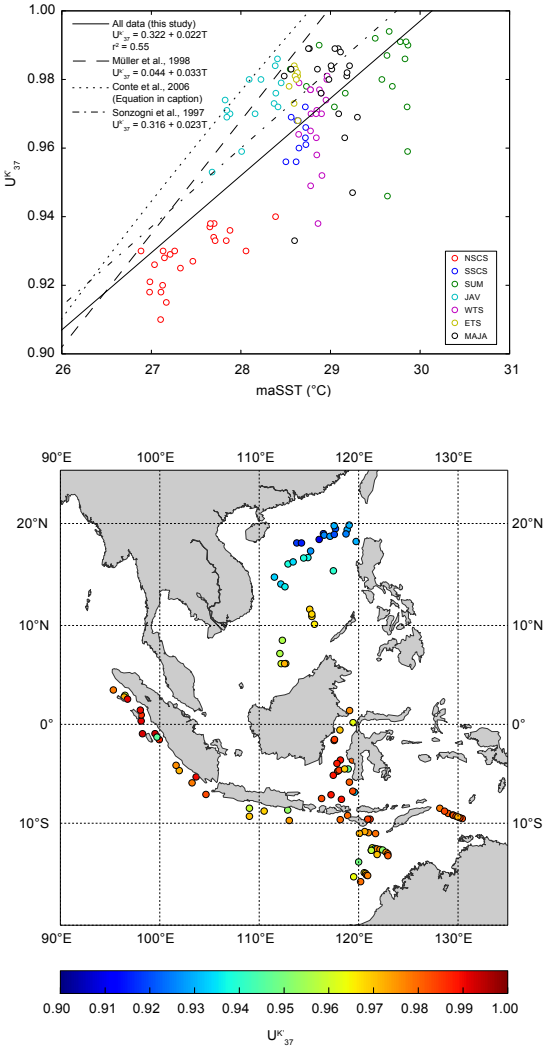

Figure 5.x - (top) $U^{K'}_{37}$ measurements from compiled datasets versus AVHRR maSST estimates. Samples are color-coded based upon regions, following the scheme shown in Figure 5.2. Additional $U^{K'}_{37}$ calibrations are additionally plotted. (bottom) Spatial distribution of $U^{K'}_{37}$ measurements.

Whilst there are some similarities between the overall spatial distribution of $U^{K'}_{37}$ and Mg/Ca_{cor}, for example generally lower values in the South China Sea, and higher values in the Makassar Strait and coastal Sumatra, there are also some distinct differences between the two sets of measurements. In the South China Sea, Mg/Ca_{cor} exhibits a

relatively uniform spatial SST pattern, whilst $U^{K'}_{37}$ shows a zonal gradient from values of ~0.96 $U^{K'}_{37}$ units in the south, to ~0.91 $U^{K'}_{37}$ units in the north, equivalent to a SST gradient of ~2.0 °C. Additionally, $U^{K'}_{37}$ measurements do not show such prominently low values in the Java upwelling region as seen in Mg/Ca_{cor}, where values are as low as those in the South China Sea. The southern Makassar Strait is also characterised by high $U^{K'}_{37}$ values, which are greater than those in the Timor Sea, whilst Mg/Ca_{cor} indicates the opposite trend of relatively low values in the southern Makassar Strait, and slightly higher values in the Timor Sea.

5.5.2 Seasonal relationships of SST proxies

Figure 5.6 shows derived correlation coefficients of $U^{K'}_{37}$ and Mg/Ca_{cor} when regressed against the SST average of each month, as well as against annual SST (maSST), annual minimum SST (minSST), annual maximum SST (maxSST) and a productivity-weighted SST (nppSST), which is defined by the equation (following Sonzogni et al., 1997b):

$$nppSST = \frac{\sum_{i=1}^{12} SST_i \cdot NPP_i}{\sum_{i=1}^{12} SST_i}$$

where SST_i and NPP_i are the temperature and net primary productivity of each month, respectively.

Correlation coefficients >0.75 are found for $U^{K'}_{37}$ between November and April, whilst between May and October correlation coefficients are <0.25. Such a strong seasonal pattern is surprising, since a similar approach based upon core-tops from the eastern equatorial Pacific found correlations >0.79 for all months of the year (Timmermann et al., 2014). However, the correlation between $U^{K'}_{37}$ and maSST (0.74) is not significantly weaker than monthly coefficients found between November and April, and thus the pattern of $U^{K'}_{37}$ could be equally interpreted as a reflection of maSST rather than a monthly or seasonal preference. Despite the division of our samples between the northern and southern hemispheres, and the antiphase-SST relationship observed between the hemispheres, correlation coefficients for $U^{K'}_{37}$ versus minSST or maxSST do

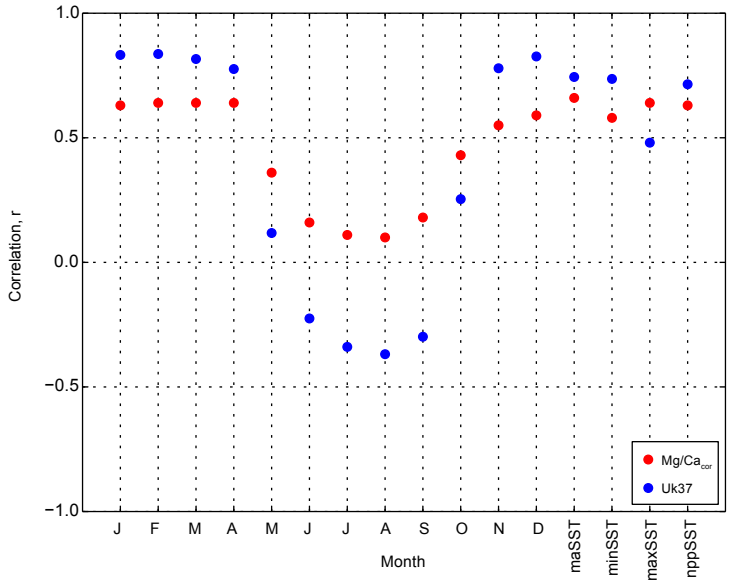

Figure 5.6 - Spatial correlations of $U^{K'}_{37}$ and Mg/Ca_{cor} versus monthly SST, mean annual SST (maSST), annual minimum SST (minSST), annual maximum SST (maxSST) and net primary productivity weighted SST (nppSST).

not exceed coefficients for maSST, which suggests that growth patterns of alkenone producers are not a function of the annual temperature cycle. Productivity weighted SST (nppSST) also shows no improvement in correlation when compared to maSST, indicating that annual growth and export rates of alkenones are not well-represented by a simple linear function of overall surface productivity.

Mg/Ca_{cor} shows a similar correlation pattern to $U^{K'}_{37}$, with the highest correlation coefficients between November and April, and lower coefficients between May and October. However, Mg/Ca_{cor} correlation coefficients show a less pronounced seasonal pattern, with lower values than their $U^{K'}_{37}$ counterparts between November and April (>0.64) and higher between May and October (<0.43), which may indicate a lower sensitivity of Mg/Ca to seasonal temperature variability than $U^{K'}_{37}$. As with $U^{K'}_{37}$, no improvement in correlation coefficients of Mg/Ca are noted with minSST, maxSST or nppSST versus maSST.

5.5.3 Residual patterns of $U^{K'}_{37}$ and Mg/Ca SST

To investigate spatial patterns of SST variability recorded in proxies we calculate the residual temperature at each site, which is the difference between the expected SST from calibration equations, and the satellite-derived maSST estimate (Figure 5.7). For $U^{K'}_{37}$, we calculate residuals using the calibration equation of Müller et al. (1998) ($U^{K'}_{37}$ = 0.044 + 0.033T), which is statistically identical (within our temperature range) to another global calibration of Conte et al. (2006), and the culture-derived regression of Prahl et al. (1988). For Mg/Ca, we use the calibration of Dekens et al. (2002) ($Mg/Ca = 0.38e^{0.09T}$), which has identical temperature sensitivity to the calibration of Lea et al. (2000). We additionally investigated the effect of using different calibration equations for both $U^{K'}_{37}$ and Mg/Ca_{cor} to calculate SST residuals (not shown), and found that although the magnitude of SST residuals varies, the spatial pattern is relatively robust to the calibration chosen. Since we primarily assess the spatial variability of SST residuals, rather than offsets occurring as a result of differing calibrations, we furthermore normalise our residual SST estimates by the respective means and standard deviations of each variable. Positive residuals indicate regions where the estimated SST from proxy measurements overestimates maSST, and vice versa.

Spatial patterns of $U^{K'}_{37}$ SST residuals are characterised by several groups of positive residuals in the Java upwelling region, the southern Makassar Strait, the eastern Timor Sea and a smaller cluster in the northern South China Sea. These regions, with the exception of the Makassar Strait, are characterised by strong seasonal cycles of NPP in antiphase with the seasonal SST cycle (Figure 5.2). Positive residuals are consistent with the growth of alkenone-producing coccolithophores during low-productivity, low-nutrient months, a finding that has been replicated in the eastern Pacific (Prahl et al., 2010; Kienast et al., 2012), meaning that calibrations using productivity-weighted SST are not appropriate for these regions (e.g. Sonzogni et al., 1997b).

The cluster of positive $U^{K'}_{37}$ residuals in the northern South China Sea appear to be at odds with sediment trap studies, which found a strong seasonal cycle of coccolithophore production peaking in boreal spring and winter, when SSTs are at their minimum (Wiesner et al., 1996; Chen et al., 2007). However, water samples from the northernmost

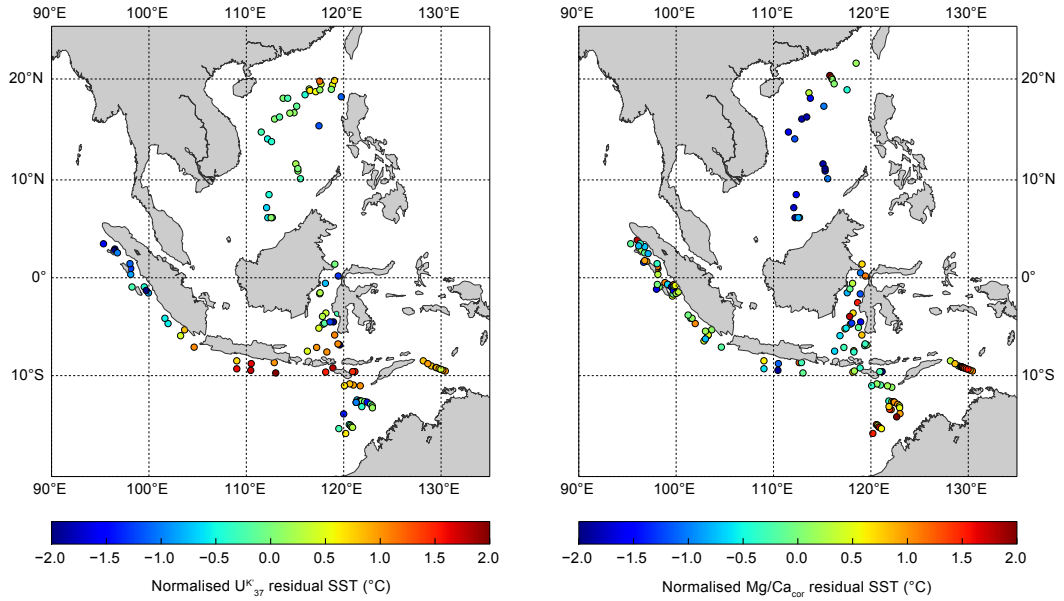

Figure 5.7 - Normalised residual SST for $U^{K'}_{37}$ calculated with the calibration of Müller et al. (1998) (left) and Mg/Ca_{cor} calculated with the calibration of Dekens et al. (2002) (right).

shelf area found larger abundances of *E. huxleyi* and *G. oceanica* during boreal summer and autumn (Chen et al., 2007), suggesting that growth patterns in shelf areas may differ from the more central regions. Rosell-Melé et al. (2013) also documented non-linear relationships between $U^{K'}_{37}$ measurements and alkenone fluxes from a global compilation of sediment trap studies, which suggests that $U^{K'}_{37}$ signals can be attenuated by complex sedimentation processes, especially in regions of high productivity. We therefore propose that the northernmost South China Sea samples were influenced by advection or resuspension of alkenones from the high-productivity shelf environment which may record a different $U^{K'}_{37}$ signal to the more central basin regions.

The small group of positive residuals in the southern Makassar Strait is also not well explained by seasonality of NPP as this region has a relatively weak annual NPP cycle. However, during the boreal winter and spring (when SSTs are at their warmest) westerly winds drive fresh surface waters from the Java Sea into the Makassar Strait, providing well-stratified, low-nutrient waters that are favourable conditions for the growth of alkenone producing coccolithophores (Tyrell and Merico, 2004). In contrast, groups of

negative residuals are found in the western Timor Sea, coastal Sumatra and in the southern South China Sea, where the seasonal cycles of SST and NPP are generally weaker and the temperature signal may therefore be more representative of an annual average.

Mg/Ca_{cor} residual SSTs present a widely different pattern to $U^{K'}_{37}$. The most negative residuals are observed in the South China Sea, where sediment traps suggest that *G. ruber* grows preferentially during late boreal summer and early fall (Wiesner et al., 1996), i.e. during the warmest months of the year, and thus we should expect the inverse residual behaviour to what we observe. This may hint at a secondary control, for example calcite undersaturation, in driving low residual SSTs in this location. It is also surprising to note that residual SSTs in the Java upwelling region are not significantly offset from values from the Makassar Strait or coastal Sumatra, given that sediment traps predict the highest fluxes of *G. ruber* during the peak upwelling season, which should induce cooler SSTs (Mohtadi et al., 2009). However, residual Mg/Ca SSTs in the Sumatra and Java upwelling region are based upon Mg/Ca measurements that have been corrected for different cleaning methodologies. In this study we have used a Mg/Ca correction factor of 15 % for non-reductively cleaned samples, following the recommendation of Rosenthal et al. (2004), though other studies have suggested that a lower Mg/Ca correction may be appropriate (e.g. 6.6% in Xu et al., 2010). Without paired samples of both reductively- and non-reductively-cleaned samples, we are unable to make predictions as to whether the correction factor is at the high or low end of these estimations, and thus our resdiual patterns in these regions cannot be robustly constrained. In any case, Mg/Ca residuals from these regions are imprinted by significantly more scatter than their $U^{K'}_{37}$ counterparts, which is suggestive of secondary mechanisms unrelated to seasonal temperature influences on *G. ruber* Mg/Ca.

5.5.4 Analytical concerns for the $U^{K'}_{37}$ 'warm-end'

An inherent problem of the $U^{K'}_{37}$ paleothermometer at the 'warm end' (>24 °C) of the calibration spectrum, where the $U^{K'}_{37}$ value approaches unity, is that concentrations of $C_{37:3}$ alkenones are eventually reduced towards zero. At these low concentrations, which approach the detection limits of modern analytical methods, minor analytical errors can

result in non-trivial (>2 °C) errors in temperature estimations, typically towards warmer temperatures due to the preferential absorption of the $C_{37:3}$ versus the $C_{37:2}$ alkenone in the chromatographic system (Grimalt et al., 2001; Pelejero and Calvo, 2003). Bentaleb et al. (2002) further suggested, based upon a transect of water samples and in-situ temperature measurements in the West Pacific, that the limit of $U^{K'}_{37}$ lies at 26.4 °C with saturated values occurring above this limit. However, this appears to be a pessimistic estimate given the number of high-temperature modern and paleotemperature records which are able to resolve SST variability exceeding this value (e.g. Pelejero and Grimalt, 1997; Sonzogni et al, 1997a,b, Kienast et al., 2012; de Garidel-Thoron et al., 2007; Wang et al., 2013; Fraser et al., in review).

We make an assessment of this phenomena in our study by comparing alkenone concentrations of new $U^{K'}_{37}$ measurements with residual SSTs, with the expectation that SST residuals are skewed to positive values at low concentrations. In contrast to this expectation, our results document the opposite relationship, with the data skewed towards the most negative residuals at lowest concentrations (Figure 5.8). A map of the distribution of alkenone concentrations in these samples (Figure 5.8) shows that the majority of these low-concentration samples are clustered in the western Timor Sea. It is therefore unclear whether the relationship between alkenone concentrations and residual SSTs is causative or a coincidence of sample distribution, but there is little evidence for a signal biased by limited detection of $C_{37:3}$ alkenones. Further consideration must be given to the wider compiled dataset, where analytical differences between studies may result in different responses to low-concentration samples. At the time of writing no specific alkenone concentration data was available from these studies, although the authors of Pelejero and Grimalt (1997) note that 'total C_{37} abundances range between 200 and 1000 ng/g', which gives concentrations sufficiently above threshold limits for detection (Villanueva and Grimalt, 1996).

For high-temperature paleoclimate reconstructions, the question of whether there exists an upper-limit to the $U^{K'}_{37}$ thermometer remains unanswered (c.f. Pelejero and Calvo, 2003). If we consider the linear calibrations of Müller et al. (1998) ($U^{K'}_{37}$ = 0.044 + 0.033T) or Sonzogni et al. (1997b) ($U^{K'}_{37}$ = 0.316 + 0.023T), then we would assume an upper-limit to $U^{K'}_{37}$ temperatures (i.e. when $U^{K'}_{37}$ = 1) of 29.0 °C or 29.9 °C, respectively.

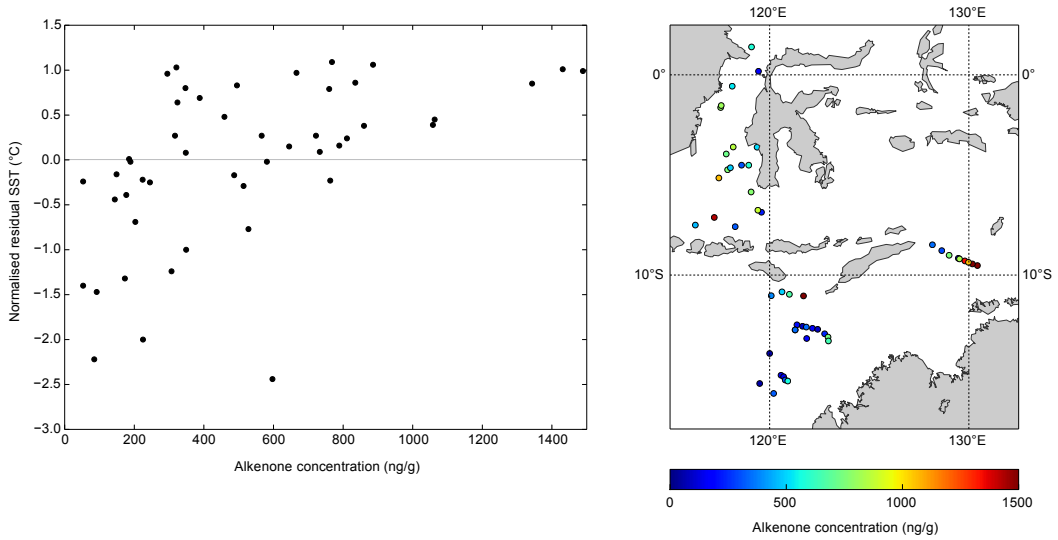

Figure 5.8 - (left) Alknone concentrations (ng/g) versus $U^{K'}_{37}$ normalised SST residuals calculated from the equation of Müller et al. (1998) and AVHRR maSST estimates. (right) Spatial distribution of alkenone concetrations in the Makassar Strait, Java Sea and Timor Sea.

This has clear implications in that regions where SSTs exceed 29.0 °C or 29.9 °C, a $U^{K'}_{37}$ value of 1 will be recorded, and thus a bias to low $U^{K'}_{37}$ values will always be recorded in regions where all, or part, of the seasonal SST cycle exceeds this limit. Other studies have suggested that the $U^{K'}_{37}$ curve approaches an asymptote at high temperatures (e.g. Sikes and Volkman, 1993; Goni et al., 2001), but in the absence of high-precision measurements where $U^{K'}_{37} > 0.95$, the exact shape of such a curve is not clear. For samples compiled here, we observe a lower sensitivity to temperature than suggested by global calibrations, consistent with a flattening of the curve at the warm end of the $U^{K'}_{37}$ spectrum. A logarithmic regression fit yields no significantly better correlation ($r^2 = 0.56$) than a linear fit ($r^2 = 0.55$) meaning that it is unclear whether the relationship trends towards an asymptote or whether there exists a definitive limit where $U^{K'}_{37} = 1$. However, it is interesting to note that no values reach the limit of detection (i.e. $U^{K'}_{37} = 1$) in these datasets despite some regions where annual minimum SSTs are in excess of 29.5 °C.

5.5.5 Secondary influences on foraminiferal Mg/Ca

Carbonate ion ($[CO_3^{2-}]$) effects have been posited as an important control on Mg/Ca recorded in foraminifera, with increasing water depths and reduced calcite-saturation states resulting in a progressive decrease in Mg/Ca (Rosenthal and Lohmann, 2002; Dekens et al., 2002; Regenberg et al., 2006; 2014). This may be important in the West Pacific due to the relatively shallow depth of the calcite-saturation horizon, in particular in the South China Sea. We compared our measured Mg/Ca_{cor} ratios, and residual Mg/Ca_{cor} SSTs, to depth profiles of calcite-saturation states ($\Delta[CO_3^{2-}]$) (Figure 5.9). $\Delta[CO_3^{2-}]$ was calculated by subtracting $[CO_3^{2-}]$ at saturation (based on Jansen et al., 2002) from in situ $[CO_3^{2-}]$. In situ $[CO_3^{2-}]$ was derived in the South China Sea from the SouthEast Asian Time-series Study (SEATS) (Chou et al., 2007), whilst in the Makassar Strait, Timor Sea and eastern Indian Ocean, in situ $[CO_3^{2-}]$ was calculated from closely located World Ocean Circulation Experiment (WOCE) water-column measurements, using with the program co2sys (Lewis and Wallace, 1998).

Mg/Ca_{cor} and $\Delta[CO_3^{2-}]$ show a weak positive correlation ($r^2 = 0.30$), suggesting a limited control of $\Delta[CO_3^{2-}]$ on Mg/Ca in this region (Figure 5.9). Other studies have suggested the existence of a threshold below which Mg/Ca ratios become affected by $\Delta[CO_3^{2-}]$ (e.g. below $\Delta[CO_3^{2-}]$ values of 21.3 ± 6.6 μmol/kg in Regenberg et al., (2014)). Whilst samples below this threshold show on average lower Mg/Ca_{cor} values than those above (Figure 5.9), there is no significantly better correlation ($r^2 = 0.31$) for these limited samples than when considering the entire dataset, thus the effect of the threshold is unclear. The most significant problem with this methodology likely lies in the geographic distribution of samples. The lowest Mg/Ca_{cor} ratios are found in the South China Sea, which is to be expected given the lowest maSSTs in this region. Yet the South China Sea is also the most calcite-undersaturated of all regions in this study, and therefore the low $\Delta[CO_3^{2-}]$ - low Mg/Ca_{cor} relationship observed could purely be an artifact of the data distribution. A more suitable approach is therefore to compare the residual SST estimates with $\Delta[CO_3^{2-}]$, as this eliminates potential bias' resulting from geographic and climatic variability (Figure 5.9). This relationship shows a weaker correlation than using Mg/Ca_{cor} values ($r^2 = 0.16$), although we note that the group of lowest residuals (< -1 °C) in the South China Sea are all found at $\Delta[CO_3^{2-}]$ values of < 21.3 μmol/kg. The dominant

factor of residual SST distribution appears, therefore, to not be controlled to first order by the calcite-saturation state, although it may have a more significant influence on low-$\Delta[CO_3^{2-}]$ (< 21.3 μmol/kg) sites.

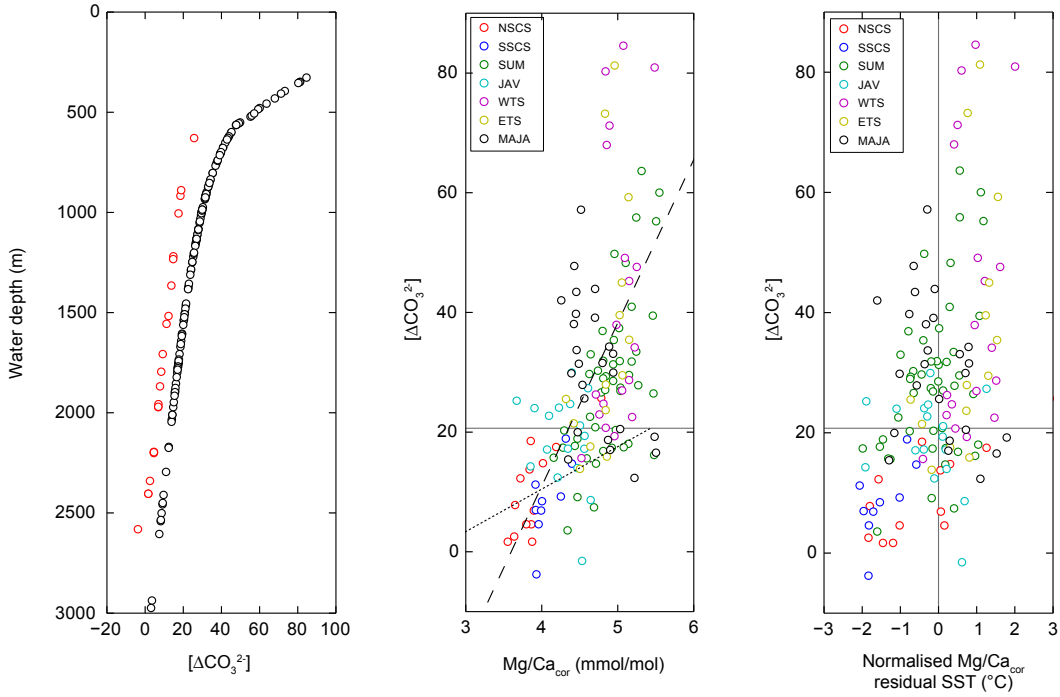

Figure 5.8 - (left) Carbonate ion saturation states ($\Delta[CO_3^{2-}]$) versus water depth for sites with Mg/Ca measurements. Red circles represent sites in the South China Sea, where $\Delta[CO_3^{2-}]$ is derived from SouthEast Asian Time Series (SEATS) stations (Chou et al., 2007), whilst black circles represent sites in the Makassar Strait, Timor Sea and Eastern Indian Ocean where $\Delta[CO_3^{2-}]$ is derived from World Ocean Circulation Experiment (WOCE) stations. (middle) Mg/Ca_{cor} versus $\Delta[CO_3^{2-}]$. Sites are color-coded by region following the scheme from Figure 5.2. Dashed line represents the regression for the entire dataset ($r^2 = 0.30$) whilst the dotted line represents the regression for sites below a critical $\Delta[CO_3^{2-}]$ threshold of 21.3 μmol/kg ($r^2 = 0.31$), following Regenberg et al., (2014) (horizontal grey line). (right) Normalised Mg/Ca_{cor} residual SSTs calculated from the equation of Dekens et al. (2002) versus $\Delta[CO_3^{2-}]$.

In addition to $[CO_3^{2-}]$ effects, salinity variability may also have an effect on the Mg/Ca paleothermometer. Arbuszewski et al. (2010) documented a ~27 % sensitivity of *G. ruber* Mg/Ca per salinity increase unit, based upon a core-top transect from the Atlantic Ocean. However, this estimate was likely affected by carbonate dissolution (Hönisch et al., 2013; Regenberg et al., 2014), and more recent studies have indicated a sensitivity in

the range of 3-4 % per salinity unit (Hönisch et al., 2013). Correcting Mg/Ca variability for salinity provides a challenge in the West Pacific, as the seasonal cycle of temperature, precipitation and winds related to the Asian Monsoon systems drive strong salinity changes throughout the year (which could result in SST uncertainties upwards of 1 °C with a 4 % sensitivity). Thus, corrections for salinity also rely heavily on high-quality climatological data (e.g. satellite or in-situ measurements) and knowledge of ecological preferences of foraminifera, in terms of both their seasonal and depth distributions. Some attempts to quantify the latter have been made based upon paired $\delta^{18}O$ and Mg/Ca measurements in this region (e.g. Mohtadi et al., 2011), by comparisons of measured $\delta^{18}O$ with expected equilibrium $\delta^{18}O$ of calcite. This approach is however hampered by low quality water-column data and uncertainty in $\delta^{18}O$/salinity relationships, which are based upon relatively few $\delta^{18}O$ measurements made on corals and sclerosponges (e.g. Morimoto et al., 2002; Grottoli et al., 2010). In addition, the amplitude of the seasonal cycle of salinity and temperature often outweighs depth-related variability within the mixed layer in the West Pacific, thus the depth and seasonal distributions of *G. ruber* cannot be considered separately. Future studies may therefore incorporate more robust statistical approaches that consider variability of both Mg/Ca and $\delta^{18}O$ in both the depth and time domain.

5.6 Conclusions and Recommendations

Understanding the underlying causes of divergence among different proxy records of SST is important in understanding the past climate response to external forcings. In this study we have shown that spatial patterns of $U^{K'}_{37}$ core-top SST estimates in the West Pacific can be related to seasonal production variability, for example regions with strong cycles of NPP and SST, such as the Java upwelling region, are biased towards temperatures of low-productivity months, consistent with similar relationships documented in the East Pacific (Prahl et al., 2010; Kienast et al., 2012). However, we cannot rule out additional influences such as lateral advection/resuspension of alkenones in driving $U^{K'}_{37}$ changes, and thus records must be carefully considered with this in mind. The choice of $U^{K'}_{37}$ calibration is also an important consideration in high-temperature paleoclimate records, as our results indicate a considerably lower sensitivity of $U^{K'}_{37}$ to

temperature (0.022 $U^{K'}_{37}$ units/°C) above 26 °C than suggested by the most widely applied global calibrations of Müller et al (1998) or Conte et al. (2006) (> 0.03 $U^{K'}_{37}$ units / °C), which could generate differences in the magnitude of deglacial temperature changes in paleoclimate records of more than 1 °C. It is also possible that $U^{K'}_{37}$ based SSTs are underestimated in the highest temperature regions where the $U^{K'}_{37}$ reaches unity for at least part of the year, and thus the magnitude of SST change from the deglacial to present day may also be underestimated in regions where modern temperatures exceed ~29 °C.

Mg/Ca temperature estimates from the West Pacific do not provide such a clear spatial pattern as $U^{K'}_{37}$ estimates, and appear to be biased by secondary factors including the [CO_3^{2-}] effect as demonstrated most strongly in core-top samples from the South China Sea. Combined proxy-model approaches (e.g. Wang et al., 2013; Timmermann et al., 2014) that have attempted to account for past variations in seasonality have shown that differences between the Mg/Ca and $U^{K'}_{37}$ paleothermometers can be well replicated by the different seasonal-weighting of temperature signals. In the context of our results, this is surprising as we find that there are no consistent seasonal differences between the two proxies, with some regions recording $U^{K'}_{37}$ and Mg/Ca signals in-phase with each other, whilst in other regions signals are biased towards opposite seasons. Suggestions of a summer bias in Mg/Ca temperatures, and winter bias in $U^{K'}_{37}$ temperatures in the West Pacific as proposed by Timmermann et al. (2014) is also not borne out by our modern core-top relationships (Figure 5.6). The inclusion of further parameters into proxy-model comparisons, in particular the influence of salinity, into both core-top and paleo-records may therefore yield further insights into these discrepancies.

Throughout this study we note that core-top compilations are prone to large uncertainties due to inter-laboratory methodological and analytical differences. In particular, Mg/Ca measurements are impacted by cleaning procedures, where non-reductively cleaned samples may overestimate temperature by >1.5 °C when compared to reductively cleaned samples. This may lead to considerable errors in calculations of Mg/Ca-SST relationships. Based on this, we recommend that Mg/Ca and $U^{K'}_{37}$ core-top datasets used for calibration should be measured in single laboratories, or include a number of paired samples measured in multiple laboratories to allow some quantification

of inter-laboratory offsets. Furthermore, a consistent analytical procedure should be followed between laboratories for (e.g. using the same size fractions of foraminifera, using the same cleaning techniques) for both modern and paleoclimate temperature reconstructions.

5.7 References

Anand, P., Elderfield, H., and Conte, M. H. (2003). Calibration of Mg/Ca thermometry in planktonic foraminifera from a sediment trap time series. Paleoceanography, 18(2).

Arbuszewski, J., deMenocal, P., Kaplan, A., and Farmer, E. C. (2010). On the fidelity of shell-derived $\delta^{18}O_{seawater}$ estimates. Earth and Planetary Science Letters, 300(3), 185-196.

Behrenfeld, M. J., O'Malley, R. T., Siegel, D. A., McClain, C. R., Sarmiento, J. L., Feldman, G. C., Milligan, A. J., Falkowski, P. G., Letelier, R. M., and Boss, E. S. (2006). Climate-driven trends in contemporary ocean productivity. Nature, 444(7120), 752-755.

Bentaleb, I., Fontugne, M., and Beaufort, L. (2002). Long-chain alkenones and $U^{K'}_{37}$ variability along a south–north transect in the Western Pacific Ocean. Global and Planetary Change, 34(3), 173-183.

Brassell, S. C., Eglinton, G., Marlowe, I. T., Pflaumann, U., and Sarnthein, M. (1986). Molecular stratigraphy: a new tool for climatic assessment. Nature, 320(6058), 129-133.

Chen, Y. L. L., Chen, H. Y., and Chung, C. W. (2007). Seasonal variability of coccolithophore abundance and assemblage in the northern South China Sea. Deep Sea Research Part II: Topical Studies in Oceanography, 54(14), 1617-1633.

Chou, W. C., Sheu, D. D., Lee, B. S., Tseng, C. M., Chen, C. T. A., Wang, S. L., and Wong, G. T. F. (2007). Depth distributions of alkalinity, TCO_2 and $\delta^{13}C_{TCO2}$ at SEATS time-series site in the northern South China Sea. Deep Sea Research Part II: Topical Studies in Oceanography, 54(14), 1469-1485.

Conte, M. H., Sicre, M. A., Rühlemann, C., Weber, J. C., Schulte, S., Schulz-Bull, D., and Blanz, T. (2006). Global temperature calibration of the alkenone unsaturation index (UK′ 37) in surface waters and comparison with surface sediments. Geochemistry, Geophysics, Geosystems, 7(2).

Dekens, P. S., Lea, D. W., Pak, D. K., and Spero, H. J. (2002). Core top calibration of Mg/Ca in tropical foraminifera: Refining paleotemperature estimation. Geochemistry, Geophysics, Geosystems, 3(4), 1-29.

de Garidel-Thoron, T., Rosenthal, Y., Beaufort, L., Bard, E., Sonzogni, C., and Mix, A. C. (2007). A multiproxy assessment of the western equatorial Pacific hydrography during the last 30 kyr. Paleoceanography, 22(3).

de Villiers, S., Greaves, M., and Elderfield, H. (2002). An intensity ratio calibration method for the accurate determination of Mg/Ca and Sr/Ca of marine carbonates by ICP-AES. Geochemistry, Geophysics, Geosystems, 3(1).

Elderfield, H., Vautravers, M., and Cooper, M. (2002). The relationship between shell size and Mg/Ca, Sr/Ca, $\delta^{18}O$, and $\delta^{13}C$ of species of planktonic foraminifera. Geochemistry, Geophysics, Geosystems, 3(8), 1-13.

Fraser, N., Kuhnt, W., Holbourn, A., Bolliet, T., Andersen, N., Blanz, T., Beaufort, L. (in review). Precipitation variability within the West Pacific Warm Pool over the past 120 ka: evidence from the Davao Gulf, southern Philippines. Paleoceanography.

Goñi, M. A., Hartz, D. M., Thunell, R. C., and Tappa, E. (2001). Oceanographic considerations for the application of the alkenone-based paleotemperature $U^{K'}_{37}$ index in the Gulf of California. Geochimica et Cosmochimica Acta, 65(4), 545-557.

Grimalt, J. O., Calvo, E., and Pelejero, C. (2001). Sea surface paleotemperature errors in $U^{K'}_{37}$ estimation due to alkenone measurements near the limit of detection. Paleoceanography, 16(2), 226-232.

Grottoli, A. G., Adkins, J. F., Panero, W. R., Reaman, D. M., and Moots, K. (2010). Growth rates, stable oxygen isotopes ($\delta^{18}O$), and strontium (Sr/Ca) composition in two species of Pacific sclerosponges (Acanthocheatetes wellsi and Astrosclera willeyana) with $\delta^{18}O$ calibration and application to paleoceanography. Journal of Geophysical Research: Oceans (1978–2012), 115(C6).

Hönisch, B., Allen, K. A., Lea, D. W., Spero, H. J., Eggins, S. M., Arbuszewski, J., deMenocal, P., Rosentahl, Y., Russell, A. D., and Elderfield, H. (2013). The influence of salinity on Mg/Ca in planktic foraminifers–Evidence from cultures, core-top sediments and complementary $\delta^{18}O$. Geochimica et Cosmochimica Acta, 121, 196-213.

Jansen, H., Zeebe, R. E., and Wolf-Gladrow, D. A. (2002). Modeling the dissolution of settling CaCO3 in the ocean. Global Biogeochemical Cycles, 16(2), 11-1.

Kawahata, H., Nishimura, A., and Gagan, M. K. (2002). Seasonal change in foraminiferal production in the western equatorial Pacific warm pool: evidence from sediment trap experiments. Deep Sea Research Part II: Topical Studies in Oceanography, 49(13), 2783-2800.

Kienast, M., Steinke, S., Stattegger, K., and Calvert, S. E. (2001). Synchronous tropical South China Sea SST change and Greenland warming during deglaciation. Science, 291(5511), 2132-2134.

Kienast, M., MacIntyre, G., Dubois, N., Higginson, S., Normandeau, C., Chazen, C., and Herbert, T. D. (2012). Alkenone unsaturation in surface sediments from the eastern equatorial Pacific: Implications for SST reconstructions. Paleoceanography, 27(1).

Kisakürek, B., Eisenhauer, A., Böhm, F., Garbe-Schönberg, D., and Erez, J. (2008). Controls on shell Mg/Ca and Sr/Ca in cultured planktonic foraminiferan *Globigerinoides ruber* (white). Earth and Planetary Science Letters, 273(3), 260-269.

Kuhnt, W., et al. (2005). Cruise report SONNE-185: Variability of the Indonesian Throughflow and Australasian climate history of the last 150000 years (VITAL), report, Inst. für Geowiss., Christian-Albrechts-Univ. zu Kiel, Kiel, Germany.

Kuhnt, W. et al. (2011). Cruise report SONNE-217: Variability of the Indonesian Throughflow within the Makassar-Java passage (MAJA). Report, Inst. für Geowiss., Christian-Albrechts-Univ. zu Kiel, Kiel, Germany.

Laepple, T., and Huybers, P. (2013). Reconciling discrepancies between Uk37 and Mg/Ca reconstructions of Holocene marine temperature variability. Earth and Planetary Science Letters, 375, 418-429.

Lea, D. W., Mashiotta, T. A., and Spero, H. J. (1999). Controls on magnesium and strontium uptake in planktonic foraminifera determined by live culturing. Geochimica et Cosmochimica Acta, 63(16), 2369-2379.

Lea, D. W., Pak, D. K., and Spero, H. J. (2000). Climate impact of late Quaternary equatorial Pacific sea surface temperature variations. Science, 289(5485), 1719-1724.

Lewis, E., Wallace, D., and Allison, L. J. (1998). Program developed for CO2 system calculations (p. 38). Carbon Dioxide Information Analysis Center, managed by Lockheed Martin Energy Research Corporation for the US Department of Energy.

Locarnini, R. A., A. V. Mishonov, J. I. Antonov, T. P. Boyer, H. E. Garcia, O. K. Baranova, M. M. Zweng, C. R. Paver, J. R. Reagan, D. R. Johnson, M. Hamilton, and D. Seidov, 2013. World Ocean Atlas 2013, Volume 1: Temperature. S. Levitus, Ed., A. Mishonov Technical Ed.; NOAA Atlas NESDIS 73, 40 pp.

Martin, P. A., and Lea, D. W. (2002). A simple evaluation of cleaning procedures on fossil benthic foraminiferal Mg/Ca. Geochemistry, Geophysics, Geosystems, 3(10), 1-8.

Mix, A. C. (2006). Running hot and cold in the eastern equatorial Pacific. Quaternary Science Reviews, 25(11), 1147-1149.

Mohtadi, M., Steinke, S., Groeneveld, J., Fink, H. G., Rixen, T., Hebbeln, D., ... and Herunadi, B. (2009). Low-latitude control on seasonal and interannual changes in planktonic foraminiferal flux and shell geochemistry off south Java: A sediment trap study. Paleoceanography, 24(1).

Mohtadi, M., Lückge, A., Steinke, S., Groeneveld, J., Hebbeln, D., and Westphal, N.

(2010). Late Pleistocene surface and thermocline conditions of the eastern tropical Indian Ocean. Quaternary Science Reviews, 29(7), 887-896.

Mohtadi, M., Oppo, D. W., Lückge, A., DePol-Holz, R., Steinke, S., Groeneveld, J., Hemme, N., and Hebbeln, D. (2011). Reconstructing the thermal structure of the upper ocean: Insights from planktic foraminifera shell chemistry and alkenones in modern sediments of the tropical eastern Indian Ocean. Paleoceanography, 26(3).

Morimoto, M., Abe, O., Kayanne, H., Kurita, N., Matsumoto, E., and Yoshida, N. (2002). Salinity records for the 1997–98 El Nino from Western Pacific corals. Geophysical Research Letters, 29(11), 35-1.

Müller, P. J., Kirst, G., Ruhland, G., von Storch, I., and Rosell-Melé, A. (1998). Calibration of the alkenone paleotemperature $U^{K'}_{37}$ index based on core-tops from the eastern South Atlantic and the global ocean (60° N - 60° S). Geochimica et Cosmochimica Acta, 62(10), 1757-1772.

Ni, Y., Foster, G. L., Bailey, T., Elliott, T., Schmidt, D. N., Pearson, P., Haley, B., and Coath, C. (2007). A core top assessment of proxies for the ocean carbonate system in surface-dwelling foraminifers. Paleoceanography, 22(3).

Nürnberg, D., Bijma, J., and Hemleben, C. (1996). Assessing the reliability of magnesium in foraminiferal calcite as a proxy for water mass temperatures. Geochimica et Cosmochimica Acta, 60(5), 803-814.

Pelejero, C., and Grimalt, J. O. (1997). The correlation between the $U^{K'}_{37}$ index and sea surface temperatures in the warm boundary: The South China Sea. Geochimica et Cosmochimica Acta, 61(22), 4789-4797.

Pelejero, C., Grimalt, J. O., Heilig, S., Kienast, M., and Wang, L. (1999). High-resolution UK 37 temperature reconstructions in the South China Sea over the past 220 kyr. Paleoceanography, 14(2), 224-231.

Pelejero, C., and Calvo, E. (2003). The upper end of the UK′ 37 temperature calibration revisited. Geochemistry, Geophysics, Geosystems, 4(2).

Prahl, F. G., and Wakeham, S. G. (1987). Calibration of unsaturation patterns in long-chain ketone compositions for palaeotemperature assessment. Nature, 330, 367-369.

Prahl, F. G., Muehlhausen, L. A., and Zahnle, D. L. (1988). Further evaluation of long-chain alkenones as indicators of paleoceanographic conditions. Geochimica et Cosmochimica Acta, 52(9), 2303-2310.

Prahl, F. G., Rontani, J. F., Zabeti, N., Walinsky, S. E., and Sparrow, M. A. (2010). Systematic pattern in–Temperature residuals for surface sediments from high latitude and other oceanographic settings. Geochimica et Cosmochimica Acta, 74(1), 131-143.

Regenberg, M., Nürnberg, D., Steph, S., Groeneveld, J., Garbe-Schönberg, D., Tiedemann, R., and Dullo, W. C. (2006). Assessing the effect of dissolution on planktonic foraminiferal Mg/Ca ratios: Evidence from Caribbean core tops. Geochemistry, Geophysics, Geosystems, 7(7).

Regenberg, M., Steph, S., Nürnberg, D., Tiedemann, R., and Garbe-Schönberg, D. (2009). Calibrating Mg/Ca ratios of multiple planktonic foraminiferal species with $\delta^{18}O$-calcification temperatures: Paleothermometry for the upper water column. Earth and Planetary Science Letters, 278(3), 324-336.

Regenberg, M., Nielsen, S. N., Kuhnt, W., Holbourn, A., Garbe-Schönberg, D., and Andersen, N. (2010). Morphological, geochemical, and ecological differences of the extant menardiform planktonic foraminifera *Globorotalia menardii* and *Globorotalia cultrata*. Marine Micropaleontology, 74(3), 96-107.

Regenberg, M., Regenberg, A., Garbe-Schönberg, D., and Lea, D. W. (2014). Global dissolution effects on planktonic foraminiferal Mg/Ca ratios controlled by the calcite-saturation state of bottom waters. Paleoceanography, 29(3), 127-142.

Reynolds, R. W., Smith, T. M., Liu, C., Chelton, D. B., Casey, K. S., and Schlax, M. G. (2007). Daily high-resolution-blended analyses for sea surface temperature. Journal of Climate, 20(22), 5473-5496.

Rincón-Martínez, D., Lamy, F., Contreras, S., Leduc, G., Bard, E., Saukel, C., Blanz, T., Mackensen, A., and Tiedemann, R. (2010). More humid interglacials in Ecuador during the past 500 kyr linked to latitudinal shifts of the equatorial front and the Intertropical Convergence Zone in the eastern tropical Pacific. Paleoceanography, 25(2).

Rosell-Melé, A., and Prahl, F. G. (2013). Seasonality of UK′ 37 temperature estimates as inferred from sediment trap data. Quaternary Science Reviews, 72, 128-136.

Rosenthal, Y., and Lohmann, G. P. (2002). Accurate estimation of sea surface temperatures using dissolution-corrected calibrations for Mg/Ca paleothermometry. Paleoceanography, 17(3), 16-1.

Rosenthal, Y., Oppo, D. W., and Linsley, B. K. (2003). The amplitude and phasing of climate change during the last deglaciation in the Sulu Sea, western equatorial Pacific. Geophysical Research Letters, 30(8).

Rosenthal, Y., et al. (2004). Interlaboratory comparison study of Mg/Ca and Sr/Ca measurements in planktonic foraminifera for paleoceanographic research. Geochemistry, Geophysics, Geosystems, 5(4).

Saher, M. H., Rostek, F., Jung, S. J. A., Bard, E., Schneider, R. R., Greaves, M., Ganssen, G. M., Elderfield, H., and Kroon, D. (2009). Western Arabian Sea SST during the penultimate interglacial: A comparison of $U^{K'}_{37}$ and Mg/Ca paleothermometry. Paleoceanography, 24(2).

Schneider, B., Leduc, G., and Park, W. (2010). Disentangling seasonal signals in Holocene climate trends by satellite-model-proxy integration. Paleoceanography, 25(4).

Sikes, E. L., and Volkman, J. K. (1993). Calibration of alkenone unsaturation ratios ($U^{K'}_{37}$) for paleotemperature estimation in cold polar waters. Geochimica et Cosmochimica Acta, 57(8), 1883-1889.

Sonzogni, C., Bard, E., Rostek, F., Lafont, R., Rosell-Mele, A., and Eglinton, G. (1997). Core-top calibration of the alkenone index vs sea surface temperature in the Indian Ocean. Deep Sea Research Part II: Topical Studies in Oceanography, 44(6), 1445-1460.

Sonzogni, C., Bard, E., Rostek, F., Dollfus, D., Rosell-Melé, A., and Eglinton, G. (1997b). Temperature and salinity effects on alkenone ratios measured in surface sediments from the Indian Ocean. Quaternary Research, 47(3), 344-355.

Steinke, S., Kienast, M., Groeneveld, J., Lin, L. C., Chen, M. T., and Rendle-Bühring, R. (2008). Proxy dependence of the temporal pattern of deglacial warming in the tropical South China Sea: toward resolving seasonality. Quaternary Science Reviews, 27(7), 688-700.

Steph, S., Regenberg, M., Tiedemann, R., Mulitza, S., and Nürnberg, D. (2009). Stable isotopes of planktonic foraminifera from tropical Atlantic/Caribbean core-tops: Implications for reconstructing upper ocean stratification. Marine Micropaleontology, 71(1), 1-19.

Stott, L., Poulsen, C., Lund, S., and Thunell, R. (2002). Super ENSO and global climate oscillations at millennial time scales. Science, 297(5579), 222-226.

Stott, L., Timmermann, A., and Thunell, R. (2007). Southern hemisphere and deep-sea warming led deglacial atmospheric CO2 rise and tropical warming. science, 318(5849), 435-438.

Tanaka, Y., and Kawahata, H. (2001). Seasonal occurrence of coccoliths in sediment traps from West Caroline Basin, equatorial West Pacific Ocean. Marine Micropaleontology, 43(3), 273-284.

Timmermann, A., Sachs, J., and Elison Timm, O. (2014). Assessing divergent SST behavior during the last 21 ka derived from alkenones and G. ruber-Mg/Ca in the Equatorial Pacific. Paleoceanography.

Tyrrell, T., and Merico, A. (2004). Emiliania huxleyi: bloom observations and the conditions that induce them. In Coccolithophores (pp. 75-97). Springer Berlin Heidelberg.

Villanueva, J., and Grimalt, J. O. (1996). Pitfalls in the chromatographic determination of

the alkenone $U^{K'}_{37}$ index for paleotemperature estimation. Journal of Chromatography A, 723(2), 285-291.

Visser, K., Thunell, R., and Stott, L. (2003). Magnitude and timing of temperature change in the Indo-Pacific warm pool during deglaciation. Nature, 421(6919), 152-155.

Wang, Y. V., Leduc, G., Regenberg, M., Andersen, N., Larsen, T., Blanz, T., and Schneider, R. R. (2013). Northern and southern hemisphere controls on seasonal sea surface temperatures in the Indian Ocean during the last deglaciation. Paleoceanography, 28(4), 619-632.

Wiesner, M. G., Zheng, L. F., Wong, H. K., Wang, Y. F., and Chen, W. (1996). Fluxes of particulate matter in the South China Sea. Particle Flux in the Ocean, 293-312.

Xu, J., Kuhnt, W., Holbourn, A., Regenberg, M., and Andersen, N. (2010). Indo-Pacific Warm Pool variability during the Holocene and Last Glacial Maximum. Paleoceanography, 25(4).

5.8 Supplementary Information

Supplementary Information Table 5.1 - Summary of compiled new and previously published $U^{K'}_{37}$ and Mg/Ca measurements

Sample	Latitude (°N)	Longitude (°E)	Water depth (m)	Region[a]	*G. ruber* Mg/Ca (mmol/mol)[b]	*G. ruber* Mg/Ca_{cor} (mmol/mol)[c]	$\Delta[CO_3^{2-}]$[d]	$U^{K'}_{37}$ [e]	Alkenone conc. (ng/g)	maSST[f] (°C)
SO95 17922	15.42	117.46	4221	NSCS	-	-	-	0.940	-	28.39
SO95 17924	19.41	118.85	3438	NSCS	-	-	-	0.929	-	27.21
SO95 17925	19.85	119.05	2979	NSCS	-	-	-	0.930	-	27.13
SO95 17926	19.00	118.73	3761	NSCS	-	-	-	0.925	-	27.32
SO95 17928	18.27	119.75	2486	NSCS	-	-	-	0.930	-	28.06
SO95 17930	20.33	115.78	629	NSCS	4.78	4.78	25.69	-	-	26.44
SO95 17931	20.10	115.96	1005	NSCS	4.19	4.19	17.51	-	-	26.58
SO95 17932	19.95	116.04	1365	NSCS	3.84	3.84	13.76	-	-	26.66
SO95 17933	19.53	116.23	1972	NSCS	3.89	3.89	6.89	-	-	26.81
SO95 17934	19.03	116.46	2665	NSCS	-	-	-	0.918	-	26.98
SO95 17935	18.88	116.53	3143	NSCS	-	-	-	0.926	-	27.04
SO95 17936	18.77	117.12	3809	NSCS	-	-	-	0.928	-	27.15
SO95 17937	19.50	117.67	3428	NSCS	-	-	-	0.921	-	26.98
SO95 17938	19.79	117.54	2840	NSCS	-	-	-	0.930	-	26.88
SO95 17941	21.52	118.48	2201	NSCS	3.86	3.86	4.59	-	-	26.63
SO95 17943	18.95	117.55	917	NSCS	3.85	3.85	18.51	0.920	-	27.13
SO95 17944	18.66	113.64	1219	NSCS	4.02	4.02	14.80	-	-	26.93
SO95 17945	18.13	113.78	2404	NSCS	3.55	3.55	1.68	0.918	-	27.11
SO95 17946	18.13	114.25	3464	NSCS	-	-	-	0.915	-	27.17
SO95 17947	18.47	116.03	3765	NSCS	-	-	-	0.910	-	27.10
SO95 17948	16.71	114.90	2855	NSCS	-	-	-	0.937	-	27.65
SO95 17949	17.35	115.17	2195	NSCS	3.80	3.80	4.60	0.927	-	27.46
SO95 17950	16.09	112.90	1868	NSCS	3.65	3.65	7.81	0.938	-	27.70
SO95 17951	16.29	113.41	2340	NSCS	3.64	3.64	2.55	0.934	-	27.70
SO95 17952	16.67	114.47	2882	NSCS	-	-	-	0.938	-	27.66

Sample	Latitude (°N)	Longitude (°E)	Water depth (m)	Region[a]	*G. ruber* Mg/Ca (mmol/mol)[b]	*G. ruber* Mg/Ca_{cor} (mmol/mol)[c]	$\Delta[CO_3^{2-}]$[d]	$U^{K'}_{37}$ [e]	Alkenone conc. (ng/g)	maSST[f] (°C)
SO95 17954	14.80	111.53	1517	NSCS	3.72	3.72	12.27	0.933	-	27.71
SO95 17955	14.12	112.18	2404	NSCS	3.87	3.87	1.68	0.933	-	27.84
SO95 17956	13.85	112.59	3387	NSCS	-	-	-	0.936	-	27.88
SO95 17957	10.90	115.30	2197	SSCS	3.96	3.96	4.60	0.968	-	28.62
SO95 17958	11.62	115.08	2581	SSCS	3.93	3.93	-3.77	0.969	-	28.56
SO95 17959	11.14	115.29	1957	SSCS	3.92	3.92	6.98	0.968	-	28.64
SO95 17960	10.12	115.56	1707	SSCS	4.25	4.25	9.24	0.966	-	28.72
SO95 17961	8.51	112.33	1795	SSCS	4.00	4.00	8.45	0.956	-	28.50
SO95 17962	7.18	112.08	1970	SSCS	3.99	3.99	6.89	0.956	-	28.62
SO95 17963	6.17	112.67	1233	SSCS	4.40	4.40	14.72	0.963	-	28.72
SO95 17964	6.16	112.21	1556	SSCS	3.92	3.92	11.23	0.961	-	28.73
SO95 17965	6.16	112.55	889	SSCS	4.32	4.32	18.91	0.972	-	28.72
GeoB10008	-0.95	98.26	934	SUM	5.68	4.94	31.32	0.992	-	29.50
GeoB10010	-1.17	97.98	2937	SUM	4.99	4.34	3.58	-	-	29.45
GeoB10014	1.68	96.98	1158	SUM	6.29	5.47	26.46	-	-	29.84
GeoB10016	1.59	96.66	1900	SUM	5.28	4.59	15.61	-	-	29.78
GeoB10022	-0.50	98.85	706	SUM	6.28	5.46	39.46	-	-	29.68
GeoB10024	-0.77	99.27	1381	SUM	5.33	4.63	22.56	-	-	29.71
GeoB10025	-0.67	99.12	1149	SUM	5.50	4.78	26.63	-	-	29.71
GeoB10026	-0.94	99.52	1641	SUM	5.14	4.47	18.90	0.994	-	29.66
GeoB10027	-0.80	99.65	875	SUM	5.34	4.64	33.00	-	-	29.68
GeoB10028	-0.70	99.76	522	SUM	6.33	5.50	55.23	-	-	29.68
GeoB10029	-1.49	100.13	974	SUM	5.45	4.74	30.26	-	-	29.62
GeoB10033	-1.56	99.95	1756	SUM	4.92	4.28	17.40	0.987	-	29.63
GeoB10034	-4.16	101.50	995	SUM	5.32	4.63	29.71	-	-	29.16
GeoB10036	-5.34	103.66	1502	SUM	5.41	4.70	20.81	0.990	-	28.87
GeoB10038	-5.94	103.25	1891	SUM	4.78	4.16	15.72	0.978	-	28.73
GeoB10039	-5.86	103.29	1799	SUM	5.53	4.81	16.84	-	-	28.76
GeoB10040	-6.47	102.86	2605	SUM	5.39	4.69	7.43	-	-	28.57
GeoB10041	-6.27	103.01	1540	SUM	4.94	4.30	20.27	-	-	28.61
GeoB10042	-7.11	104.64	2457	SUM	5.14	4.47	9.14	0.983	-	28.55
GeoB10044	-8.50	109.02	3346	JAV	5.21	4.53	-1.53	0.959	-	28.01
GeoB10047	-9.31	109.02	1780	JAV	4.68	4.07	17.09	0.970	-	27.88
GeoB10049	-8.78	110.50	1289	JAV	4.49	3.90	24.01	0.969	-	27.84

Sample	Latitude (°N)	Longitude (°E)	Water depth (m)	Region[a]	*G. ruber* Mg/Ca (mmol/mol)[b]	*G. ruber* Mg/Ca_{cor} (mmol/mol)[c]	$\Delta[CO_3^{2-}]$[d]	$U^{K'}_{37}$ [e]	Alkenone conc. (ng/g)	maSST[f] (°C)
GeoB10050	-9.47	110.45	1221	JAV	4.22	3.67	25.24	0.971	-	27.84
GeoB10058	-8.68	112.64	1113	JAV	5.30	4.61	27.33	-	-	27.64
GeoB10059	-8.68	112.87	1370	JAV	4.71	4.10	22.73	0.953	-	27.68
GeoB10061	-9.73	113.02	2170	JAV	4.84	4.21	12.41	0.974	-	27.82
GeoB10063	-9.64	118.15	2501	JAV	5.34	4.64	8.64	0.980	-	28.22
GeoB10064	-9.53	118.30	2033	JAV	5.14	4.47	13.99	-	-	28.21
GeoB10065	-9.22	118.89	1284	JAV	4.86	4.23	24.09	0.980	-	28.09
GeoB10068	-9.59	121.15	2010	JAV	4.43	3.85	14.27	0.986	-	28.41
GeoB10069	-9.59	120.92	1249	JAV	5.03	4.37	24.70	0.984	-	28.38
SO189/2_002	-5.48	103.01	1972	SUM	5.42	4.71	14.73	-	-	28.82
SO189/2_003	-4.70	101.96	1707	SUM	5.91	5.14	18.04	0.972	-	29.04
SO189/2_009	-4.16	101.64	1128	SUM	5.56	4.83	27.04	0.976	-	29.16
SO189/2_011	-3.83	101.23	911	SUM	5.53	4.81	31.92	-	-	29.24
SO189/2_027	-1.88	99.61	1002	SUM	5.92	5.15	29.54	-	-	29.49
SO189/2_028	-1.67	99.68	1758	SUM	5.66	4.92	17.38	-	-	29.60
SO189/2_031	-1.30	99.72	1734	SUM	5.10	4.43	17.69	0.946	-	29.64
SO189/2_032	-1.62	100.00	1751	SUM	5.84	5.08	17.47	-	-	29.64
SO189/2_034	-1.46	100.23	560	SUM	5.87	5.10	48.27	-	-	29.59
SO189/2_035	-0.87	99.80	755	SUM	5.77	5.02	37.39	-	-	29.67
SO189/2_038	-0.79	99.91	517	SUM	6.03	5.24	55.86	-	-	29.68
SO189/2_041	0.34	98.13	674	SUM	5.96	5.18	40.95	0.991	-	29.78
SO189/2_048	0.95	98.13	457	SUM	6.11	5.31	63.63	0.986	-	29.83
SO189/2_053	1.00	98.03	82	SUM	6.33	5.50	167.95	-	-	29.82
SO189/2_059	1.15	98.07	479	SUM	6.38	5.55	60.02	-	-	29.82
SO189/2_060	1.45	98.05	551	SUM	5.70	4.96	49.78	0.990	-	29.86
SO189/2_072	2.83	96.39	913	SUM	5.78	5.03	31.87	-	-	29.86
SO189/2_076	2.82	96.61	1108	SUM	5.79	5.03	27.43	-	-	29.89
SO189/2_080	2.95	96.50	1088	SUM	6.06	5.27	27.83	0.959	-	29.86
SO189/2_084	2.99	96.22	861	SUM	6.03	5.24	33.45	-	-	29.83
SO189/2_089	2.78	96.42	916	SUM	5.96	5.18	31.79	0.972	-	29.86
SO189/2_097	2.56	96.76	1136	SUM	5.79	5.03	26.88	0.991	-	29.84
SO189/2_101	2.49	97.12	767	SUM	5.52	4.80	36.90	-	-	29.87
SO189/2_104	3.20	96.78	1013	SUM	5.57	4.84	29.33	-	-	29.92
SO189/2_112	3.87	96.01	81	SUM	6.74	5.86	168.37	-	-	29.82

Sample	Latitude (°N)	Longitude (°E)	Water depth (m)	Region[a]	*G. ruber* Mg/Ca (mmol/mol)[b]	*G. ruber* Mg/Ca_{cor} (mmol/mol)[c]	$\Delta[CO_3^{2-}]$[d]	$U^{K'}_{37}$ [e]	Alkenone conc. (ng/g)	maSST[f] (°C)
SO189/2_114	3.49	95.33	1535	SUM	5.72	4.97	20.34	0.978	-	29.69
SO189/2_118	3.52	96.31	804	SUM	5.69	4.95	35.39	-	-	29.87
SO189/2_121	3.28	96.15	1031	SUM	5.53	4.81	28.97	-	-	29.85
SO189/2_139	1.76	96.77	1854	SUM	6.30	5.48	16.17	-	-	29.82
SO189/2_147	-0.69	98.07	1052	SUM	5.68	4.94	28.55	-	-	29.51
SO185-18456	-9.53	130.43	348	ETS	4.96	4.96	81.26	0.983	1489	28.60
SO185-18457	-9.45	130.18	394	ETS	4.83	4.83	73.21	0.984	1838	28.60
SO185-18458	-9.02	129.01	2045	ETS	4.50	4.50	13.85	0.981	760	28.63
SO185-18459	-8.50	128.17	1741	ETS	4.64	4.64	17.60	0.978	347	28.54
SO185-18460	-8.79	128.64	1876	ETS	4.86	4.86	15.90	0.983	295	28.61
SO185-18462	-9.09	129.24	1455	ETS	4.42	4.42	21.47	-	-	28.64
SO185-18463	-9.10	129.28	1311	ETS	4.84	4.84	23.67	-	-	28.64
SO185-18464	-9.12	129.32	1206	ETS	4.32	4.32	25.53	-	-	28.65
SO185-18465	-9.14	129.39	1082	ETS	4.84	4.84	27.95	-	-	28.64
SO185-18466	-9.16	129.42	1004	ETS	5.06	5.06	29.50	-	-	28.64
SO185-18467	-9.17	129.47	899	ETS	-	-	-	0.968	185	28.64
SO185-18468	-9.20	129.53	803	ETS	5.15	5.15	35.43	0.982	835	28.63
SO185-18469	-9.24	129.64	704	ETS	5.02	5.02	39.55	-	-	28.62
SO185-18470	-9.30	129.80	603	ETS	5.05	5.05	44.99	0.981	1343	28.60
SO185-18471	-9.37	129.98	485	ETS	5.14	5.14	59.25	0.973	1058	28.59
SO185-18474	-11.17	122.15	1605	JAV	4.56	4.56	19.37	-	-	28.53
SO185-18475	-11.03	121.70	1771	JAV	4.56	4.56	17.21	0.979	1551	28.45
SO185-18476	-10.95	120.99	986	JAV	4.39	4.39	29.95	0.976	666	28.39
SO185-18477	-10.83	120.62	1480	JAV	4.50	4.50	21.11	0.973	495	28.37
SO185-18478	-11.02	120.08	1769	JAV	4.34	4.34	17.23	0.972	388	28.41
SO185-18479	-12.45	121.37	2974	WTS	-	-	-	0.963	203	28.84
SO185-18480	-12.52	121.65	2295	WTS	-	-	-	0.938	85	28.86
SO185-18481	-12.56	121.84	1897	WTS	4.52	4.52	15.65	0.977	348	28.88
SO185-18482	-12.62	122.15	1508	WTS	4.84	4.84	20.72	0.976	189	28.90
SO185-18483	-12.63	122.31	1356	WTS	4.76	4.76	22.95	-	-	28.90
SO185-18484	-12.66	122.37	1247	WTS	4.81	4.81	24.74	-	-	28.90
SO185-18485	-12.67	122.41	1132	WTS	5.06	5.06	26.96	0.952	92	28.90
SO185-18488	-12.89	122.76	555	WTS	5.09	5.09	49.11	0.974	245	28.95
SO185-18489	-13.05	122.93	431	WTS	4.85	4.85	67.98	0.980	733	28.96

Sample	Latitude (°N)	Longitude (°E)	Water depth (m)	Region[a]	*G. ruber* Mg/Ca (mmol/mol)[b]	*G. ruber* Mg/Ca_{cor} (mmol/mol)[c]	$\Delta[CO_3^{2-}]$[d]	$U^{K'}_{37}$ [e]	Alkenone conc. (ng/g)	maSST[f] (°C)
SO185-18490	-13.24	122.95	407	WTS	4.89	4.89	71.22	0.981	645	28.96
SO185-18491	-13.82	122.99	327	WTS	5.07	5.07	84.57	-	-	28.95
SO185-18492	-14.14	122.65	350	WTS	5.49	5.49	80.93	-	-	28.92
SO185-18493	-13.42	122.08	599	WTS	5.15	5.15	45.25	-	-	28.91
SO185-18494	-13.38	121.92	839	WTS	5.22	5.22	34.16	-	-	28.91
SO185-18495	-13.12	121.86	1609	WTS	4.96	4.96	19.32	0.970	177	28.90
SO185-18496	-12.70	121.28	2541	WTS	-	-	-	0.971	224	28.85
SO185-18497	-12.70	121.28	2535	WTS	-	-	-	0.958	349	28.85
SO185-18499	-14.91	120.57	1383	WTS	5.19	5.19	22.52	0.965	144	28.78
SO185-18500	-14.98	120.70	1167	WTS	4.71	4.71	26.28	0.970	149	28.78
SO185-18501	-15.14	120.78	742	WTS	4.98	4.98	37.93	0.977	317	28.78
SO185-18502	-15.19	120.91	564	WTS	5.25	5.25	47.60	0.977	566	28.78
SO185-18503	-15.31	121.08	354	WTS	4.84	4.84	80.28	-	-	28.75
SO185-18505	-15.79	120.20	1045	WTS	5.15	5.15	28.69	0.979	324	28.65
SO185-18506	-15.31	119.50	2410	WTS	-	-	-	0.964	53	28.64
SO185-18507	-13.85	120.00	2450	WTS	-	-	-	0.949	53	28.78
SO217-18514	-4.53	118.95	652	MAJA	4.26	4.26	42.02	0.947	597	29.25
SO217-18515	-3.63	119.37	678	MAJA	-	-	-	0.981	514	29.18
SO217-18516	-1.64	117.54	930	MAJA	-	-	-	0.983	789	29.01
SO217-18517	-1.54	117.57	699	MAJA	4.45	4.45	39.76	0.984	811	29.01
SO217-18518	-1.14	117.84	620	MAJA	4.70	4.70	43.93	-	-	29.04
SO217-18519	-0.57	118.12	1657	MAJA	4.87	4.87	18.69	0.970	528	29.09
SO217-18521	0.51	118.93	991	MAJA	4.39	4.39	29.82	-	-	29.08
SO217-18522	1.40	119.09	986	MAJA	4.94	4.94	29.95	0.976	581	28.89
SO217-18523	0.18	119.44	2175	MAJA	5.22	5.22	12.35	0.963	173	29.16
SO217-18524	-1.66	118.91	1561	MAJA	4.47	4.47	19.98	-	-	29.41
SO217-18525	-2.56	118.64	1822	MAJA	5.50	5.50	16.56	-	-	29.38
SO217-18526	-3.62	118.17	1523	MAJA	5.03	5.03	20.51	0.989	860	29.09
SO217-18527	-3.97	117.82	1617	MAJA	5.48	5.48	19.22	0.988	722	29.11
SO217-18528	-4.76	117.89	1785	MAJA	4.90	4.90	17.03	0.982	763	29.19
SO217-18529	-4.66	118.03	1915	MAJA	4.35	4.35	15.43	0.984	487	29.21
SO217-18530	-5.24	117.34	872	MAJA	4.94	4.94	33.09	-	-	29.02
SO217-18531	-5.17	117.45	1085	MAJA	4.54	4.54	27.89	0.989	1063	29.05
SO217-18532	-5.93	116.83	628	MAJA	4.45	4.45	43.43	-	-	28.89

Sample	Latitude (°N)	Longitude (°E)	Water depth (m)	Region[a]	*G. ruber* Mg/Ca (mmol/mol)[b]	*G. ruber* Mg/Ca_{cor} (mmol/mol)[c]	$\Delta[CO_3^{2-}]$[d]	$U^{K'}_{37}$ [e]	Alkenone conc. (ng/g)	maSST[f] (°C)
SO217-18534	-7.52	116.27	563	MAJA	4.43	4.43	47.76	0.983	459	28.85
SO217-18535	-7.14	117.22	506	MAJA	4.52	4.52	57.16	0.989	1431	28.76
SO217-18536	-7.47	118.24	835	MAJA	4.89	4.89	34.29	-	-	28.70
SO217-18537	-7.60	118.25	930	MAJA	4.49	4.49	31.42	-	-	28.75
SO217-18538	-7.60	118.27	908	MAJA	-	-	-	0.989	321	28.75
SO217-18539	-6.95	119.37	853	MAJA	4.46	4.46	33.71	-	-	28.61
SO217-18540	-6.88	119.59	1201	MAJA	4.56	4.56	25.63	0.933	225	28.60
SO217-18541	-6.78	119.41	739	MAJA	4.42	4.42	38.06	0.983	886	28.56
SO217-18542	-5.87	119.07	925	MAJA	4.80	4.80	31.55	0.981	768	28.48
SO217-18544	-4.53	118.59	2010	MAJA	-	-	-	0.969	307	29.30
SO217-18545	-5.10	118.73	714	MAJA	4.70	4.70	39.12	-	-	29.06

[a] Scheme of different regions is shown in Figure 5.2 .
[b] Raw Mg/Ca values, prior to correction. Data compiled from Regenberg et al. (2014), Mohtadi et al. (2011), and new measurements of this study.
[c] Mg/Ca values with 15 % correction (following Rosenthal et al., 2014) applied to samples from Mohtadi et al. (2011) to account for differences in cleaning methodology.
[d] $\Delta[CO_3^{2-}]$ calculated using SouthEast Asian Time Series (SEATS) stations (Chou et al., 2007) and World Ocean Circulation Experiment (WOCE) stations. See Section 5.5.6.
[e] $U^{K'}_{37}$ data compiled from Pelejero and Grimalt (1997), Mohtadi et al. (2011) and new measurements of this study.
[f] maSST derived from Advanced Very High Resolution Radiometer (AVHRR) satellite SST estimations (Reynolds et al., 2007)

Chapter 6

Conclusions and Outlook

In this thesis, we have studied the evolution of hydroclimate and oceanic circulation in the western equatorial Pacific (WEP) region during the late Pleistocene, and investigated some aspects of geochemical SST proxies used for paleoclimate reconstructions. Together, these findings add to the body of existing literature to improve our knowledge of past climate dynamics in a region of the world that is still poorly understood.

Past hydrologic variability in the WEP was investigated through a multi-proxy analysis on sediment core MD06-3075, located in the Davao Gulf in the southern Philippines. This record, which extends over the past 120 ka, shows that during times of strong precessional cyclicitiy, past sediment discharge driven by precipitation changes reacted to local precessional insolation forcing. During periods of increased local insolation forcing, sediment discharge was reduced, and vice versa. Such a finding is in agreement with several speleothem and sediment core records of precessional-scale hydroclimate variability in the WEP, and implicates the role of the Intertropical Convergence Zone (ITCZ) and Walker Circulation in driving past precipitation variability in the WEP, although the relative importance of each is still unquantified. A greater number of paleoclimate records covering a wider spatial extent in the WEP, together with novel modeling approaches, may help to resolve this issue in the future. In contrast, during periods of weakened precessional insolation forcing and lower sea level, the hydroclimate response was muted and precipitation was reduced, likely induced by widespread subsidence of air masses over the entire Sunda Shelf region. Millennial-scale climate variability was also assessed based on records from this core, with a focus on the last deglaciation. Inferred wetter conditions observed during Heinrich Stadial 1 appear to contradict with the established notion of a global southward shift in the mean ITCZ position during this time period, but are in agreement with more recent modeling results that imply a more complex precipitation response to past rapid climate changes in the WEP.

A compilation of benthic foraminiferal carbon isotope ($\delta^{13}C$) were used to study changes in deep and intermediate oceanic circulation in the WEP and Indonesian Throughflow (ITF) over the more recent glacial-interglacial cycle, with a focus on the past two glacial terminations. The most striking features of these compiled records are two distinct

troughs in $\delta^{13}C$ in sediment core MD06-3067, located at 6 °N off the east coast of the island of Mindanao ~1600 m water depth, occurring during Terminations I and II. We interpret this as an intrusion of (or increased proportion of) North Pacific Intermediate Water (NPIW) at mid-depths in the West Pacific during glacial terminations, which may be related to the onset of the Pacific Meridional Overturning Circulation. Such an intrusion of NPIW to the low latitudes, at such depth, has not been previously documented, and would require a major reorganization of Pacific intermediate water masses during past deglacials. These troughs in core MD06-3067 are furthermore coeval with increased ventilation of AAIW recorded in sediment core MD97-2120 in the southwest Pacific, which is reflected to result from increased production of AAIW resulting from a southward shift of the westerlies in the Southern Hemisphere. Such processes may therefore be intricately linked to the storage and release of carbon in the ocean on glacial-interglacial timescales. Further studies may therefore focus on the West Pacific region, including shallower and deeper waters, as an indicator of past intermediate water variability linked to climatic changes occurring in the North Pacific.

The ITF respresents an important pathway of water masses from the Pacific to Indian Ocean, and yet is has been historically under-represented in paleocirculation studies. Our new benthic foraminiferal $\delta^{13}C$ results provide the first insight into deglacial intermediate and deep water circulation variability in the central ITF pathways, complementing existing records of ITF outflow variability from the Timor Sea and eastern Indian Ocean. Our results indicate a long-term shift in the source of intermediate waters from the LGM to present in the ITF passages. At the onset of the last deglacial period, poorly-ventilated NPIW dominated the 'northwestern' route, whilst the 'southeastern' route was sourced from better ventilated AAIW. Records from the Timor Sea suggest weaker vertical mixing of the water column and increased influenced of Indian Ocean intermediate waters into the Timor Sea, consistent with an overall reduced ITF in this time period. Over the course of the deglaciation and Holocene, our results indicate a general strengthening of the deep and intermediate ITF component. However, the northwestern passage remained relatively isolated over the deglaciation, and only became better ventilated during the late Holocene, in line with modern observations of a relatively weak contribution of NPIW to the deep and intermediate ITF. These results are a first attempt

to study past ITF deep and intermediate water mass variability, and show that the ITF transport likely changed in the past due to variability in the intermediate structure of water masses in the WEP. However, we note that large areas of the ITF, in particular the inflow regions and the Banda Sea, remain unaccounted for, and thus these areas may form the basis for future circulation studies.

A modern core-top study of two commonly used proxies for paleotemperature reconstructions, the Mg/Ca ratio of the planktonic foraminifera *G. ruber*, and the $U^{K'}_{37}$ alkenone unsaturation index, indicate significant complexities exist in recorded proxy signals which extend beyond simple annual average SST variability. In particular, results from $U^{K'}_{37}$ measurements suggest a lower sensitivity of $U^{K'}_{37}$ to temperature at high temperatures than previous global calibrations would suggest. This has implications, in that existing $U^{K'}_{37}$-based paleotemperature records from the WEP likely underestimate the magnitude of deglacial temperature rise, and thus existing records should be reconsidered with this in mind. Furthermore, residual patterns of $U^{K'}_{37}$ SST estimates suggests a control of seasonal productivity variability on $U^{K'}_{37}$, with temperatures biased towards low-productivity months in regions of highly variable production regimes (e.g. in upwelling areas). Our Mg/Ca results show a less consistent seasonal signal in residual SST patterns, although results are complicated by errors induced by analytical and methodological uncertainties (in particular with regards to different foraminiferal cleaning procedures between compiled datasets). Since our calibrations and regressions cover only a relatively small temperature range in the WEP (between 24 and 30°C), these uncertainties, which likely induce errors upwards of 1 °C, can have a significant impact on our results. Furthermore, we show that Mg/Ca values can be biased by the carbonate ion saturation state, and we recommend that studies in the future investigate the influence of additional variables such as salinity and pH. However, incorporating these variables may require more robust statistical approaches than have been employed here.

A number of Mg/Ca and $U^{K'}_{37}$ based SST reconstructions now exist in the western equatorial Pacific, covering a range of timescales. But to effectively understand what information on past SST variability Mg/Ca and $U^{K'}_{37}$ signals can give us, each record must be judged and interpreted individually with respect to past changes in seasonal production, ecology (e.g. salinity, pH) and post depositional (e.g. calcite undersaturation,

bioturbation) conditions. Recent proxy-model approaches have reported success in using seasonal-weighting of modeled temperatures in explaining discrepancies between the two proxies over the last deglacial period and Holocene. However, we suggest that more proxy-model comparisons of modern relationships between proxy recorders and SST, incorporating a greater number of climatic variables, would yield insights into the main drivers of inter-proxy differences, which could then be applied to improve interpretations of paleoclimate records.